Magnetic Current Inspired Antennas For Wearable Applications

by

Sree Pramod Pinapati

B. Eng. (Electrical & Electronics Engineering, First Class Honors), 2014

Thesis submitted for the degree of

Doctor of Philosophy

in

School of Electrical & Electronic Engineering
Faculty of Engineering, Computer & Mathematical Sciences
The University of Adelaide

2018

Supervisors:

Prof. Christophe Fumeaux, School of Electrical & Electronic Engineering

Dr. Damith Chinthana Ranasinghe, School of Electrical & Computer Science

To those who have put me here today.
Hard work never brings fatigute. It brings satisfaction - Shri Narendra Modi

Contents

Abstract

Since the year 2000 there has been a growing interest in an area known as body-worn communications for diverse applications ranging from healthcare to security. An integral component of body-worn devices are antennas which facilitate transmission of pertinent information about the user such as location. The focus of this thesis is on the antennas, which in the context of body-centric communications are also known as body-worn or wearable antennas.

Prior to designing body-worn antennas there are some subsidiary issues that must be addressed. One of these subsidiary issues is realizing a robust and reliable connection between rigid and flexible devices. This issue must be addressed as textile antennas will be interfaced with rigid electronic devices when viewed from a holistic system perspective. Consequently, this thesis investigates connection strategies and proposes implementations realized solely from textile materials that can connect rigid and flexible devices.

The second subsidiary issue is related to antenna ground planes. Ground planes for wearable antennas are likely to be bent, given the inherent curvature of the human body. In this regard it is important to appreciate the effects of conformal ground planes on the performance of body-worn antennas, which is an issue that is addressed in this thesis.

The final pragmatic issue that must be addressed for wearable antennas is user comfort. The issue of user comfort can best be understood by considering the extent of the ground plane. Generally, to isolate the antenna from the deleterious effect of the human body, a ground plane is used. The most common method of realizing ground planes for body-worn antennas is to use metalized fabrics, which are available with high conductivity. However, conductive fabric ground planes can be uncomfortable, especially if extended ground planes are used to enhance the isolation between the antenna and the human body. Combining conductive fabrics and conductive embroidered structures which are realized through conductive yarns is an attractive option to enhance the wearability of extended ground planes. This hybrid approach is attractive as conductive yarns tend to be less intrusive than conductive fabrics. A challenge in using computerized embroidery however is the accurate characterization and modeling

of conductive embroidered structures. The two aforementioned issues are addressed in this thesis through the use of scattering experiments and introduction of an effective modeling parameter.

Focusing now on the antennas themselves, it is generally accepted that the design of body-worn antennas is a challenging task. Primarily, the design of body-worn antennas is quite demanding as the antenna performance must be insensitive to the effect of the human body, which is a very lossy and complicated propagation medium. An additional consideration is the potential deformation of the antenna geometry which will depend on where the antenna is placed on the human body. To ensure robust performance, the aforementioned factors must be accounted for in the design phase of the antenna.

Consequently, it is vital to select appropriate antenna topologies for body-worn applications. Radiating cavities, or more specifically closed and semi-closed cavity antennas are attractive for wearable applications as they are robust to environmental effects and exhibit high performance with a simple fabrication process. However, closed and semi-closed cavity antennas can be rather large, which can inhibit their deployment for body-worn scenarios. Additionally, realizing dual-band or multi-band closed and semi-closed cavity antennas is challenging as the operating frequency is determined by fixed ratios. In regards to the these challenges, this thesis proposes and validates the following solutions:

1. A new miniaturized low-profile semi-closed UHF cavity antenna is proposed and experimentally validated. This new topology is shown to be robust to the effects of the human body and mechanical deformations. A salient feature of this antenna is the exploitation of computerized embroidery to realize the cavity walls.

2. A new dual-band cavity antenna is realized by the integration of two similar radiating elements operating as equivalent magnetic currents into a single cavity. The antenna is targeted to cover the lower and upper microwave ISM bands. The incorporation of a planar feeding element and a largely independent control of both the lower and upper microwave ISM bands is an attractive feature of this design.

As previously mentioned, obtaining steady performance for body-worn antennas under adverse environmental conditions is a challenging task. One method to deal with

this issue is to utilize frequency reconfigurable antennas. In this context this thesis presents a new proof-of-concept frequency reconfigurable cavity-backed slot antenna. An attractive feature of this antenna is that the reconfiguration elements, i.e varactors, are embedded inside the cavity structure which helps to insulate them from adverse external forces. Additionally, the proposed antenna can be impedance matched through a planar feeding mechanism over a large fractional tuning range of 20% without requiring lumped matching elements.

Overall, this thesis holistically investigates a range of issues related to the realization and utilization of wearable antennas for body-worn applications. Thus the contributions of this thesis lay a strong foundation for future wearable antenna deployment.

Originality Declaration

For a thesis that does contain work already in the public domain.

I certify that this work contains no material which has been accepted for the award of any other degree or diploma in my name in any university or tertiary institution and, to the best of my knowledge and belief, contains no material previously published or written by another person, except where due reference has been made in the text. In addition, I certify that no part of this work will, in the future, be used in a submission in my name for any other degree or diploma in any university or other tertiary institution without the prior approval of the University of Adelaide and where applicable, any partner institution responsible for the joint award of this degree.

I give permission for the digital version of my thesis to be made avaliable on the web, via the University's digital research repository, the Library Search and also through web search engines, unless permission has been granted by the University to restrict access for a period of time.

I acknowledge the support I have received for my research through the provision of an Australian Government Research Training Program Scholarship.

Signed

13/07/2018
Date

Acknowledgments

This thesis is a shared achievement among many people. First and foremoest among these individuals is Prof. Christophe Fumeaux. Under the guidance of Prof. Christophe Fumeaux I began my PhD journey in 2014. Right from the beginning Prof. Fumeaux provided the right amount of guidance and independence. Prof. Fumeaux has taught me many theoretical concepts and more importantly how to do research. Specifically, how to systematically investigate complicated concepts in a rigorous manner and to challenge my inherent biases on what the results should be. At anytime when I had technical doubts Prof. Fumeaux was available for extensive discussions. Additionally, Prof. Fumeaux has been very diligent in editing manuscripts to ensure that they are of a very high quality. Nearing the final stages of my PhD candidature when I shared my thoughts on how to make new novel technical contributions Prof. Fumeaux was very supportive of my thoughts and additionally showed me new aspects that I had not thought of. I will forever treasure the lessons that I have acquired from Prof. Fumeaux.

The second individual that I am indebted to is Dr. Damith Ranasinghe. Dr. Ranasinghe is an excellent scholar who has a very deep and broad knowledge of various fields. Dr. Ranasinghe right from the very beginning has provided a lot of guidance on how to write technical articles. His comments on numerous publications have always provided an interesting external perspective which greatly improved the quality of the publications. Additionally, Dr. Ranasinghe is a very pragmatic scholar whose research projects are driven by real world applications. Consequently, the biggest lesson that Dr. Ranasinghe has taught me is to always have a practical application in mind.

Dr. Thomas Kaufmann was the first scholar that I had the pleasure of interacting with in the field of applied electromagnetics. I had the great pleasure of working with Dr. Kaufmann from 2013 - 2014. Dr. Kaufmann was always frank and honest in his criticism which helped me develop scientific rigour. With the acquisition of a position in Switzerland in 2015 a large part of this thesis occurred without the supervision of Dr. Kaufmann. Nonetheless, the time that I spent under his guidance has left an indelible mark on me for which I am truly grateful for.

I have had the great pleasure of working with extremely knowledgeable and diligent individuals within the group of Applied Electromagnetics Group at the University of

Adelaide. I must thank Dr. Withawat Withayachumnankul, Dr. Nghia Nguyen-Trong, Dr. Shengjian (Jammy) Chen, Dr. Zahra Shaterian, Dr. Tiamoning (Echo) Niu, Dr. Chengjun (Charles) Zou, Dr. Ali Karami Horestani, Dr. Cheng Zhao, Ms. Wendy Lee, Mr. Andrew Udina, Mr. Deshan Govender and Dr. Fengxue Liu, Mr. Weijie (Jack) Gao, Mr. Xiaojing Lv, Ms. Jin Huang, Ms. Naliah Mastura, Mr. Xiaolong, Dr. Nicholas Lawrence and Mr. Ali Malakooti.

In addition to my supervisors I must also thank the technical staff within the School of Electrical and Electronics Engineering. The staff who consisted of: Mr. Pavel Simick, Mr. Ian Linke, Mr. Hayden Westell, Mr. Alban O' Brien, Mr. Aubrey Benjamin Slater, Mr. Mitchell Carli, Mr. Philip Schmidt, Mr. Danny Giacomo and Mr. Brandon Pullen. Without the support of the technical staff very few of my designs would have seen the light of day. I am especially grateful to Mr. Ian Linke who was always available for discussions of any sort ranging from how to fabricate wearable antennas to discussing how the human brain works. Mr. Linke has provided me with not only technical support but also moral support during my PhD. I must also thank Mr. Aubrey Slater as he was my primary contact with all my technical requests. I also can not go without acknowledging the extraordinary support that I have received from Mr. Alban O' Brien who tolerated my rather unorthodox method of carrying out experiments.

The administration staff consisting of Mr. Paul Arthur, Mrs. Rose-Marie Descalzi, Mrs. Jodie Schluter, Ms. Laura McNarma, Ms. Elizabeth Franca Guest also deserve my recognition as they have always been ready to support in me when I came in with last minute requests.

To support my health I have been in the care of Dr. Millie Vukovic, Dr. Lydia Kovacev, Dr. Stephanie Taylor, Dr. Tracey Hsieh and Prof. Richard Clarke. The competent care of these individuals ensured that I was in robust health during the duration of my PhD.

I have been very fortunate to have excellent friends. Whilst each of my friends has supported me tremendously I must mention certain individuals. First and foremost of these friends is Mr. Brendan Sean Thomas. Brendan, or otherwise affectionately and somewhat mockingly called Brenny darling has been a close friend since my undergraduate days. Brendan has always patiently listened to my numerous complaints about life, research and everything in between. Rarely if ever, would Brendan turn a deaf ear. Additionally at the later stages Brendan showed an interest in reading my thesis for which I will always be grateful. Thank you Brendan for all that you have done for me. Words simply can't express my eternal gratitude to you and your family.

Dr. Nghia Nguyen-Trong has been a friend with me since my undergraduate and postgraduate days. Dr. Nguyen-Trong was always happy to help me when I presented technical questions to him in my early days of research. The patience, diligence and positive outlook of life of Dr. Nguyen-Trong are aspects that I would like to replicate in my life one day. Additionally, Dr. Nguyen-Trong despite being an excellent and rare individual shows immense humility which is a admirable quality among high achievers.

Ms. Wendy Lee has been a friend since my first days of postgraduate studies. Her easy going nature, friendliness and willingness to help me at anytime have made a difficult journey pleasant and enjoyable. Additionally, Wendy has forgiven me of my many transgressions which is an admirable quality. It is my sincere wish that we will be friends forever.

Dr. Shengjian (Jammy) Chen has been a close friend for me throughout my PhD study. As friends we have worked together, got frustrated together and succeeded together. I consider myself truly blessed to have shared company with Dr. Shengjian (Jammy) Chen.

Whilst not directly related to my academic pursuits I must acknowledge the support of Mr. Simon Blackett, Mr. John Thomolaris, Mr. Sasha Zadyochuck, Mr. Ryan Graetz and Mrs. Ali Jones. These five individuals supported in some of the most miserable times over the last few years and consequently our friendship has grown stronger. Words can't express how much I care for you. My best wishes will always be with you.

Since 2016 it has been my pleasure to be in the company of Ms. Jacinda Jansen Roberts. The amazing and deep discussions that we shared immeasurably enriched my life. Not to mention the dancing, great meals and fantastic company. Thank you Jacinda for being my friend and I hope we stay friends for the rest of our time on this earth.

Finally, I must express my gratitude to my family. My family has molded me into the person who I am today. Special thanks to my mother. Whilst in the final year of undergraduate when I was contemplating doing a PhD my mother encouraged me to take the plunge and do a PhD. At times, my mother seemed more determined for me to get my doctoral degree than myself. This thesis is as much yours as it is mine.

Lots of love and gratitude to all.

Conventions

Typesetting

This document was compiled using LaTeX 2ε. TexStudio was used as the text editor that was interfaced with LaTeX 2ε. All images have been created using MATLAB and Inkscape.

Spelling

American English spelling conventions have been adopted in this thesis.

Referencing

The Harvard referencing style has been utilized in this thesis.

Units

This thesis has adopted the International System of Units (SI Units).

Abbreviation

MHz	Megahertz
GHz	Gigahertz
EBG	Electromagnetic Bandgap
UWB	Ultra-wide band
PRS	Partially Reflective Surface
GPS	Global Positioning System
ISM	Industrial Scientific and Medical
WLAN	Wireless Local-Area Network
PCS	Personal Communications Services
PIFA	Planar Inverted-F Antenna
CMA	Characteristic Mode Analysis
CRLH	Composite Right/Left Handed
TE	Transverse Electric
TM	Transverse Magnetic
SMA	Subminiature Version A
PDMS	Polydimetylsiloxane
TPU	Thermoplastic Polyurethane
RFID	Radio Frequency Identification
TEM	Transverse Electromagnetic
RCS	Radar Cross Section
MM1	Modeling Method 1
MM2	Modeling Method 2
DC	Direct Current
UHF	Ultra High Frequency
dB	Decibel
PCB	Printed Circuit Board
CRLH-TL	Composite Right/Left-Handed Transmission Line
HIS	High Impedance Surface
HMSIC	Half-Mode Substrate-Integrated Cavity
SIC	Substrate Integrated Cavity

Awards and Scholarships

2016

- IEEE Antennas and Propagation Society Travel Grant Award

2015

- 3 Minute Thesis (3MT) School Finalist
- 3 Minute Thesis (3MT) Faculty Winner

2014

- Australian Postgraduate Award

Publications

Journal Articles - Organized in reversed chronological order

[1] N. Nguyen-Trong, **S. P. Pinapati,** D. Hall, A. Piotrowski and C. Fumeaux, "Ultra-Low-Profile and Flush-Mounted Monopolar Antennas Integrated into a Metallic Cavity", *IEEE Antennas and Wireless Propagation Letters*, vol. 17, pp. 86-89, 2018

[2] **S.P. Pinapati,** D.C. Ranasinghe and C. Fumeaux, "Textile Multilayer Cavity Slot Monopole For UHF Applications", *IEEE Antennas and Wireless Propagation Letters*, vol. 16, pp. 2542-2545, August. 2017.

[3] **S.P. Pinapati,** T. Kaufmann, D.C. Ranasinghe and C. Fumeaux, "Wearable dual-band stripline-fed half-mode substrate-integrated cavity antenna", *Elec. Letters*, vol. 52, no. 6, pp. 424-426, March. 2016.

Conference Articles - Organized in reversed chronological order

[1] **S.P. Pinapati,** D. C. Ranasinghe and C. Fumeaux, Bandwidth Enhanced Dual-Band Half-Mode Substrate-Integrated Cavity, *Australian Microwave Symposium (AMS)*, 2018. In Print.

[2] **S.P. Pinapati,** S. J. Chen, D. C. Ranasinghe and C. Fumeaux, "Detuning Effects of Wearable Patch Antennas", in *Asia-Pacific Microwave Conference (APMC)*, November. 2017, pp. 162-165. **Finalist for best student paper award.**

[3] **S.P. Pinapati,** N. Nguyen-Trong, A. Piotrowski and C. Fumeaux, "Integration of a Wideband Low-Profile Monopolar Antenna onto Curved Metallic Surfaces", in *International Conference on Electromagnetics in Advanced Applications (ICEAA)*, September. 2016, pp. 203-206.

[4] **S.P. Pinapati,** D. Ranasinghe and C. Fumeaux, "Characterization of conductive textiles for wearable RFID applications", in *International Conference on Electromagnetics in*

Advanced Applications (ICEAA), November. 2016, pp. 341-344. **Winner of Antennas and Propagation Society Travel Grant**

[5] **S.P. Pinapati,** T. Kaufmann, I. Linke, D. Ranasinghe and C. Fumeaux, "Connection strategies for wearable microwave transmission lines and antennas", in *International Symposium on Antennas and Propagation (ISAP)*, November. 2015, pp. 1-4.

List of Figures

List of Tables

Chapter 1

Introduction

THE current chapter lays the foundation for this thesis by firstly providing a brief overview of body-worn communications. An integral component of body-worn communications are wearable antennas which are the focus of this thesis. Then the specific objectives of this dissertation are provided. Thereafter the layout of this dissertation is discussed and the original contributions are presented which concludes the chapter.

1.1 Introduction

Since the first demonstration of wireless communication by the renowned scientist Heinrich Hertz, antennas have undergone a tremendous development. This is evident by the pervasiveness of portable wireless communication equipment such as mobile phones.

Recently a new wireless communication paradigm referred to as body-worn communications has gained attention [64]. Body-worn communications entails scenarios where an individual hosts devices in close proximity to their body which are able to acquire and wirelessly transmit information about the user. The application areas for body-worn communications range from medical to military communications.

Integral components of body-worn communications are wearable antennas which are needed to facilitate wireless communication. As the name implies wearable antennas are devices that will be worn by an individual. To satisfy both physical and electromagnetic criteria, wearable antennas will generally need to be: unobtrusive, highly flexible and insensitive to the effects of the human body tissue - which will be in close proximity to the antenna. Consequently there is a need for wearable antennas which exhibit the aforementioned characteristics.

Thus this dissertation investigates the design, fabrication and realization of various wearable antennas that are unobtrusive, highly flexible and display performance that is largely unaffected by the presence of the human body.

1.2 Objectives

The main investigation areas for this thesis are:

- Study of practical issues related to the design, implementation and realization of textile antennas.
  - In a typical body-worn communications scenario, flexible wearable antennas will be connected to rigid devices. Connecting flexible and rigid devices is a challenging task due to the different mechanical properties of each device. Quite often, connections between flexible and rigid devices has been achieved using conductive epoxy. Conductive epoxy which is suitable

for validation purposes is limited in practical applicability as it is prone to breaking after repeated mechanical stress. To realize a more practical connection between flexible and rigid devices, this thesis proposes and investigates various textile based connection strategies. The emphasis of the investigation is on electrical performance and mechanical robustness of the proposed strategies for testing wearable antennas.

– Generally, wearable antennas will be integrated into clothing attire. Depending on the location on the human body the antennas may be bent. When bent the geometry of the ground plane is likely to be changed. In such scenarios the antenna may radiate in undesired ways. Consequently it is crucial to appreciate the effect non-planar ground planes may have on the performance of wearable antennas. In this context this thesis investigates the effects of two forms of ground plane curvature: cylindrical and spherical, and what implications these two forms of curvature have on the far-field radiation characteristics of wearable antennas.

– There are a wide variety of methods that can be used to realize wearable antennas. One method that has gained a lot of attention is through embroidery techniques. Specifically, utilizing computerized embroidery with conductive yarns to realize textile antennas. The utilization of computerized embroidery raises an important question. Specifically, *how to optimize the fabrication parameters to realize the highest possible conductivity whilst minimizing fabrication complexity?* Consequently this thesis systematically investigates the effects of three fabrication parameters to determine the optimum balance between fabrication complexity and electrical performance. The three fabrication parameters are: stitch/grid spacing, embroidery density and embroidery layout. An additional pertinent question is *how to accurately model and characterize embroidered structures?* The later question is investigated by proposing and examining two characterization and modeling techniques which can be used in the design of embroidered textile antennas.

- Realization of compact antenna topologies with high immunity to the effects of adverse environmental conditions.

  - A significant challenge in wearable antenna design is realizing antennas that are insensitive to the effect of the human body and mechanical deformations. The human body being a very complex propagation medium can significantly degrade the performance of antennas which are in close proximity to human body tissue [65]. Additionally due to the inherent curvature of the human body, wearable antennas may become geometrically deformed. The variations in geometry can in turn cause undesired performance variation. Thus it is imperative that an appropriate antenna topology be chosen for wearable applications. One such topology that has gained interest is low-profile closed and semi-closed cavity antennas. Cavity antennas have an inherent ground plane which helps to isolate them from the human body. Additionally, due to tight field confinement, closed cavity antennas are relatively immune to the effects of mechanical deformations. Whilst these are attractive features, closed cavity antennas tend to be electrically large, which can be detrimental to their deployment in wearable situations. Therefore this thesis investigates various techniques to realize compact cavity antennas.

- Development of wearable antennas that have stable performance under various adverse operating conditions.

  - Wearable antennas will be subjected to various adverse environmental conditions which can degrade performance compared to their intended design. For example, the operating frequency of a wearable antenna may be altered by moisture or bending, which could mean that the wearable antenna no longer satisfies the design specifications. One method to diminish such effects is to use a frequency reconfigurable antenna to compensate for alterations in the operating frequency. An important parameter for frequency reconfigurable antennas is the tuning range. For textile frequency reconfigurable antennas the question becomes how much tuning range is needed to compensate for variations in the operating frequency due adverse environmental conditions. To address the last question this thesis numerically and experimentally investigates the maximum detuning in operation frequency

of a textile patch antenna. Finally, the design of a new proof-of-concept compact low-profile frequency reconfigurable cavity-backed slot antenna is presented. The attractive features make the proposed antenna a strong candidate for future adaptive body-worn antennas.

1.3 Thesis structure

The organizational structure of the thesis which is graphically displayed in Fig. 1.1 is as follows:

Part I - Overview

Chapter 1 - Introduction

Chapter 2 - Background

Part II - Practical issues

Chapter 3 - Connection Strategies

Chapter 4 - Conformal Ground Planes

Chapter 5 - Embroidered Antennas

Part III - Cavity antennas

Chapter 6 - Miniaturized Ultra-High Frequency Antenna

Chapter 7 - Dual-Band Half-Mode Substrate-Integrated Cavity

Part IV - Adaptive antennas

Chapter 8 - Detuning Quantification

Chapter 9 - Multi-layer Cavity-Backed Broad-Slot Reconfigurable Antenna

Part V - Conclusions

Chapter 10 - Summary and Outlook

Figure 1.1. The organizational structure of this thesis.

- Introduction and Background (Chapters 1 - 2)
  - These two chapters set the tone for this thesis. The current chapter has presented a brief motivation for wearable antenna research whereas the second chapter elaborates on the various materials and associated fabrication processes to realize wearable antennas. Thereafter the method to realize wearable antennas in this thesis is presented. Afterwards an evaluation of numerous wearable antennas is provided. Finally key aspects of the literature review are summarized with concluding remarks that ends the chapter.
- Practical Aspects (Chapter 3 - 5)
  - The first major section of this thesis focuses on practical aspects related to the realization and utilization of textile wearable antennas. Chapter three begins this section by motivating the need for robust connection strategies based on a literature review. After the motivation, three new textile based connection strategies are briefly introduced and the geometry to evaluate their electrical performance is provided. Then simulation results are presented for each connection strategy to evaluate any potential impact they may have on the nominal geometry. The focus then shifts to the manufacturing process and experimental validation of each connection strategy. Following the experimental validation, concluding remarks which summarize the chapter are provided and the chapter is closed.
  - Chapter four is devoted to the effects of non-planar ground planes of the antenna far-field radiation characteristics. Initially the effects of conformal ground planes are quantified from a vehicular perspective. The vehicular case represents an off-body to on-body communications scenario which from a holistic system perspective is bound to happen within the global concept of body-worn communications. The first step of the investigation is to determine a suitable antenna for which to quantitatively study the effect of conformal ground planes. After having determined a suitable planar dimension, the effects of cylindrical and spherical ground plane curvature are numerically investigated. Afterwards, the focus shifts onto characterizing the effects of ground plane curvature on the far-field radiation characteristics from a body-worn (on-body to on-body) perspective. An important difference in the body-worn case is the size of the ground plane. Finally, concluding remarks are presented and the chapter is closed.

  - The last chapter in this section focuses on the utilization of computerized embroidery to realize robust textile ground planes. Initially an elaboration on the attractive aspects of using computerized embroidery to realize textile antenna structures is presented. Thereafter the fabrication method which is used to realize various embroidered structures with different fabrication parameters is presented and leads into a discussion on the experimental method used to quantify the performance of the embroidered structures. The focus of the chapter then shifts to examining, via scattering experiments, the variation in performance of embroidered structures subject to three fabrication parameters. To quantify the performance of the various embroidered structures two modeling methods, namely homogenizing the embroidered structures and approximating the physical distribution of the threads, are proposed, together with a characterization method. Finally, a selected embroidered structure is used as a ground plane for a textile patch antenna to validate the characterization and modeling methods. Simulations and measurements for the textile patch with the embroidered ground plane are presented and the chapter is ended with concluding remarks.

- Wearable Cavity Antennas (Chapters 6 - 7)

  - The second major section of this thesis pertains to wearable cavity antennas. Chapter six is devoted to the design and experimental validation of a new miniaturized UHF antenna. This chapter begins by presenting a literature review of various wearable UHF antennas after which the proposed geometry is introduced and briefly described. The focus is then shifted to the design, manufacture and experimental validation of the antenna. In the final stages of the chapter a design variation is proposed and a summary is provided which concludes the chapter.

  - Chapter seven presents a dual-band slot-loaded half-mode substrate-integrated cavity antenna which follows the same organization as chapter six. The antenna is designed to cover the lower and upper microwave ISM bands. At both bands, i.e the lower and upper microwave ISM bands, the radiation occurs through independent mechanisms. This allows a largely independent design of both bands. Additionally to enhance wearability, the antenna is excited through a planar feeding mechanism. Finally, a design variation is

presented wherein the bandwidth at the lower frequency can be substantially enhanced.

- Frequency Reconfigurable Antennas (Chapter 8 - 9)
  - Chapter eight in this thesis area lays the ground work for the realization of textile frequency reconfigurable antennas. Specifically, a numerical and experimental study is performed to observe the maximum variations in operating frequency of a textile modular patch antenna when subjected to three adverse conditions. These three adverse conditions are: moisture absorption, antenna curvature and proximity to human body tissue. From the numerical and experimental study initial guidelines on how much tuning range textile antennas may need are presented.
  - The final technical chapter of this thesis begins by presenting a review of various notable frequency reconfigurable antennas. Then the topology for a new type of frequency-reconfigurable cavity-backed slot antenna is presented. Afterwards, the focus shifts to the detailed design methodology for the new frequency reconfigurable antenna. After expanding on the design procedure, the fabrication procedure for the antenna is presented which leads into a discussion on the measured performance. Concluding remarks are then provided and the chapter is closed.
- Conclusions and Future Work
  - The last chapter summarizes the main contributions of the work undertaken in this thesis with suggestions for future work. A concluding remark ends the thesis.

1.4 Original Contributions

- Chapter 3: The standout contribution is the development of a new fully textile connection strategy known as the “wing solution”. This connection strategy exhibits similar performance to conductive epoxy up to 6.0 GHz with excellent mechanical stability. Its application is mostly for the connection to testing apparatus via coaxial cables. The contents of this chapter resulted in a publication entitled “Connection Strategies for Wearable Microwave Transmission Lines and

Antennas" which was presented at the *International Symposium on Antennas and Propagation (ISAP), 2015.*

- Chapter 4: The main contribution of this chapter is a quantitative investigation into the variations in the far-field characteristics of a low-profile wideband monopolar antenna. Through numerical methods it is shown that either radially asymmetrical and symmetrical deformation of the ground plane can significantly alter the far-field radiation characteristics. A section of the results presented in this chapter resulted in a publication entitled "Integration of a Wideband Low-Profile Monopolar Antenna onto Curved Metallic Surfaces" that was presented at the *International Conference on Electromagnetics in Advanced Applications (ICEAA), 2017*.

- Chapter 5: One of the major contributions of this chapter is the systematic investigation, through scattering experiments, to quantify the performance variation of embroidered structures as a function of three fabrication parameters. The three fabrication parameters are: stitch spacing, embroidery density and embroidery layout. Initial results into the effects of embroidery density resulted in a publication with the title "Characterization of Conductive Textiles for Wearable RFID Applications" which was presented at the *International Conference on Electromagnetics in Advanced Applications (ICEAA), 2016* and was **awarded a travel grant**. The second major contribution is an empirical validation that embroidered structures can in general be modeled and characterized by approximating the physical distribution of the conductive threads with an effective sheet resistance. The final major contribution is that embroidered ground planes can serve as a partial replacement for bulk metal ground planes. The combined outcomes of this chapter are being prepared into a publication with a tentative title "Effect of Various Embroidery Fabrication Parameters to Realize Polarization Independent Structures" that will be submitted to *an IEEE journal.*

- Chapter 6: The major contribution of this chapter is the development and validation of a new low-profile compact UHF multi-layer cavity-backed slot-monopole antenna, fed by a shielded stripline. The antenna features a relatively large -10 dB impedance bandwidth of 3.8% for a cavity thickness of $0.0149\lambda_0$ where λ_0 is the free-space wavelength at 923 MHz. The outcomes of this chapter resulted in

a publication entitled "Textile Multi-Layer Cavity Slot-Monopole for UHF Applications" in *IEEE Antennas and Wireless Propagation Letters.* A secondary contribution relates to a design variation wherein the cavity size can be substantially miniaturized whilst retaining a similar free-space bandwidth.

- Chapter 7: The major contribution of this chapter is the realization of a new dual-band slot-loaded half-mode substrate-integrated cavity antenna that operates at 2.45 GHz and 5.8 GHz. A salient feature of this antenna is that the lower and upper frequency bands can largely be independently controlled. Noteworthy is the fact that a planar feeding mechanism excites two different modes at two widely separated frequencies. A secondary contribution which is based on a design variation demonstrates that the bandwidth at the lower band can be significantly enhanced through the introduction of an aperture slot without increasing the cavity thickness. The outcomes of this chapter resulted in two publications. The first one is entitled "Wearable Dual-Band Stripline-Fed Half-Mode Substrate-Integrated Cavity Antenna" which was published in Electronics Letters. Based on the design variation a publication entitled "Bandwidth Enhanced Dual-Band Half-Mode Substrate-Integrated Cavity" was presented at the *Australian Microwave Symposium (AMS), 2018*.

- Chapter 8: The major outcome of this chapter is a quantification into the maximum variation in operating frequency of a textile modular patch antenna when subjected to three adverse conditions. The hostile environmental conditions are moisture absorption, antenna curvature and proximity to human body tissue. Through numerical and experimental methods it is demonstrated that the operating frequency *can shift upwards* when in close proximity to human body tissue. Additionally it is demonstrated that textile frequency reconfigurable antennas may need to adjust their operation frequency for both upshifts and downshifts around the nominal operating frequency. The outcome of this study resulted in a publication entitled "Detuning Effects of Wearable Patch Antennas" which was presented at *Asia Pacific Microwave Conference (APMC), 2017*. This paper **was a finalist for the best student paper award**.

- Chapter 9: The major outcome of this chapter is the design of a new type of frequency reconfigurable antenna. The proposed antenna displays a large fractional tuning range without the need for impedance matching elements. An additional salient feature of the proposed antenna is that the reconfiguration elements are

embedded within the cavity which helps to shield them from adverse external forces.

Chapter 2

Background

THIS chapter begins by motivating the need for wearable antennas from an application perspective. Various methods to realize wearable antennas are presented and discussed in terms of their advantages and disadvantages. After this, the proposed means to realize wearable antennas in this thesis are presented. The focus then shifts to provide a broad overview of various wearable antennas that have been proposed in the literature. The key aspects of this literature review are then summarized which concludes the chapter.

2.1 Wearable Antennas

The concept of body-worn communications which entails devices integrated into clothing attire as shown in Fig. 2.1 [1] has attracted increased attention since its inception in the 1990's [64]. The application areas for body-worn communications range from healthcare to security/military and personal entertainment [64].

Figure 2.1. A vision of what a security orientated body-worn communications scenario will look like where an individual has multiple wireless communication devices integrated into their clothing. Generally these devices will be transmitting information about the status of the user with other devices which are either on or off the body. This image is reproduced from [1].

Body-worn antennas shown as the red circles in Fig. 2.1 are an integral component of body-worn communications. Body-worn antennas are also known as wearable antennas and therefore this thesis will use these terms interchangeably. The design of body-worn antennas is a challenging task for two primary reasons: firstly the antenna should be insensitive when placed in close proximity to human body tissue and secondly the antenna performance should be stable when the device is curved around body tissue with variation in shape due to the bearer's movements.

2.2 Materials for Flexible Antennas

Wearable antennas can be realized using various materials such as: conductive polymers, conductive inks and conductive textiles. Herein a brief overview of the advantages and disadvantages of using each of the aforementioned materials is presented.

Conductive polymers are novel materials which have attracted increased attention for antenna applications for two main reasons. Firstly they are extremely flexible as shown in Fig. 2.2 and Fig. 2.3 and secondly they can be easily patterned to a range of shapes using standard photolithography techniques [3]. The main limitation of conductive polymers stems from the difficulties in simultaneously obtaining a large conductivity and a suitable thickness. High conductivity polymers usually display material thicknesses that are smaller than a skin depth. This means that the currents within the conductive polymer are confined to an inadequate thickness which increases the ohmic losses within the material and impairs the radiation efficiency [66]. For example the meandered dipole antenna presented in [2] and shown in Fig. 2.2 displayed a peak simulated realized gain of -3 dBi whilst an equivalent copper antenna had a peak simulated gain of 0 dBi. Whilst there have been efforts aimed at raising the thickness of conductive polymers this is not without challenges due to limitations in material processing [66].

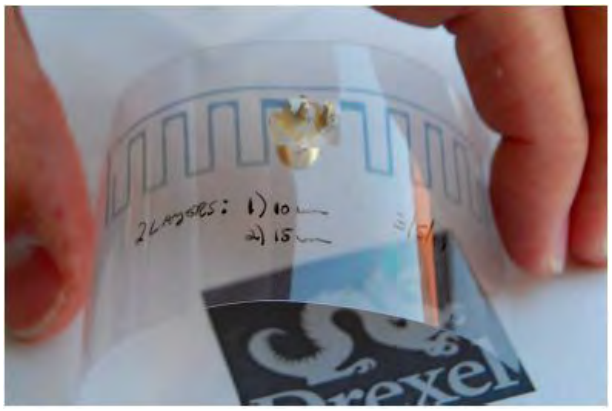

Figure 2.2. A highly flexible conductive polymer based meandered dipole. This image is reproduced from [2].

To circumvent the low radiation efficiency of conductive polymer antennas various strategies have been proposed. These include chemical treatment and the use of non-resonant structures such as monopoles [3] as shown in Fig. 2.3. The latter option raises the radiation efficiency due to a low current density through the antenna which reduces ohmic losses. The issue with using non-resonant antennas, i.e. planar monopoles,

is that they often lack a ground plane which leads to undesired power absorption when placed in close proximity to human body tissue [65]. Incorporating a ground plane into such non-resonant structures generally tends to dramatically reduce the radiation performance.

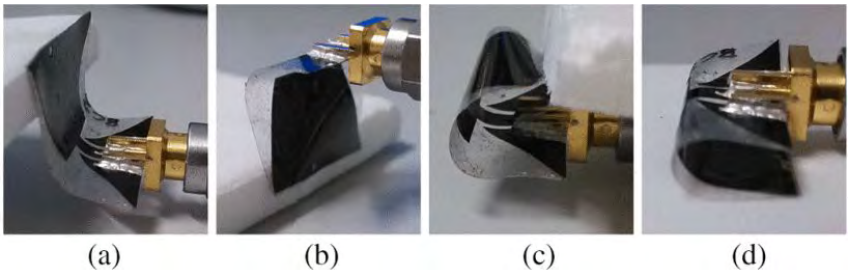

Figure 2.3. A conductive polymer planar monopole antenna as reproduced from [3].

From the preceding discussions it can be concluded that the main drawbacks of using conductive polymer antennas for wearable applications are: low radiation efficiency and associated limitations in the realizable antenna geometry.

In recent years inkjet printed technology has also been proposed to realize flexible antennas. In this method an inkjet printer as shown in Fig. 2.4 [4] is loaded with conductive ink. The printer then deposits the ink in the form of a desired geometry onto a substrate such as paper to realize structures like those shown in Fig. 2.5 [5].

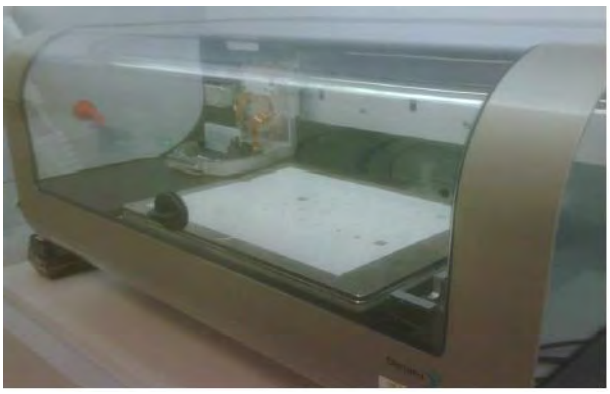

Figure 2.4. A typical inkjet printer that can be used in the realization of flexible microwave devices. This image is reproduced from [4].

One of the major limitations of using inkjet printing techniques to realize wearable antennas is again the limited efficiency. Most of the literature on inkjet printed antennas tend not to show the radiation efficiency, but it can be assumed to be quite low [67]. The reason for the low radiation efficiency of inkjet printed antennas is most likely due

to the thickness of the printed conductive layers being less than a skin depth which impairs the radiation efficiency as previously discussed.

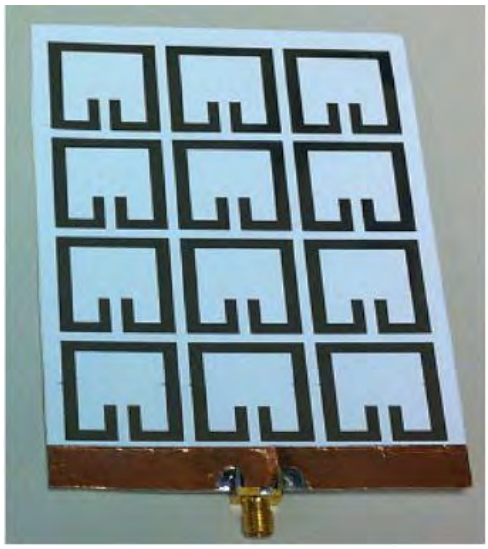

Figure 2.5. A periodic ground plane structure realized through inkjet printing technology as reproduced from [5].

Recently conductive textiles which consist of a base non-conductive material that has been impregnated with conductive elements such as silver or nickel have gained attention as a means to realize wearable antennas [68]. Generally there are two forms of conductive textiles that can be used for wearable antennas: conductive fabrics and conductive yarns/threads. Due to reasons of material processing conductive fabrics tend to be highly efficient whereas conductive threads tend to be inefficient. Considering now the fabrication of textile antennas: textile materials must be combined with the appropriate textile fabrication techniques. Two commonly used textile techniques are manual processing and sewing/embroidery which are herein discussed.

An example of a conductive fabric that has been manually processed to realize a flexible wideband dipole antenna operating at 5.8 GHz is shown in Fig. 2.6. In this context manual processing refers to patterning the conductive textile to any desired shape using bladed tools such as scissors. An additional benefit of using conductive fabrics is that they can easily adhered to textile substrate materials such as foam, felt or cotton. By combining conductive fabrics and textile substrates it is possible to realize cavity antennas such as patch antennas as shown in Fig. 2.7 [6]. The main disadvantage of using conductive fabrics is that the patterning accuracy is limited by the microscopic structure of the conductive fabrics. At the microscopic level the conductive fabrics are made from tightly interwoven thread bundles as shown in Fig. 2.8. When the fabric is

cut several bundles of threads are simultaneously removed. Generally this translates to an approximate patterning accuracy of 1 mm which might be too large for some applications [35].

Figure 2.6. A wideband dipole antenna patterned from a conductive fabric. The textile dipole is excited through a balun which has been fabricated from Rogers Duroid 5880.

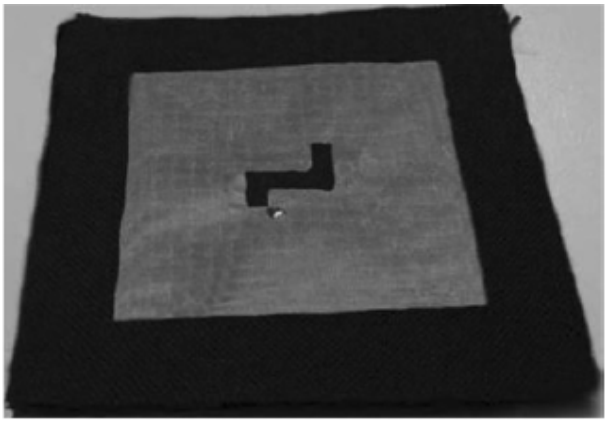

Figure 2.7. A textile patch antenna realized from the combination of conductive textiles and textile substrates. This image is reproduced from [6]

An alternative textile-based fabrication procedure that has gained attention to realize wearable antennas is the use of sewing/embroidery techniques. In this technique a computerized embroidery machine as shown in Fig. 2.9 is used in conjunction with conductive yarns to realize a desired geometry. The main advantage of this method is

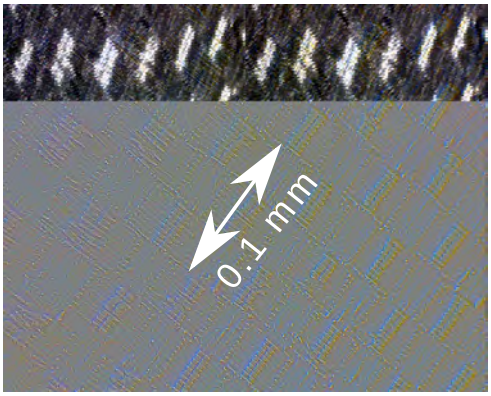

Figure 2.8. A microscopic view of a conductive fabric which shows that such fabrics are made from tightly interwoven bundles of threads.

that a variety of geometries can be realized with high accuracy as shown in Fig. 2.10 [7] and Fig. 2.11 [69]. An added benefit is that the embroidery can be done directly into clothing attire as shown in Fig. 2.12 which shows a range of dipole antennas embroidered into military garments [8].

Figure 2.9. A computerized embroidery machine that can be used for the realization of textile antennas.

Despite the advantages of using sewing/embroidery techniques to realize wearable antennas there are also certain challenges that are encountered. These challenges arise

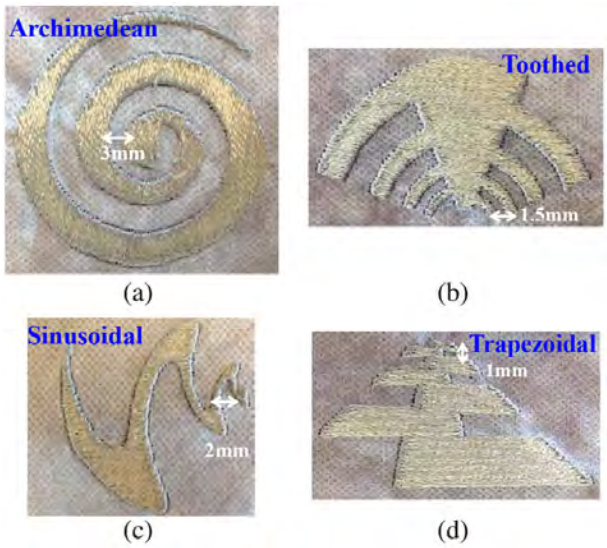

Figure 2.10. A variety of textile antennas made from computerized embroidery showing the high accuracy that can be achieved through a computerized embroidery machine as reproduced from [7].

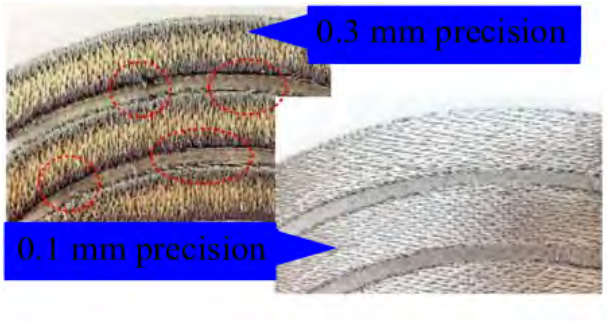

Figure 2.11. Embroidered structures with sub-milimeter precision as adapted from [8].

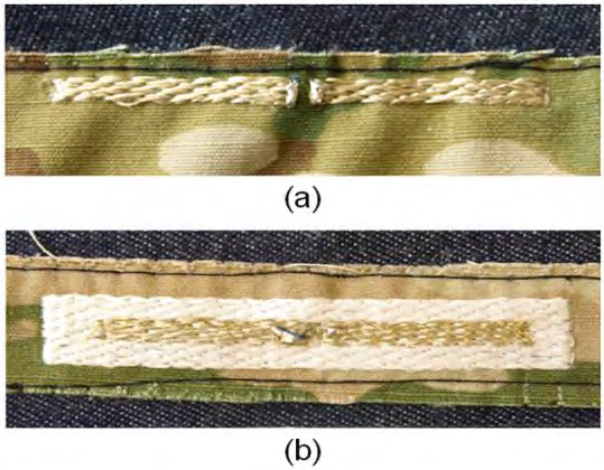

Figure 2.12. Dipole antennas integrated into military clothing attire that have been realized through computerized embroidery as reproduced from [8].

from the microscopic nature of the conductive threads that must be used. As previously discussed conductive textiles consist of a core material which has been incorporated with some conductive material. For example consider Fig. 2.13 [9] which shows a microscopic view of a conductive thread. This specific thread consists of a polyester yarn which has been helically wrapped by a conductive copper-nickel alloy fiber [9]. Generally the core material of conductive threads are rather stiff compared to standard embroidery threads. This means when conductive threads are operated in an embroidery machine they are subject to significant mechanical forces which can cause the threads to break. An additional consideration that can cause further difficulty when using computerized embroidery is the type of threads that can be used. There are two types of threads commonly used for embroidery based wearable antennas: multifilament and monofilament as shown in Fig. 2.14 [10]. While multifilament threads tend to be more conductive, they are also more difficult to use. Due to the mechanical tension on the threads the individual filaments can be torn apart and entangled within the machine causing frequent thread breakages.

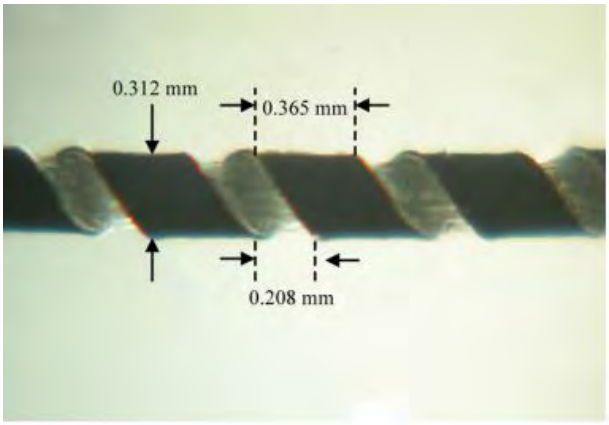

Figure 2.13. A microscopic view of a conductive yarn which shows a polyester core which is encapsulated by a conductive material. This image is reproduced from [9].

From the preceding discussions it is evident that there are both advantages and disadvantages of using the aforementioned conductive materials and associated fabrication techniques. A summary of these advantages and disadvantages is provided in Tab. 2.1.

By properly integrating the aforementioned conductive textile materials and fabrication techniques it is possible to achieve structures that are difficult to realize using a single textile material or fabrication technique. For example by combining conductive fabrics, conductive yarns and textile/foam substrates it is possible to realize closed cavity structures as shown in Fig. 2.15 [11]. Additionally from Table 2.1 it can be seen

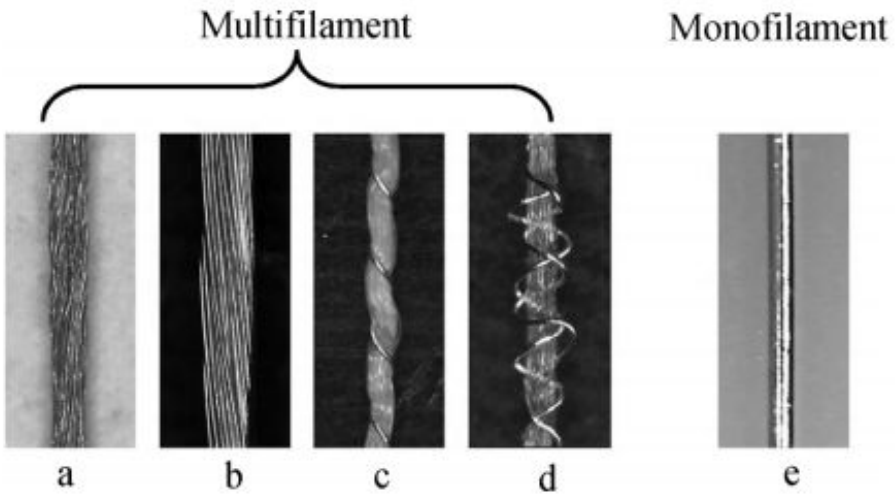

Figure 2.14. A depiction of a series of multifilament threads and a monofilament thread as reproduced from [10].

Materials	Advantages	Disadvantages
Conductive polymers	Low profile Extremely flexible	Limited efficiency Limited realizable geometries
Conductive inks	Low profile Extremely flexible	Limited realizable geometries Limited efficiency
Conductive fabrics	Easy to use High efficiency	Limited patterning resolution
Conductive threads	Direct integration into clothing High accuracy	Limited efficiency Thread breakages

Table 2.1. The advantages and disadvantages of using the aforementioned materials to realize wearable antennas.

that conductive fabrics have high efficiency but limited patterning resolution. On the other hand conductive threads can be accurately patterned but have a limited efficiency. Thus by combining these two materials it is possible to combine the high efficiency of conductive fabrics and the accurate patterning of conductive threads to obtain textile antennas that are reasonably efficient [70]. This approach is very versatile as a variety of geometries can be realized in a simple manner. For these reasons this hybrid approach will be one of the favored technique utilized in this thesis.

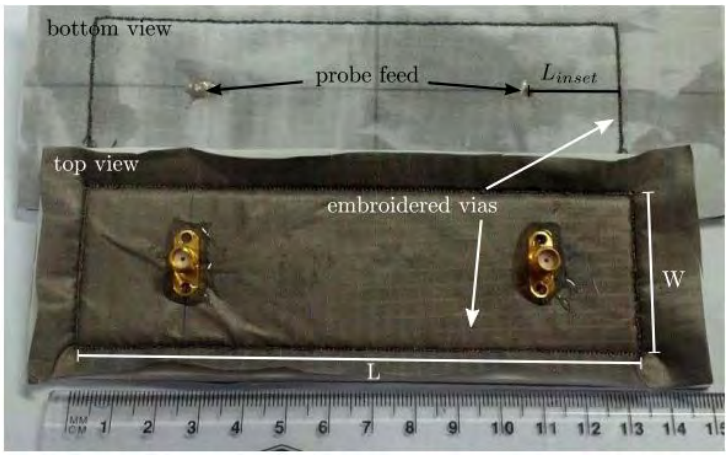

Figure 2.15. A textile substrate integrated waveguide realized through a combination of conductive fabrics, conductive yarns and a foam substrate as reproduced from [11].

2.3 Textile Based Wearable Antennas

In this section a summary of various textile based wearable antennas that have been proposed and evaluated is presented. The aim of this section is to get an appreciation of what kind of wearable antennas can be realized and the current state of the art in textile wearable antennas.

2.3.1 Clothing Antennas

A specific type of textile wearable antennas are so called clothing antennas. These are antennas which exploit the structure of certain clothing items to realize radiating elements. An example would be using the shape of a metallic button to create radiating elements as shown in Fig. 2.16 [12]. The advantage of button antennas is that they are relatively immune to effects of bending due to their rigidity and small size. Additionally it is straight forward to integrate them into clothing attire utilizing textile techniques such as sewing.

The button antenna presented in [12] was a dual-band radiator with center frequencies at 2.4 GHz and 5.2 GHz. As can be seen from Fig. 2.16 the antenna consisted of two discs with identical dimensions of D_d atop two cylinders which protruded from a textile substrate. The antenna was fed by the center post that was itself excited through a microstrip line on the top layer of the substrate. The radiation at the lower band occurred due to currents generated between the two discs through capacitive effects. At the higher band the radiation occurred from currents that were primarily on the lower

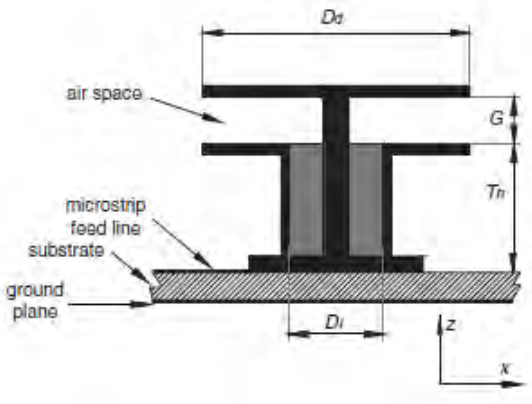

Figure 2.16. A button antenna as reproduced from [12].

disc. In terms of the far-field performance omni-directional patterns were obtained with a measured peak gain of approximately 2.4 dB at both bands.

In addition to buttons another common item on clothing attire are zips such as those found on jeans. Based on the commonly found zip a textile monopole antenna was realized as shown in Fig. 2.17 [13]. This antenna consisted of a zip that was sewn onto a felt substrate with a small partially overlapped conductive textile based ground plane on the opposite side. By varying the length of the zip as shown in Fig. 2.17(a) an adjustable operating frequency could be obtained. For this study the antenna was designed to operate at 2.5 GHz. To serve as a reference an identical monopole antenna was realized through conductive textiles only. Experimental results showed that the zip antenna had similar performance to the conductive textile based monopole with a -10 dB impedance bandwidth from 2.5 GHz to 2.7 GHz. The radiation patterns of the zip antenna were also quite similar to a standard monopole antenna which validated the proposed topology.

2.3.2 Ultra-Wideband Textile Antennas

As mentioned in chapter 1 the operating frequency of wearable antennas can be detuned due to adverse environmental conditions such as bending. One method to mitigate the severity of such detuning effects is to utilize ultra-wideband antennas which have a very large -10 dB impedance bandwidth to provide a "buffer" zone.

One of the earliest ultra-wideband textile antennas presented in [14] was a planar disc monopole that was realized from conductive fabrics as shown in Fig. 2.18. The authors mentioned that it was very difficult to cut the conductive fabric to the required

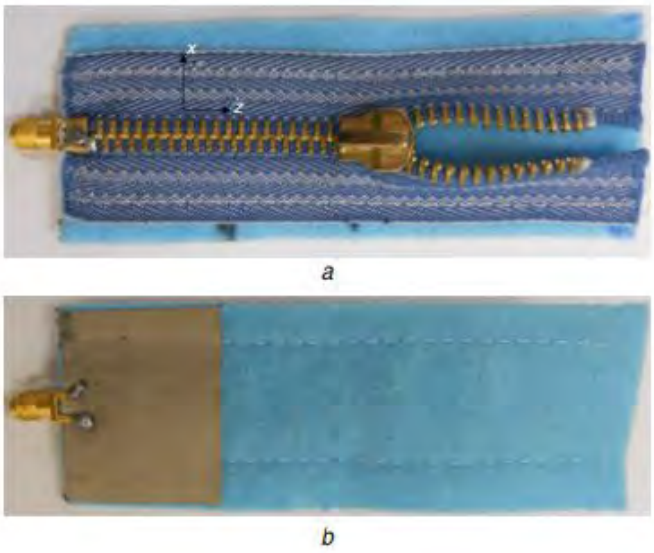

Fig. 2 *Antenna prototype*
a Zip antenna upper side
b Zip antenna back side

Figure 2.17. A monopole zip antenna as reproduced from [13].

tolerance of 0.5 mm, especially around the transmission line and feed, due to the microscopic structure of the conductive fabric as previously discussed. Later work investigated the use of a computerized embroidery machine to realize wideband antennas such as the spiral antenna shown in Fig. 2.19 [15]. Whilst both the conductive textile and embroidered antennas demonstrated a large bandwidth they both lacked a ground plane which caused performance degradation when placed in close proximity to human body tissue.

Some researchers have tackled the daunting task of obtaining textile ultra-wideband antennas with full ground planes. For example the ultra-wideband antenna presented in [16] and shown in Fig. 2.20 realized UWB operation by combining various radiating elements and broadbanding techniques. Courtesy of the full ground plane the antenna was demonstrated to be robust to the effects of the human body. Whilst this antenna presented a significant achievement it had one main limitation which was the extremely complicated design procedure. This antenna featured approximately 24 parameters which needed to be jointly optimized to achieve the desired performance. This was demonstrated to be a very challenging task. Unfortunately no information on

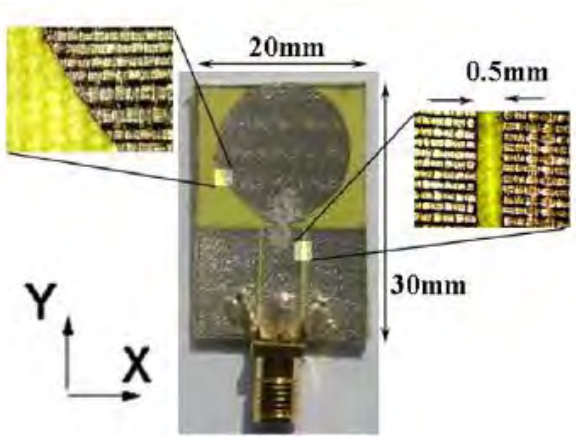

Figure 2.18. A planar disc UWB monopole antenna as reproduced from [14].

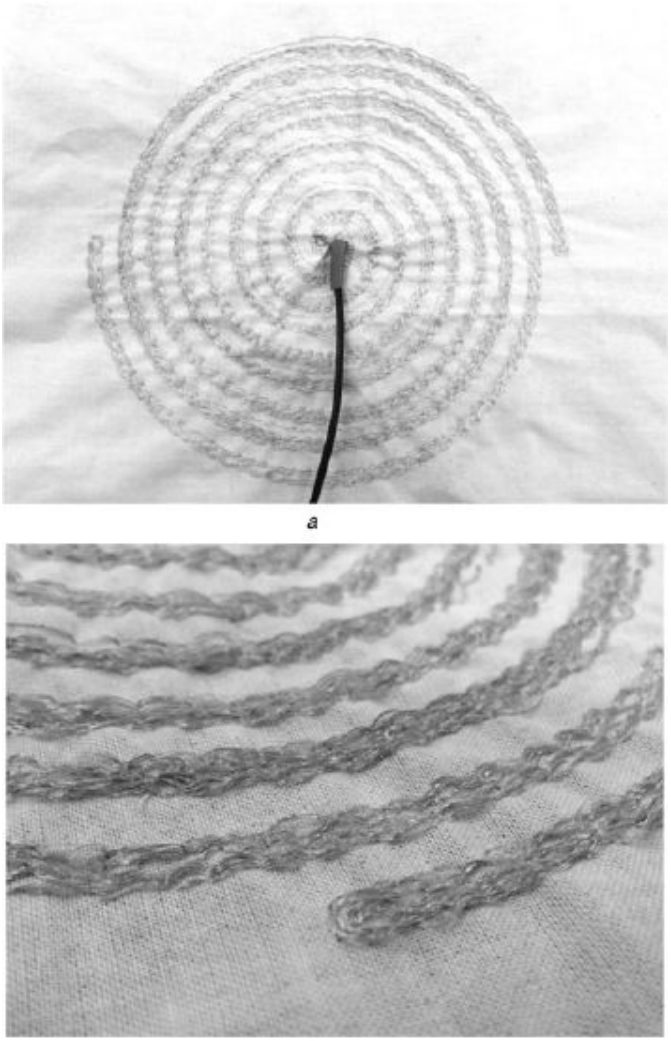

Figure 2.19. A embroidered UWB spiral antenna as reproduced from [15].

the effects of bending were provided which makes it difficult to ascertain the practical suitability of the antenna.

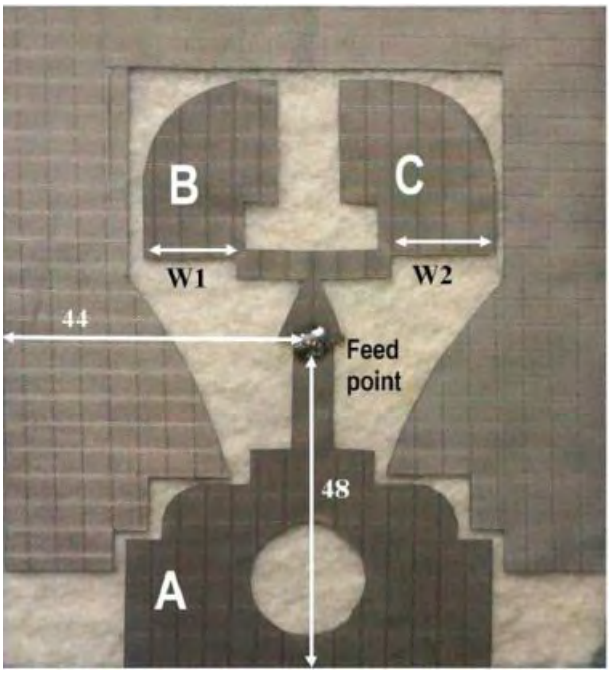

Figure 2.20. A textile UWB antenna with a full ground plane as reproduced from [16].

To alleviate some of the concerns of the aforementioned design the same authors presented a simplified UWB antenna as shown in Fig. 2.21 [17]. This simplified antenna was a multi-layer topology where the top layer consisted of a standard UWB monopole, the middle layer contained a circular patch that was capacitively coupled to the top layer and the bottom layer contained a full ground plane. The authors claimed that by optimizing the dimensions of the top monopole and the central patch ultra-wideband unidirectional operation could be achieved. Whilst this was a comparatively simpler design than that presented in [16] it was still heavily dependent on extensive numerical optimization tools as claimed by the authors. Additionally minimal information on the design method was provided. None the less the antenna was experimentally demonstrated to be robust to the effects of the human body as the measured reflection coefficient for when the antenna was placed on a human chest or arm was very similar to the free-space case.

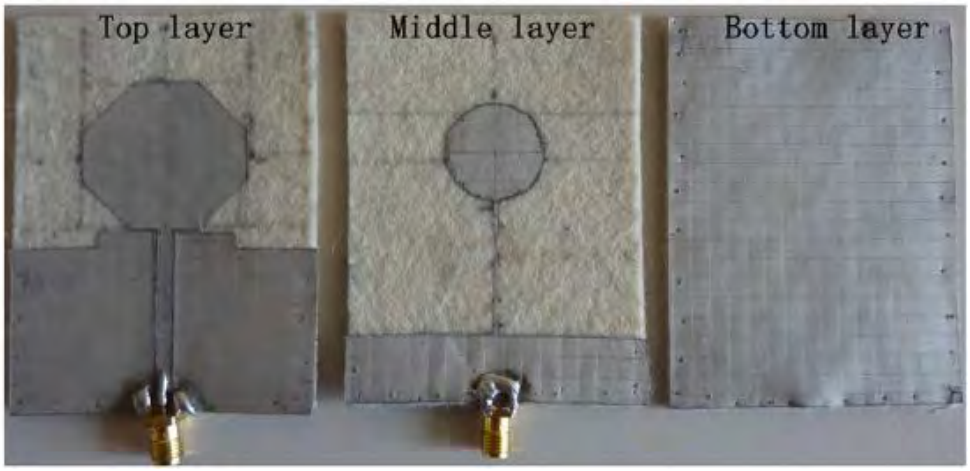

Figure 2.21. Multi-layer textile UWB antenna with full ground plane as reproduced from [17].

2.3.3 Resonant Antennas

Single Resonance

Resonant antennas are attractive for wearable applications where a specific frequency band needs to be covered which is a scenario of practical relevance. Therefore it is not surprising that a majority of wearable antennas are resonant structures.

As dipole antennas are a fundamental antenna geometry they have often been used for wearable applications. For example the study presented in [18] examined the suitability of bow-tie, meandered and folded meandered topologies for wearable applications. The suitability of each antenna was examined by placing them in close proximity to human body tissue and observing the performance variation. The bow-tie, shown in Fig. 2.22 and folded antennas displayed a significant variation in the operating characteristics which was attributed to the alterations in the input impedance caused by being in close proximity to the human body. On the contrary the folded meandered dipole was demonstrated to be more robust to the effects of the human body. This was attributed to the fact that the folded dipole had a larger input impedance compared to the other topologies that were investigated. This means that a larger variation in the input impedance was necessary to cause a noteworthy performance degradation.

The variation in input impedance of dipole antennas when placed in close proximity to human body tissue is primarily due to the lack of an isolating structure between the dipole and the human body. This is a general concept: wearable antennas which are separated from body tissue by an isolating structure tend to display a high degree of robustness to the effects of the human body. Normally the isolating structure is a ground

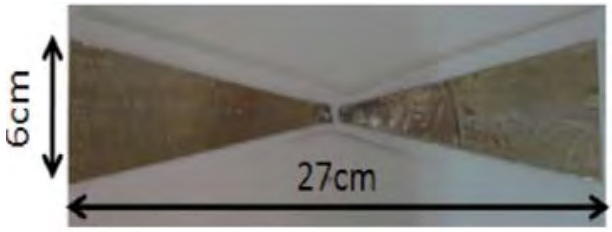

Figure 2.22. A textile bow-tie dipole antenna as reproduced from [18].

plane. Thus it stands to reason that antenna topologies that have an inherent ground plane will generally be relatively insensitive to the effects of the human body. Antennas which have inherent ground planes are generally open, closed or semi-closed cavities.

The most common open cavity antenna is the patch antenna. Patch antennas are very attractive for wearable applications as they have a simple design process and a ground plane which isolates them from the deleterious effects of the human body. These attractive features have led to the widespread deployment of patch antennas in wearable applications. Additionally patch antennas tend to feature a moderate directivity which is generally suitable for wearable applications. In certain situations however such as military communications a larger directivity may be desired. By the addition of extra elements patch antennas can display a larger directivity. The additional elements can either be multiple radiating elements or parasitic structures which enhance the gain. One type of parasitic structure that has gained attention in recent years are partially reflective surfaces (PRS) which usually come in one of two forms: a metallic sheet which has an aperture that has been periodically etched out or a periodic repetition of some metalized geometry. An example of both forms is shown in Fig. 2.23(a) and Fig. 2.23(b) respectively. Typically the inclusion of a PRS with an antenna results in a topology as shown in Fig. 2.24.

The means by which the inclusion of a PRS increases the directivity has been justified through a ray optics approach which is herein briefly summarized. Part of the fields that are radiated from the antenna leak through the PRS which is denoted as 0 in Fig. 2.24 whilst the remaining fields are reflected back from the PRS to the ground plane. These reflected fields are then redirected back towards the PRS where once again there is partial leakage through the PRS which is denoted as 1 in Fig. 2.24 [19]. It can be analytically shown that the fields that are leaked through the PRS can constructively interfere and produce a high directivity [71]. For a more detailed explanation

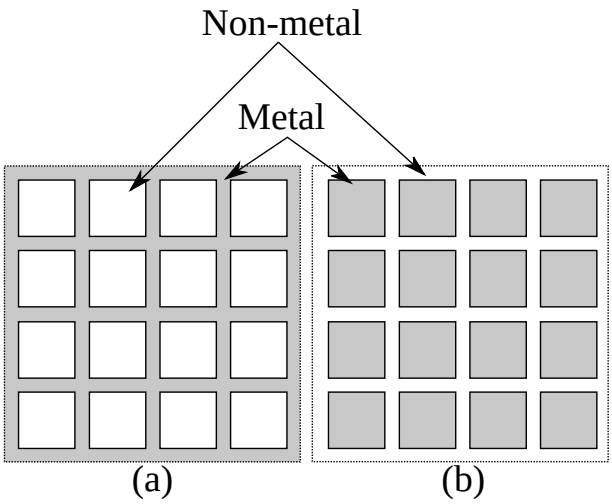

Figure 2.23. Two common variants of a PRS: (a) A metallic sheet with a periodic aperture and (b) A periodic repetition of a metalized geometry.

on the operating principle of a PRS and the analytical derivation of the directivity enhancement the reader is referred to [71]. Antennas which are incorporated with a PRS are also known as Fabry-Pérot antennas.

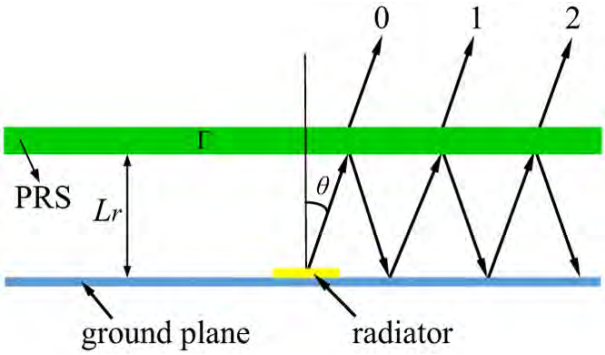

Figure 2.24. A visual representation of the partial leakage and reflection of the radiated fields from a patch antenna through a PRS structure. This image is reproduced from [19].

To examine the suitability of Fabry-Pérot antennas for wearable applications a textile Fabry-Pérot antenna shown in Fig. 2.25 was presented in [20]. In this design the radiating element was a textile patch antenna. This study did not utilize any of the two aforementioned PRS structures but rather used a combination of felt and rubber superstrates to achieve the desired multiple reflections and and energy leakage between the radiating element and the superstrates. Based on numerical results it was shown that the Fabry-Pérot antenna exhibited a directivity of 15 dB which would be more than double the directivity of what an identical patch antenna would exhibit without the dielectric superstrates. It was numerically and experimentally demonstrated that

this directivity improvement was largely unaffected when the total structure was bent which was a noteworthy observation as wearable antennas will be bent [72].

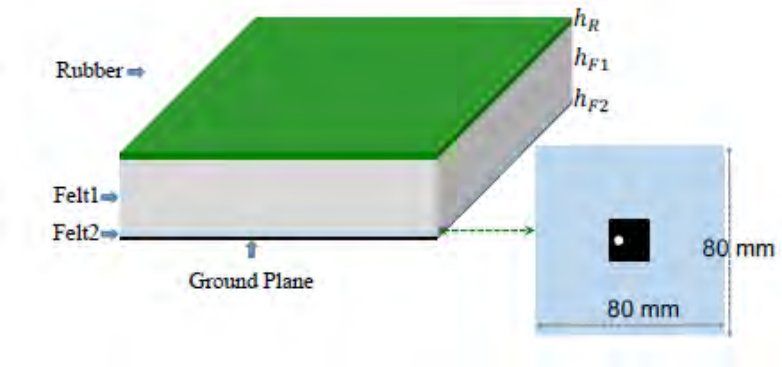

Figure 2.25. The proposed Fabry-Pérot antenna presented in [20] from which this image has been reproduced.

Closed cavities have also gained increased attention for wearable applications. This increased attention is because they can be made relatively insensitive to the effects of the mechanical deformations and display a high immunity to the effects of the human body. Additionally due to the tight confinement of fields within closed cavities they are largely immune to the effects of mechanical deformations [21]. An additional benefit of closed cavity structures is that they can easily be integrated with a planar feeding mechanism as shown in Fig. 2.26 making them attractive for wearable applications.

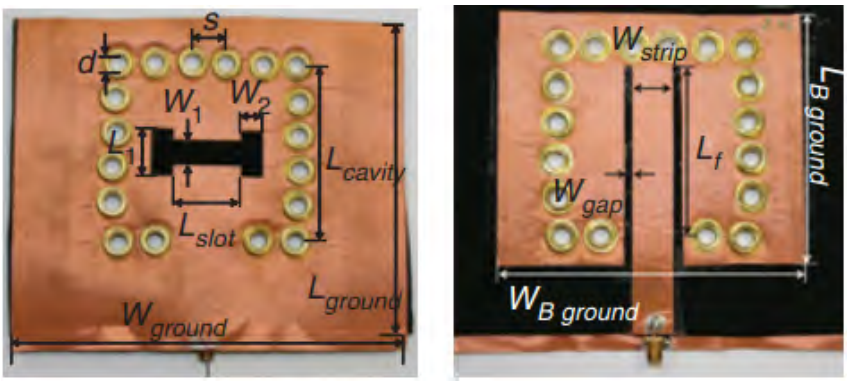

Figure 2.26. A textile cavity backed slot antenna as reproduced from [21].

For the aforementioned reasons the work presented in [22] and shown in Fig.2.27 featured a rectangular cavity operating at the fundamental TE_{10} mode with a circular resonant slot. Both the cavity and the slot were dimensioned for radiation at 5.8 GHz. The main contribution of this work was the large bandwidth of 6.10% which was achieved for a relatively shallow cavity thickness of $0.02\lambda_0$. The other attractive features of the

antenna were the insensitivity to the effects of the human body tissue and stable performance when bent as determined from experimental results. The main limitation of this design however was the large planar dimensions of the cavity which came to $0.63\lambda_0 \times 1.08\lambda_0$. Generally this is one of the main limitations for closed cavity structures. The planar dimensions are required to be a minimum of $0.5\lambda_G \times 0.5\lambda_G$ where λ_G is the guide wavelength. The issue of planar dimensions can become particularly problematic depending on the operating frequency [1].

To reduce the planar dimensions of closed cavities folding techniques have been proposed. By applying folding techniques the planar dimensions can be significantly reduced, however at the cost of making the cavity multi-layer. Based on the application of folding techniques various miniaturized microwave structures were proposed and evaluated in [23]. Notably a folded cavity-backed patch antenna was presented as shown in Fig. 2.28. This geometry was obtained by firstly folding a standard closed cavity to realize the multi-layer folded cavity. Then an aperture was cut on the top ground plane to realize the folded cavity-backed patch antenna. Compared to the unfolded cavity structure presented in [21] the structure proposed in [23] exhibited a reduction in the planar dimensions of 43%. To evaluate the robustness of the antenna to mechanical deformations bending studies were performed where it was experimentally demonstrated that there was minimal variation in the reflection coefficient and only mild variations in the radiation patterns. Furthermore the antenna was demonstrated to be robust to the effects of the human body as placing the antenna in close proximity to the human body resulted in no significant variation in either the reflection coefficient or radiation patterns.

An alternative method to miniaturize closed cavities is to exploit the inherent electromagnetic symmetry of the cavity which results in a semi-closed cavity structure. Compared to folding techniques this method can result in a similar or larger reduction in the planar dimensions without increasing the cavity thickness [24]. For example the work presented in [24] halved the size of a fully closed circular cavity which operated at 5.8 GHz. This was achieved by observing that there was a perfect magnetic conductor boundary condition across the diameter of the antenna. This allowed the cavity to be cut across the diameter with a minimal alteration in the resonance frequency. At this stage the cavity is semi-closed and is known as a half-mode substrate-integrated cavity (HMSIC). Performance-wise the antenna radiated through an effective magnetic dipole

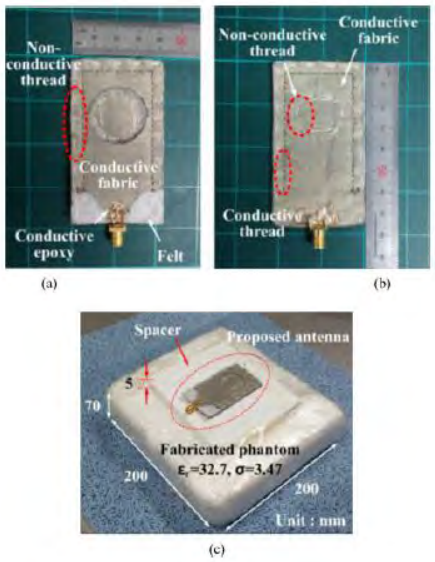

Figure 2.27. A textile cavity backed slot antenna as reproduced from [22].

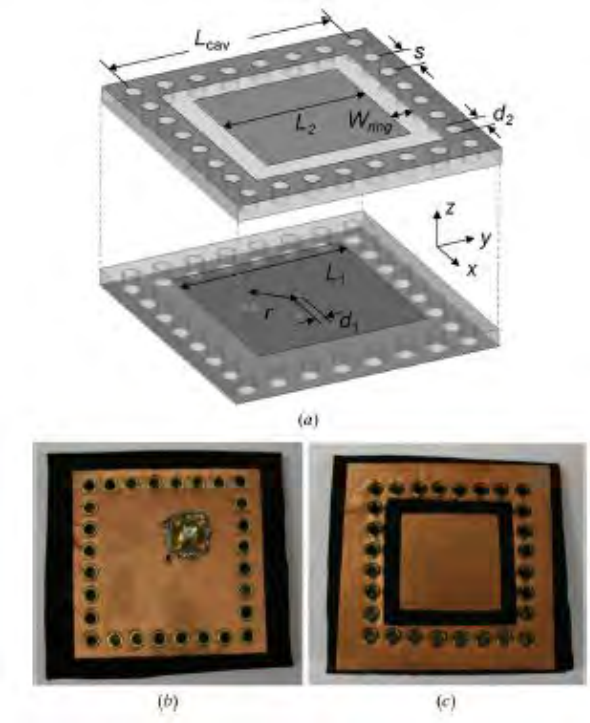

Figure 2.28. A folded cavity backed patch antenna as reproduced from [23].

at the open aperture of the cavity which was deduced from the field equivalence principle [73]. The antenna featured a very high simulated radiation efficiency of 97.2%. Whilst the measured radiation efficiency was not presented given the good agreement between simulations and measurements it was suggested that the measured radiation

efficiency would be very similar to the simulated value. An experimental realization of the final structure is shown in Fig. 2.29.

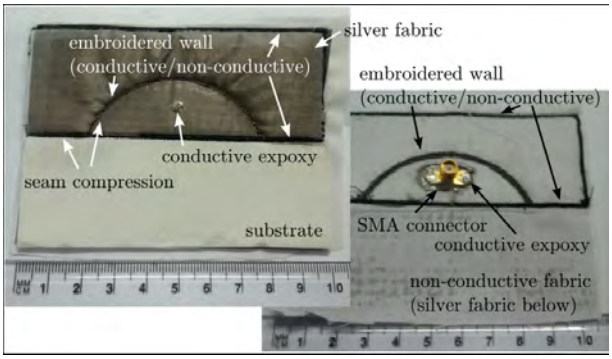

Figure 2.29. A textile half-mode substrate-integrated cavity antenna as reproduced from [24].

The half-mode substrate-integrated cavity can once again be cut in the plane orthogonal to the original cut as there exists an additional perfect magnetic conductor boundary condition in this plane. This concept of making two orthogonal cuts into a cavity resonator was used in [25] to create what was referred to as a quarter-mode cavity resonator as shown in Fig. 2.30. For additional miniaturization two slots were cut out of the top ground plane as shown in Fig. 2.30. The radiation mechanism was largely the same as for the half-mode substrate-integrated cavity with a caveat: as there were two perpendicular open apertures there were two radiating magnetic currents. The combination of radiation from these two apertures resulted in slant linear polarization. It was shown that despite the small size the quarter-mode cavity antenna could still display high immunity to the effects of the human body by a properly optimized bottom ground plane extension denoted as gnd_{ext} in Fig. 2.30. Whilst the effects of mechanical deformation were not investigated it can be assumed that the antenna would be robust due to the compact size.

Multi-Resonant Structures

Generally there are a range of frequency bands that may be utilized for wearable applications such as the global positioning system (GPS) [26], industrial, scientific and medical communications (ISM) [26–28], global system for mobile communications (GSM), personal communications services (PCS) and wireless local-area network (WLAN) [29, 30]. To simultaneously cover these bands multi-band textile antennas have been proposed and some selected contributions are herein discussed.

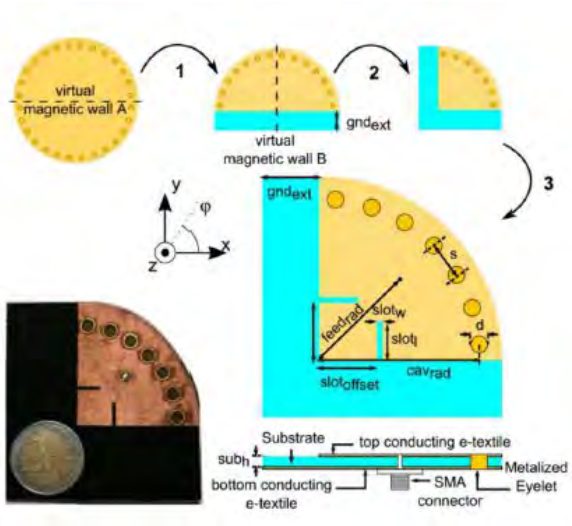

Figure 2.30. A textile quarter mode cavity resonator antenna as reproduced from [25].

As a first example a dual-band antenna with omni-directional patterns at the 915 MHz ISM band and broadside radiation patterns at the 1.575 GPS L1 band was presented in [26]. This antenna was designed for integration into a military beret as shown in Fig. 2.31. The total structure consisted of two independently fed antennas which utilized a common ground plane incorporated inside the beret. The lower operation band was achieved by a circular ring patch antenna that was short-circuited to the ground plane, whereas the higher band was achieved by a truncated corner square patch antenna. As there were two radiating elements that were independently fed it was demonstrated that each band could be independently optimized. Performance-wise the antenna was experimentally shown to be robust to the effects of the human body and exceptionally robust to mechanical deformations as a substrate compression of 12% was needed for the operating frequencies to sufficiently shift such that the antenna did not cover the desired bands. The main limitation of this design was the rather low peak gain at the lower band which was estimated to be below -20 dB.

In contrast to the previously mentioned dual-fed antenna a highly miniaturized planar inverted-F antenna (PIFA) using a single feed was presented in [27] as shown in Fig. 2.32. The antenna was designed for operation at 433 MHz and 2.4 GHz where the total antenna size came to $0.20\lambda_0 \times 0.12\lambda_0 \times 0.01\lambda_0$ at the lower frequency of operation. The main contribution of this work was the exploitation of ground plane resonances for bandwidth enhancement at the lower band whilst obtaining a compact resonator size. This was achieved by first designing a standard PIFA at 433 MHz. Then to enhance the bandwidth the ground plane was modified to radiate at 433 MHz. This was

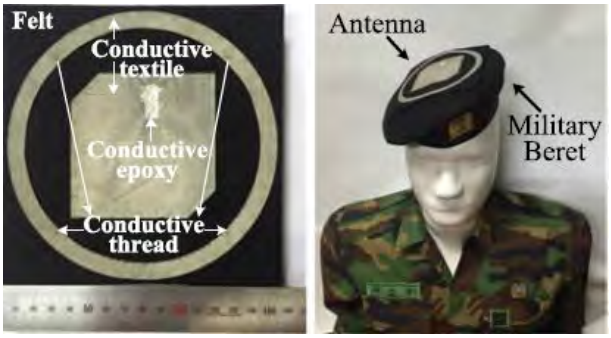

Figure 2.31. A dual-band textile antenna exploiting two independently fed radiators with omni-directional and broadside radiation patterns for integration into a military beret as reproduced from [26].

achieved by exploiting characteristic mode analysis (CMA) where it was shown that the ground plane could resonate at 433 MHz through the addition of slots as shown on the right of Fig. 2.32. After having completed the design at the lower band a L-shaped slot was introduced on the top layer to generate another band centered at 2.4 GHz. In terms of performance it was shown that by overlapping the resonance frequency of the PIFA and the ground plane a relatively large bandwidth of 10% was achieved at the lower band. Additionally the obtained bandwidth of 13% at the higher band was much higher than a conventional PIFA. The main limitation of this work was the performance degradation at the lower band when the antenna was placed in close proximity to human body tissue. This was attributed to the ground plane slots which caused radiation to leak into the human body. This was exacerbated considering that the ground plane was itself a radiating element at these frequencies. In contrast minimal performance degradation was observed at the higher band as the ground plane behaved as an isolating element.

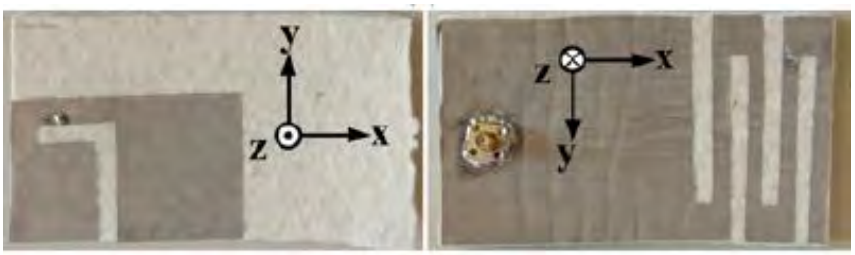

Figure 2.32. A dual-band slot loaded PIFA for operation at 433 MHz and 2.4 GHz as reproduced frrom [27].

The authors of [28] also presented a dual-band antenna that was excited by a single feed. Their antenna shown in Fig. 2.33 was based on the simultaneous excitation of

the TM_{11} and TM_{02} modes of a circular patch antenna for operation at 2.45 and 5.8 GHz respectively. As the resonance frequencies of both modes were related by a fixed ratio for a given patch size it was claimed that the independent optimization of both frequencies without modifying the structure would have been very difficult. To obtain a larger degree of independent control for both modes the top layer of the patch was modified to contain two arc shaped slots and a shorting pin as shown in Fig. 2.33. By properly optimizing the position of the slots and the shorting pin it was demonstrated that the two modes of the patch antenna could be somewhat independently optimized to obtain the desired resonance frequencies. Performance-wise the antenna was experimentally demonstrated to be robust to the effects of bending and loading by the human body.

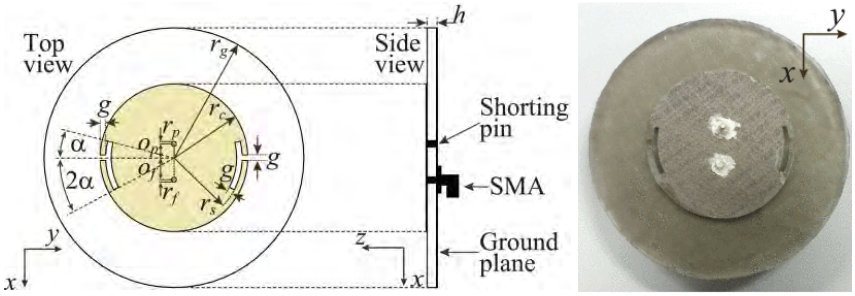

Figure 2.33. A dual-band textile patch antenna with resonance frequencies at 2.45 and 5.8 GHz. This image is adapted from [28].

A different type of dual-band antenna which was also excited through a single feed was presented in [29]. The antenna based on the quarter-mode cavity resonator was designed to resonate at 2.4 and 5.8 GHz. This work utilized a shorting pin to merge the second and third higher order modes of the cavity to provide a wide -10 dB impedance bandwidth of 12% at the higher band. Performance-wise the antenna was experimentally demonstrated to be robust with regards to human body effects as it was shown that the antenna could be placed against the human body with minimal variation in the radiation characteristics. One of the main advantages of the antenna was the very simple geometry as shown in Fig. 2.34. As the antenna was a semi-open rectangular cavity it is very simple to fabricate which is a desirable feature for wearable applications.

Multi-band textile antennas are very desirable for wearable applications as they can potentially cover multiple frequency bands. For this reason a fully embroidered multi-band antenna was presented in [30] which covered the GSM, PCS and WLAN bands with center frequencies of 900 MHz, 1.9 GHz and 2.45 GHz respectively. The structure shown in Fig. 2.35 can be viewed as an asymmetric slot loaded dipole antenna with an

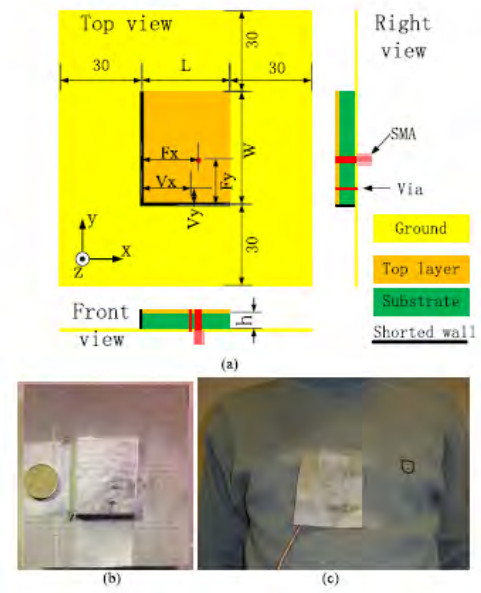

Figure 2.34. A dual-band quarter-mode cavity antenna as reproduced from [29].

additional loop for impedance matching purposes. As previously mentioned the main limitation of using a dipole or any antenna structure without an isolating structure such as a ground plane is the performance degradation when placed in close proximity to the human body. It was shown that the antenna needed to have a minimum spacing of 10 mm from the human body tissue to fully cover all three bands.

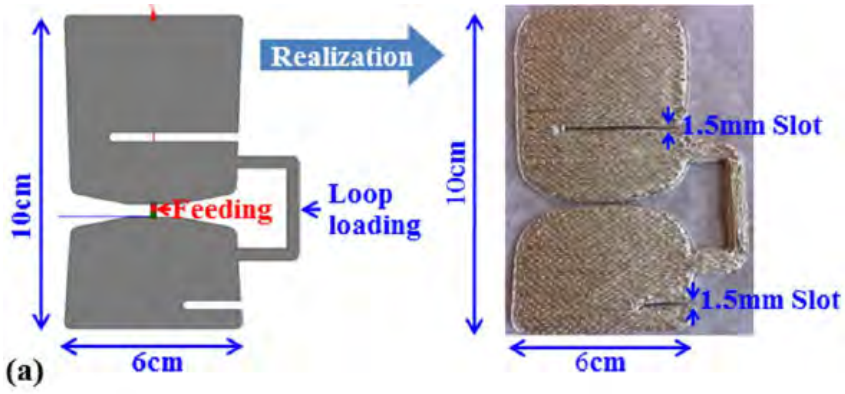

Figure 2.35. An embroidered multi-band antenna as reproduced from [30].

Metamaterial-inspired antennas

Metamaterials which derive their name from the greek prefix "meta" meaning beyond are artificially synthesized periodic structures with homogenized properties that are not naturally available. They are usually constructed by periodically repeating an

electrically small base geometry known as a unit cell as shown in Fig. 2.36, which is adapted from [31]. The type of artificial synthesized materials that have been utilized for wearable applications include but are not limited to: hard/soft surfaces, electromagnetic bandgap (EBG) structures and composite right/left handed (CRLH) structures. Textile based wearable antennas which utilize the aforementioned artificially synthesized structures are herein discussed.

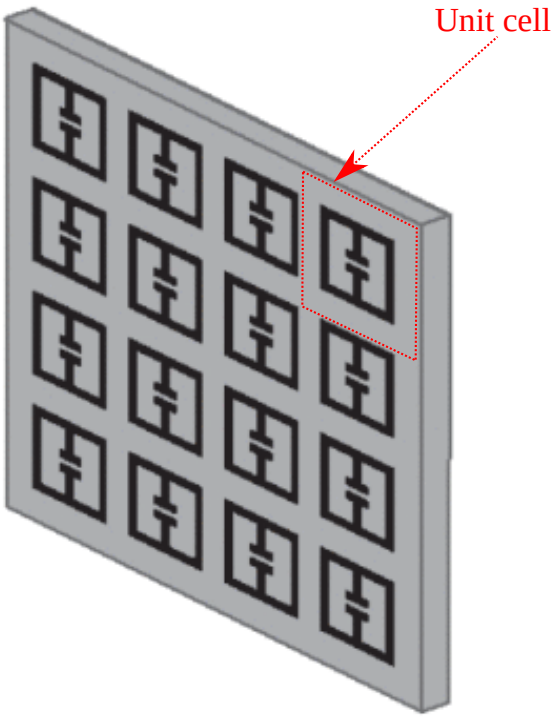

Figure 2.36. A model which shows the typically periodic nature of metamaterials. This figure has been adapted from [31] where the text, dashed arrow and dashed red line has been incorporated by the author of this thesis.

Hard surfaces are structures which facilitate the propagation of TE and TM modes whilst soft surfaces inhibit the propagation of TE and TM modes within a certain frequency band [74]. The inhibitive properties of soft surfaces were utilized in [32] to diminish the effects of surface waves and enhance the broadside radiation of a circular patch antenna operating at 4 GHz. In this study a textile soft surface which consisted of multiple shorted circular rings was designed to display a bandstop feature which overlapped with the resonance frequency of the circular patch antenna. Then the textile soft surface surrounded the circular patch antenna as shown in Fig. 2.37. By comparing the simulated radiation patterns with and without the soft surface it was concluded that

the soft surface significantly enhanced the broadside radiation thus indirectly suggesting that the soft surface reduced surface waves. Additionally through both simulation and measurement results it was demonstrated that when the antenna was bent the textile soft surface diminished the propagation of surface waves. This was a particularly important observation as textile antennas are expected to be bent [72] which may alter the radiation patterns and cause the antenna to radiate in undesired directions.

Whilst surface waves are undesired for wearable applications where broadside radiation is required they are perfectly suited for wearable applications where endfire radiation is desired such as for on-body communications, for example between various sensor nodes. To this end the authors of [33] presented a circular patch antenna with a resonance frequency of 5.8 GHz based on the TM_{01} surface-wave mode. To enhance the propagation of the surface wave the antenna was periodically loaded with an EBG structure as shown in Fig. 2.38. Essentially the presence of the EBG changed the boundary condition along the circumference of the antenna which improved the propagation of the surface wave. To quantify the improvement in surface wave propagation a numerical study was performed which examined the variation in the transmission coefficient between two circular patch antennas placed at different locations on the human body with and without the EBG. The numerically obtained results showed that the transmission coefficient, S_{21}, could be enhanced by 7.07 dBi with the presence of the EBG. Shifting from simulation to measurement results it was further proved that the inclusion of the EBG significantly enhanced the endfire radiation of the patch antenna by 3.08 dBi. Due to the required periodic nature of the EBG these performance improvements came at the cost of increased planar dimensions of the overall structure.

The previously discussed textile EBG based antennas have been based on the concept of using the properties of the EBG to alter the radiation characteristics of an antenna. It is also possible to directly use artificially synthesized materials as radiating elements. This can be achieved by using the CRLH transmission line. To appreciate how CRLH transmission lines can be used in the design of antennas a brief overview of CRLH transmission lines is herein provided. For a more detailed discussion on these structures the reader is referred to [75–78].

Naturally occurring materials exhibit both positive permittivity and permeability [77]. These natural materials are also known as right handed materials. On the contrary artificially synthesized materials can display both *negative* permittivity and permeability and display behavior that is opposite to naturally occurring right handed materials.

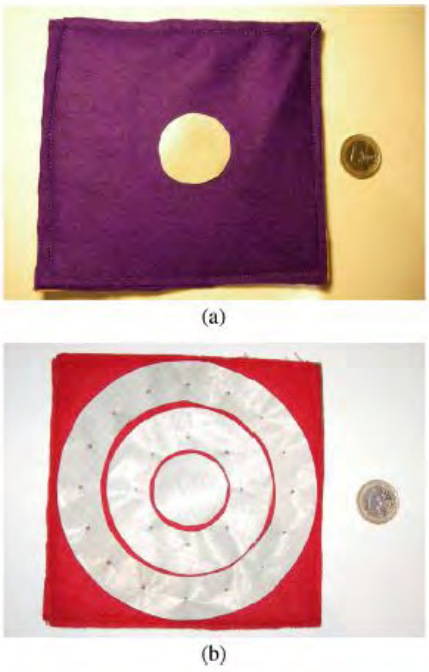

Figure 2.37. A patch antenna with (a) and without (b) a textile soft surface as reproduced from [32].

Figure 2.38. A patch antenna periodically loaded with a EBG structure for surface wave enhancement as reproduced from [33].

As a consequence of this opposite property they earn the name left handed materials. CRLH transmission lines are then structures which exhibit both left and right handed behaviour. A generic transmission line modeling approach of a CRLH structure is shown in Fig. 2.39. The right handed (naturally occurring) component are represented by L_R and C_R whilst the left handed (artificially created) component are represented by C_L and L_L.

Now if it can be intuitively understood that the right handed section of a CRLH structure display a positive phase constant then the left handed section should display a *negative* phase constant. This is in-fact observed for practical CRLH structures as shown in Fig. 2.40 [34] which shows the dispersion diagram for a typical CRLH transmission

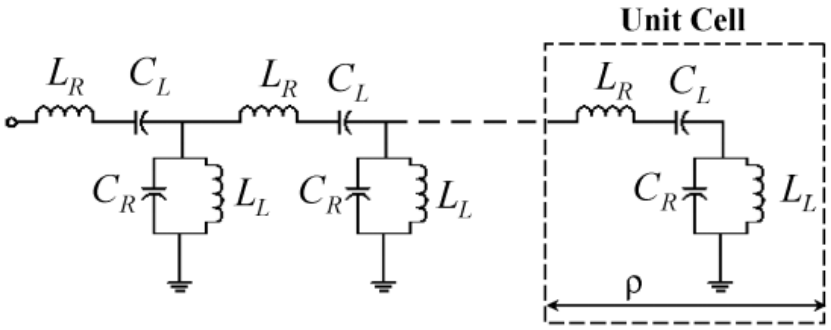

Figure 2.39. Generic model of a CRLH transmission line as reproduced [34].

line in both the left handed and right handed regions. From Fig. 2.40 it can be seen that there are terms such as $\omega_{+(N-1)}$ and $\omega_{-(N-1)}$. These are also known as positive and negative order modes as they correspond to the propagation frequencies within the right and left handed regions respectively. Additionally corresponding negative and positive order modes such as the ω_{+1} and ω_{-1} display largely similar field distributions and can therefore have similar radiation characteristics.

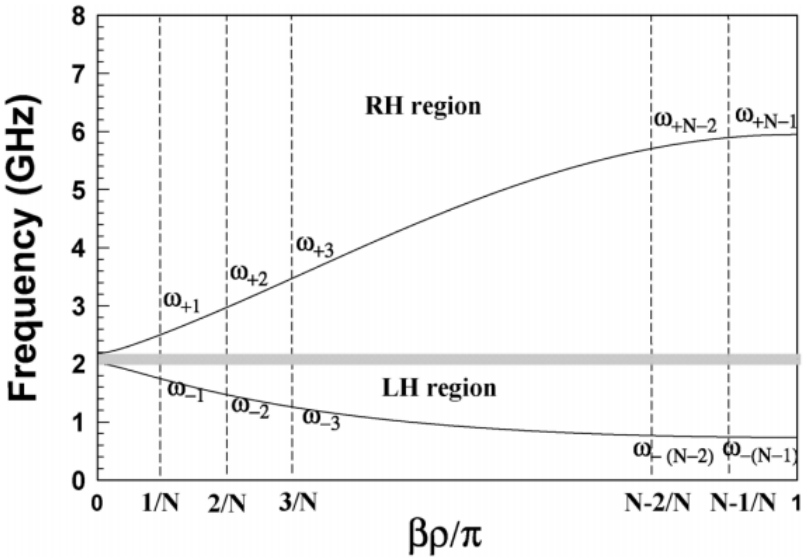

Figure 2.40. Dispersion diagram of a CRLH structure as reproduced [34].

For these attractive reasons a dual-band antenna exploiting the CRLH concept was presented in [35]. The antenna which was based on a slotted shorted patch antenna as shown in Fig. 2.41 displayed two radiation bands centered at 2.45 GHz and 5.2 GHz which corresponded to the first negative and positive modes. By making the lower

resonance correspond to the first negative order mode the antenna displayed a compact planar size of $0.2\lambda_0 \times 0.2\lambda_0$ at the lowest frequency of operation which would be in stark contrast to the dimensions of a standard patch antenna which would be $0.5\lambda_0 \times 0.5\lambda_0$ at the same operating frequency. Despite the very small resonator size the antenna was relatively insensitive to the effects of bending and proximity to human body tissue as corroborated through simulation and measurement data. Concerning the far-field performance the antenna displayed broadside radiation patterns at both bands which was a consequence of the excitation of the first negative and positive order modes. Despite the impressive performance characteristics the antenna had one major performance limitation: the low radiation efficiency at the lower band due to the extensive miniaturization. Specifically the simulated radiation efficiency at the lower band was 17%. The other drawback for this design was the tight tolerances needed to cover the lower and upper bands. For the lower band an accuracy of $\pm$ 0.2 mm was needed whilst the higher band required a tolerance of $\pm$ of 0.5 mm which as previously mentioned can be difficult to achieve for conductive fabrics.

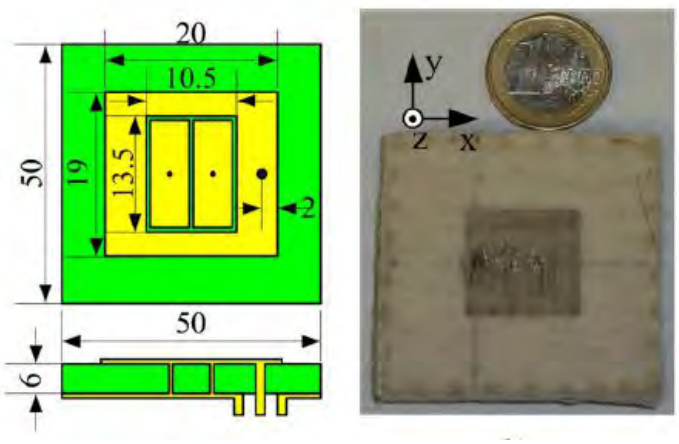

Figure 2.41. A slotted shorted patch resonator based on the CRLH transmission line as reproduced from [35].

2.3.4 Antenna Arrays

In a realistic body-worn communications scenario there may be a wide spatial range which needs to be covered by the textile antenna. Generally it is difficult to cover a large spatial range with a single antenna. However if properly designed multiple antennas which are optimally separated could be used to enhance the spatial coverage. This was one of the aims of the work presented in [36]. A second aim was to

demonstrate that a textile antenna array could be experimentally realized whilst being mindful on the effects of bending on the performance of the individual elements. In regards to the first aspect an eight element textile patch antenna array was designed and fabricated as shown in Fig. 2.42. Experimentally it was demonstrated that the array could be bent without causing a noticeable degradation in the reflection coefficient of the individual elements. Whilst no experimental results regarding the effects of bending on the radiation patterns of the array were provided it was suggested that the patterns could be somewhat affected [36]. After having demonstrated that a textile antenna array could be realized the next step was to replace the patch antenna with a self-complementary structure as shown in Fig. 2.43 to realize a wideband array. For the unacquainted reader a brief overview of self-complementary structures is herein provided. To appreciate what a self-complementary structure is, the concept of complementary structures must first be understood. Consider a dipole antenna as shown in Fig. 2.44(a) which consists of two metallic arms separated by a gap. The *complementary* structure would be a slot of the same length and width of the dipole on an infinite ground plane as shown in Fig. 2.44(b). The dipole and slot are known as complementary structures because when they are properly combined they can form a metallic sheet with no gaps [73]. A self-complementary structure is then a structure which combines a radiating element and its complement (with dual feed) into the one geometry as in Fig. 2.43. By numerically investigating the performance of a single self-complementary structure which showed some nulls over certain angular ranges it was numerically shown that by properly spacing and rotating a number of the self-complementary antennas a broad angular range with a relatively stable gain could be obtained. Unfortunately this study did not present experimental results to validate the simulated results in regards to the last aspect.

Whilst all of the wearable antennas that have so far been evaluated operated over the microwave frequency range the millimeter wave region has also attracted interest due to the high data rates, wide bandwidth and small form factor [79]. Motivated by these advantages a textile based millimeter wave patch antenna array was presented in [37] where the main contribution was to demonstrate that textile materials could be utilized at the millimeter wave range. To this end a 2×2 array of microstrip patch antennas fed by a microstrip line was fabricated. The substrate was a standard cotton substrate and the ground plane was realized through a conductive fabric. Unfortunately the radiating elements and the associated microstrip feedline could not be realized from conductive textiles due to difficulties in patterning conductive textiles to the required

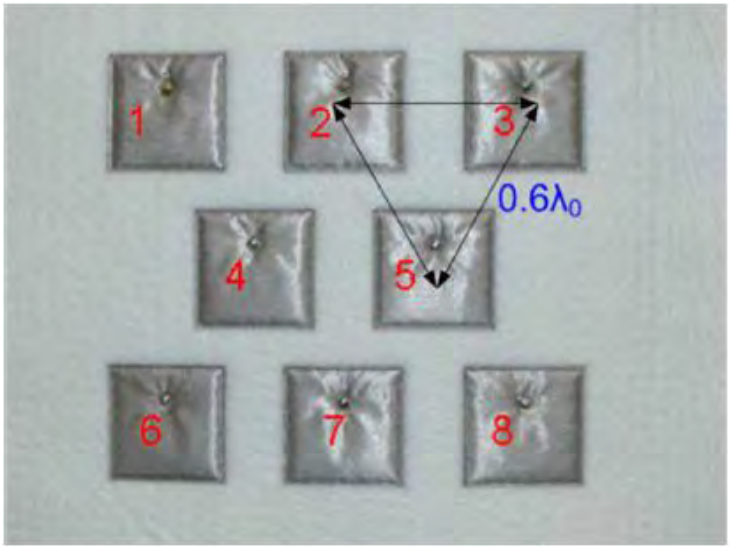

Figure 2.42. A textile antenna array based on probe fed patches as reproduced from [36].

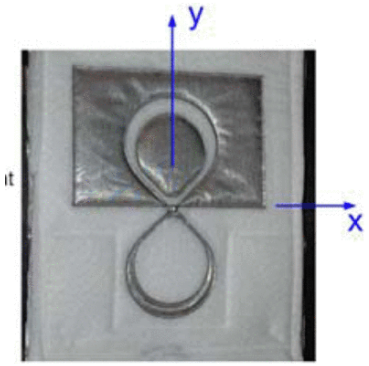

Figure 2.43. A self-complementary antenna as reproduced from [36].

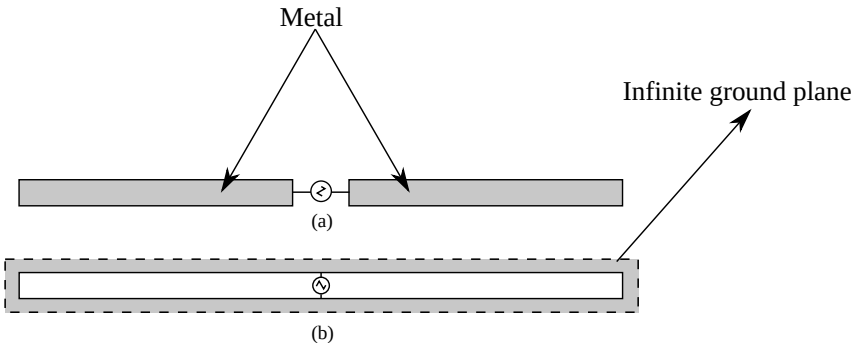

Figure 2.44. From top to bottom: (a) A dipole antenna and (b): the complementary slot antenna on an infinite ground plane.

sub-millimeter accuracy. Thus copper tape was used for the radiating elements and feeding mechanism as shown in Fig. 2.45. Regarding the performance it was experimentally and numerically demonstrated that the antenna could be placed directly onto

human body tissue as shown in Fig. 2.45 with minimal performance degradation in both the reflection coefficient and the radiation patterns. Whilst the demonstration of a semi-textile based millimeter wave antenna array was a noteworthy achievement the main limitation of this work was a moderate radiation efficiency. Whereas simulations predicted a radiation efficiency of 45% the measurements produced a radiation efficiency of 41%. It was found that the major contributor to the low efficiency was the loss tangent, δ, of the cotton substrate which was experimentally determined to be 0.02 across the desired frequency range.

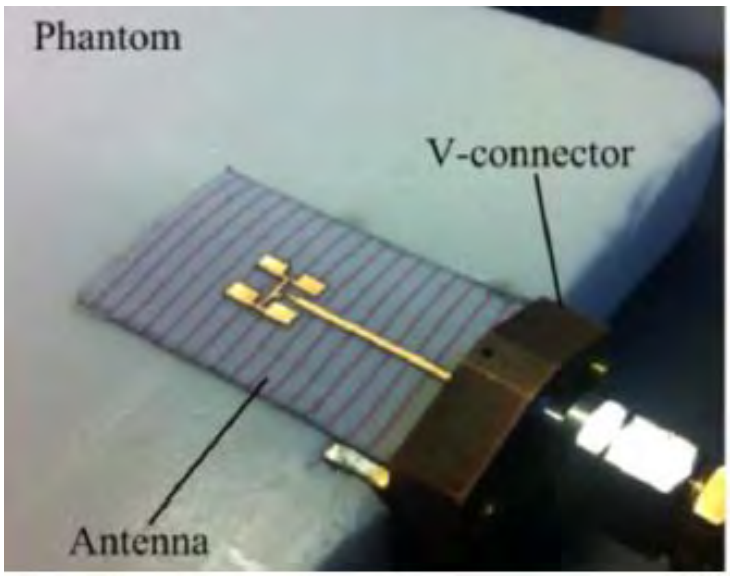

Figure 2.45. A semi-textile antenna array at 60 GHz as reproduced from [37].

2.3.5 Practical aspects

Whilst the previous discussions have largely focused on new antenna topologies this section focuses on additional aspects that should be considered to enhance the practicality of wearable antennas. For example a majority of the previously discussed antennas have utilized an SMA connector as the feeding mechanism which is elegant for validation purposes but limited in practical applicability for reasons of user comfort. To address this issue the work shown in Fig. 2.46 and presented in [38] investigated an aperture coupled feeding mechanism for patch antennas. In this configuration, the radiating and feeding element can be physically separated thus allowing for a largely independent optimization of both components. Performance-wise it was demonstrated that simultaneous bending of the antenna and feed did not result in significant performance degradation as quantified by minimal variation in the reflection coefficient.

However given the exposed nature of the feed the antenna needed to be separated from human body tissue by a spacer which came at the cost of decreased user comfort.

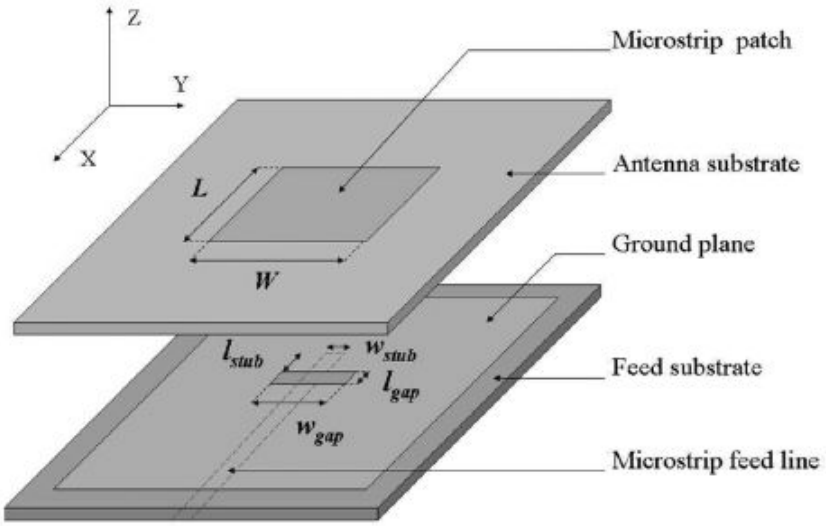

Figure 2.46. A textile aperture coupled patch antenna as reproduced from [38].

Previous discussions have shown that wearable antennas will be subject to adverse environmental conditions such as bending and proximity to human body tissue. Whilst the effects of some adverse conditions such as bending and proximity to human body tissue can be accounted for in the design process there are other conditions which are very difficult to account for such as moisture absorption through rain or sweat as these effects are highly statistical [80]. An additional adverse condition pertains to the sturdiness of textile materials. For example textile antennas are expected to be washed [80]. Washing can present significant mechanical forces on the textile materials which may become damaged [80]. This physical damage can then cause an alteration in the electrical properties of the materials which may result in obtained performance that is different from the simulated performance. For these reasons it is of interest to examine protection techniques for wearable antennas. In this context protection techniques refers to some form of physical barrier between the antenna and external influences such as moisture and mechanical forces. One solution is to encapsulate wearable antennas such that they are mechanically sealed from external influences. One material that can be used for encapsulation is polydimethylsiloxane (PDMS) which is a highly flexible hydrophobic material. To investigate the efficacy of encapsulating antennas to guard against the previously mentioned adverse conditions an innovate solution proposed in [39] incorporated a textile meandered dipole embedded into a PDMS material

as shown in Fig. 2.47. By encapsulating the antenna in PDMS a mechanical barrier to external factors such as moisture was created whilst retaining the high flexibility of the antenna. The authors claimed that the antenna could be repeatedly stretched and flexed over a period of two months with minimal variations in the reflection coefficient. Whilst this resulted in a mechanically insulated antenna the process to encapsulate the antenna was a challenging task as noted by the authors of this work.

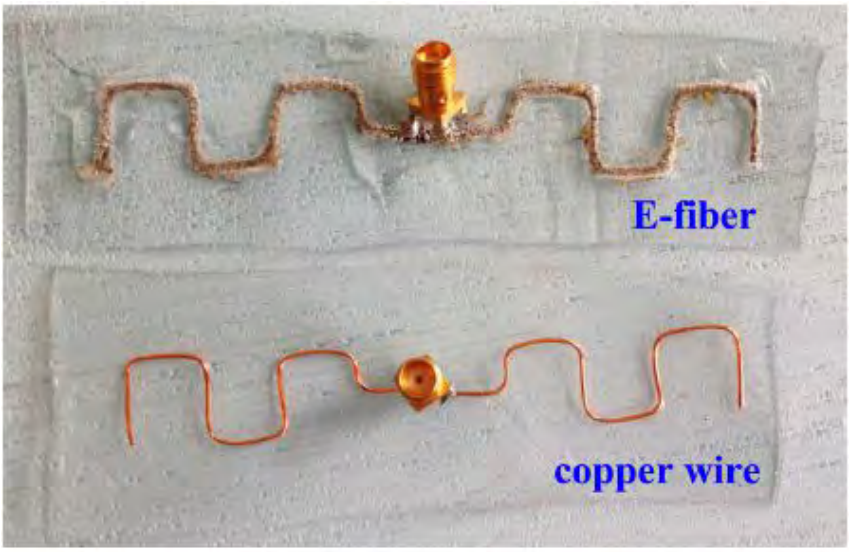

Figure 2.47. A textile and copper wire dipole antenna embedded into PDMS as reproduced from [39].

An alternative and somewhat simpler method on encapsulating wearable antennas was presented in [81]. In this work a textile wearable antenna was firstly wrapped in a breathable thermoplastic polyurethane (TPU) coating. Then a iron was used to mold the plastic coating around the antenna which provided the required mechanical seal. Afterwards to evaluate the effect of the mechanical seal the encapsulated antenna was washed, allowed to dry and new measurements were taken to examine the variation in the radiation efficiency. Experimentally it was shown that without the protective coating the radiation efficiency decreased by 11% across six washing cycles whereas with the protective coating the variation in radiation efficiency across the washing cycles decreased by 8%. This clearly demonstrated that incorporating the protective layer helped to desensitize the antenna from adverse conditions such as mechanical degradation and moisture absorption.

2.4 Summary

This chapter has begun by reviewing materials and techniques that can be used to realize flexible antennas. The advantages and disadvantages of each materials and techniques were summarized and the proposed method used to realize wearable antennas in this thesis was presented in detail. Then a broad overview of wearable antennas was provided. From the above discussions six key points can be extracted as mentioned below.

1. Combining conductive textiles and computerized embroidery results in antenna structures that exploit the advantages of both methods, i.e. accuracy of patterning and high efficiency.

2. Closed or semi-closed cavity resonators are attractive for wearable applications as they exhibit tight field confinement and have a ground plane. These two factors assist in making them relatively insensitive to external influences.

3. Closed cavity resonators tend to be electromagnetically large at their fundamental mode of operation which may inhibit their practical applicability depending on the operational frequency.

4. Generally speaking there are a range of frequency bands that are suitable for wearable applications such as ISM, GSM, PCS and WLAN.

5. Most of the textile antennas presented utilize an SMA connector as the feeding mechanism which can limit their practical applicability in systems integrated into clothing.

6. When subjected to adverse environmental influences such as moisture absorption or mechanical degradation the performance of wearable antennas can be altered. To mitigate this effect encapsulation techniques have been proposed and evaluated.

Chapter 3

Connection Strategies

FROM a broad perspective, wearable structures can be divided into two categories: fully flexible and rigid but miniaturized. Whilst fully flexible devices are preferred for wearable applications for reasons of user comfort, their utilization does raise some unique challenges that must be addressed. One of these challenges pertains to obtaining a reliable connection between flexible and rigid devices. For example if a flexible wearable antenna is to be connected to an RFID chipset then it is paramount that the connection between the antenna and the RFID chipset be robust enough to handle different forms of mechanical strain whilst retaining desired electrical performance. In this chapter the issue of connections is investigated by examining three textile connection strategies based on the merits of electrical and mechanical suitability. The results of this chapter present a new textile connection strategy known as the wing solution. The proposed solution is a strong candidate for interfacing flexible wearable devices with rigid devices.

3.1 Introduction

Wearable systems consist of two main components: an antenna required for wireless communications and electronic circuitry required for acquisition of the information to be transmitted. Whilst there has been tremendous advances in the realization of fully flexible antennas, the development of fully flexible electronics still requires improvement. Therefore, wearable antennas must at some point interface with rigid devices when viewed from a holistic system perspective. Quite often this interfacing is made with conductive epoxy [24, 82] as shown in Fig. 3.1. Whilst being an elegant solution for testing purposes, conductive epoxy is prone to cracking when subjected to mechanical force. Additionally, conductive epoxy is expensive and requires 24 hours curing time for maximum bond strength leading to delays in fabrication. To mitigate some of the difficulties associated with conductive epoxy several interesting solutions have been proposed in the literature. These include: soldering, snap-on buttons, magnetic contacts and hook and loop connectors which are herein described.

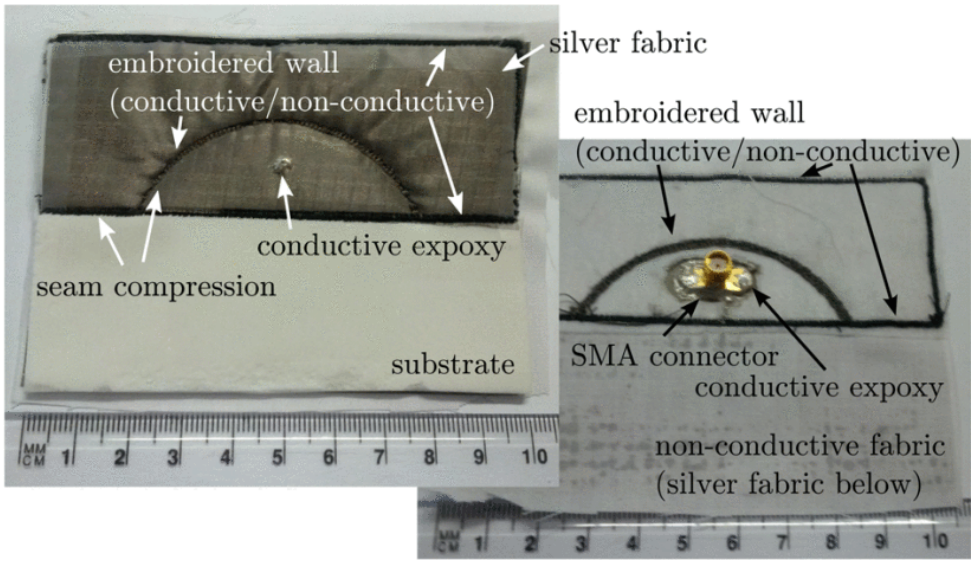

Figure 3.1. A textile antenna utilizing conductive epoxy to realize a connection between the feeding element (SMA connector) and the antenna. This image is reproduced from [24].

The work presented in [40] investigated the use of soldering techniques to obtain a robust connection between an SMA connector and a textile shielded stripline over a frequency range from 10 MHz to 7.0 GHz. The shielded stripline was itself realized by ironing a conductive fabric known as ShieldIt Super onto a fleece substrate. Performance-wise the shielded stripline displayed a measured reflection coefficient below -20 dB and a transmission coefficient of approximately -0.6 dB up to 7.0 GHz.

Three different solder types, namely copper laden solder, tin-lead solder and indium solder were investigated to see which type offered the best mechanical bond. From this study it was determined that copper laden solder offered the best bond as a force of 72.36 newtons was needed to physically separate the SMA connector from the conductive fabric. In contrast the tin-lead solder resulted in the worst bond as only 60 newtons of force was required to disconnect the SMA connector from the conductive fabric. This difference was attributed to the differing amount of mechanical interaction of the fabric with the different solder types as shown in Fig. 3.2(a) and Fig. 3.2(b). One interpretation of these results is as following: when using solder to obtain a connection between textile and rigid materials, care has to be taken to find the specific type of solder that can result in the optimum bond. Generally this might not be an easy task as there are a range of conductive elements and materials that are used in the realization of conductive textiles.

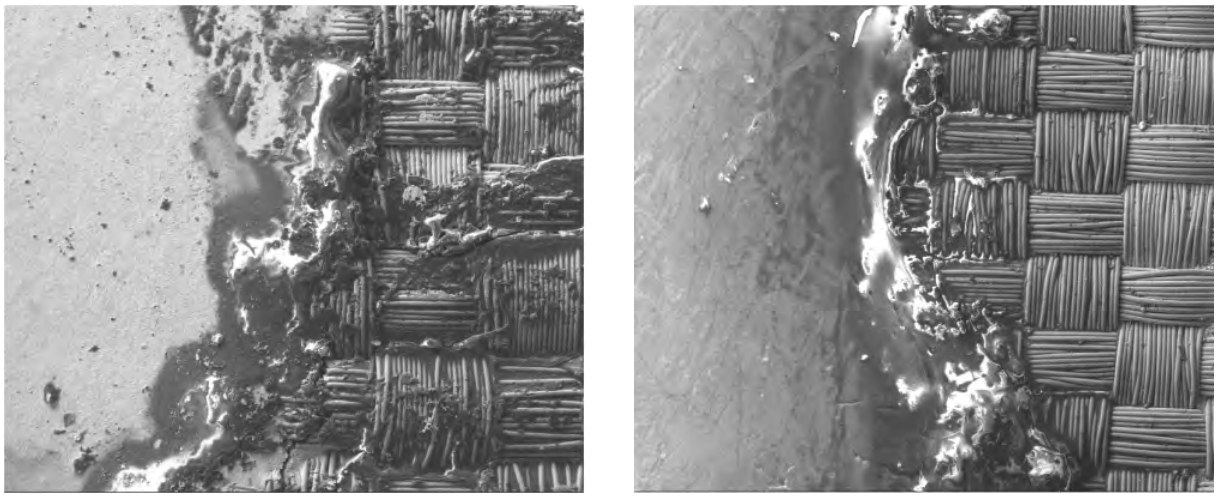

(a) (b)

Figure 3.2. From left to right (a) Microscopic view of conductive fabric with the application of copper laden solder and (b) Microscopic view of conductive fabric with the application of tin-lead solder. This image is reproduced from [40].

Snap-on buttons which are often used in textile applications have also been used in the design of textile microwave components such as antennas and transmission lines. Initial work investigating snap-on buttons focused on realizing dedicated connectors as shown in Fig. 3.3 for military applications. These dedicated buttons were shown to work uptil 3.0 GHz [41]. Aimed at a more readily available solution, commercial snap-on buttons were utilized as a potential replacement for expensive subminiature

version A (SMA) connectors [42]. In this study the snap-on buttons were used to feed a microstrip line on a flexible substrate as shown in Fig. 3.4. The authors of this study found that the buttons had their own non-negligible reflection due to the unique geometry which limits their usable frequency range to 3.0 GHz. Based on these promising initial results, further investigations into the applicability of snap-on buttons were conducted [83] where it was found that snap-on buttons can be used to obtain a reliable connection between a textile wideband UHF dipole antenna and a rigid RFID chipset. Integration of the snap-on buttons for a balanced transmission line demonstrated a usable frequency range from 0.1 GHz to 5.0 GHz where the buttons had an transmission coefficient varying from -0.29 dB to -0.76 dB across the aforementioned frequency range.

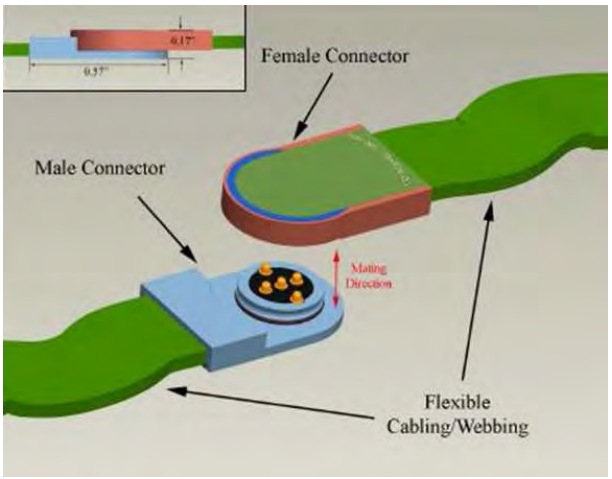

Figure 3.3. Dedicated snap-on buttons developed for military applications as reproduced from [41].

An innovative solution presented in [43] proposed the use of permanent magnets to obtain a robust mechanical connection between textile and rigid materials. The geometry used to investigate the suitability of using magnets as a mechanical connection is shown in Fig. 3.5 and herein described. A textile transmission line was realized on a denim substrate. Then the textile substrate was partially overlapped with two rigid FR-4 substrates as shown in the top of Fig. 3.5. Lastly permanent magnets with opposite polarity were then placed on the top and bottom sides of the overlapped regions of the textile and rigid substrate. Due to the attractive force between the magnets, the textile and rigid substrates were tightly compressed which led to an excellent mechanical connection. The entire structure was fed through two SMA connectors which were adhered to the two FR-4 boards. Performance-wise it was experimentally shown that

Figure 3.4. Commerical snap-on buttons used as a replacement for a SMA connector in a textile microstrip line as reproduced from [42].

a mechanically robust connection was achievable with a peak transmission coefficient of -0.8 dB up to an operation frequency of 3.0 GHz.

The utilization of conductive hook and loop velcro connectors was presented in [44] as shown in Fig. 3.6. This solution is more flexible than those discussed previously. By making disconnected microstrip lines on a FR-4 substrate and bridging these gaps with conductive hook and loop connectors, a stable electrical connection was achieved. Neglecting the study using solder, this is the only study that presented measurement results covering the lower and upper microwave industrial scientific and medical (ISM) bands, centered at 2.45 GHz and 5.8 GHz respectively, which are of interest for wearable applications [84]. Unfortunately, the hook and loop connectors were extremely lossy. The same transmission line fabricated without any gaps displayed a measured transmission coefficient of approximately -0.8 dB at the upper limit of the frequency range whilst with a hook and loop connector the transmission coefficient decreased to -5.0 dB for a gap size of 1 mm. Additionally, as previously mentioned, the tests were done on a rigid FR-4 substrate which would naturally offer more mechanical support to the hook and loop connectors than a flexible substrate.

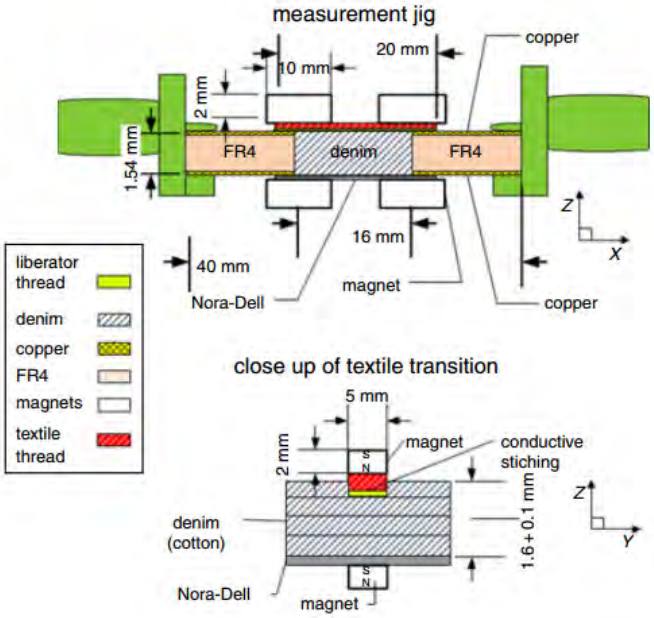

Figure 3.5. Permanent magnets used to secure a textile transmission line structure to a rigid FR-4 substrate as reproduced from [43].

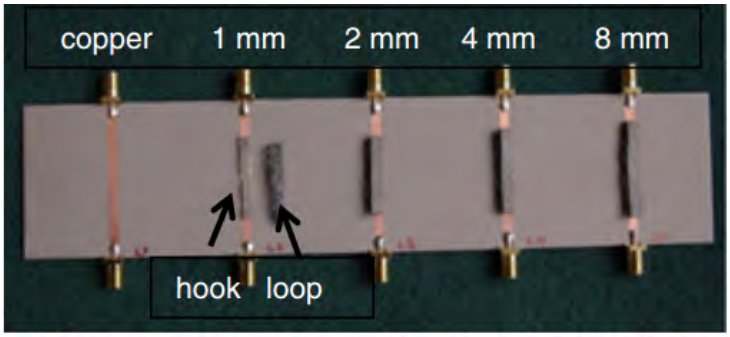

Figure 3.6. Conductive hook and loop connectors used to bridge a gap in a microstrip line fabricated on a FR-4 substrate as reproduced from [44].

From the aforementioned studies it can be observed that the solutions that have been investigated have often been bandwidth limited. In the studies where the bandwidth was extended it was found that the connection strategy became extremely lossy, limiting their use at higher frequencies with the exception of the study using solder which had other difficulties. Additionally (neglecting the snap-on buttons) none of the presented solutions are fully textile in nature. To obtain connection strategies amenable to textile techniques that perform well at high frequencies, a study is performed using three potential solutions. The investigated solutions are: snap-on buttons, butterfly clasps and the wing solution. The various solutions are used to realize a connection

between the inner pin of a SMA connector and the top layer of the microstrip transmission line. The performance of the transmission line is used as a metric to evaluate the validity of the proposed solutions. As the aim of this study is to find a feasible alternative to conductive epoxy, a transmission line using conductive epoxy as the connection strategy is used as a reference.

3.2 Geometry Overview

For the purposes of this study a perpendicularly fed back-to-back microstrip line is chosen as it allows easy access to the interface between the inner pin of the SMA connector and the top layer of the microstrip line. Furthermore, a microstrip line can easily be designed to have broadband characteristics allowing for validation of the proposed solutions over a large frequency range. The nominal geometry without any connection strategy is shown in Fig. 3.7. The main design parameters are the width of the microstrip line which is designed for a 50 Ω characteristic impedance and the additional segment L_T which is determined based on two criteria: 1) physical clearance required for fabrication; and 2) impedance matching purposes. Specifically by optimizing L_T the operation bandwidth can be altered due to the interference of the left and right fields. The planar substrate dimensions (W_S and L_S) along with the length of the transmission line (L_T) are chosen for simplicity of fabrication. The substrate thickness is chosen to be as small as possible as a thick substrate will result in a wider transmission line which can excite modes other than the fundamental quasi-TEM mode resulting in undesired behavior [85]. In terms of the materials that are used ShieldIt NSC95R-CR conductive fabric is used for the metalization layers and a Cumming Microwave PF-4 low loss foam is used as the substrate. By using these materials the transmission line becomes very flexible. The thickness of the substrate is set at 1.6 mm for the aforementioned reason. The proposed solutions: snap-on buttons, butterfly clasps and the wing solution are depicted in Fig. 3.8 where it is observed that all the proposed solutions result in a change of geometry at the interface of the inner pin and transmission line.

3.3 Simulations

Given the non-trivial mechanical nature of the solutions, as shown in Fig. 3.8 their presence could potentially cause variations in the operating characteristics of the transmission line. For example, the looped arms of the butterfly clasp could introduce some

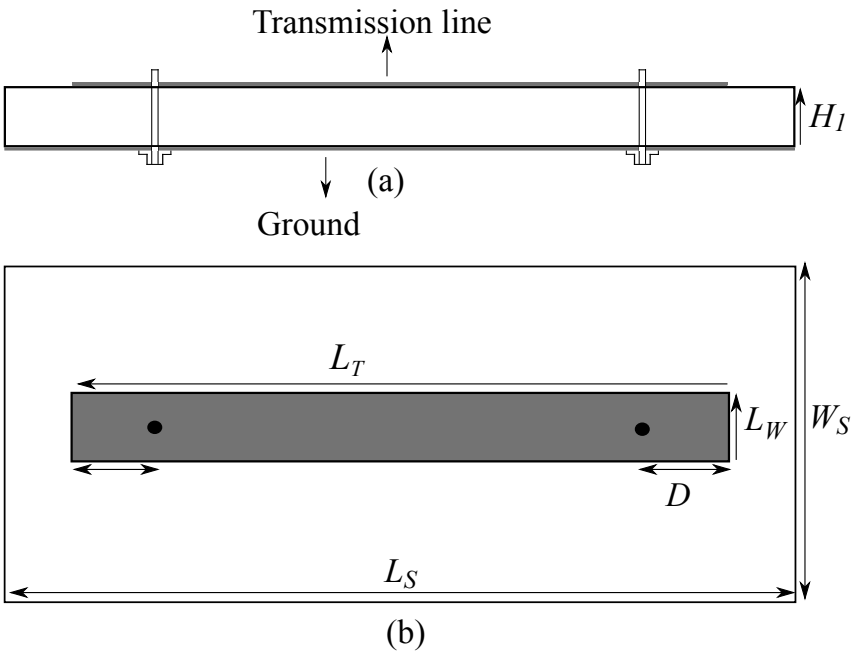

Figure 3.7. Schematic view of the microstrip line geometry used to evaluate the connection strategies - (a) Side view, (b) Top view. The parameters are $L_S = 60$ mm, $W_S = 50$ mm, $L_T = 37.5$ mm, $D = 2$, $L_W = 7.5$ mm, $H_1 = 1.6$ mm.

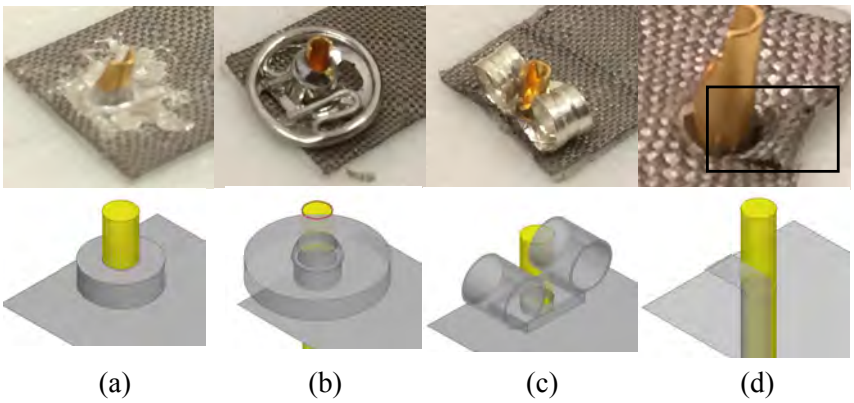

Figure 3.8. Depiction of the proposed connection strategies from left to right: (a) Conductive epoxy, (b) Snap-on buttons, (c) Butterfly clasps, (d) Wing solution. Top row shows the physical structure of each connection strategy and the bottom row shows the approximation of the connection strategy for simulation purposes.

inductance. Therefore, to evaluate any potential impact of the connection strategies simulations were performed where the nominal geometry was modified to incorporate the connection strategies as shown in the bottom row of Fig. 3.8. The snap-on buttons are modeled as a hollow cylindrical tube through the substrate representing the male portion of the button and a cylindrical object with a spherical bulge on the

top side representing the female portion. The butterfly clasps are modeled as two hollowed cylindrical objects on a rectangular base with a central circular hole pressing against the inner pin of the SMA connector. The wing solution is approximated by a thin piece of conductive material wedged in between the inner pin and teflon of the SMA connector. To serve as a reference, simulations where the the inner pin made a clean cut through the top layer are also performed. This situation is termed as the ideal case. The simulations for the ideal case and the cases where the connection strategies are incorporated will be discussed in Section 3.5. In all the simulations the substrate is modeled with a relative permittivty (ϵ_r) of 1.06 and a dielectric loss tangent (δ) of 0.0001. The conductive fabric is modeled as a lossy metallic infinitely thin object with a sheet resistance of 0.04 $\Omega/\square$.

3.4 Manufacture

The fabrication of the transmission line without any of the aforementioned connection techniques begins by cutting out a 1.6 mm thick piece of Cumming Microwave PF-4 foam to the overall dimensions of the structure. The ground plane is then cut out from ShieldIt NSC95R-CR conductive silver fabric with two holes to prevent short circuiting the SMA connectors and allowing the fields to pass from the teflon into the substrate. The central microstrip line is cut out with two small holes to accommodate the inner pin of the SMA connectors. Bonding of the silver fabric to the substrate is achieved by using foam-backed double-sided adhesive. The SMA connectors are fixed to the ground plane through a combination of conductive and non-conductive epoxy. The conductive epoxy is used to establish an electrical connection from the SMA connector body to the ground plane and the non-conductive epoxy is added on top to establish a strong mechanical connection. As previously mentioned, a reference transmission line is created where conductive epoxy is used to form a bond between the inner pin and the transmission line as depicted in Fig. 3.8(a). As the connection strategies have a non-trivial geometry, the required fabrication procedure is unique to each solution which is herein described.

In the standard form snap-on buttons do not have the clearance to accommodate the inner pin of the SMA connector. The first step is therefore to flay open the inner tubing of the male and female section as shown in Fig. 3.9(b). Then the male portion of the button is trimmed down to leave only the inner tubing which is then riveted through

the substrate as shown in Fig. 3.9(b) and Fig. 3.9(c). The inner pin of the SMA is then pushed through the male portion of the button. At this stage the inner pin of the SMA should be going through the substrate whist being clasped by the male portion of the button which is inside the substrate leading to a tight connection. Then the female section of the button comes in from the top side and mates with the male section securely locking in the inner pin of the SMA in the process as shown in Fig. 3.9(d).

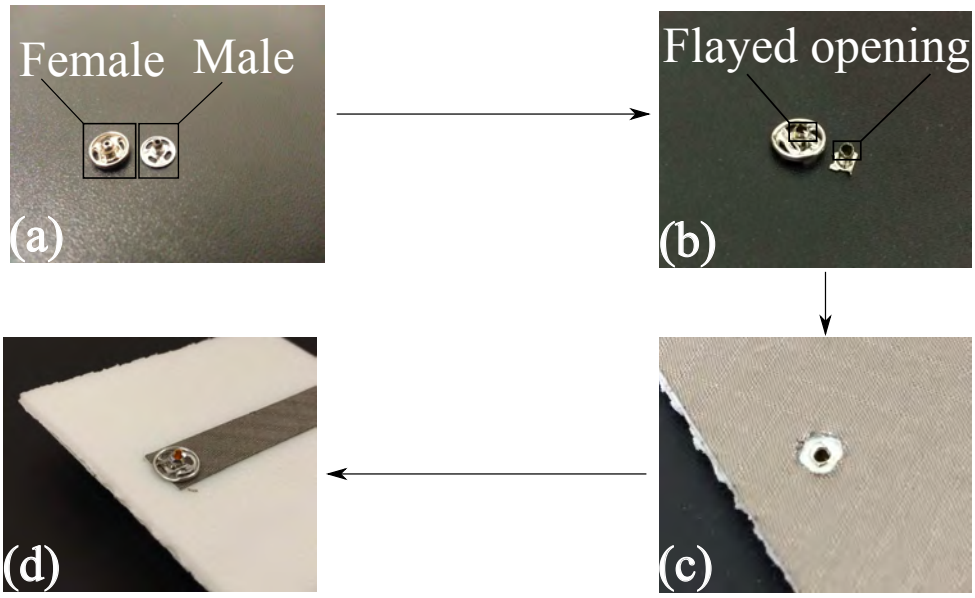

Figure 3.9. Fabrication procedure for the snap-on buttons connection strategy

In using the butterfly clasps, the first step is to protrude the inner pin of the SMA connector through the central circular hole on the rectangular base of the butterfly clasps. This is achieved by bringing the butterfly clasps from the top side of the transmission line and then pushing them firmly onto the substrate. Unfortunately when the inner pin of the SMA passes through the central circular hole, the looped arms of the clasps tend to spread outwards. This can be simply compensated for by pressing the arms inwards such that they are in mechanical contact with the inner pin of the SMA. In this way the inner pin of the SMA is held in place by the looped arms of the clasp which enlarge the contact area of the SMA inner pin.

The wing solution is unique among all the solutions in that it does not require any additional components but can be fabricated completely from the conductive fabric. Essentially the fabrication procedure for the wing solution is like the standard fabrication except that at both ends of the transmission line an additional narrow segment is included as shown in Fig. 3.10(a). This extra section can have an arbitrary length in the initial stages as it will be cut down later but for simplicity of fabrication it is suggested

that the extra length should not exceed 10 mm. This extra section is pulled through the hole in the substrate which was made to accommodate the inner pin of the SMA connector as shown in Fig. 3.10(b) and Fig. 3.10(c). The SMA connector is itself temporarily modified by removing the inner pin. The extra section of the transmission line is then pulled through the vacancy in the teflon made possible by removing the inner pin. The inner pin is then re-inserted into the SMA connector and the extra section of transmission line becomes wedged in between the inner pin and the teflon, leading to a robust connection as shown in Fig. 3.10(d). The extra section of the transmission line is then trimmed down.

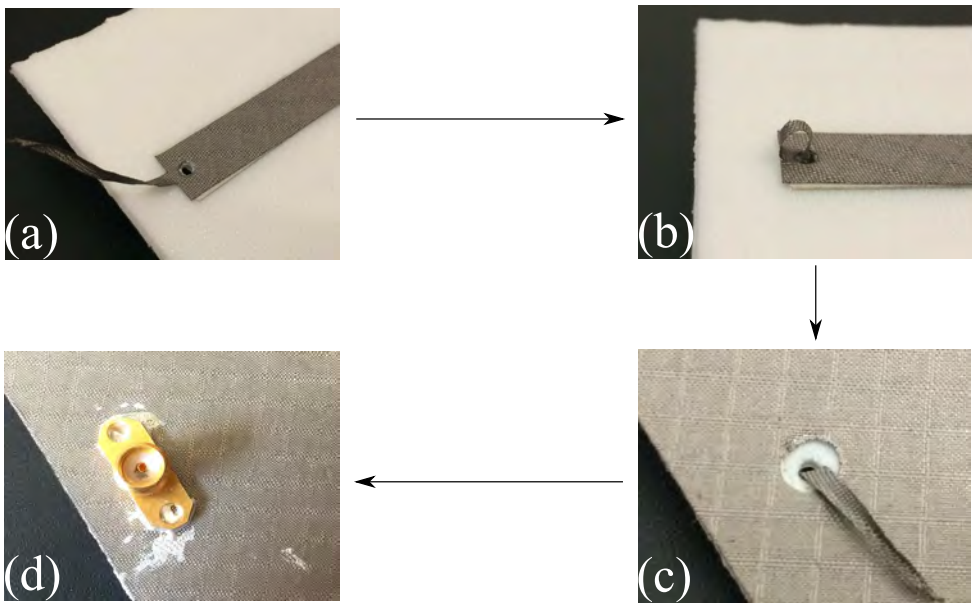

Figure 3.10. Fabrication procedure for the wing connection strategy

3.5 Results

The simulated and measured results are compared in Fig. 3.11 and Fig. 3.12. To serve as a reference against which to compare the proposed solutions the simulation results for an ideal case is presented. As the simulation results for the ideal case, conductive epoxy and the wing solution are highly similar only the results for the ideal case are shown. The simulation results for the ideal connection reveal a reflection coefficient (S_{11}) below -15 dB and a transmission coefficient (S_{21}) above -0.7 dB where the performance degrades with increasing frequency which is to be expected given the increasing material loss. Regarding the transmission coefficient it is observed that simulation results predict less loss than the measurements across all connection strategies. This is

most likely due to the modeling of the silver fabric. In simulations the silver fabric was modeled as a lossy conductor with sheet resistance of 0.04 Ω/□ which is an empirically determined value based on using fabric glue as the bonding mechanism [86]. In this study the fabric is bonded using foam-backed double-sided adhesive which will naturally have a different and in this case higher loss. Additionally the foam layer begins to act as a dielectric layer at higher frequencies due to the non-negligible thickness (roughly in the order of 1 - 2 mm) which will add to the discrepancy between simulations and measurements. Focusing now on the connection strategies, it is observed that the most severe discrepancy between simulations and measurements for both the reflection and transmission coefficient comes from the snap-on buttons. This is attributed to the severe compression of the substrate leading to altered transmission properties. This effect is also observed to a much milder degree for the butterfly clasps.

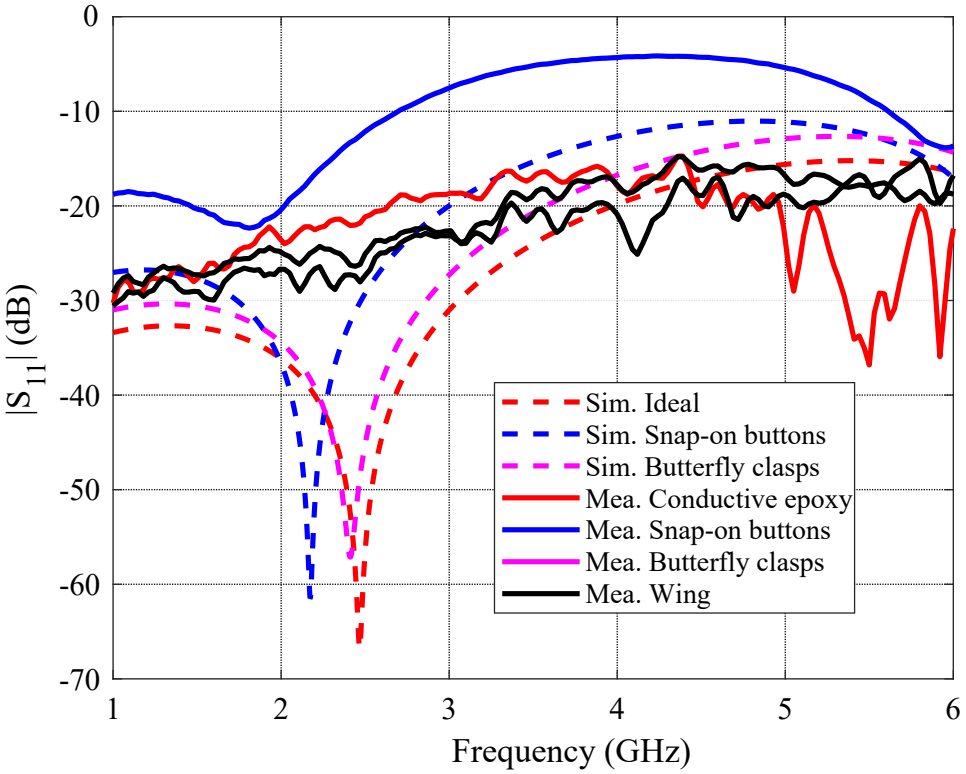

Figure 3.11. Simulated and measured reflection coefficient for connection strategies. Dashed lines are simulations and solid lines are measurements.

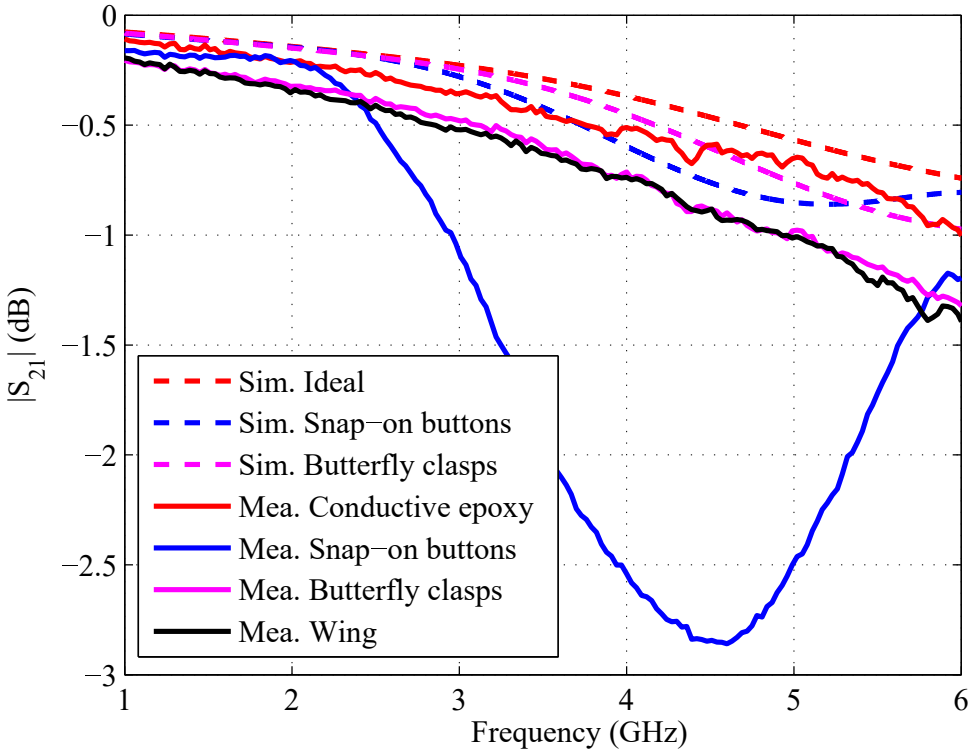

Figure 3.12. Simulated and measured transmission coefficient for connection strategies. Dashed lines are simulations and solid lines are measurements.

3.6 Comparisons

Of the three investigated solutions, the snap-on buttons exhibit the most severe impact on the performance of the transmission line which is attributed to the substrate compression. This suggests that if snap-on buttons are to be used to realize a connection between flexible and rigid materials, the potential variations in geometry in the flexible materials must be accounted for in the design process. While this is in principle possible based on empirical observation of the compression due to the buttons, this increases the complexity of the design. The butterfly clasps, whilst being a simple solution, are unfortunately rather fragile and are prone to variations in the geometry in practical situations arising from mechanical tension, thus making them difficult to use in rugged environments. The most exemplary solution in terms of electrical and mechanical performance is the wing solution as it does not require any additional components whilst offering excellent electrical performance rivaling that of conductive epoxy.

3.7 Conclusions

In this chapter three textile based strategies for realizing an electrical connection between rigid and flexible devices were numerically and experimentally investigated upto 6.0 GHz. Both electrical and mechanical performance were considered to make a holistic judgment. It was demonstrated that two of the proposed solutions, namely snap-on buttons and butterfly clasps, have a non-negligible effect on the performance of the structure which was attributed to the effects of substrate compression. This suggests that if either of these solutions were to be employed, the effects of substrate compression must be accounted for. The final solution, i.e. the wing solution, presents a viable alternative to conductive epoxy based on the permits of electrical and mechanical performance whilst being the most economical.

Chapter 4

Conformal Ground Planes

WEARABLE antenna structures which are realized from textile materials will be bent. Bending will result in variations in the ground plane geometry. The geometrical variations in the ground plane can in turn affect the radiation patterns. Variations in the radiation patterns may have important implications as the antenna might behave differently than expected. Consequently, to appreciate what effect conformal ground planes have on the performance of antennas, this chapter numerically investigates two forms of ground plane curvature. The two forms that are investigated are: cylindrical and spherical.

4.1 Introduction

From a system perspective, body-worn communications could entail a situation where off-body devices communicate with on-body devices. As a hypothetical example of relevance to defense, consider the case where a vehicular antenna communicates with a body-worn antenna [26, 45]. In such practical situations, the antennas are unlikely to have planar ground planes. For example, the antenna on the vehicle would most likely have a curved ground plane due to the inherent curvature of the vehicle. A similar statement can be made for the body-worn antenna. In this context, it is important to appreciate the effect of conformal ground planes on antenna characteristics and more specifically *on the far-field radiation characteristics* such as the gain patterns.

A recent investigation into the effects of curved ground planes on the gain patterns of a monopolar antenna was presented in [45]. This study showed that there was an appreciable variation in the end-fire gain of a low-profile monopolar antenna when mounted onto a curved ground plane which was integrated into a military helmet. The helmet mounted monopolar antenna which was itself placed on a human body phantom is shown in Fig. 4.1(a). The interior side of the helmet showing the curved ground plane is depicted in Fig. 4.1(b)

Figure 4.1. A monopolar antenna integrated onto a metalized helmet for military applications. This image is adapted from [45].

From the preceding study, it can be deduced that the far-field radiation characteristics such as the gain patterns can be highly dependent on the ground plane geometry [45]. Consequently, appreciating the effects of curved ground planes is an important and somewhat classical practical consideration [87, 88]. However, a systematic study into the effects of extended ground plane curvature on far-field antenna characteristics is

lacking. Aiming at filling this gap, the current chapter numerically studies the variation in far-field radiation performance of a low-profile monopolar antenna. The rationale for selecting this antenna will become clear in the following discussions.

4.2 Vehicular Scenario

4.2.1 Monopolar Antenna

The first step of the investigation is to determine the antenna for which to quantitatively study the effect of curved ground planes. The most suitable antenna type for this investigation can be deduced from the vehicular to human communications scenario provided in section 4.1. In such a scenario, antennas with omni-directional radiation patterns are preferred [89]. One type of antenna with a long and rich history that has omni-directional patterns is the monopolar antenna [90–94]. Attractively, monopolar antennas have an inherent ground plane which facilitates their integration into metallic structures such as vehicle roofs [45, 89] and makes them a natural choice for this investigation. A schematic of the low-profile monopolar antenna which is used in this investigation is shown in Fig. 4.2 and the operation principle of this antenna is herein briefly described.

In the most basic form this low-profile monopolar antenna can be viewed as a top loaded monopole. The top metalized layer of the loaded monopole is connected to the ground plane through three shorting vias that are separated by 120°. From the field equivalence principle, it can be shown that there is a magnetic current generated in between each shorting rod. The combination of these magnetic currents then acts as an effective magnetic current loop. In turn, the effective magnetic current loop radiates as an electrical monopole with omni-directional radiation patterns [95]. Alternatively, monopolar antennas can be seen as center-shorted patch antennas operating with a uniform field distribution [96]. For a more detailed discussion on the operating principle of monopolar antennas the reader is referred to [90–94]. In this study, for bandwidth enhancement, a monocone is selected to excite this center-fed shorted patch antenna. The numerical values of the critical parameters are provided in the caption of Fig. 4.2. The simulated reflection coefficient for the monopolar antenna is shown in Fig. 4.3 where it is observed that the antenna exhibits a reflection coefficient below -10 dB from 0.8 GHz to 2.9 GHz.

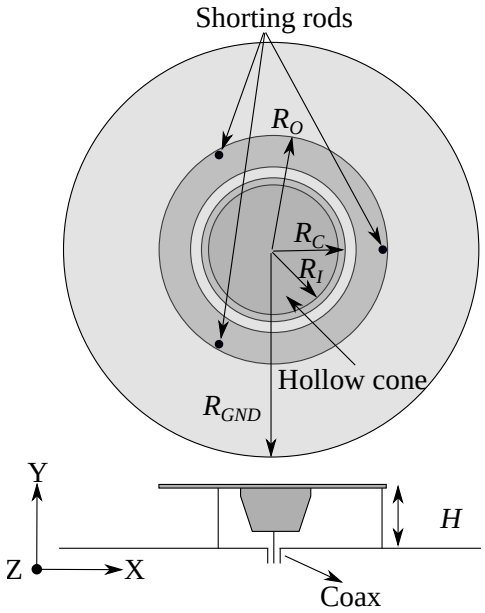

Figure 4.2. Schematic view of the low-profile monopolar antenna under investigation. $R_{GND} = 175$ mm, $R_I = 33$ mm, $R_C = 37.5$ mm, $R_O = 53$ mm and $H = 25$ mm.

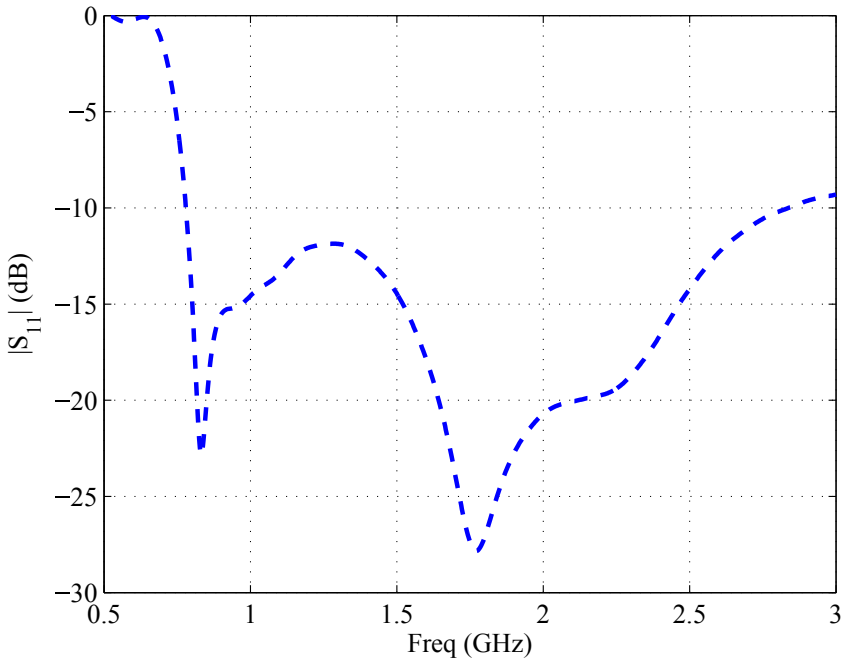

Figure 4.3. Simulated reflection coefficient of the low-profile monopolar antenna.

4.2.2 Ground Plane Effects

The first step in appreciating the effects of ground plane curvature is to determine a suitable ground plane size. Generally, ground planes can be characterized into two distinct regions based on their size. The first region is where the ground plane is small.

In this case the ground plane effects primarily pertain to impedance matching. The second region is where the ground plane is a medium to large size. In the latter scenario, the ground plane effects tend to be manifested in the far-field radiation characteristics. For the present study the second region is of interest.

To assist in determining the ground plane size, we consider the application presented in section 4.1, where the monopolar antenna is integrated onto a vehicle roof. In such a case the vehicle body would act as a ground plane and specifically given the large dimensions of typical vehicles, the antenna would operate with an *electrically large ground plane*. Intuitively, an electrically large ground plane will tend to concentrate the far-field radiation into the region above the ground plane. The distribution of the far-field radiation into the region above the electrically large ground plane is depicted in Fig. 4.4. It is important to appreciate that with an electrically large ground plane the radiation patterns become conical in the upper half-space with maximum gain at a positive elevation angle. Unfortunately, this is typically undesired for vehicular applications where communications often takes place at low elevation angles.

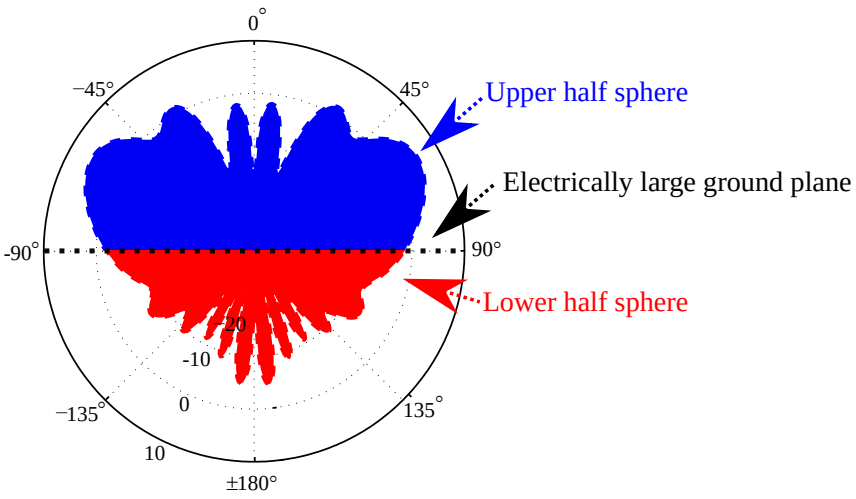

Figure 4.4. Depiction of the far-field radiation patterns when the ground plane is several wavelengths large. It is clearly observed that there is more radiated power in the upper half sphere than to the lower half sphere. The dotted black line represents the antenna ground plane.

Quantitatively, the effects of an electrically large ground plane on the far-field radiation characteristics can be represented by a large upper to lower half-space radiated power ratio, for example 10:1. Thus, the next step of the investigation is to increase the size of the ground plane till this ratio is achieved. The power ratio can be obtained by numerically evaluating

$$\frac{P_{RADUPPER}}{P_{RADLOWER}} = \frac{\int_0^{2\pi}\left\{\int_0^{\pi/2}\frac{E(\theta,\phi)^2}{\eta}\sin(\theta)d\theta\right\}d\phi}{\int_0^{2\pi}\left\{\int_{\pi/2}^{\pi}\frac{E(\theta,\phi)^2}{\eta}\sin(\theta)d\theta\right\}d\phi}. \tag{4.1}$$

To quantitively represent the effects of an electrically large ground plane for the low-profile monopole introduced previously, a numerical study is performed where the power ratio is calculated across a number of different ground plane dimensions at 0.9 GHz and 2.45 GHz with the aim of finding a power ratio of 10:1. By considering these two frequencies, it is possible to get an appreciation of how the far-field characteristics vary across the entire bandwidth of the antenna.

The variation in the radiated upper to lower half-space power ratio at a frequency of 0.9 GHz and 2.45 GHz for numerous ground plane radii is shown in Fig. 4.5. Across both frequencies, an increasing radiated upper to lower half-space power ratio is correlated with a larger ground plane radius. Noteworthy is the oscillatory nature of the curves. The oscillations are attributed to the well known effects of ground plane resonances which cause frequency dependent ripples in the angular pattern as shown in Fig. 4.6. Importantly, the power ratio at 0.9 GHz is smaller than the power ratio at 2.45 GHz for a particular ground plane radius. This is because the ground plane is electrically smaller at 0.9 GHz than it is at 2.45 GHz. As the ground plane is electrically smaller at the lower frequency, the variations in the power ratio at the lowest frequency provide the most conservative estimate. As shown by the solid black line, the desired radiated power ratio of 10:1 is obtained at a ground plane radius of R_{GND} = 925 mm at 0.9 GHz. At the same ground plane radius, the power ratio at 2.45 GHz is 15:1. It is important to note that the typical maximum dimensions of vehicle roofs are approximately 2 meters and thus a ground plane radius of 925 mm is a reasonable approximation of the typical dimensions of vehicle roofs.

4.2.3 Curved ground planes

Having numerically approximated the effects of an electrically large ground plane, the effects of ground plane curvature can now be investigated. For the sake of completeness, two forms of curvature are investigated: cylindrical and spherical. In both cases the section of the ground plane immediately below the antenna is left uncurved. The uncurved section which has the same dimension as the maximum outer radius of the antenna (R_O) is to prevent geometry variations which could affect the impedance

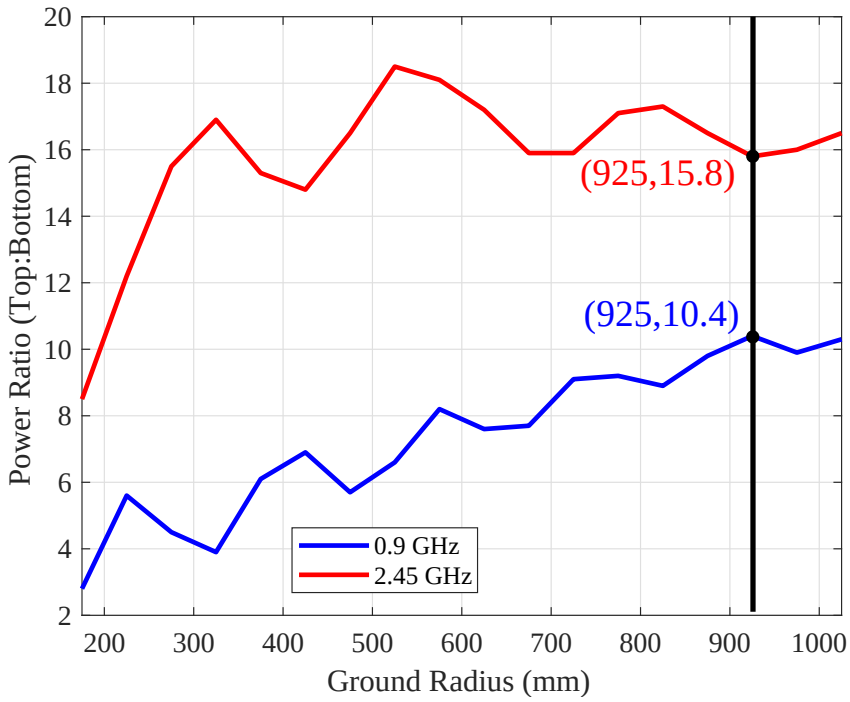

Figure 4.5. The variation of the radiated power ratio in the upper to lower half-space for the monopolar antenna as a function of the ground plane radius. The oscillatory nature of the curves is attributed to the effect of ground plane ripples. The power ratio variation is shown for two frequencies: 0.9 GHz and 2.45 GHz.

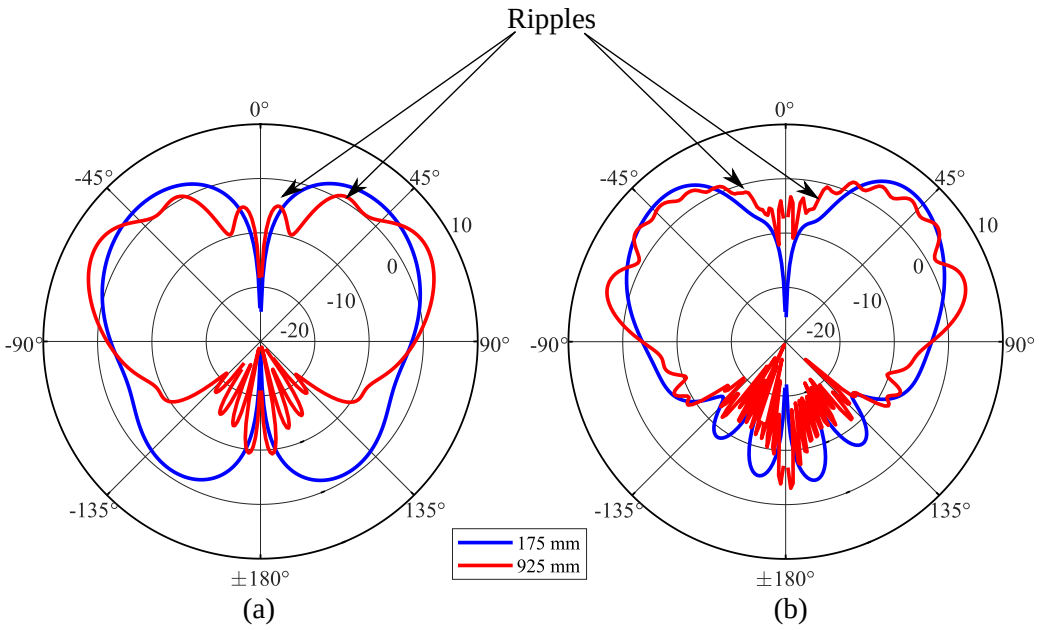

Figure 4.6. Simulated radiation patterns for a ground plane radius of 175 mm and 925 mm at: (a) 0.9 GHz and (b) 2.45 GHz. For both frequencies the arrows show the increasing number of ripples in the radiation patterns as the radius of the ground plane increases.

matching. Specifically, if a section of the ground plane with maximum outer radius of R_0 is curved then the impedance matching will be influenced [45]. The next phase of the investigation is to curve the ground plane around cylinders and spheres of different bending radius. To illustrate the concept of the bending radius, we consider Fig. 4.7 which represents a cylindrical or spherical cross section at a bending radius R_B. In the following bending studies, the curved section of the ground plane which is denoted as R_C is kept constant at the same value as $R_{GND} - R_O$ which in this case comes to 872 mm. Intimately related to the bending radius is the bending angle. The bending angle which is denoted as θ in Fig. 4.7 is the angle created by the points ABC. It is important to note that the bending angle is determined from where the curved section of the ground plane begins and *not from the center of the structure which is denoted as O in Fig. 4.7.* The bending angle in degrees can be calculated as $\theta = (R_C/R_B) \times (180/\pi)$. From Fig. 4.7 an effective ground plane radii that can be defined. The effective ground plane radius, denoted as R_{TOTAL}, is defined as $R_{EFF} + R_O$.

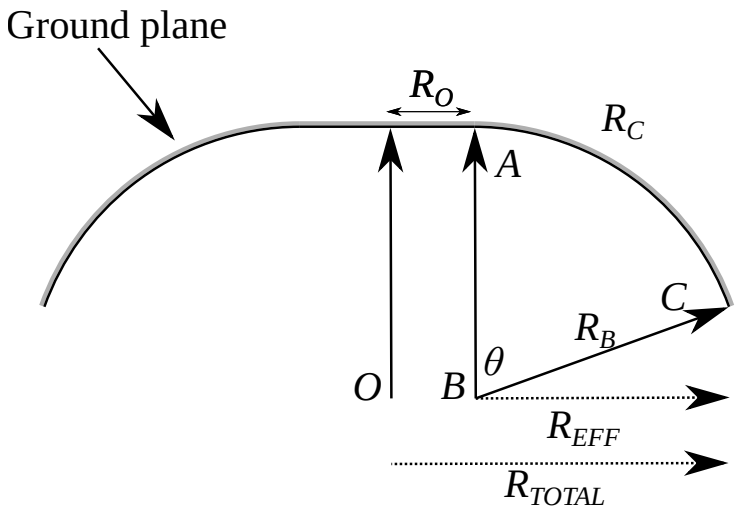

Figure 4.7. Cross section of either cylindrical or spherical bending. The bending radius is denoted as R_B. There is also an effective radii denoted as R_{TOTAL}.

The variation in the radiated power ratio as a function of the effective total ground plane radius, R_{TOTAL}, at 0.9 GHz and 2.45 GHz is shown in Fig. 4.8(a) and Fig. 4.8(b) respectively. Three curves are presented in Fig. 4.8. The red and blue curves correspond to the variation in power ratio under cylindrical and spherical bending as a function of the effective total ground plane radius. The black curve corresponds to the variation in the power ratio assuming a flat ground plane as a function of the effective total ground plane radius.

Clearly, it is observed that the variation for the cylindrical case is less severe than for the spherical case. This is because the cylindrical case is only curved in a single dimension whilst the spherical case is curved in 2 dimensions. Additionally, it can be seen that at a certain effective total ground plane radius, the power ratio for either the cylindrically and spherically curved cases are significantly lower than that for the flat case. These results suggest that the effectively smaller ground plane dimensions is not the dominating factor in reducing the power ratio. Rather, the reduction in power ratio is attributed to the curvature of the ground plane which serves to guide the radiated fields into the region below the ground plane. In this context it is preferable to quantify the variations in the far-field characteristics as a function of the bending angle. Henceforth, unless otherwise stated, the variation in the far-field characteristics will be expressed as a function of bending angle. To appreciate how the ground plane geometry appears at different bending angles, consider the insets of Fig. 4.8(a). At a bending angle of 40°, the ground plane represents a segment of a sphere. On the contrary, at a bending angle of 160°, the ground plane is almost a fully closed sphere.

The variation of the end-fire gain as a function of bending angle at 0.9 GHz and 2.45 GHz is shown Fig. 4.9(a) and Fig. 4.9(b) respectively. Across both frequencies it can be observed that changing the bending angle can substantially influence the end-fire gain. For example, at 0.9 GHz the end-fire gain varies from -1.5 dB from the flat case to 0.1 dB and 0.3 dB assuming cylindrical and spherical bending angles of 20° respectively. At 2.45 GHz the end-fire gain increases from -3.5 dB from the flat case to 0.1 dB for either cylindrical or spherical bending angles of 20°.

The simulated gain patterns for flat, cylindrically and spherically 180° curved cases at 0.9 GHz and 2.45 GHz are shown in the first and second rows of Fig. 4.10 respectively. Essentially, it can be observed that increasing the bending angle results in radiation patterns which are less conical. To summarize, the salient conclusions from the aforementioned discussions are as follows. Firstly, if the presented low-profile monopolar antenna were to be integrated into a vehicle, then the antenna functions with an electrically large ground plane, resulting in conical patterns. These conical patterns are undesirable for vehicular to on-body communications as the goal is to have maximum gain in the end-fire direction. Secondly, even a modest degree of curvature (i.e. 20°) can significantly enhance the end-fire gain.

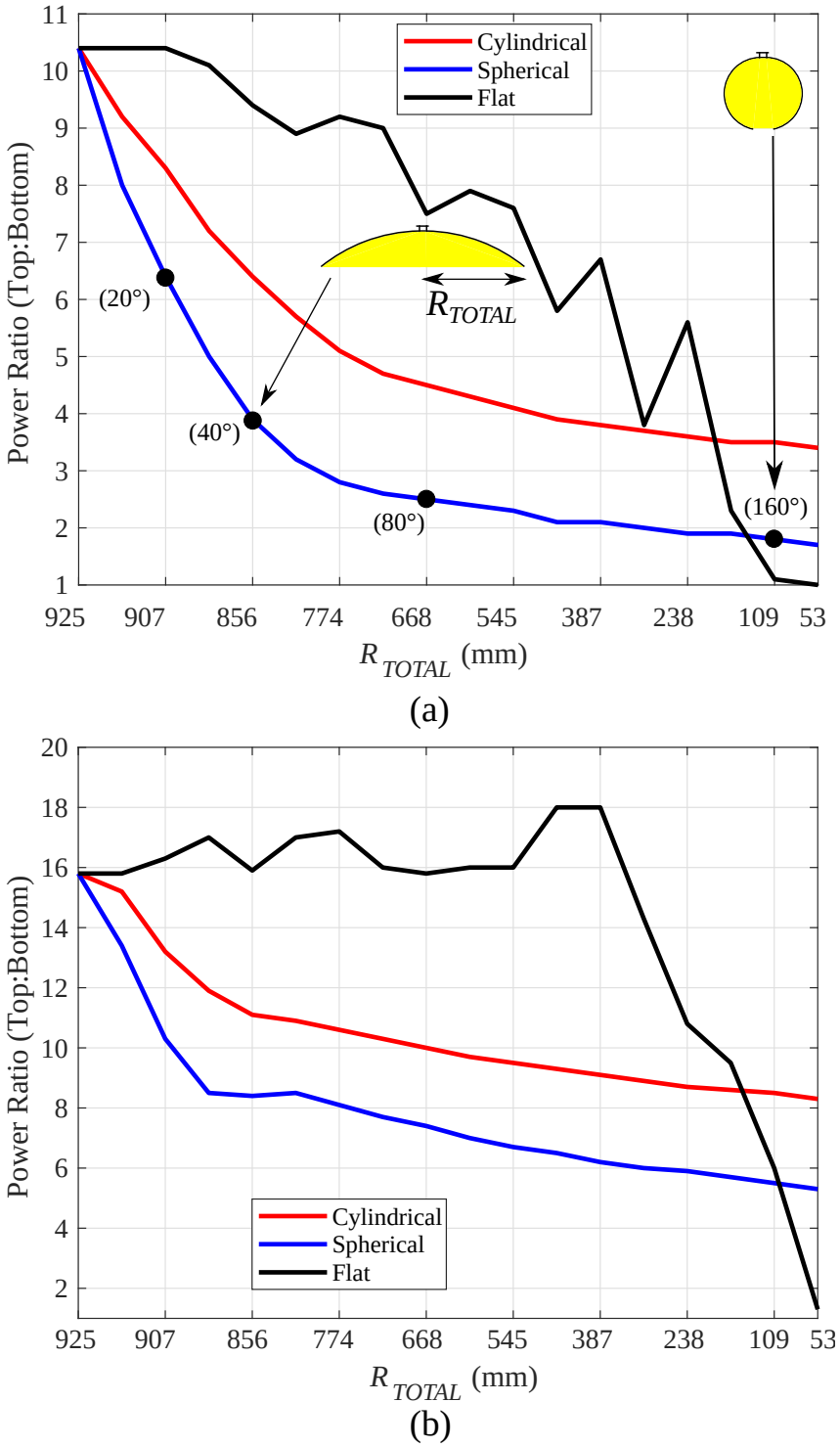

Figure 4.8. Simulated variation in the ratio of radiated power in the upper to lower half-space for cylindrical and spherical bending at: (a) 0.9 GHz and (b) 2.45 GHz.

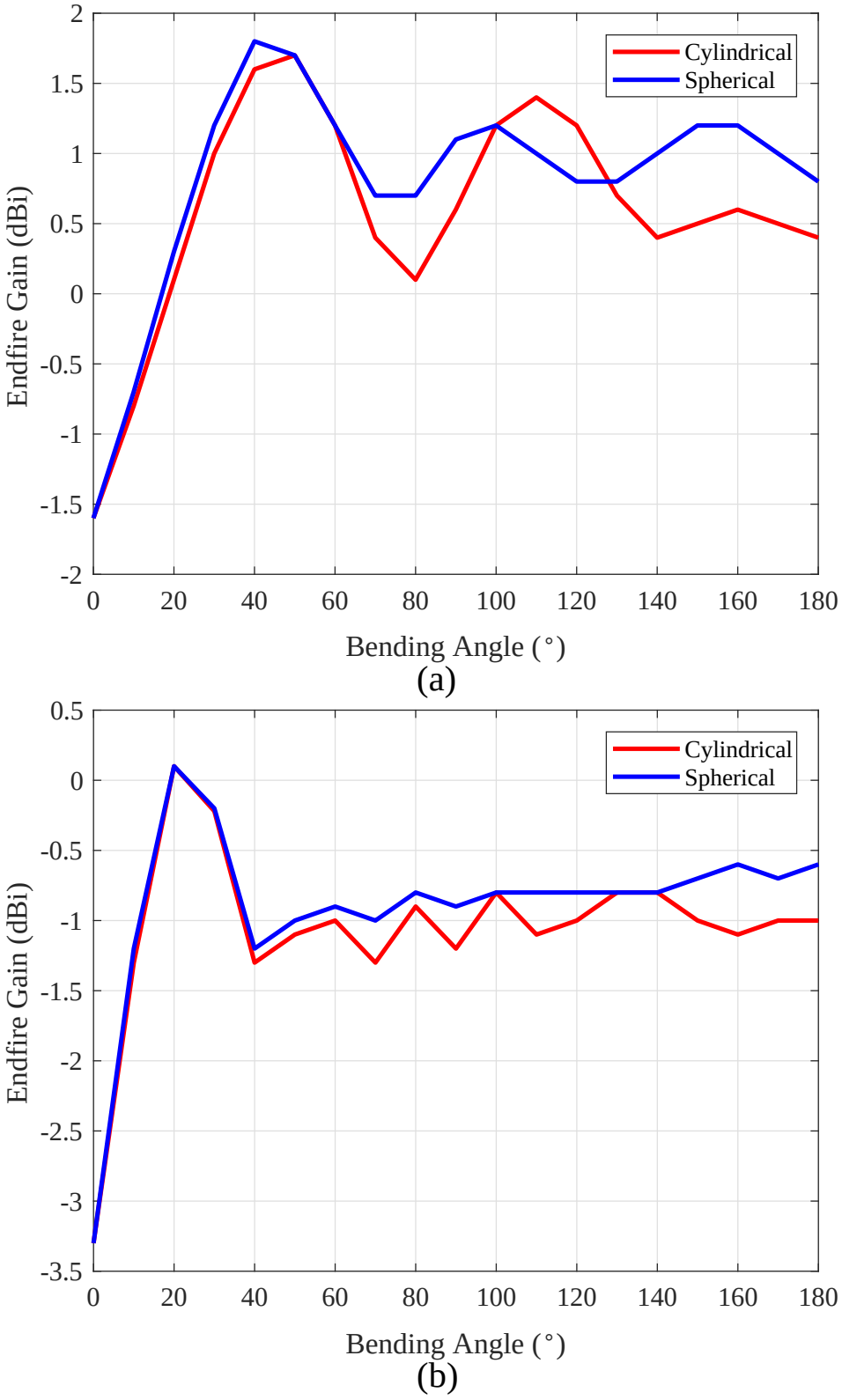

Figure 4.9. Simulated variation in the end-fire gain for cylindrical and spherical bending at (a): 0.9 GHz and (b) 2.45 GHz.

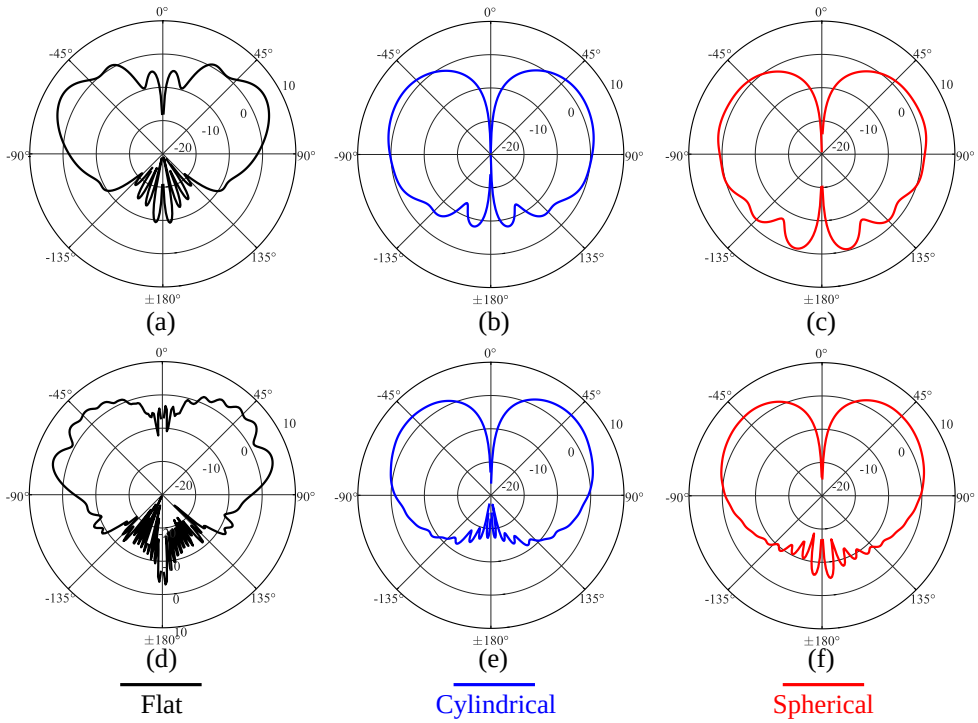

Figure 4.10. Radiation patterns showing the realized gain of the monopolar antenna using an electrically large ground plane. From top left to bottom right the radiation patterns at (a) Flat ground plane (0.9 GHz), (b) Cylindrical curvature at $\theta = 180^\circ$ (0.9 GHz), (c) Spherical curvature at $\theta = 180^\circ$ (0.9 GHz), (d) Flat ground plane (2.45 GHz), (e) Cylindrical curvature at $\theta = 180^\circ$ (2.45 GHz) and (f) Spherical curvature at $\theta = 180^\circ$ (2.45 GHz).

4.3 On-Body Scenario

In this section the effects of conformal ground planes are investigated from a body-worn perspective. In this case the application could be communications between various on-body devices. For example, an antenna on the torso which may be communicating with another antenna on the forearm region [33]. For the body-worn case the variation in the far-field radiation characteristics is only investigated at 2.45 GHz. As stated in section 4.2.2, to study the effects of ground plane curvature a medium to large sized ground plane is required. At 0.9 GHz a medium to large sized ground plane could intrude upon user comfort and is hence not considered in this study. Additionally, as there is no need for a large bandwidth, the exciting monocone is replaced with the inner pin of an SMA connector. It must be also be emphasized that realizing a monocone in textile technology can be quite a challenging task. Finally, the thickness of the antenna is reduced from 25 mm to 5 mm which is a reasonable value for body-worn applications [59]. The ground plane radius is set at 122 mm which presents a

reasonable value for wearable applications [53]. The topology of the antenna and the critical parameter values are provided in Fig. 4.11. The simulated reflection coefficient of the antenna is shown in Fig. 4.12.

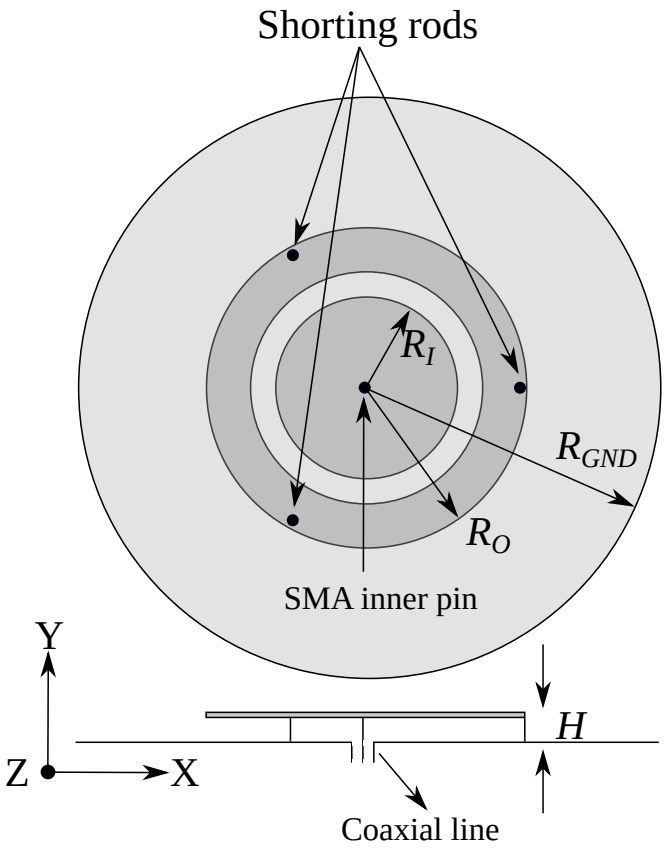

Figure 4.11. Schematic view of the low-profile monopolar antenna under investigation. R_{GND} = 122 mm, R_I = 4 mm, R_O = 21 mm and H = 5 mm.

The variation in the power ratio at 2.45 GHz as a function of bending angle is shown in Fig. 4.13(a). Clearly, as the bending angle increases the power ratio decreases in a similar manner as for the vehicular case. The variation in the end-fire gain as a function of bending angle is shown in Fig. 4.13(b) where it can be seen that increasing the bending angle from 0° to 100° steadily increases the end-fire gain. Beyond a bending angle of 100° the end-fire gain remains relatively stable. The simulated radiation patterns for three scenarios, namely no bending and a bending angle of 90° and 180° respectively is shown in the first row of Fig. 4.14. A depiction of the ground plane geometry at each of the three scenarios is shown in the second row of Fig. 4.14. As can be expected from the variations in the power ratio and end-fire gain, as the bending angle increases the radiation patterns become more omni-directional.

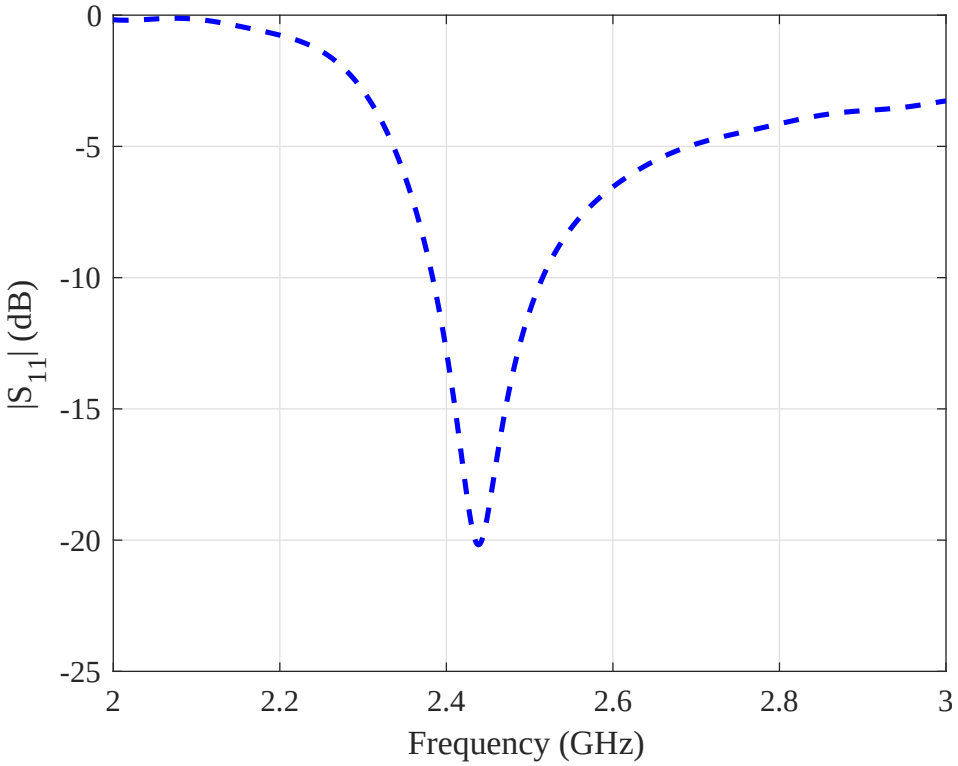

Figure 4.12. Simulated reflection coefficient for the low-profile monopolar antenna designed to study the effects of a ground plane curvature from a body-worn perspective.

4.4 Conclusions

This chapter has investigated the effects of conformal ground planes on the far-field radiation characteristics of a low-profile monopolar antenna at 0.9 GHz and 2.45 GHz. To begin with, the effects of conformal ground planes were investigated from a vehicular perspective. The vehicular case was studied as this could represent communications between vehicles and body-worn antennas as could occur in defense scenarios. Persisting with the vehicular scenario, it was deduced that the antenna would operate with an electrically large ground plane. To approximate the effects of an electrically large ground plane on the far-field radiation characteristics, a numerical study was performed where the ground plane size was progressively increased till a large upper to lower half-space radiated power ratio, namely 10:1 was obtained. After having approximated an electrically large ground plane, the effects of ground plane curvature were investigated by bending the ground plane cylindrically and spherically. From the bending studies it was deduced that even a mild degree of ground plane curvature, for example a bending angle of 20°, could significantly alter the far-field radiation characteristics as evidenced by the appreciable variations in the ratio of radiated power

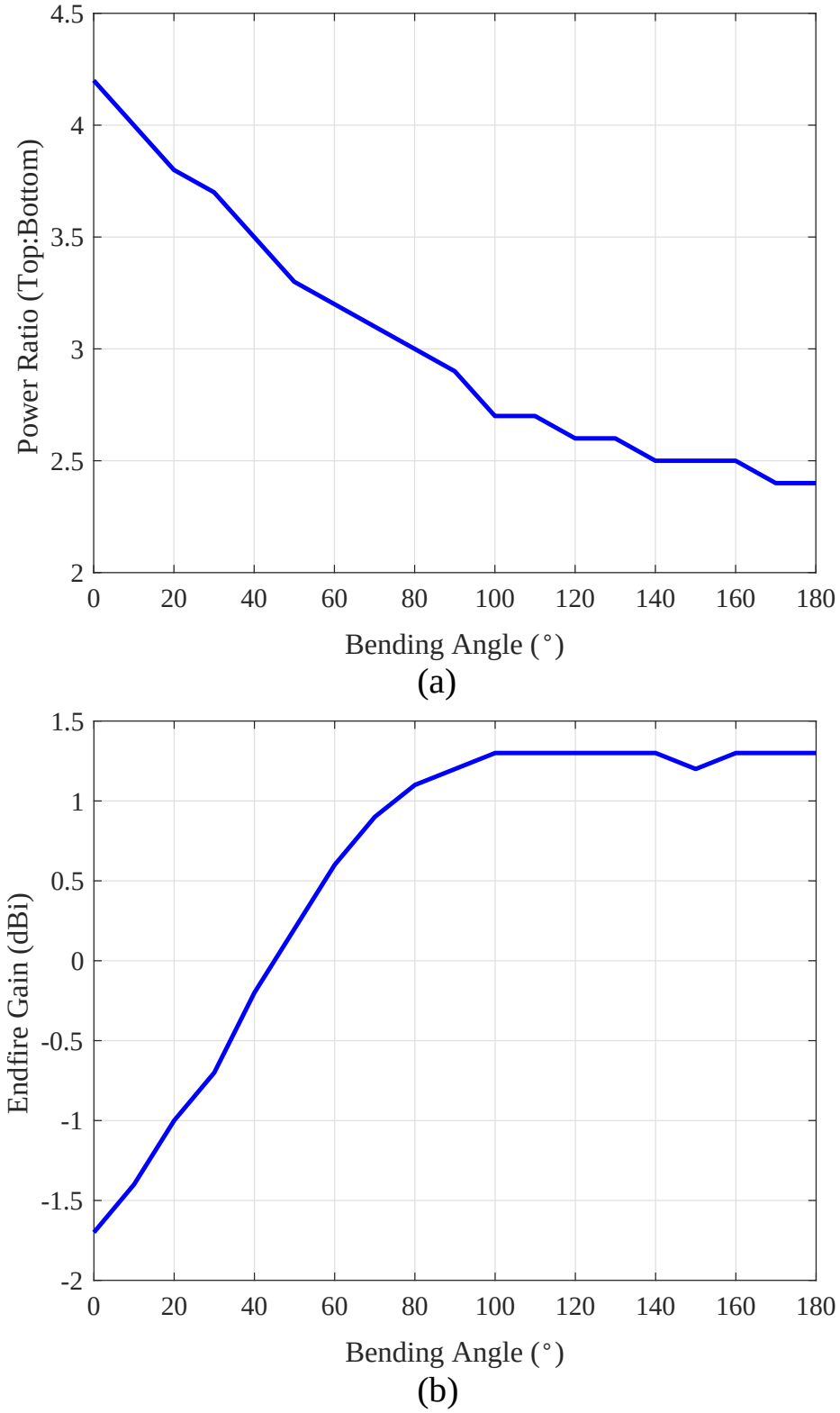

Figure 4.13. Simulated variation for the body-worn case showing (a) the ratio of radiated power in the upper to lower half space and (b) the end-fire gain.

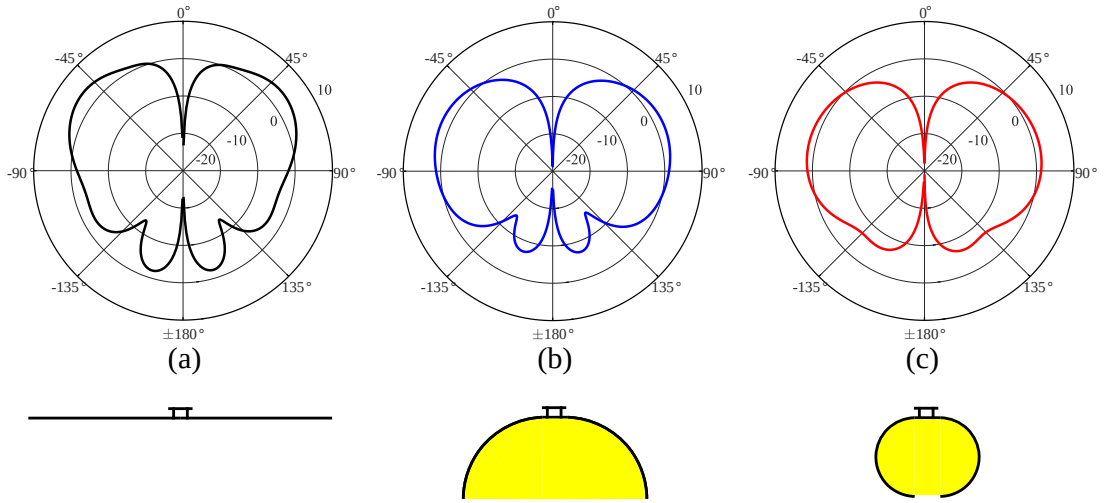

Figure 4.14. Radiation patterns showing the realized gain of the monopolar antenna using a ground plane radius of 122 mm. The radiation patterns are shown for three cases: (a) Flat, (b) Bending angle of 90°, and (c) Bending angle of 180°. The bottom row shows the ground plane geometry at each of the bending angles.

in the upper to lower half-space and the end-fire gain. The variation in the far-field characteristics were attributed to the curvature of the ground plane which served to better direct the radiated fields into the region below the ground planes. Lastly, the study was repeated for a body-worn scenario. For the body-worn scenario, only the variations in the far-field radiation characteristics at 2.45 GHz were considered. As for the vehicular case, it was demonstrated that increasing the bending angle resulted in a reduced power ratio and an increase in the end-fire gain. For the on-body case the variations at 0.9 GHz were not considered as this would require a relatively large ground plane size which could intrude upon user comfort. The question of how to realize a relatively large ground plane size without intruding upon user comfort is addressed in the next chapter.

Chapter 5

Embroidered Antennas

THIS chapter investigates the use of computerized embroidery to realize high performance textile antennas. One of the challenges in using computerized embroidery to realize textile antennas is optimizing the fabrication parameters to obtain the highest performance possible whilst minimizing the fabrication complexity. An additional challenge is to accurately model and characterize the embroidered structures. To address these questions, this chapter investigates through scattering experiments the effect of three fabrication parameters, namely grid/stitch spacing, embroidery density and embroidery layout, on the electrical performance of embroidered structures. Then to characterize the embroidered structures, an effective frequency-dependent sheet resistance is determined through two modeling techniques. The first modeling technique is to assume that the embroidered structure can be approximated as a homogeneous sheet with a certain effective sheet resistance. The second modeling technique is to consider the physical distribution of the threads and find an effective sheet resistance. Finally, the validity of the characterization and modeling techniques is investigated by utilizing a selective embroidered structure as a ground plane for a textile patch antenna. Lastly, it is shown that embroidered ground planes can be advantageously used for textile antennas.

5.1 Introduction

As discussed in chapter 2 section 2.2, computerized embroidery is an attractive method to fabricate wearable microwave devices such as antennas and transmission lines because it is inherently a textile based technique [97]. Examples of embroidered structures are illustrated in Fig. 5.1 and Fig. 5.2. The main advantage of utilizing computerized embroidery is that complex geometries can easily be realized with a high precision in a time-bound and automatized manner. Additionally, the embroidery can be done directly into clothing which is particularly noteworthy as this raises the possibility of having part of the clothing attire functioning as ground planes. Embroidered ground planes are very attractive as, if properly designed, they may serve as a replacement to fully metallized textile ground planes leading to savings in material costs as shown in various realizations in Fig. 5.3. For these attractive reasons, there has been a great interest in wearable structures fabricated solely from computerized embroidery [46–49, 98–101].

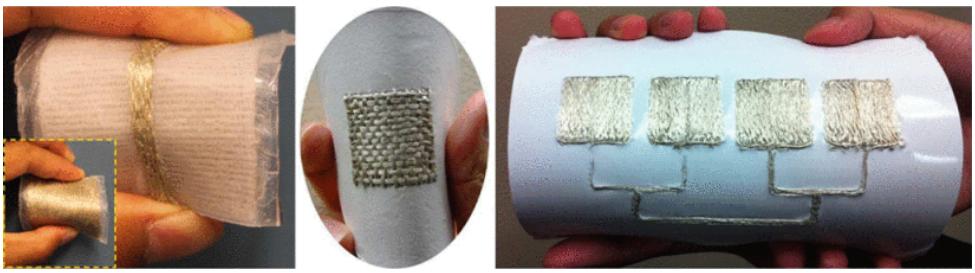

Figure 5.1. Embroidered transmission lines, patch antennas and arrays as reproduced from [46].

When utilizing computerized embroidery, one of the main challenges is to realize embroidered structures that have similar performance to their purely metallic counterparts. It has previously been determined that the performance of embroidered structures is highly dependent on the fabrication parameters [102, 103]. Generally there are four fabrication parameters that must be considered when realizing antennas through computerized embroidery:

1. Grid spacing.
2. Stitch spacing.
3. Embroidery density.
4. Embroidery layout.

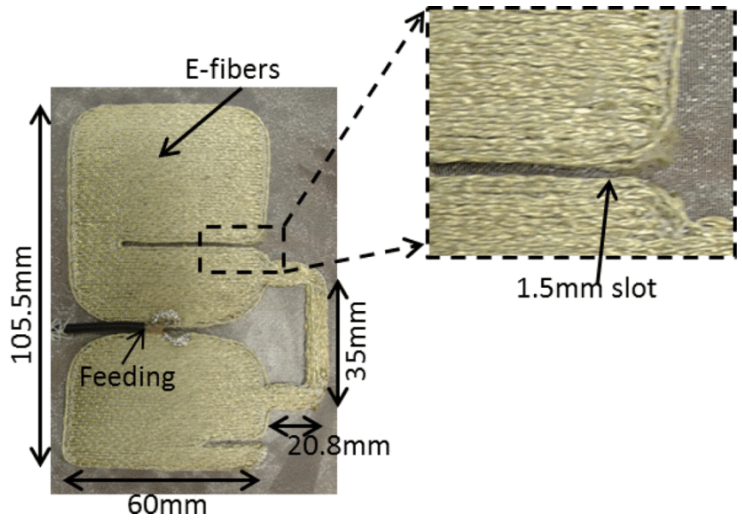

Figure 5.2. An asymmetric slot loaded dipole antenna that has been realized solely from computerized embroidery. This image is reproduced from [47].

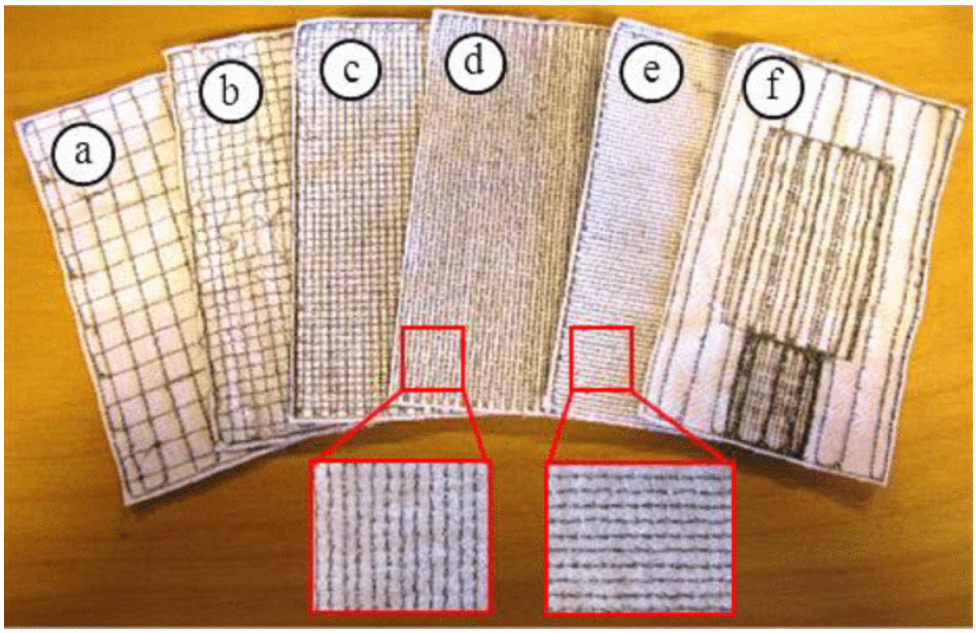

Figure 5.3. Various embroidered ground planes for patch antennas as reproduced from [48].

Intuitively, grid spacing can be understood as the physical separation between adjacent threads. The grid spacing is a fundamental fabrication parameter as it is related to how densely the conductive threads are laid out as shown in Fig. 5.4. For example, an embroidered surface that is tightly packed with conductive threads is expected to display behavior that is close to that of a pure metallic sheet [49, 104]. However, an excessively small grid spacing will result in increased fabrication complexity and material consumption. On the contrary, if the grid spacing is excessively sparse, then the

efficiency of the resulting device can be decreased as this will cause high current density through individual threads which will in turn raise the ohmic losses [48]. Thus it is important to judiciously choose the grid spacing to balance fabrication complexity and electrical performance.

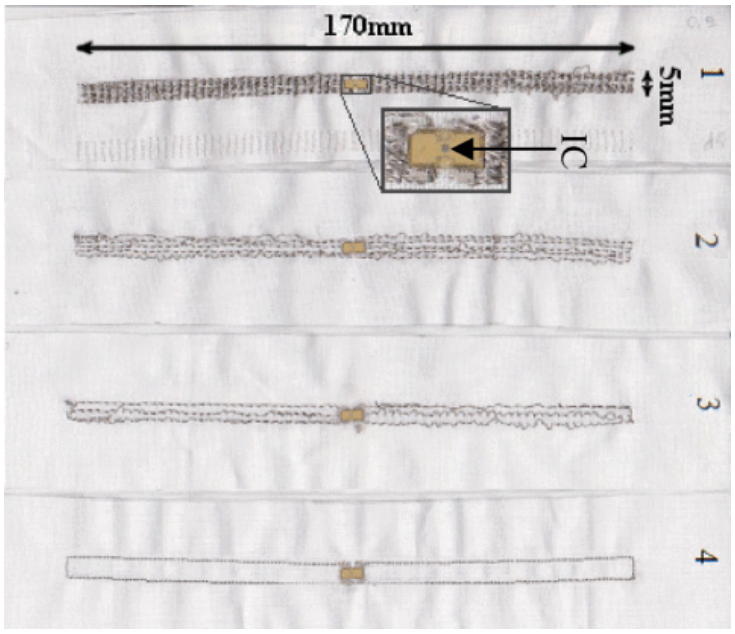

Figure 5.4. A variety of dipole antennas realized with different grid spacings reproduced from [49].

Closely related to the grid spacing is the stitch spacing. Whereas the grid spacing represents the distance between adjacent threads, the stitch spacing represents the separation between each stitch. An example of an embroidered structure with equal grid and stitch spacing is shown in Fig. 5.5(a). On the contrary, an embroidered structure with unequal grid and stitch spacings is shown in Fig. 5.5(b). It is pertinent to judiciously select the stitch spacing as an excessively small stitch spacing will increase the fabrication complexity.

Another important fabrication parameter that must be considered is the embroidery density. In this thesis, embroidery density refers to the number of repetitive embroidery passes on the same track. The embroidery density can have a significant influence on the performance as it is directly related to the amount of conductive material that is present. For example, a higher embroidery density results in more conductive material per unit area which will generally tend to reduce the ohmic losses per thread and hence increase the efficiency. However an excessively high embroidery density may actually result in performance degradation [103]. The performance degradation at excessively high embroidery densities is thought to be due to surface roughness. Surface

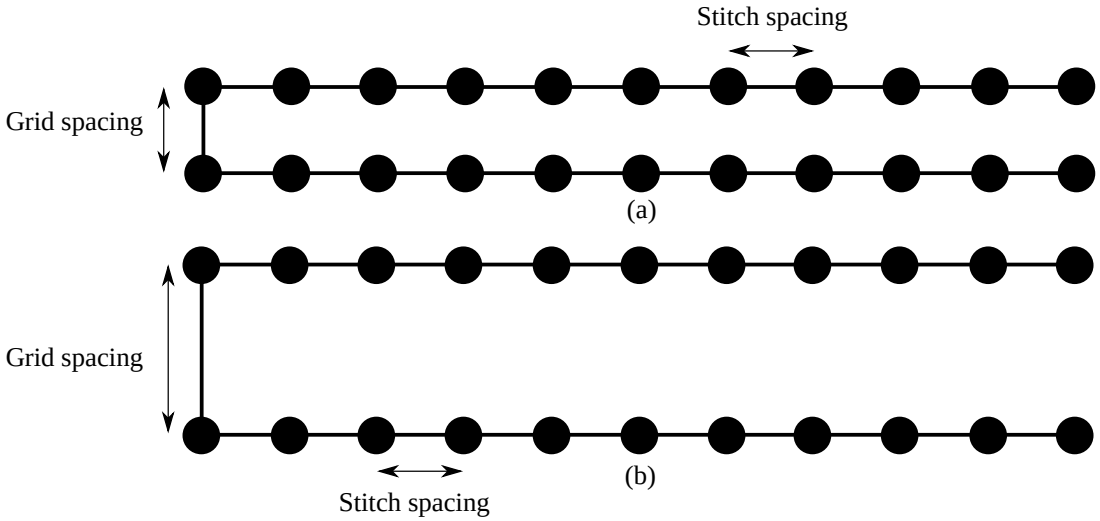

Figure 5.5. An example of an embroidered structure with equal stitch and grid spacing (a) and unequal stitch and grid spacing (b).

roughness is a term which refers to some form of aberrations of a material which result in a non-planar surface. It has been shown that surface roughness can significantly degrade the conductivity [105]. The effects of surface roughness can be particularly potent for embroidered structures as the conductive threads naturally take undulating paths [106].

The last fabrication parameter that can significantly influence the performance is embroidery layout. In this thesis embroidery layout refers to how the conductive threads are physically placed within some structure. There are two primary ways conductive threads can be placed: in parallel or perpendicular to each other in a meshed configuration. The layout of the threads is very important as it gives an indication of what sort of current distributions can be supported. For example, if an embroidered structure has conductive threads perpendicular to each other, i.e in a meshed configuration, then it might be reasonable to expect that the embroidered structure could support current distributions in any two planar directions [99]. This feature might be crucial for certain antennas, such as circularly polarized patch antennas.

As briefly alluded to in the discussions on grid and stitch spacing, an additional consideration that pertains to all of the aforementioned parameters is fabrication complexity. That is the grid and stitch spacing, embroidery density and embroidery layout should be judiciously selected such that the embroidered structure displays the desired performance without making the fabrication process unnecessarily difficult, whilst optimizing the amount of material that is used.

In the literature, the effects of fabrication parameters have been investigated for specific antenna topologies such as patch or dipole antennas [49, 101, 104]. Thus the obtained results are specific to the antennas that were used. An appreciation of the effects of fabrication parameters on performance in a more generic manner is desired as this would assist in the realization of a wide range of microwave components. This generalization of the considerations will be one of the aims of this chapter.

Shifting from fabrication to modeling and characterization of embroidered structures, it is generally accepted that these are difficult tasks [102, 106–108]. Modeling refers to an electromagnetically accurate representation of the embroidered structures within simulations. Characterization commonly refers to obtaining *effective* parameters that can account for the measured performance.

Both of these tasks tend to be challenging because embroidered structures are generally inhomogeneous, irregular, and can include non-negligible air gaps [102, 107]. One modeling method that has been used is to assume that embroidered structures can be simplified to a bulk homogeneous material with a certain *effective* conductivity. The *effective* conductivity can be determined by numerically fitting simulated results to measured results. This method of homogenizing embroidered structures has been shown to be acceptable in certain cases and not acceptable in other cases. This seeming contradiction in the same method is most likely because different antenna structures were used. For example, the work presented in [49] showed that it was possible to model an embroidered dipole as an homogeneous sheet with a bulk conductivity. Later work by the same authors in [101] showed that *it was not possible* to model an embroidered patch antenna as an homogeneous material with a bulk conductivity. These examples demonstrate the inherent limitation of using a geometry-specific approach to characterize embroidered structures: the results are only suitable for the particular topology that is used.

The importance of appreciating the effects of fabrication parameters and the need for accurate modeling and characterization techniques can be further elucidated through the following situation which expands on the concept of using embroidery techniques to realize ground planes for textile antennas:

In wearable applications it may be desirable to replace fully metalized ground planes (such as conductive fabrics used in chapter 3) with loosely embroidered ground planes. The main reason to investigate the efficacy of replacing fully metalized ground planes

is that substantial savings in material costs may be obtained. To serve as a viable replacement the embroidered ground plane must have polarization-independent performance and provide sufficient isolation from the deleterious effects of the human body on the antennas and transmission lines. Consequently it becomes important to know the minimum grid spacing required for the embroidered structure to act as a quasi-bulk metallic sheet. Concurrently, the stitch spacing must also be optimized to minimize the fabrication complexity. Additionally, the embroidery density and layout need to be jointly optimized to obtain the largest conductivity possible with minimal anisotropy. Finally, for accurate simulations the embroidered structure must be properly modeled and characterized.

From the preceding discussions two main topics can be framed as follows:

1. A generic relationship between the effects of various fabrication parameters and electrical performance of embroidered structures is desirable as this would assist in realizing embroidered structures that can behave as quasi-homogeneous metallic sheets.

2. To facilitate realistic simulations, embroidered structures must be properly characterized and modeled. Ideally a generic technique which is applicable for a broad range of embroidered structures is desirable.

To address the aforementioned topics, this chapter investigates the use of bi-static radar cross-section (RCS) measurements to establish a general relationship of the effect of various fabrication parameters on the electrical performance of embroidered structures. This is achieved by realizing a variety of embroidered structures based on the aforementioned fabrication parameters and measuring their scattering behavior. Then, to characterize the embroidered structures, a frequency-dependent effective sheet resistance is numerically determined. This achieved by modeling the embroidered structure firstly as a homogeneous sheet and secondly by approximating the physical layout of the threads. The validity of the modeling and characterization methods is then examined by using a selected embroidered structure as a ground plane for a textile patch antenna. The good correlation between the simulated and measured results for the antenna with the embroidered ground plane serves as a verification that using RCS measurements to characterize embroidered structures is appropriate. It also helps to understand which of the aforementioned modeling methods is generally applicable.

5.2 Fabrication

In this thesis a Brother PR-655c computerized machine, as shown in Fig. 2.9 in chapter 2 section 2.2, is used to realize the embroidered structures unless otherwise stated. For this study the utilized conductive threads are Statex Shieldex 117/17 2PLY with a quoted linear dc-resistance below 30 Ω/cm. For fabrication simplicity, all the embroidered structures are designed to have nominal square dimensions of 180 x 180 mm. The reason for choosing these dimensions will be explained in the next section. *It will also be shown in the next section that 180 mm $\times$ 180 mm is strictly speaking, not the final size of the samples.* The fabrication procedure is as follows:

1. Digitize the desired geometry with the desired grid and stitch spacings, embroidery density and layout in the embroidery machine control software (PE-Design Next v7.0). The embroidery density can be controlled by overlaying multiple copies of the geometry on top of each other.

2. Prepare an embroidery frame with embroidery and stabilizer fabric. In this study 1 mm thick cotton is used as the embroidery fabric. The stabilizer fabric which is optional is used to provide extra mechanical tension which helps the fabrication process by holding the conductive threads in place.

3. Operate the computerized embroidery machine with conductive threads through the top needle and non-conductive threads on the bobbin. This is what is known as single-sided embroidery. An example of an embroidered structure is shown in Fig. 5.6.

5.3 Experimental Method and Considerations

As previously mentioned, to characterize the performance of embroidered structures bi-static RCS measurements are investigated in this chapter. This method has previously been employed to extract parameters that can be used in the design of embroidered dipole antennas [109]. The exact details of this setup which is schematically shown in Fig. 5.7 are herein provided.

The bi-static RCS setup consists of two identical Narda 642 standard gain horn antennas that are equidistantly separated from a target. The transmitting horn illuminates

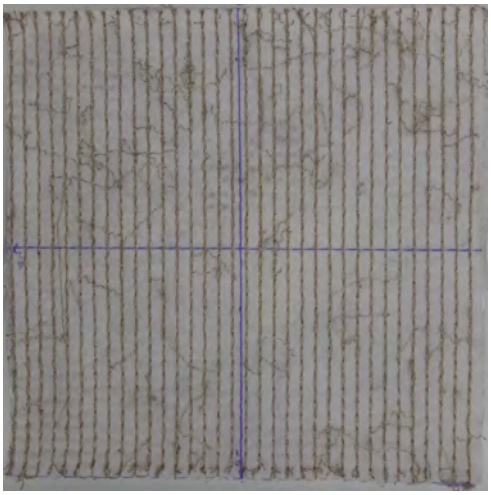

Figure 5.6. An embroidered structure with a grid/stitch spacing of 5 mm that has been prepared for this investigation.

the target which is *in the far-field of the antennas* with an incident plane wave where a portion of the incident wave is then specularly reflected by the target into the receiving horn. The horn antennas have an operation frequency ranging from 5.0 - 9.0 GHz. This frequency range is chosen as the effects of fabrication parameters become more pronounced at higher frequencies [110]. The aperture of the horns is 2.3 meters away from the sample, denoted as D in Fig. 5.7. This distance ensures that the samples are in the far-field of the antenna at the highest frequency of consideration which is 9.0 GHz. Later it will be shown that the limiting factor is that the *antennas must also be in the far-field of the samples.* The incidence angle, denoted as θ in Fig. 5.7, is 6.3°.

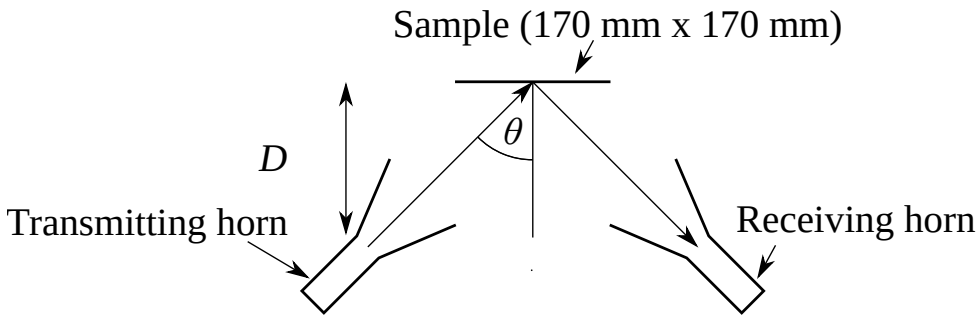

Figure 5.7. Schematic of the experimental setup. The angle of incidence theta is exaggerated for better representation.

By comparing the amount of reflected wave for the embroidered structures and a copper reference sheet of the same size, it is possible to quantify how electromagnetically alike the embroidered structure is to the copper reference. For example, if the return

from the embroidered structure is far lower than the copper reference, then that particular sample is a poor approximation of a metallic sheet. The return of the embroidered structures relative to the copper reference is quantified by the reflection coefficient which is determined according to:

$$|\Gamma| = 20\log_{10}\left(\frac{|\Gamma_S - \Gamma_B|}{|\Gamma_C - \Gamma_B|}\right). \tag{5.1}$$

In equation 5.1, Γ_S and Γ_C refer to the measured returns, expressed in linear scale, in the receiving horn from the embroidered structure ($_S$) and the copper reference ($_C$). The term Γ_B refers to the measured return, once again in linear scale, from the background environment which is included for calibration purposes, as is standard procedure [111].

The experimental bi-static RCS setup is illustrated in Fig. 5.8. The target is adhered using a thin layer of double sided adhesive onto a styrofoam block which is placed inside an anechoic chamber. The styrofoam has a negligible impact on the scattering as it has a very low relative permittivity in the order of 1.1. The double sided adhesive also has a negligible impact on the scattering as it is very thin. By having the target inside an anechoic chamber, undesired background reflections are minimized.

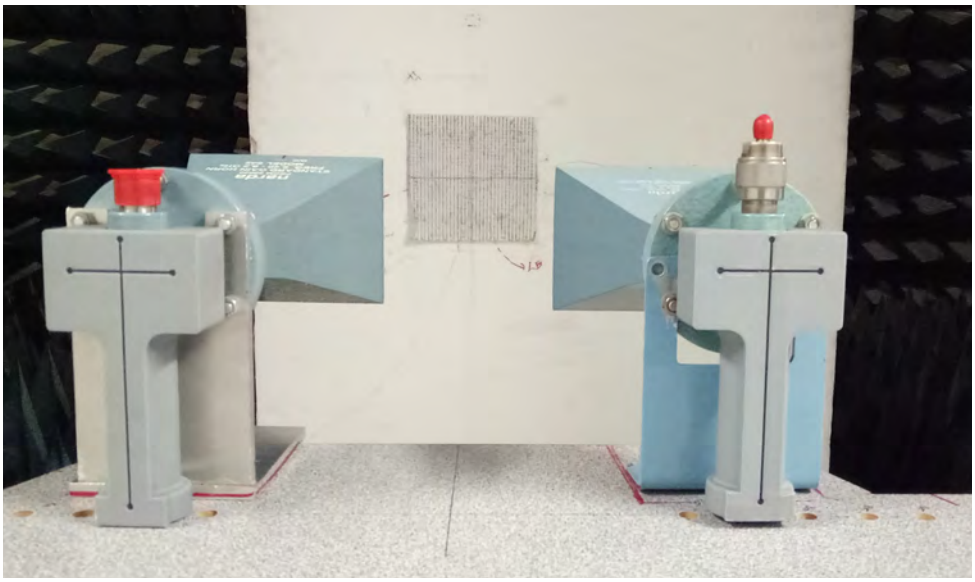

Figure 5.8. A photo of the experimental setup used to extract the properties of various embroidered surfaces.

In RCS measurements, the target size is of paramount importance. To elucidate this concept, consider Fig. 5.9 which shows the variation in the RCS of a sphere as a function of electrical size expressed in terms of the free-space wavelength. The graph is

divided into three regions: Rayleigh (green), resonance (pink) and optical (violet) region. Within the first region, the RCS increases linearly due to the increase in electrical size of the sphere. Within the second region, as the electrical dimensions of the sphere reach an order around one wavelength, the RCS becomes oscillatory. In the last region when the sphere is becoming multiple wavelengths large, the RCS progressively settles down to a steady state value. Whilst this graph shows the RCS for a sphere, the general trend is true for a variety of geometries [112].

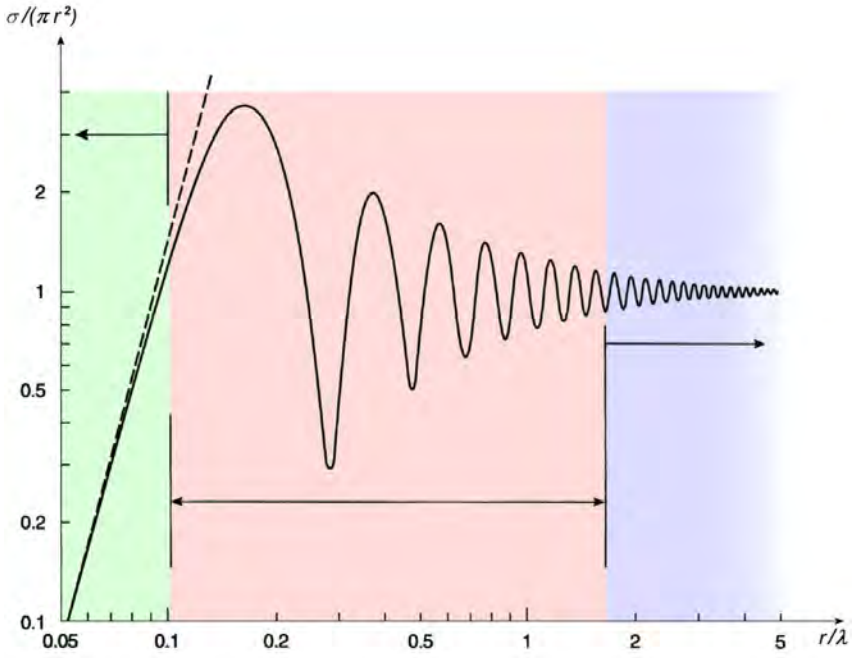

Figure 5.9. Depiction of the three classically defined radar cross section regions for a sphere. Green - Rayleigh region, pink - resonance region and violet - optical region. This image is reproduced from [50]

From the preceding discussions, it should be evident that RCS measurements are best facilitated when there are minimal oscillations from the target size which occurs in the optical region. From Fig. 5.9 a rough guideline for the *minimum* target size would be four times the free-space wavelength at the lowest frequency of operation which in this case is 5 GHz. In terms of absolute size this amounts to 240 mm $\times$ 240 mm. Realistically, the maximum attainable sample size is determined by the limits of the embroidery machine which is 180 mm x 180 mm and hence this value is chosen for the nominal sample size. A sample size of 180 x 180 mm or thereabouts places the structure roughly at the boundary between the resonance and optical region. However, after embroidering the structure it is observed that the samples are approximately 10 mm smaller than the desired dimensions due to the inherent flexibility of the cotton

fabric [110]. Consequently, both the copper reference and the embroidered surfaces are cut down to 170 mm x 170 mm. If the embroidered structures and the copper reference are not the same size then the calculated reflection coefficient will be incorrect. Consider Fig. 5.10 which shows the measured reflection coefficient for two embroidered structures at a grid/stitch spacing of 1 mm with a size of 180 mm $\times$ 180 mm and 170 $\times$ 170 mm using a copper reference of 180 mm $\times$ 180 mm. When the sample size is smaller than the copper reference, the measured reflection coefficient is significantly smaller than the measured reflection coefficient using the correct sample size. Additionally, the reflection coefficient where the sample size is smaller than the copper reference shows oscillations in the order of 0.5 dB.

Previously, it was mentioned that the samples must be *in the far-field of the antennas*. However, there is another condition that must be considered which is *that the antennas must be in the far-field of the samples*. The far-field of the samples which is calculated based on the dimensions of 170 mm x 170 mm ranges from 2.3 m at 6.0 GHz to 3.5 m at 9.0 GHz. It must be noted that the far-field of the samples is the limiting condition as the sample dimensions are greater than the dimensions of the aperture of the horn antenna. Due to limitations of the measurement setup, the maximum distance that is achievable is 2.3 m which means that both antennas are in the far-field of the sample up to 6.0 GHz beyond which they are in the radiating near-field (Fresnel region). The fact that the antennas are in the near-field of the sample beyond 6.0 GHz is not of much consequence as 6.0 GHz represents the highest microwave frequency that is generally used for wearable applications [110].

5.4 Fabrication Parameter Effects

5.4.1 Grid and Stitch Spacing

The first fabrication parameter for investigation is the grid and stitch spacing. Whilst, in general these parameters can be separated as shown in Fig. 5.5(b) this would lead to a large amount of parameters that could be optimized. Therefore, for the sake of simplicity, the stitch and grid spacing are made the same. Setting the grid spacing to be the same as the stitch spacing has the added benefit of reducing fabrication complexity. To investigate the effect of the grid and stitch spacing three samples at a single embroidery pass with grid/stitch spacings of 1, 5 and 10 mm respectively have been created. Grid/stitch spacings beyond 10 mm are not investigated due to fabrication difficulties.

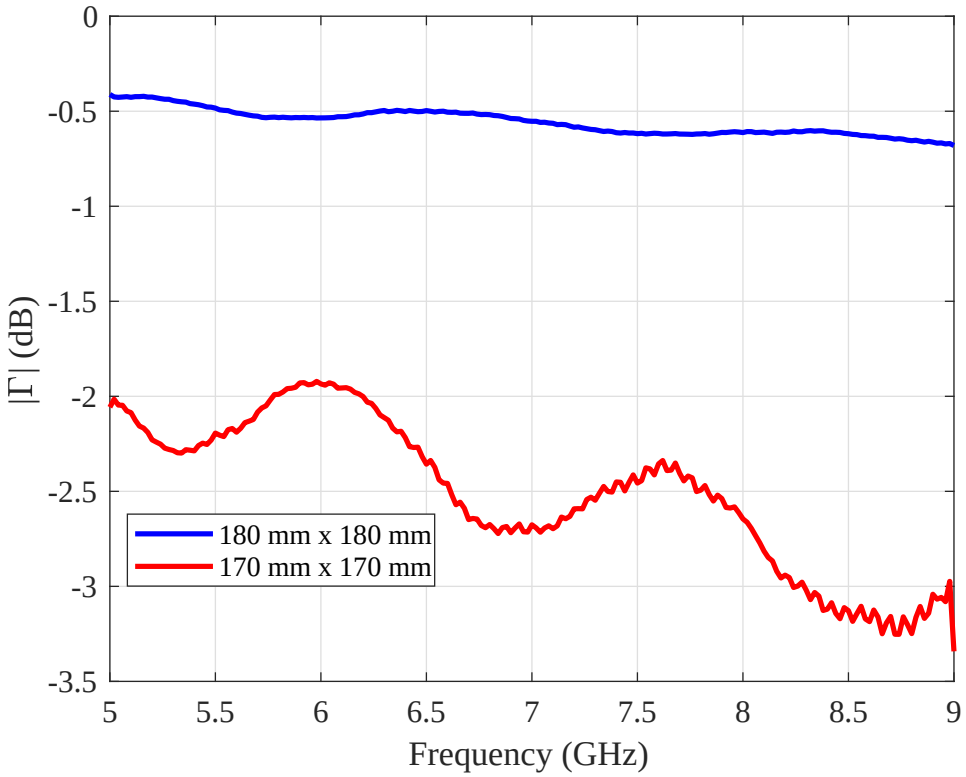

Figure 5.10. Measured reflection coefficient for an embroidered structure at a grid/stitch spacing of 1 mm with a sample size of 180 x 180 mm (blue curve) and 170 x 170 mm (red curve) whereas the copper reference was 180 x 180 mm. This graph illustrates the importance of matching the sample size to that of copper reference.

As the stitch spacing becomes increasingly sparse, the tension becomes insufficient to hold the conductive threads in place.

The three samples have the conductive threads laid parallel to each other as this represents the most simple and often used embroidery that can be performed [98]. The reflection coefficient in the scattering experiment is extracted for two orientations: the conductive threads parallel and perpendicular to the polarization of the incident electric field. Henceforth these orientations will be known as the co-polarized and cross-polarized direction respectively. The results for both directions are shown in Fig. 5.11(a) and Fig. 5.11(b) respectively. It can be seen that the reflection coefficient for the co-polarized direction is significantly larger than for the cross-polarized direction. To understand this effect consider Fig. 5.12 which shows a section of the embroidered structure with a grid/stitch spacing of 1 mm and a microscopic view of the same structure. In the microscopic image the section of the conductive threads that are visible is denoted as L' which distinguishes it from the total length of the conductive threads

which is L. When the electric field is orientated in the direction of the threads, i.e. the co-polarized direction, significant currents are induced across the length of the conductive threads which is denoted as L' in the inset of Fig. 5.12. These induced currents then generate a backwards traveling wave which results in a strong return. In contrast, when the electric field is perpendicular to the conductive threads, the currents are induced across the width of the threads denoted as W in Fig. 5.12. As the width of the threads is much smaller than the length, the strength of the induced currents in the later case is rather minimal which leads to a low return. In this sense the performance of the embroidered structures quite closely reflects that of a wire grid polarizer [113].

Regarding the measured results for the co-polarized direction, it can be seen for a grid/stitch spacing of 1 mm the reflection coefficient is almost 0 dB. This indicates that this sample behaves similarly to the copper reference under the co-polarized direction. However for grid/stitch spacings of 5 and 10 mm there is a marked reduction in the reflection coefficient. This is mainly attributed to the diminished amount of conductive threads relative to the 1 mm case, which results in less induced currents leading to a lower reflection coefficient. For the cross-polarized scenario it can be seen that the reflection coefficient is very low across all grid/stitch spacings, indicating that the structures are all largely transparent to the incident wave. As expected, this behavior is similar to that of a wire-grid polarizer.

5.4.2 Embroidery Density

The second fabrication parameter that is investigated *across all grid/stitch spacings, i.e 1, 5 and 10 mm,* is the embroidery density. To create an embroidery density of n the machine is programmed to re-embroider the same geometry n times. As previously discussed, increasing the embroidery density can reduce the losses due to a lower current density through individual conductive threads. However, an excessive embroidery density can degrade the performance [103] due to surface roughness effects. Therefore to find the optimum balance between embroidery density and surface roughness, four additional samples for all grid/stitch spacings are made where the embroidery density is linearly increased from 1 to 5 (i.e. corresponding to 1 - 5 passes). An embroidery density beyond 5 is not investigated for two reasons: firstly, the fabrication becomes extremely challenging and secondly, previous experience has shown that the effects of surface roughness usually become visible at an embroidery density of 5 [110].

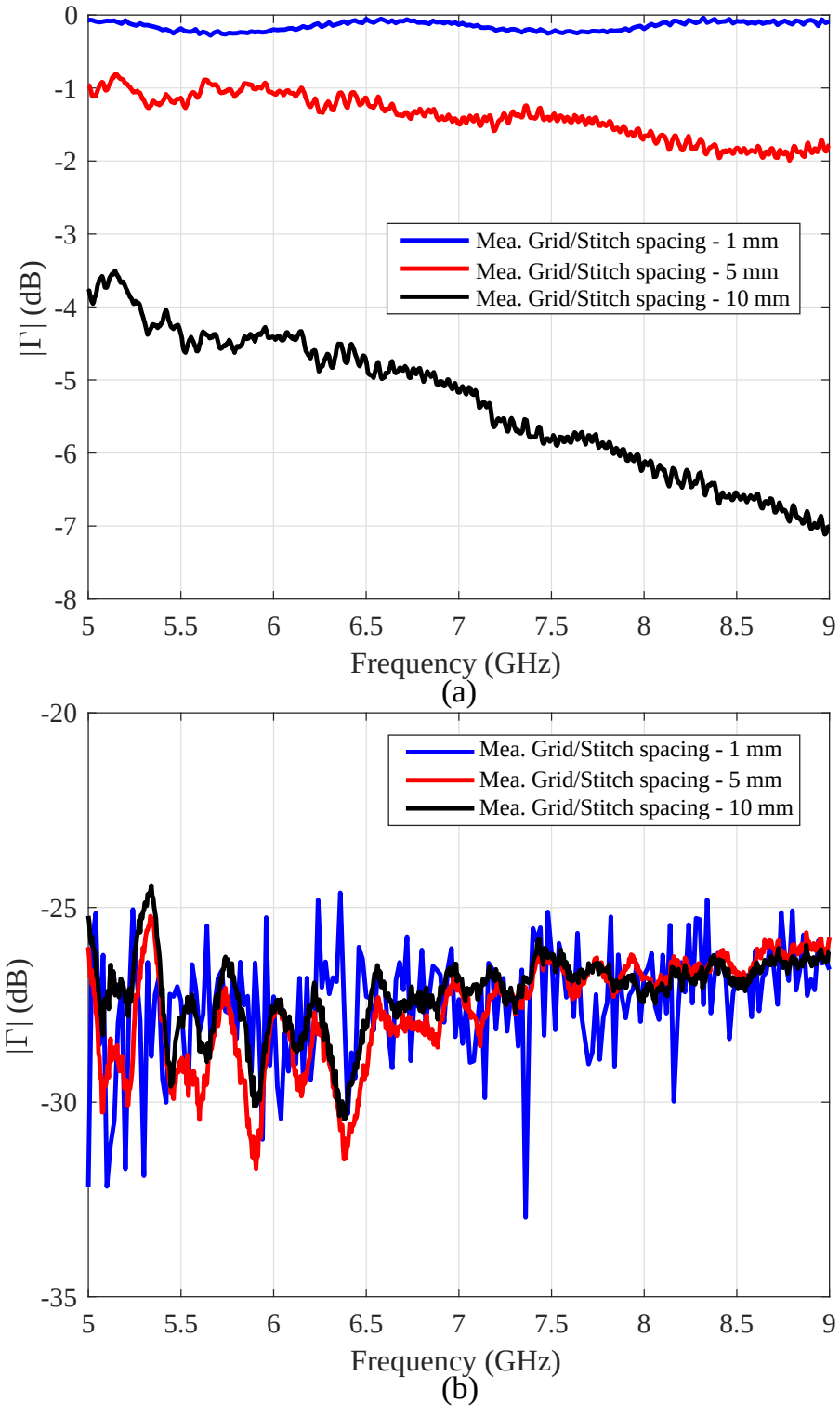

Figure 5.11. Measured reflection coefficient for the embroidered structures with a grid/stitch spacing of 1, 5 and 10 mm with an embroidery density of 1 under (a) Co-polarized direction and (b) Cross-polarized direction.

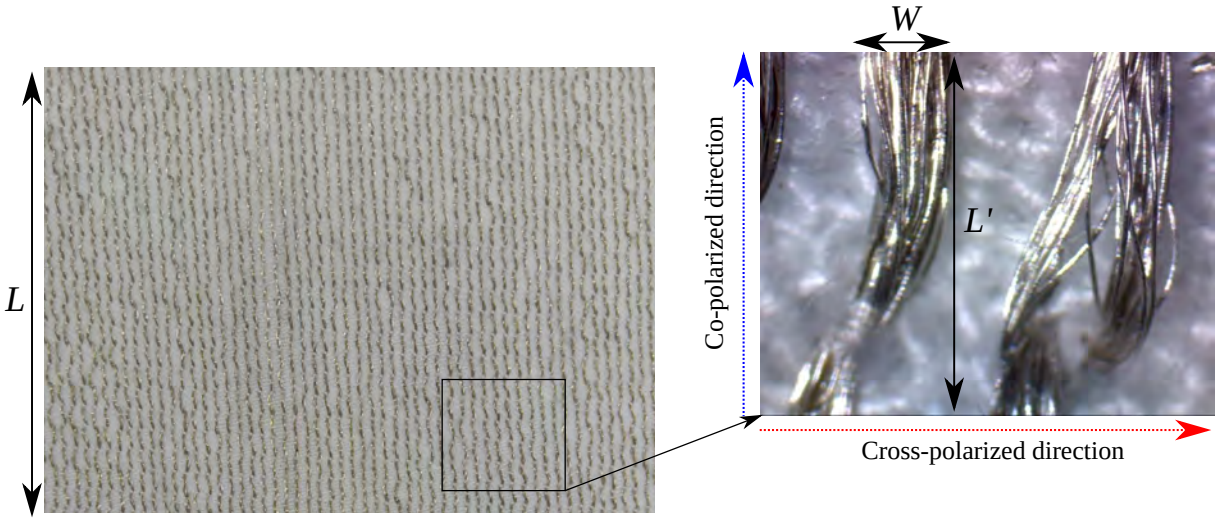

Figure 5.12. Microscopic view of the embroidered structure with a grid/stitch spacing of 1 mm showing the two main orientations of the incident electric field relative to the thread direction.

The measured reflection coefficient for an embroidery density of 1, 4 and 5 for the previously investigated grid/stitch spacing for both polarizations is provided from Fig. 5.13 to Fig. 5.15. These selective embroidery densities are shown to get a general appreciation of the effects of embroidery density on the performance. For the co-polarized direction it is observed that across all grid/stitch spacings the reflection coefficient at an embroidery density of 4 is larger than at an embroidery density of 1 with caveat: at grid/stitch spacing of 1 mm the measured reflection coefficient for an embroidery density of 4 is seemingly at the same level as the reflection coefficient for an embroidery density of 1. It is postulated that the overlap in the reflection coefficient at an embroidery density of 1 and 4 for the grid/stitch spacing of 1 mm is due to measurement inaccuracies. Additionally the reflection coefficient for a grid/stitch spacing of 1 mm at an embroidery density of 1 exhibits oscillations. These oscillations are not of much importance as they are within 0.2 dB. It is postulated that these oscillations also come from measurement inaccuracies. Neglecting the case with a grid/stitch spacing of 1 mm, the increase in the reflection coefficient for an embroidery density of 4 relative to an embroidery density of 1 is largely attributed to the decreased losses of the embroidered structures as there is less current density through individual conductive threads. Consider now the measured reflection coefficient at an embroidery density of 5 relative to an embroidery density of 4 at a grid/stitch spacing of 1 mm. At the lowest frequency, i.e. 5 GHz, the reflection coefficient for an embroidery density of 4 and 5 are almost overlapped. However, as the frequency increases the measured reflection

coefficient at an embroidery density of 5 becomes lower than that for an embroidery density of 4. Quantitatively, for a grid/stitch spacing of 1 mm at 9 GHz, the measured reflection coefficient at an embroidery density of 5 is approximately -0.7 dB. On the contrary, at the same grid/stitch spacing at 9.0 GHz the measured reflection coefficient at an embroidery density of 4 is -0.1 dB. The difference of 0.6 dB is primarily attributed to two effects. The first effect is the increasing dominance of surface roughness. At higher embroidery densities the conductive threads become more looped as shown in Fig. 5.16(b). This means that within the same global structure size of 170 mm $\times$ 170 mm the currents may take a longer length which increases the ohmic losses [105]. The second effect might be due to the degradation of the conductive threads. Consider Fig. 5.16(a) which shows the conductive threads at an embroidery density of 1 for a grid/stitch spacing of 5 mm whereas Fig. 5.16(b) shows the conductive threads at the same grid/stitch spacing, i.e 5 mm, for an embroidery density of 5. For the latter case it can be seen that the conductive threads become more intertwined. It is suspected that this intertwining leads to a more complex current distribution which may scatter waves in undesired directions. A similar trend for the measured co-polarized reflection coefficient as a function of embroidery density is observed at a grid/stitch spacing of 5 mm. However, at a grid/stitch spacing of 10 mm, the measured co-polarized reflection coefficient for an embroidery density of 4 is similar to that at an embroidery density of 5 at both the lowest and highest frequencies. These results suggest that the effects of surface roughness might be diminished at larger grid/stitch spacings. Specifically, at smaller grid spacings the threads are in closer proximity to each other. The relatively small spacing between the adjacent threads could mean that there is more intertwining between adjacent threads. As previously mentioned, the increased intertwining can cause scattering in directions other than the desired. Naturally, this effect is diminished as the threads get further apart (i.e increasing grid spacing). A similar effect could also happen with the stitch spacing. When the stitch spacing is very small the conductive threads become more looped within the global structure size leading to more surface roughness. On the contrary, when the stitch spacing is increased the conductive threads don't become as looped within the global structure size leading to less surface roughness. Considering now the cross-polarized direction, it is clearly observed that the reflection coefficient increases with a higher embroidery density across all grid/stitch spacings. This is attributed to the increased width of the conductive paths as shown in Fig. 5.16(b). It is suspected that the effects of surface roughness are

eclipsed by the increased width of the conductive threads in the cross-polarized direction. None the less, it is still observed that there is a sizable difference between the co-polarized and cross-polarized reflection coefficient.

5.4.3 Embroidery Layout

The previous investigations have quantified the performance variation of embroidered structures as a function of grid/stitch spacing and embroidery density. It is noted that increasing the grid/stitch spacing degrades the performance, but this can be somewhat compensated for by increasing the embroidery density to an optimum limit. As expected from their linear structure, all of the samples that have been investigated so far have displayed significant anisotropy as evidenced by the sizable difference between the reflection coefficient for the co-polarized and cross-polarized directions. The effects of anisotropy can be problematic for cases where polarization-independent performance is required, such as embroidered ground planes for circularly polarized antennas [101].

Therefore, in this section altering the embroidery layout is investigated as a means to mitigate the effect of anisotropy. This is achieved by embroidering a meshed configuration with the conductive threads perpendicular to each other, which is in contrast to the previous case where the conductive threads were parallel to each other. The rationale for this choice is as follows: if the conductive threads are laid perpendicular to each other then physically the "co-polarized" and "cross-polarized" scenarios become identical, which should result in an identical reflection coefficient regardless of the sample orientation. To confirm this experimentally, two meshed samples for each of the aforementioned grid/stitch spacings are created with an embroidery density of 1 and 2 *in each direction*. Higher embroidery densities are not investigated due to difficulties in fabrication. A microscopic view of the embroidered structures with an embroidery density of 1 and 2 with conductive threads perpendicular to each other at a grid/stitch spacings of 1 mm is shown in Fig. 5.17(a) and Fig. 5.17(b) respectively. As the embroidered structures with conductive threads perpendicular to each other look like meshes, they will henceforth be referred to as the meshed structures.

The measured reflection coefficient for the meshed samples across all grid/stitch spacing for the co-polarized and cross-polarized directions are shown from Fig. 5.18 to

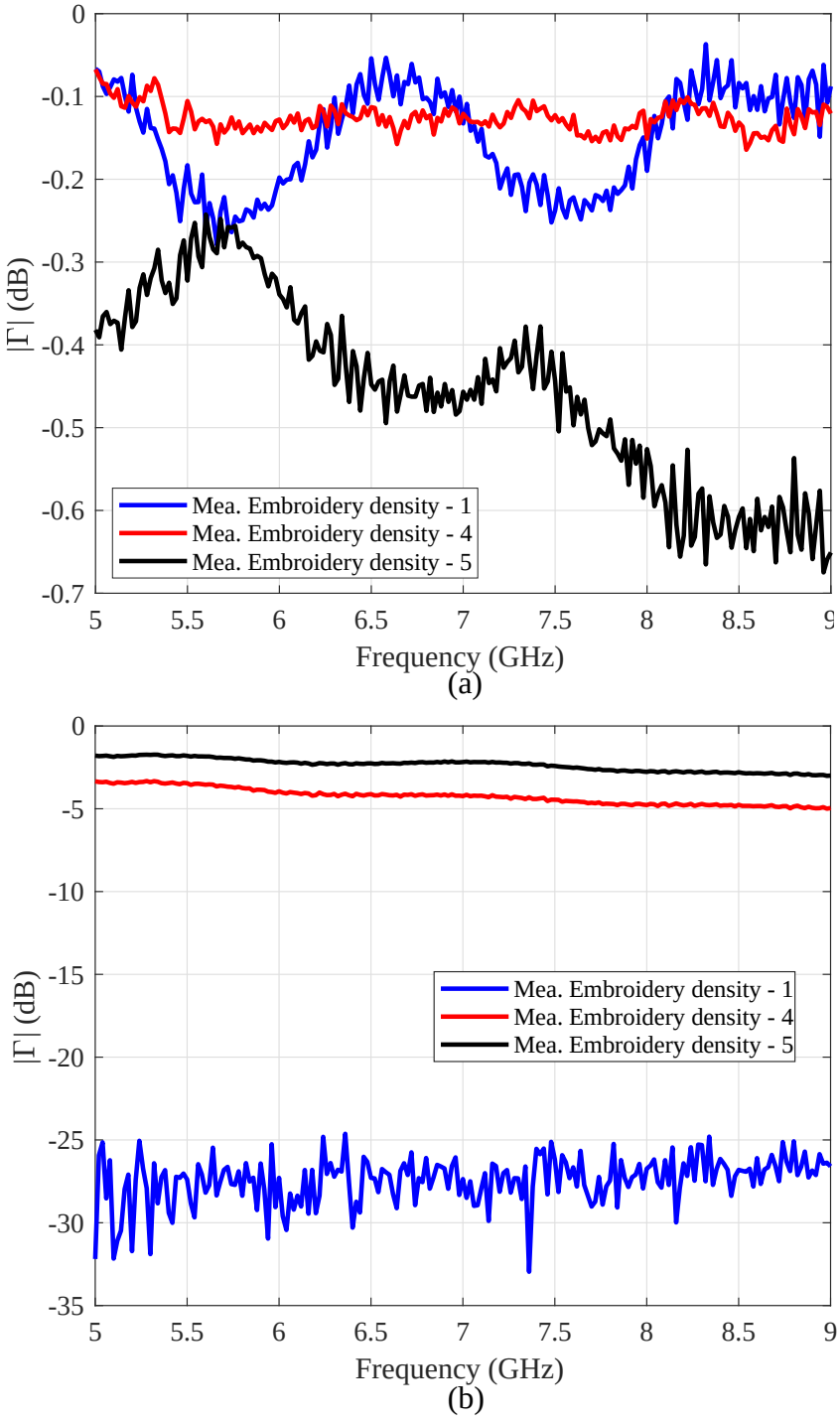

Figure 5.13. Measured reflection coefficient for the embroidered structures with a grid/stitch spacing of 1 mm and an embroidery density of 1, 4 and 5 (a) Co-polarized direction and (b) Cross-polarized direction. The overlap between the reflection coefficient for an embroidery density of 1 and 4 under the co-polarized direction is attributed to measurement inaccuracies. The mild oscillations which are in the order of 0.2 dB in the reflection coefficient under the co-polarized direction at an embroidery density of 1 are also attributed to measurement inaccuracies.

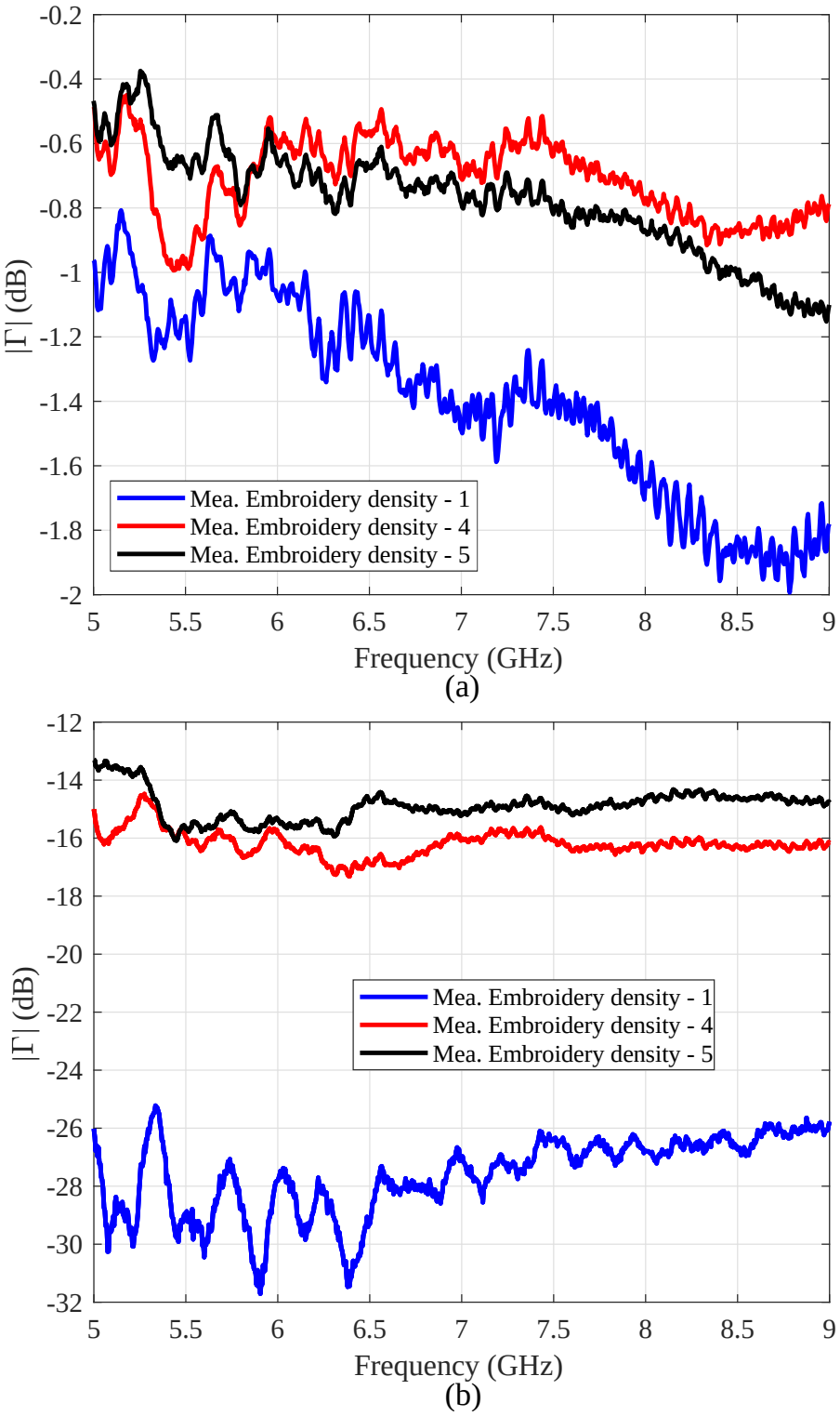

Figure 5.14. Measured reflection coefficient for the embroidered structures with a grid/stitch spacing of 5 mm and an embroidery density of 1, 4 and 5 (a) Co-polarized direction and (b) Cross-polarized direction.

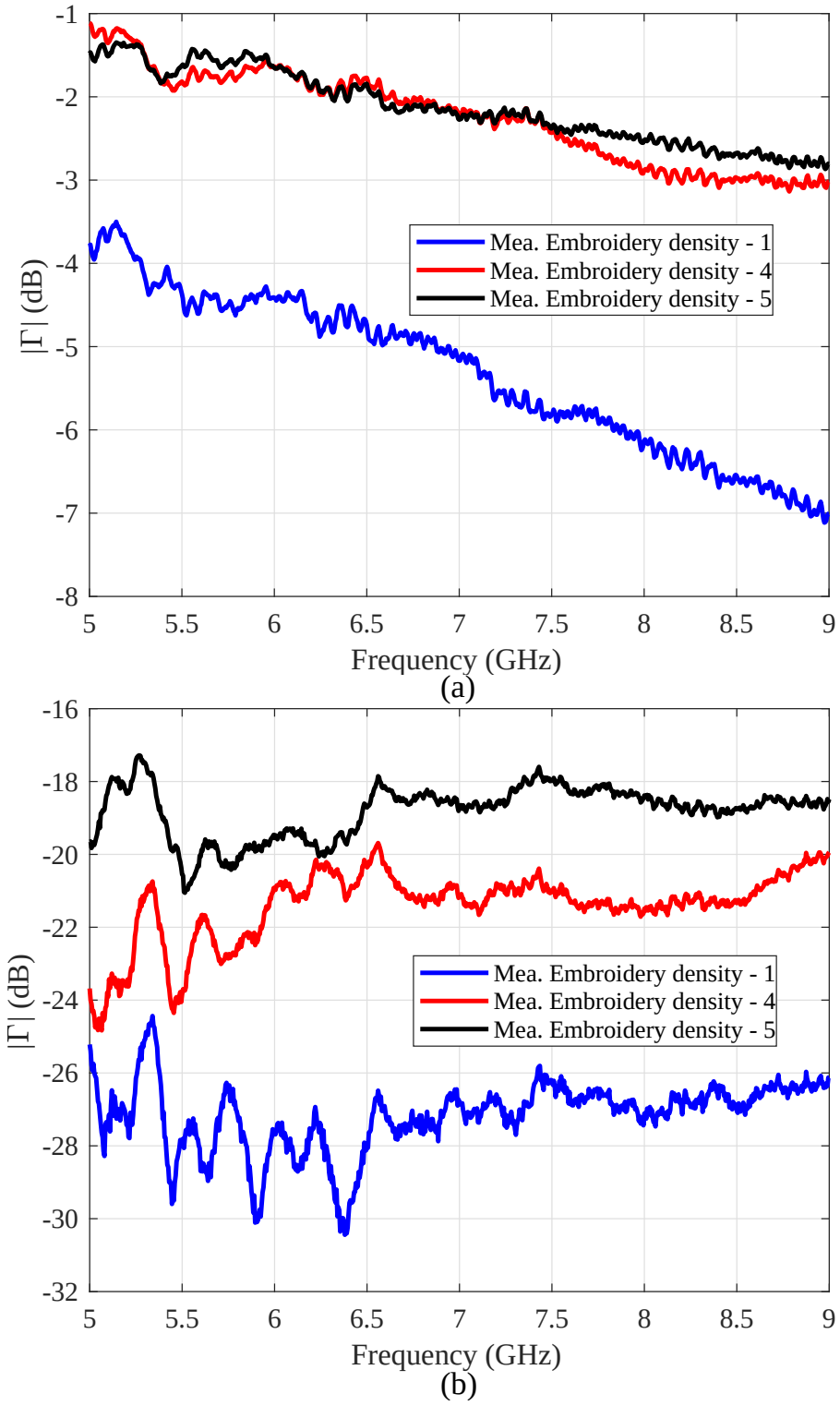

Figure 5.15. Measured reflection coefficient for the embroidered structures with a grid/stitch spacing of 10 mm and an embroidery density of 1, 4 and 5 (a) Co-polarized direction and (b) Cross-polarized direction.

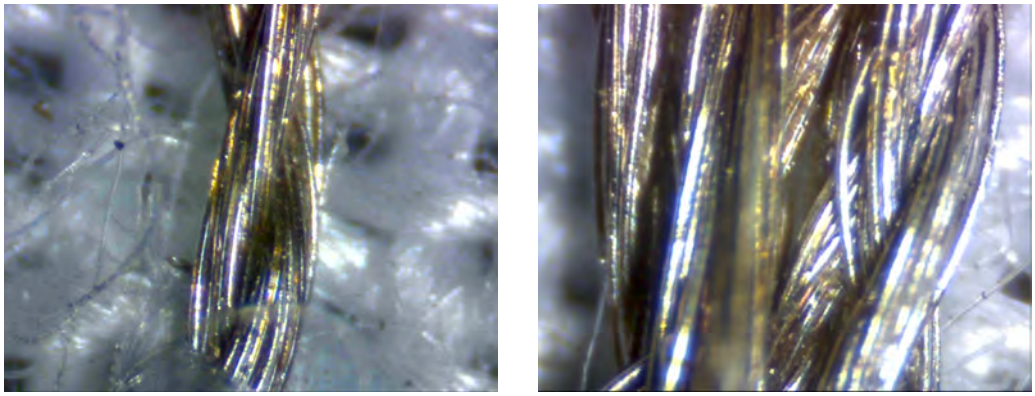

Figure 5.16. Microscopic view of the embroidered structure with a grid/stitch spacing of 5 mm at an embroidery density of (a) 1 and (b) 5.

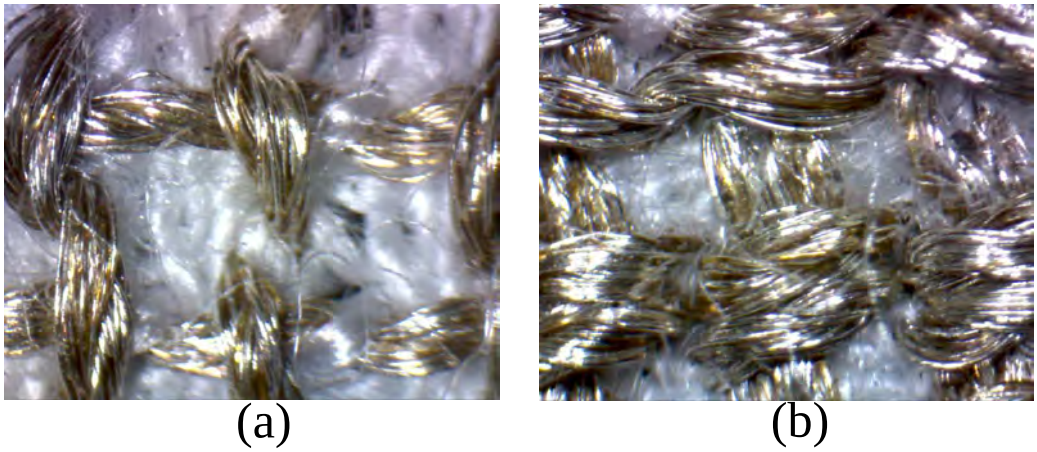

Figure 5.17. Microscopic view of the embroidered structures with a grid/stitch spacing of 1 mm where the conductive threads perpendicular to each other are at an embroidery density of (a) 1 and (b) 2.

Fig. 5.20. As expected, it is clearly seen that a largely similar reflection coefficient is obtained for both directions, suggesting that laying the conductive threads perpendicular to each other results in structures that are largely isotropic. Whilst there does appear to be some differences between the measured reflection coefficient for both orientations, these are very mild and are illustrative of the effects of fabrication non-idealities such as stray threads which can cause undesired connections as shown in Fig. 5.6. For a grid/stitch spacings of 1 mm there does appear to be some oscillations in the measured results. These oscillations are not of much importance as they are very small - within the order of 0.2 dB. It is suspected that these oscillations might come from experimental non-ideal conditions such as misalignment. For the sake of illustration,

consider Fig. 5.21 which compares the measured co-polarized and cross-polarized reflection coefficient for the meshed structure at a grid/stitch spacing of 5 mm with the co-polarized reflection coefficient for the non-meshed structure at the same grid/stitch spacing. Clearly it can be seen that the reflection coefficient for the meshed and non-meshed structures are in good correlation.

5.5 Modeling and Characterization

Having obtained an extensive set of measurements which indicate the performance of the various embroidered structures, the next task is to model and associate parameters for the embroidered structures to account for the measured performance. One often used method is to model the embroidered structures as a homogeneous sheet with a certain sheet resistance [49]. The details of this method are as follows:

1. Re-create the experimental setup in simulations.
2. Model the embroidered structure as a homogeneous sheet with a certain sheet resistance. Henceforth this modeling method will be known as MM1.
3. Numerically vary the sheet resistance of the embroidered structure till the simulated data matches to that of the measurements.

In determining the sheet resistance, it is important to consider whether a frequency independent or dependent sheet resistance should be used. Previously, it has been shown that conductive fabrics can be modeled with a *frequency-dependent* sheet resistance based on skin-depth considerations [86]. The sheet resistance for a material thickness larger than the skin-depth is calculated according to $R_S = \sqrt{\frac{\omega\mu}{2\sigma}}$ where ω is the angular frequency, μ is the permeability and σ is the DC conductivity. It is emphasized that this expression is only valid when the thickness of the conductor is larger than the skin-depth which is likely to be valid in this case, given previous experience with these threads [110].

As a first step towards characterizing the embroidered structures, the previous expression is used to determine a frequency-dependent sheet resistance for the embroidered structures where the conductive threads are parallel to each other at a grid/stitch spacings of 5 and 10 mm with an embroidery density of 1. These selective grid/stitch spacings are investigated as they have significant air voids. If the skin-depth based sheet

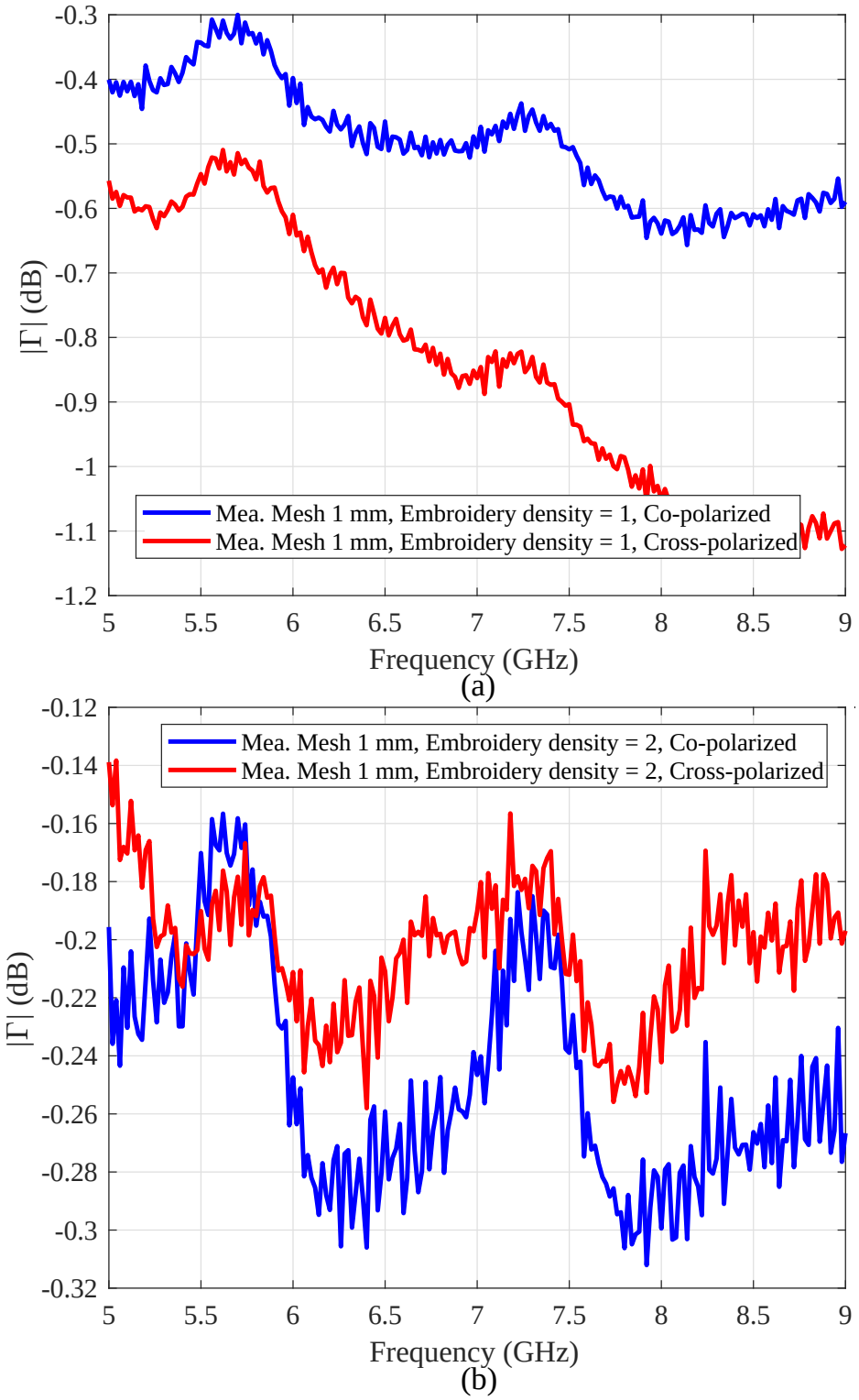

Figure 5.18. Measured reflection coefficient for the meshed embroidered structures at a grid/stitch spacing of 1 mm under the co-polarized and cross-polarized direction for an embroidery density of (a) 1 and (b) 2.

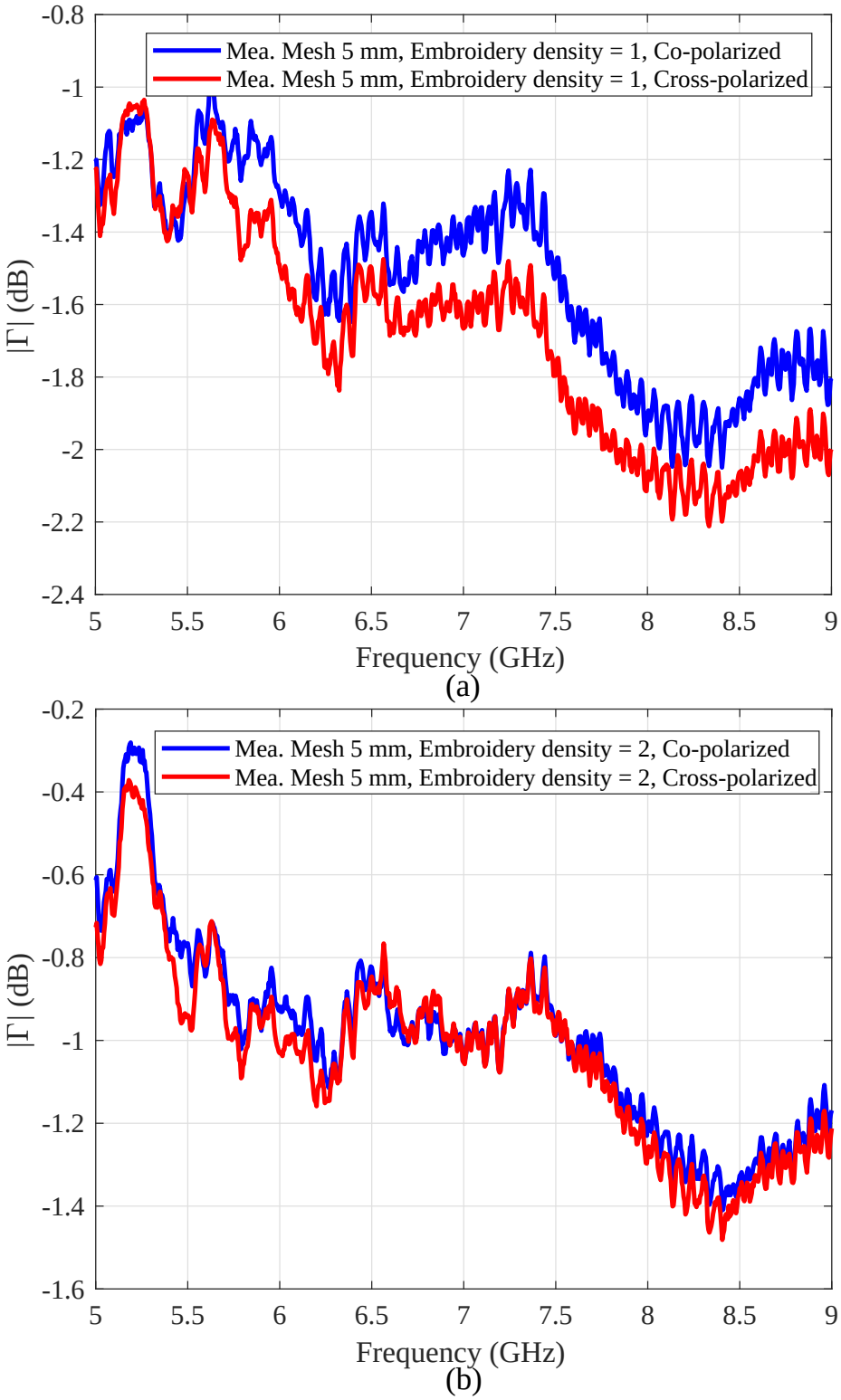

Figure 5.19. Measured reflection coefficient for the meshed embroidered structures at a grid/stitch spacing of 5 mm under the co-polarized and cross-polarized direction for an embroidery density of (a) 1 and (b) 2.

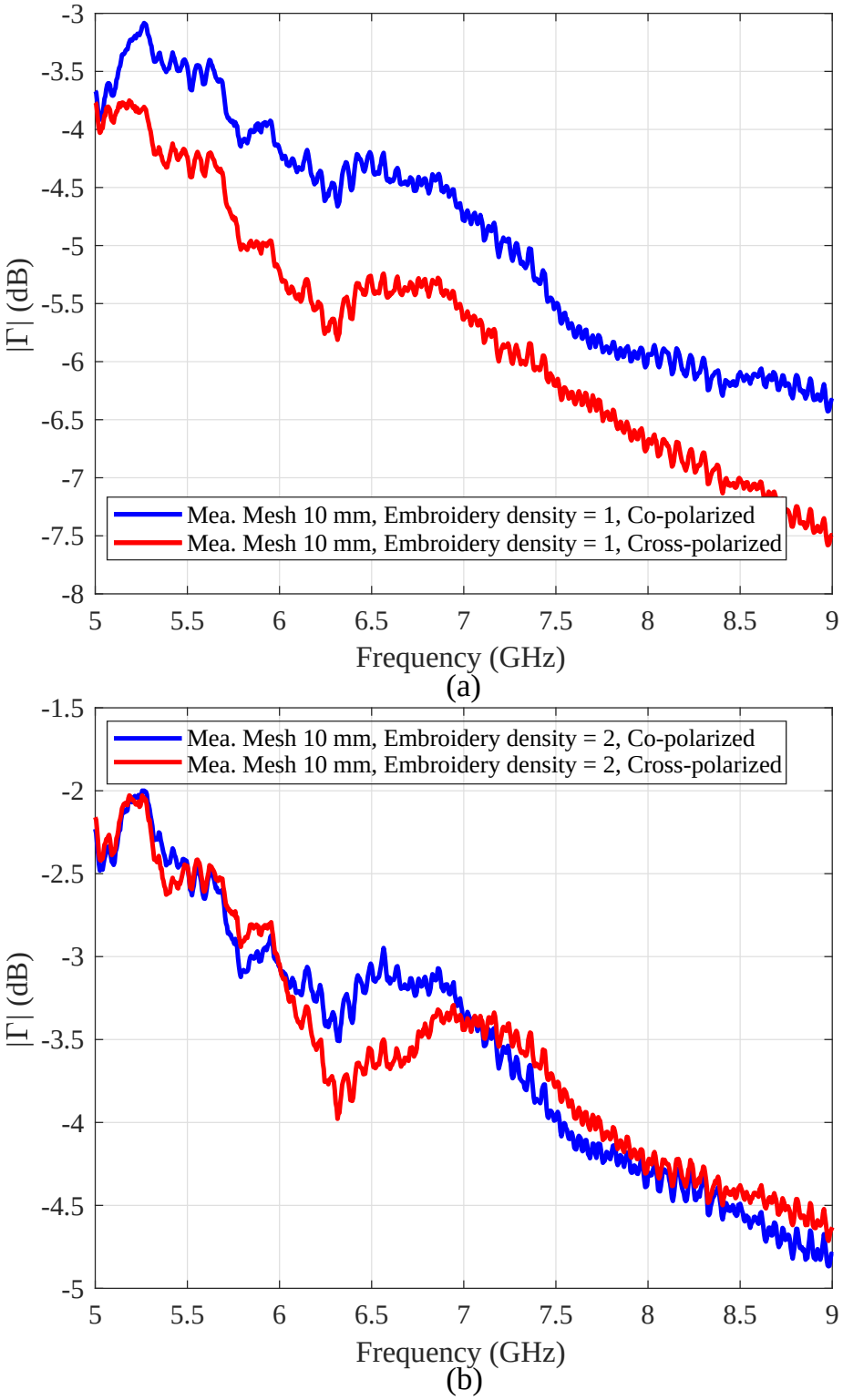

Figure 5.20. Measured reflection coefficient for the meshed embroidered structures at a grid/stitch spacing of 10 mm under the co-polarized and cross-polarized direction for an embroidery density of (a) 1 and (b) 2.

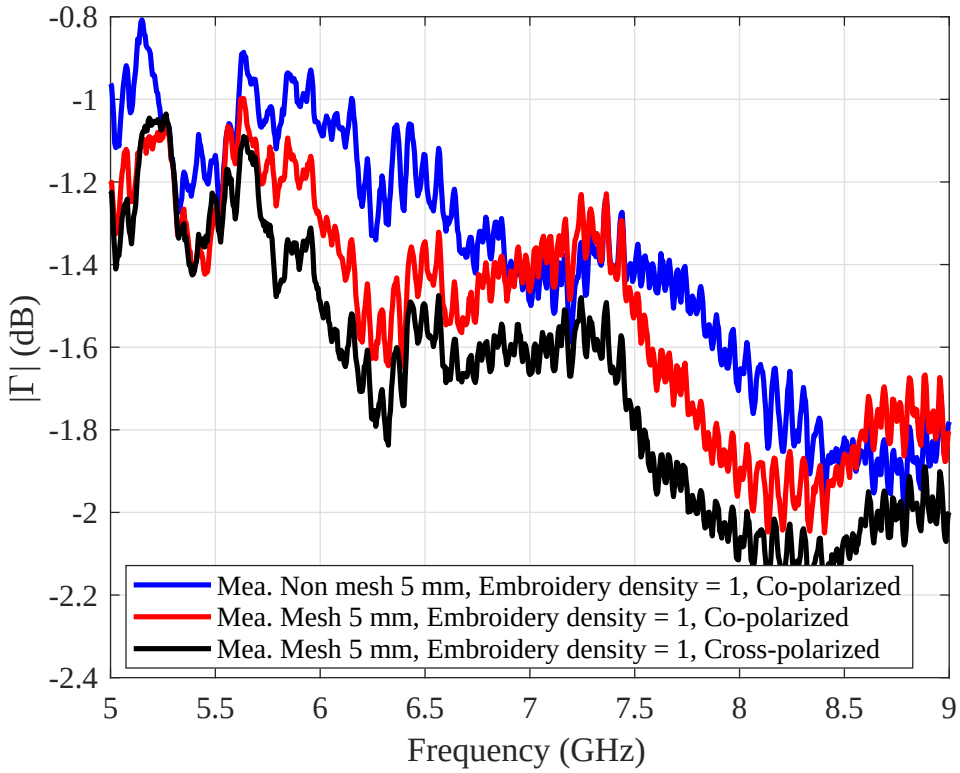

Figure 5.21. Measured reflection coefficient for the meshed structure with a grid/stitch spacing of 5 mm at an embroidery density of 1 under both the co-polarized and cross-polarized directions compared against the measured reflection coefficient for the non-meshed structure at the same stitch spacing and embroidery density under the co-polarized direction.

resistance is sufficient to capture the measured trend, then it can be assumed that the skin-depth based sheet resistance will also capture the measured trend for the structures with a grid/stitch spacing of 1 mm which have minimal air voids. An embroidery density of 1 is used as this represents the fastest variation of the reflection coefficient with frequency.

The simulated reflection coefficient based on skin-depth considerations for the aforementioned samples is shown in Fig. 5.22. For the sample with grid/stitch spacing of 5 mm, the reflection coefficient evaluated on the skin-depth based sheet resistance adequately captures the measured trend. However, for the sample with grid/stitch spacing of 10 mm, the reflection coefficient using the skin-depth based sheet resistance becomes unsuitable. The unsuitability is most likely because the structure with grid/stitch spacings of 10 mm contains significant air voids whereas the skin-depth calculation assumes a homogeneous sheet with no air voids. Alternatively, at larger grid/stitch spacings there exists significant inductance between the threads which

must be accounted for. On the contrary, when the sample is homogenized the inductance is not accounted for specifically for the individual wires. It is presumed that the lack of inductance considerations leads to the sizable discrepancy between the simulated reflection coefficient based on the sheet resistance determined from skin-depth based considerations and the measurements.

To adequately capture the measured trend for sample with grid/stitch spacing of 10 mm, the sheet resistance should vary faster than predicted by the dependence in the the skin-depth based model which varies exponentially with an exponent of 0.5. The simplest choice would be a linear fit which has an exponent of 1. For the sake of consistency, a linearly varying sheet resistance is used for all the samples. The cross-polarized sheet resistance will be addressed later.

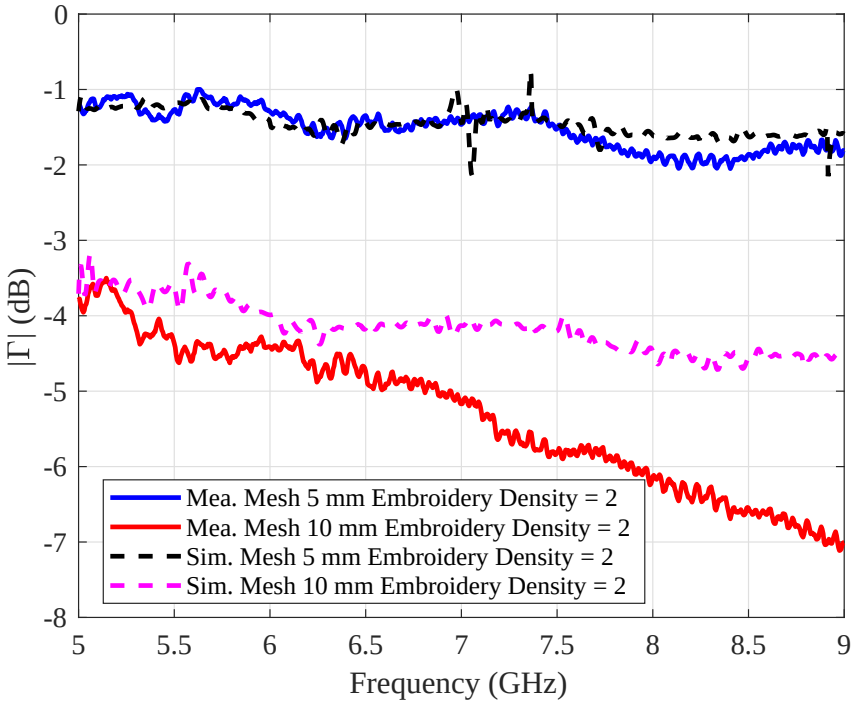

Figure 5.22. The solid lines show the measured reflection coefficient of the embroidered structures with conductive threads laid parallel to each other at grid/stitch spacings of 5 and 10 mm with an embroidery density of 1. The dashed lines show the simulated reflection coefficient for the samples when modeled as a homogenized sheet with a sheet resistance determined from skin-depth considerations.

An alternative method of characterizing the structures is to approximate the physical distribution of the threads and then perform the steps mentioned earlier, i.e. determining an effective sheet resistance for the approximated physical distribution. Utilizing

the physical distribution of the threads to determine an effective sheet resistance is expected to be generally valid for a variety of grid/stitch spacings [101]. The conductive threads can be approximated as thin rectangular strips with a width of 1 mm which is a reasonable approximation for the threads used in this investigation. Henceforth this modeling method will be known as MM2. In this case, as the currents are confined to a number of discrete elements which are physically separated from each other, the inductance is intrinsically accounted for. A depiction of both modeling methods is provided in Fig. 5.23. For the purposes of illustration, the sheet resistance for the meshed structure at a grid/stitch spacing of 5 mm and an embroidery density of 1 is also determined by modeling the physical distribution of the threads. The reason for modeling this particular embroidered structure by approximating the physical distribution of the threads will become clear in the next section. The comparison of the numerically determined sheet resistance under MM1 and MM2 for the meshed sample with a grid/stitch spacing of 5 mm under an embroidery density of 1 is provided in Fig. 5.24. The numerically determined sheet resistance for all the samples is provided in Table. 5.1. The numerically determined sheet resistance provides three salient conclusions as follows:

1. A larger grid/stitch spacing results in a lower reflection coefficient which is accounted for by a larger sheet resistance.

2. An increasing embroidery density for a particular grid/stitch spacing increases the reflection coefficient which is accounted for by a reduced sheet resistance.

3. The reflection coefficient for the meshed structures under both co-polarized and cross-polarized directions is largely the same which is accounted for by a similar sheet resistance in both directions.

Additionally, the numerically determined reflection coefficient based on the fitted sheet resistance for the meshed structures under the co-polarized and cross-polarized directions is quite similar to the corresponding co-polarized sheet resistance for the linearly embroidered structure. For example, the numerically determined sheet resistance for the meshed structure with a grid/stitch spacing of 5 mm and an embroidery density of 2 is similar to the co-polarized sheet resistance for the structure with a grid/stitch spacing of 5 mm and an embroidery density of 2 with the threads laid parallel to each other.

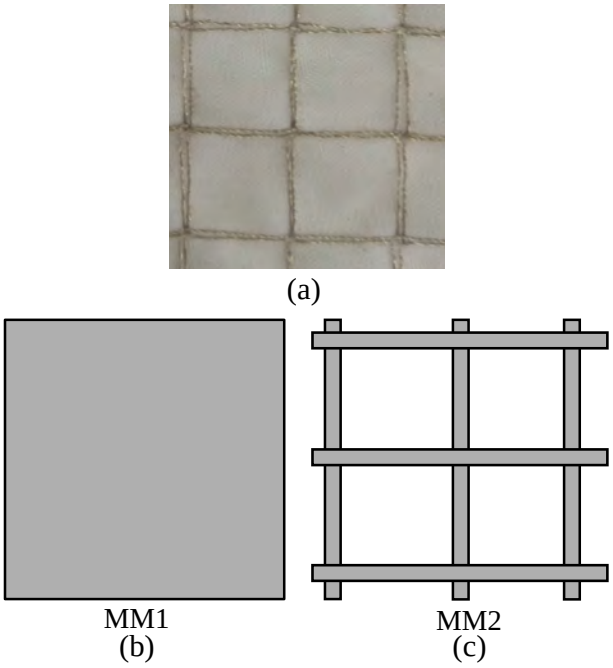

Figure 5.23. From top to bottom: (a) A meshed embroidered structure with a grid/stitch spacing of 10 mm, (b) a homogenized representation of the embroidered structure and (c) a physical representation of the embroidered structure. In the later case the width of the threads and the separation between the threads has been exaggerated for the purposes of illustration.

5.6 Embroidered Antenna Ground Planes

At this stage the embroidered structures have been modeled and characterized. The next step is to examine the validity of the modeling and characterization technique in a practical device. In this investigation this is achieved by using the meshed embroidered structure with a grid/stitch spacing of 5 mm and an embroidery density of 1 as an antenna ground plane. This structure is used as it allows for reasonable performance whilst allowing to see which modeling method MM1 or MM2 is generally valid. In regards to the performance, the meshed surfaces with a grid/stitch spacing of 10 mm are ruled out as they have a *peak reflection coefficient of* -2.5 dB. This represents nearly 50% power lost which would result in a very inefficient antenna. Whilst the meshed surfaces with a grid/stitch spacing of 1 mm have better performance than that of the 5 mm grid/stitch spaced surfaces, the fabrication of these surfaces is extremely challenging and is hence ruled out. Considering Table. 5.1, it can be seen that neglecting the embroidered surface with a grid/stitch spacing of 5 mm and an embroidery density of 1 none of the other structures are modeled using MM2. The reason for this is as follows: the performance is either inadequate as in the case of the embroidered

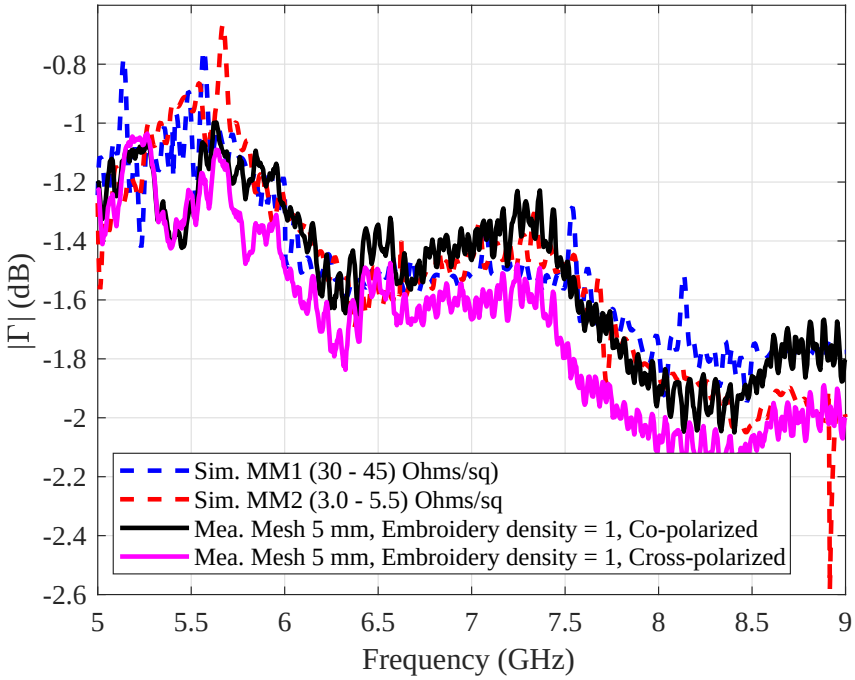

Figure 5.24. The measured reflection coefficient for the meshed 5 mm embroidered structure with an embroidery density of 1 and the numerically determined sheet resistance for the sample under two modeling methods: as a homogeneous sheet (MM1) and by approximating the physical layout of the conductive threads (MM2).

surfaces with a grid/stitch spacing of 10 mm or they are extremely difficult to fabricate as in the case of the embroidered structures with a grid/stitch spacing of 1 mm. Lastly by using the meshed structure with a grid/stitch spacing of 5 mm at an embroidery density of 1 rather than 2 the most conservative estimate of the performance is attainable. None the less by determining the sheet resistance for the samples using MM1 it is possible to get a quantitative appreciation of how the sheet resistance varies when subject to the different fabrication parameters.

5.6.1 Antenna Design

A textile patch antenna is used for demonstration as this geometry is a very common choice for wearable applications. The patch antenna is designed for a resonance frequency of 5.8 GHz which corresponds to the center frequency of the upper microwave ISM band. A schematic of the textile patch antenna utilizing the aforementioned meshed embroidered structure as a ground plane is shown in Fig. 5.25. The procedure to integrate the conductive fabric with the embroidered structure will be expanded upon in section 5.6.2. As the antenna is desired to be flexible, the substrate is

Table 5.1. Numerically determined sheet resistance for the embroidered structures using MM1.

Grid/Stitch Spacing	Embroidery Density	Thread Layout	Co-Polarized Sheet Resistance ($\Omega/\square$)	Cross-Polarized Sheet Resistance ($\Omega/\square$)
1 mm	1	Perpendicular	11 - 15	13-26
1 mm	2	Perpendicular	4 - 6	4 - 6
5 mm	1	Perpendicular	30 - 45	30 - 45
5 mm	2	Perpendicular	14 - 32	14 - 32
10 mm	1	Perpendicular	88 - 210	100 - 263
10 mm	2	Perpendicular	60 - 130	60 - 130
5 mm	1	Parallel	20 - 50	4000
5 mm	2	Parallel	14 - 32	2500
5 mm	3	Parallel	14 - 26	1805
5 mm	4	Parallel	11 - 20	1000
5 mm	5	Parallel	11 - 29	900
10 mm	1	Parallel	100 - 210	4000
10 mm	2	Parallel	60 - 120	3000
10 mm	3	Parallel	40 - 100	2000
10 mm	4	Parallel	35 - 75	2000
10 mm	5	Parallel	40 - 70	1000

realized from a 1.6 mm thick Cumming Microwave PF-4 foam with a relative permittivity (ϵ_r) of 1.06 and a loss tangent ($\tan\delta$) of 0.0001 at the desired frequency of interest. The top patch is made from Nora Dell conductive fabric whereas the ground plane is made from a combination of the Nora Dell conductive fabric and the embroidered structure. The Nora Dell fabric has a sheet resistance of 0.08 $\Omega/\square$ at the frequency of interest as determined from four-point probe measurements. For simplicity, the antenna is initially designed following the guidelines in [73]. The antenna is excited by an SMA connector which comes up from behind the ground plane where the inner pin of the SMA short circuits the top metalization layer as shown in Fig. 5.25.

The next step in simulations is to replace the conductive fabric ground plane with the hybrid conductive fabric-embroidered ground plane. This is done by gradually reducing the dimensions of the ground plane till the fundamental TM_{01} mode can no longer be supported. This is investigated by examining the electric field distribution of the

antenna at each ground plane size. Once the minimum ground plane size is determined, the bottom layer of the patch is modified to include the embroidered structure as shown in Fig. 5.25. As previously mentioned, the embroidered structure is modeled in two ways: MM1 and MM2 each with an associated sheet resistance. To serve as a reference, the patch antenna made solely from conductive fabric is also proposed to be realized. Henceforth the antenna made from conductive fabric and from a combination of conductive fabric and the embroidered structure will be known as patch one and patch two respectively. The optimized antenna dimensions are given in the caption of Fig. 5.25. Having designed both patch antennas in free-space, the next step is to examine the performance of the antennas when in close proximity to human body tissue. This is done to determine if the meshed ground can serve as a replacement to the purely conductive fabric ground plane to adequately isolate the antenna from the effect of the human body. The body is modeled as an homogeneous layer with a relative permittivity (ϵ_r) of 48 and conductivity (σ) of 5.7 S/m. These values correspond to a roughly two-third muscle equivalent model which is standard practice [59]. The dimensions of the body tissue are 150 x 150 x 5 mm. The simulated and measured results for both patches are compared in section 5.6.3.

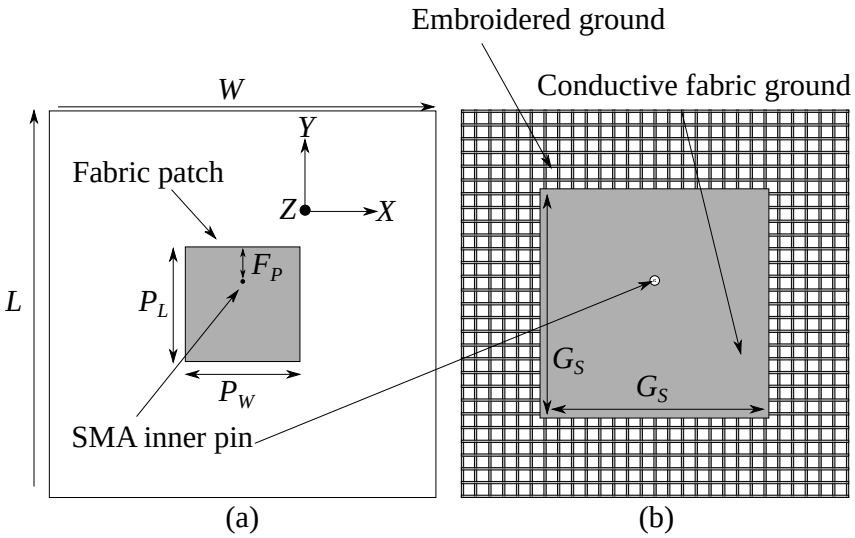

Figure 5.25. From left to right: (a) Top view of patch one and two and (b) Bottom view of patch two. The optimized dimensions are $L = W = 100$ mm, $G_S = 30$ mm, $F_P = 10$ mm, $P_L = 20$ mm, $P_W = 25$ mm. The bottom layer of patch one has a similar structure has patch two but as a purely conductive fabric ground plane with dimensions of $W \times L$.

5.6.2 Fabrication

To fabricate patch one the following procedure is implemented:

1. Cut out a 1.6 mm thick Cumming Microwave PF-4 piece to the total dimensions of the antenna (L and W in Fig. 5.25).
2. Cut out the top and bottom metalized layers of the antenna from Nora Dell conductive fabric.
3. Iron the top and bottom metalized layers on opposite sides of the 1.6 mm thick foam piece. Ironing melts the fabric into the foam.
4. Protrude the inner pin of an SMA connector through the substrate such that it punctures the top metal layer at the desired location denoted as F_P in Fig. 5.25(a). At this stage the base of the SMA should be flush with the bottom ground plane.
5. Apply conductive epoxy between the base of the SMA and the ground plane.
6. Apply conductive epoxy between the inner pin of the SMA and the top layer.
7. Apply non-conductive epoxy on top of the conductive epoxy on the ground plane for extra mechanical support.
8. Allow 24 hours for the conductive epoxy to dry.

To fabricate patch two, a largely similar procedure is implemented with the following exception: when cutting out the silver fabric for the ground plane, a small square section of dimension denoted as G_S in Fig. 5.25 is cut out from the Nora Dell fabric. Then this section is embroidered onto the meshed embroidered structure at the outer edges. Once the conductive fabric-embroidered ground plane is fabricated the remainder of the fabrication steps are the same as for patch one. The top and bottom view of the antenna is shown in Fig. 5.26(a) and Fig. 5.26(b) respectively.

5.6.3 Experimental Validation

Reflection Coefficient

The simulated and measured free-space reflection coefficient for patch one and two are shown in Fig. 5.27(a) and Fig. 5.27(b) respectively. For patch one there appears to

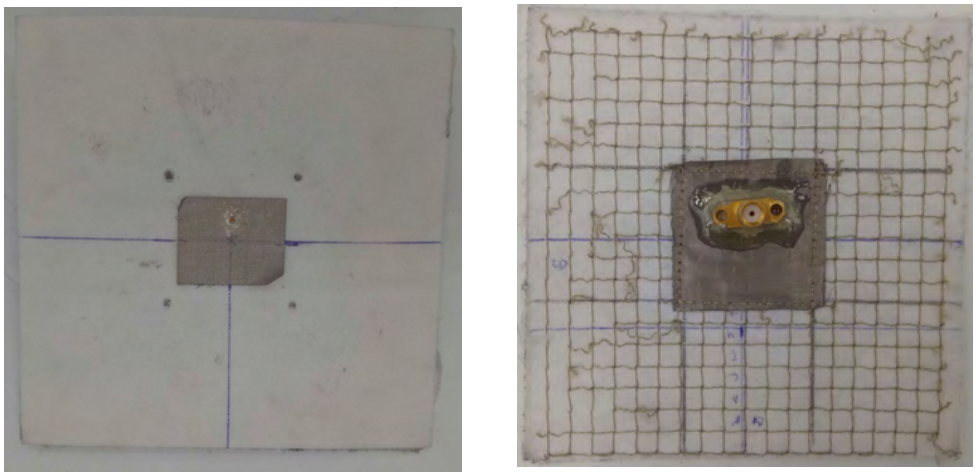

(a) (b)

Figure 5.26. A patch antenna using the meshed surface with a grid/stitch spacing of 5 mm at an embroidery density of 1 as a partial ground plane.

be a mild frequency shift which is attributed to fabrication tolerances. For patch two there are two simulation results provided. These two results correspond to the two different ways that the embroidered section of the ground plane is modeled: either as a homogeneous sheet (MM1) or by approximating the physical layout of the threads (MM2). It is emphasized that the effective sheet resistance determined from both MM1 and MM2 arise from numerical representations of the scattering measurements. For patch two both modeling methods appear to give a similar simulation result. It is also observed that the simulation results for patch two under either modeling method gives a larger bandwidth than for patch one. This is attributed to the increased losses of the embroidered structure. The measured reflection coefficient for patch two is in excellent agreement with the associated simulations. Consequently, from the perspective of the reflection coefficient either MM1 or MM2 are suitable for modeling purposes.

Radiation Patterns

The simulated and measured free-space radiation patterns for patch one are shown in Fig. 5.28(a) and (b). Generally speaking there is good agreement between the simulated and measured results for patch one. Simulations predict a peak gain of 9.1 dB which occurs at broadside whilst the measurements reveal a peak gain of 8.3 dB. The discrepancies are most likely due to limitations of the measurement setup. The simulated and measured radiation patterns for patch two using MM1 are provided in Fig. 5.28(c) and (d) whilst Fig. 5.28(e) and (f) provides the simulated and measured

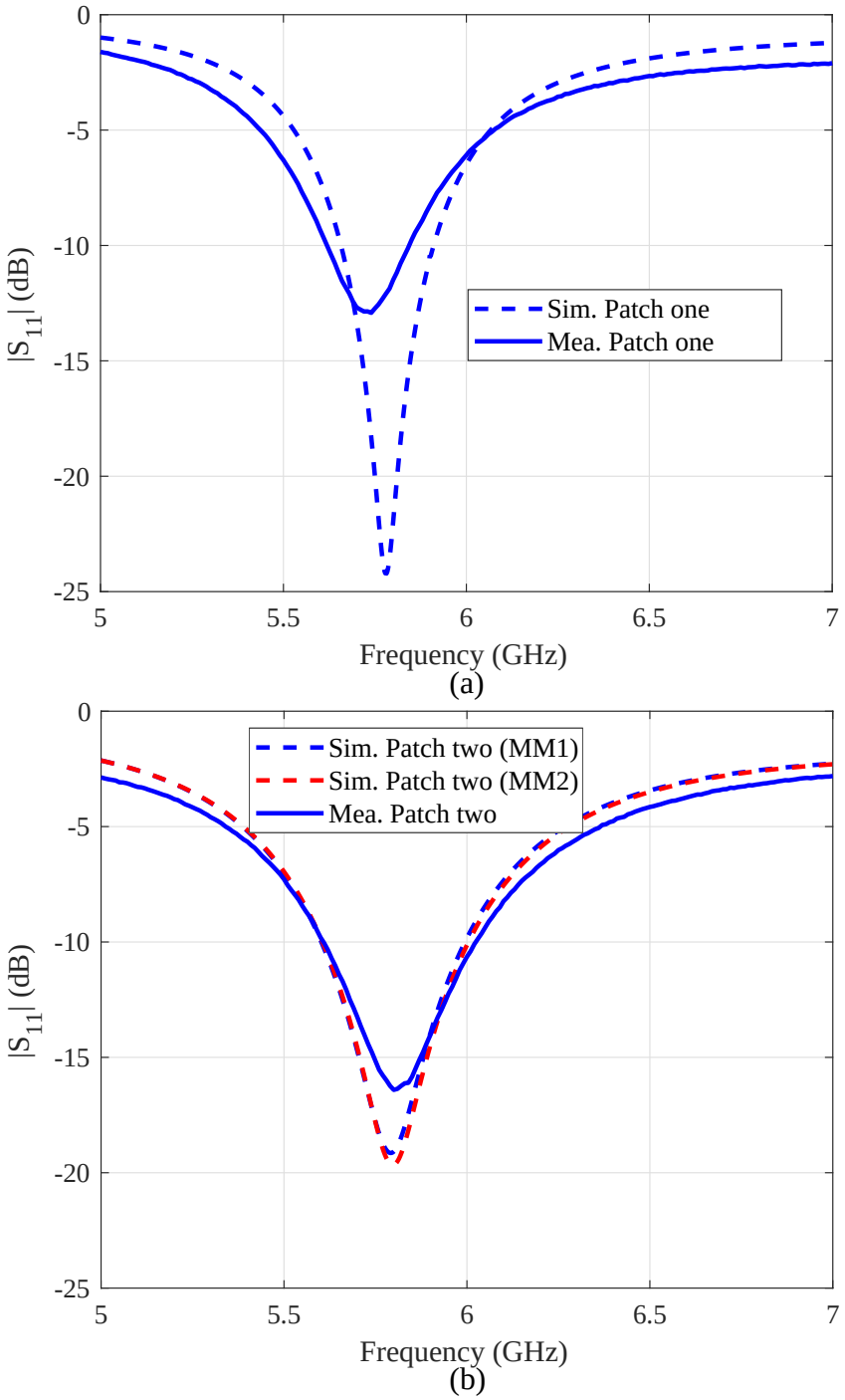

Figure 5.27. (a) Simulated and measured reflection coefficient for patch one in free-space and (b) Simulated and measured reflection coefficient for patch two in free-space.

free-space patterns using MM2. The latter modeling approach shows more back radiation which is also observed with the measured results suggesting that from a holistic perspective MM2 is more physically valid than MM1. It is suspected that MM2 is better at approximating the physical behavior, i.e the increased back radiation, as the

fields can pass through the grid in addition to accounting for the inductance between individual threads. On the contrary MM1 presents an impenetrable boundary condition which leads to minimal back radiation. In terms of the peak gain, using MM2 the simulations predict a peak broadside gain of 7.3 dB whereas measurements reveal a peak gain of 6.8 dB. Once again the mild discrepancies are attributed to limitations of our measurement setup. Having validated the performance of both antennas in free-space the next step is to examine the performance of the antenna when in close proximity to human body tissue. The human body is taken into consideration by using a commercially available broadband body tissue simulating gel from SPEAG [114]. The simulated and measured results for patch one and two when separated from the body tissue by 1 mm are shown in Fig. 5.29(a) and Fig. 5.29(b) respectively. For patch two the measured results are compared to the simulations using MM2 as it was previously shown that MM2 is more accurate at predicting the performance of the antenna. Generally speaking there is excellent agreement between simulations and measurements.

5.7 Conclusions

This chapter has begun by motivating the desire for embroidered antennas which then led into a discussion of some important issues pertaining to the utilization of computerized embroidery. These issues were primarily related to what effect *various* fabrication parameters have on the performance of embroidered structures and the means to model and characterize embroidered structures. In regards to the first aspect, this chapter has exploited bi-static RCS measurements to observe the variation in performance of embroidered structures as a function of three fabrication parameters. These parameters were:

1. Grid/Stitch spacing.
2. Embroidery density.
3. Embroidery layout.

Firstly, it was determined that the performance of embroidered structures is highly dependent on the grid/stitch spacing where a smaller grid/stitch spacing leads to higher performance. Secondly, it was found that increasing the embroidery density can improve the performance to an optimum limit. However, excessively increasing the embroidery density may cause performance degradation which was mainly attributed

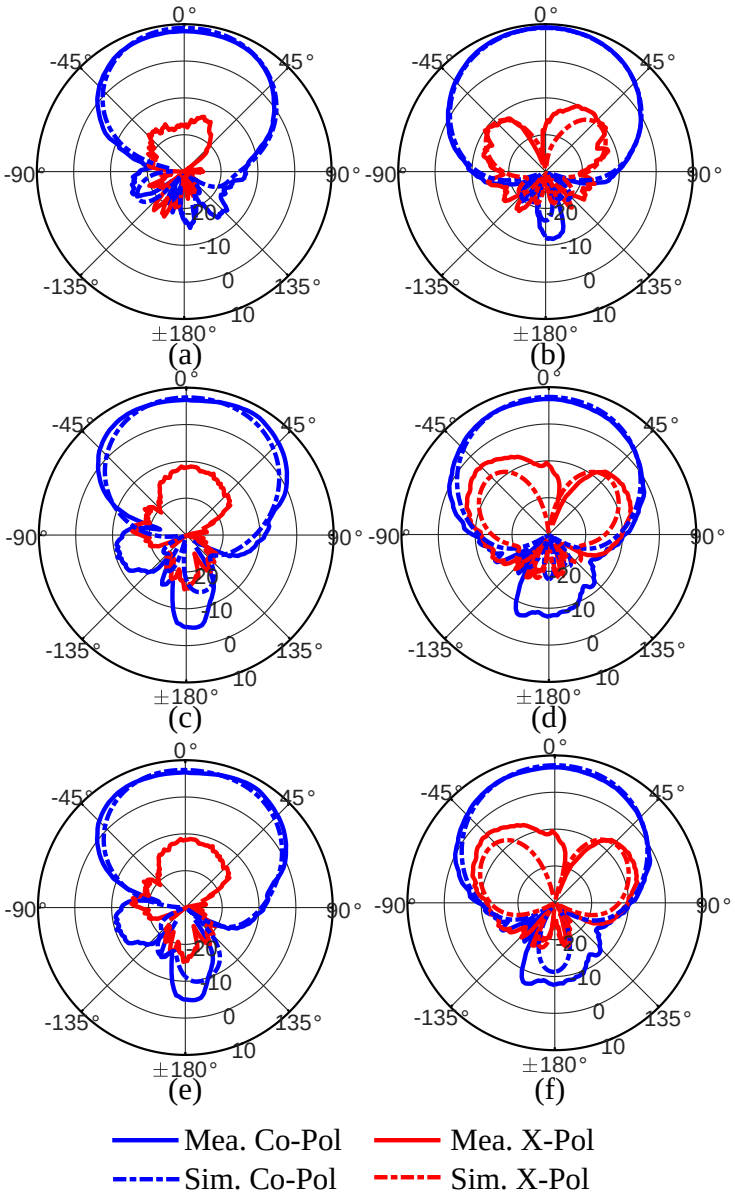

Figure 5.28. Simulated and measured radiation patterns of both patch antennas in free-space. From top left to bottom right: (a) Patch one in E-Plane, (b) Patch one in H-Plane, (c) Patch two in E-Plane, (d) Patch two in H-Plane, (e) Patch two in E-Plane and (f) Patch two in H-Plane. The simulation results in (c) and (d) are obtained using MM1 whereas the simulation results in (e) and (f) are obtained using MM2.

to the effects of surface roughness. Lastly it was confirmed that placing conductive threads perpendicular to each other can result as expected in structures that exhibit minimal anisotropy. To characterize the embroidered structures a numerically determined effective sheet resistance was developed by modeling selective embroidered structures in two methods. The first method was to assume that the embroidered

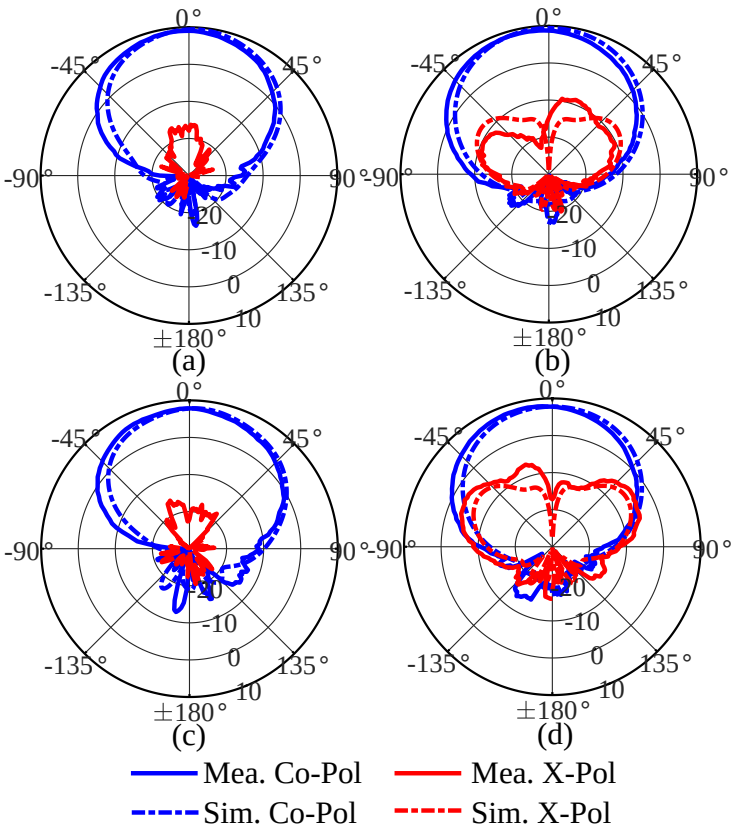

Figure 5.29. Simulated and measured radiation patterns of both patch antennas when in close proximity to the human body: (a) Patch one in E-Plane, (b) Patch one in H-Plane, (c) Patch two in E-Plane and (d) Patch two in H-Plane.

surfaces can be homogenized and the second method was to model the physical layout of the threads before determining the effective surface resistance. The validity of both modeling methods was examined by using a selected embroidered structure as a ground plane for a textile patch antenna. Based on the measured results it is concluded that approximating the physical layout of the threads is the preferred method to model embroidered structures, as it allows for coupling of fields through the ground plane and accounts for the inductance between adjacent threads. Finally it was shown that the embroidered ground planes sufficiently isolated the antenna from the human body. This suggested that for this particular thread type embroidered ground planes can serve as a partial replacement for extended ground planes made solely from conductive fabric. This last point is particularly noteworthy as it indicates that there may be substantial savings in terms of material costs when using embroidered techniques to realize textile antennas.

Chapter 6

Miniaturized Ultra-High Frequency Antenna

BODY-worn communications operating at the UHF (ultra-high frequency) band (0.86 - 0.96 GHz) are attractive due to favorable regulations. Common wearable antenna topologies such as planar inverted-F antenna (PIFA), patch antennas and cavity-backed slot antennas tend to be large at the aforementioned frequencies and display limited bandwidth. Therefore it is desirable to have a compact low-profile wearable UHF antenna with a large bandwidth. Thus in this chapter a new compact low-profile multi-layer textile antenna operating in the UHF band is presented. The antenna displays a high radiation efficiency with a large bandwidth for the compact dimensions. The antenna is fully integrated with a textile feeding mechanism to enhance wearability. Design guidelines are developed and justified by obtaining good agreement between simulations and measurements.

6.1 Introduction

There a range of potential frequencies that can be used for body-worn medical communications, one of which is the UHF band that has attracted attention due to favorable regulations [115,116]. Within the UHF band the frequency range from 0.86 - 0.96 GHz has been utilized for body-worn RFID communications [1,115–117]. One of the main challenges when working at the UHF band pertains to the antenna size: due to the relatively long wavelength most resonant wearable antennas designed for operation at the UHF band are rather large. To circumvent this issue planar inverted-F antennas (PIFA) [53,115,118] have been used. A high degree of miniaturization has also been achieved at the expense of bandwidth reduction and performance degradation when placed near body tissue [117,119,120]. Generally speaking it is a challenge to obtain a compact wearable UHF antenna isolated from the body of the wearer and with a relatively large bandwidth. It is perhaps for this reason that the literature on fully textile wearable compact UHF antennas with a broad bandwidth is rather sparse [53].

The work presented in [51] proposed a low-profile antenna operating with a large bandwidth of 8.90% centered at a frequency of 0.9 GHz. The antenna which is shown in Fig. 6.1 had a large planar dimensions of $0.41\lambda_0$. Unfortunately no information was provided for the radiation efficiency and additionally the antenna was made on PCB substrate with a relative permittivity of 2.2 which assisted miniaturization.

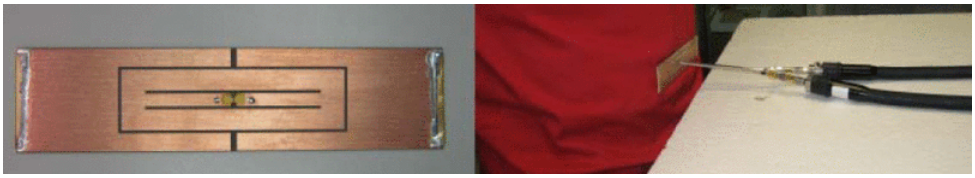

Figure 6.1. A broadband UHF antenna suitable for on-body operation as reproduced from [51].

Another recent contribution [52] presented a multi-layer patch antenna inspired by folding techniques (as shown in Fig. 6.2) resulting in a maximum planar dimension of $0.14\lambda_0$ at a operation frequency of 0.86 GHz . As a consequence of the applied miniaturization techniques a limited bandwidth of 0.44% was attained. Additionally this antenna was realized on a substrate with a relative permittivity of 3.0 which would have aided in miniaturization. Given that most textile substrates have a relative permittivity in the range of 1.0 to 1.5 [121] the size of this antenna would be rather large if implemented in textile technology.

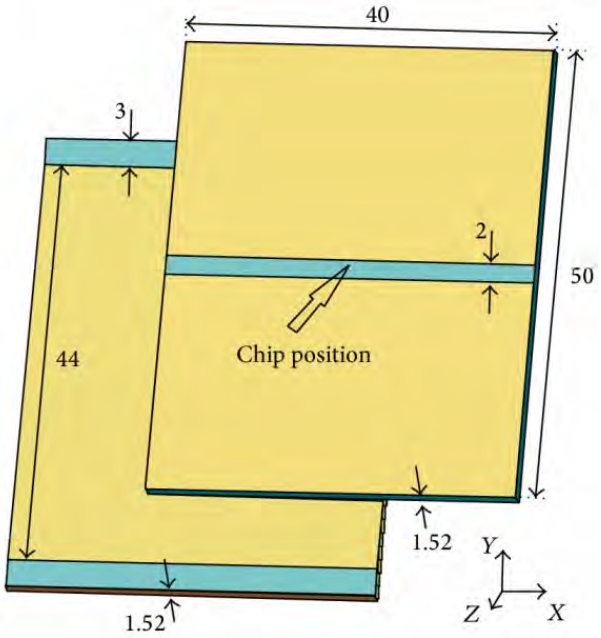

Figure 6.2. A miniaturized UHF antenna for on-body operation realized on a rigid substrate as reproduced from [52].

A flexible wearable UHF antenna which is shown in Fig. 6.3 was presented in [53]. The antenna which was based on a microstrip-line-fed quarter-wave folded patch antenna displayed dimensions of $0.23\lambda_0 \times 0.11\lambda_0 \times 0.01\lambda_0$ at its center frequency of 923 MHz. At these compact dimensions the antenna exhibited a bandwidth of 0.6% and a broadside gain of 1.3 dBi in free-space. Due to these compact dimensions the antenna was very sensitive to the effects of the human body. From simulations it was revealed that placing the antenna in close proximity to human body tissue dramatically altered the reflection coefficient and resulted in a significant reduction in the broadside gain from 1.3 dBi to -2.1 dBi. To mitigate the effects of the human body a ground plane with planar dimensions of $0.61\lambda_0 \times 0.61\lambda_0$ was incorporated into the antenna. The presence of the large ground plane made the antenna very insensitive to the effects of the human body as the the reflection coefficient and radiation patterns were relatively stable whether in free-space or in close proximity to human body tissue.

The preceding discussions have demonstrated that a compact low-profile textile antenna operating at the UHF band with a relatively broad bandwidth for the compact size is desired. Therefore in this chapter a new low-profile textile antenna is proposed exploiting multiple well know miniaturization techniques. A salient feature of the antenna is the relatively large bandwidth for the low-profile: an on-body bandwidth of

3.0% is achieved for a thickness of $0.0149\lambda_0$. The antenna is inspired by folding techniques [122] as applied to a standard cavity-backed slot antenna and design guidelines are proposed for a repeatable and scalable design.

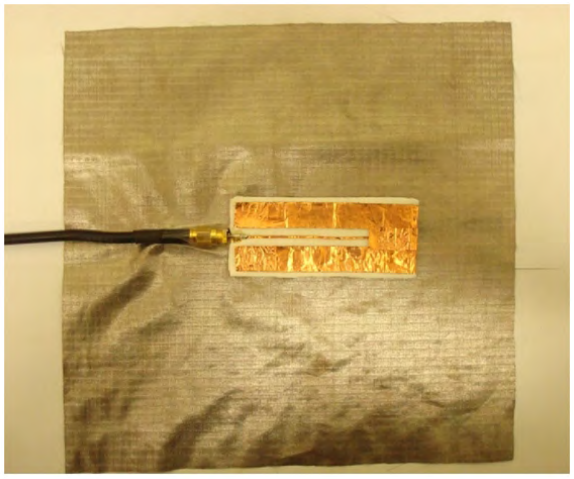

Figure 6.3. A narrow band textile UHF antenna with an extended ground plane for isolation from the human body as reproduced from [53].

6.2 Geometry Overview

A schematic of the proposed geometry is shown in Fig. 6.4. The antenna is a multi-layer semi-closed cavity-backed slot-monopole where the multi-layer topology has been inspired by folded cavity techniques. The top layer contains the radiating element (half H-Slot) whilst the middle layer contains the feeding mechanism (inset fed shielded stripline) and the bottom layer is the ground plane. The combination of the radiating slot shape and the semi-closed cavity structure help to obtain a relatively large bandwidth for the compact size.

6.3 Design Method

The practical design begins by deciding the operation frequency and on-body bandwidth. For this design the operation frequency is set at 923 MHz whilst the on-body bandwidth is set at at 3.0%. This bandwidth corresponds to the largest UHF RFID band which is the North American band.

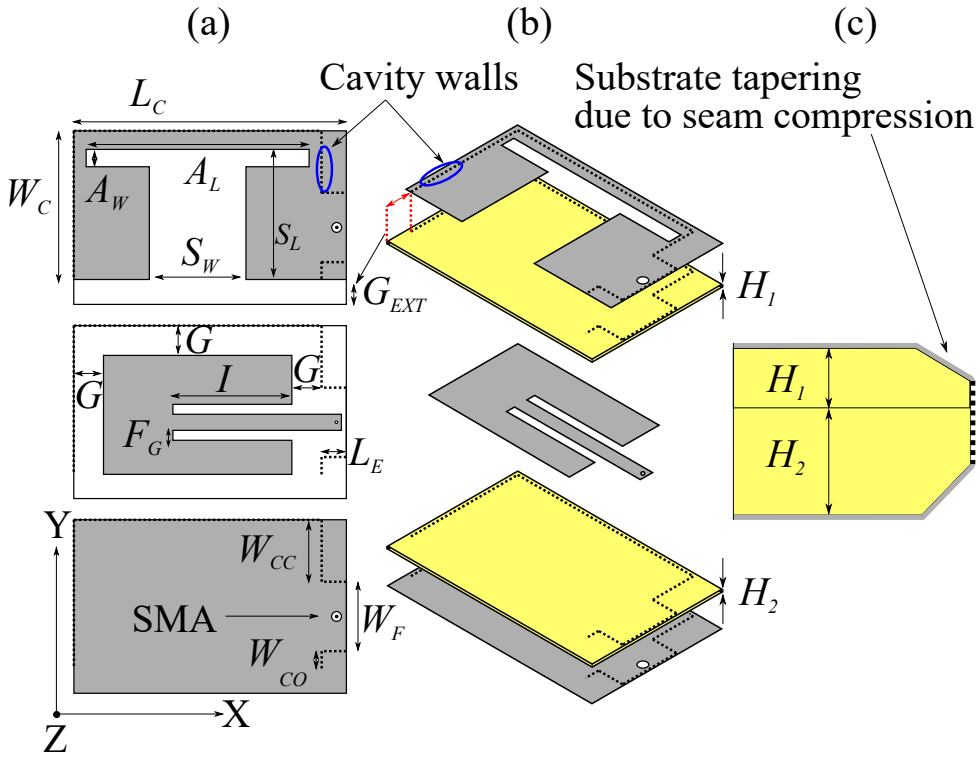

Figure 6.4. Geometry of the proposed antenna. The optimized parameters are $G_{EXT} = 10$ mm, $W_C = 60$ mm, $L_C = 100$ mm, $L_E = 10$ mm, $S_L = 52.5$ mm, $S_W = 39$ mm, $A_L = 90$ mm, $A_W = 7$ mm, $W_F = 28$ mm, $W_{CO} = 7$ mm, $W_{CC} = 25$ mm, $G = 12$ mm, $I = 43$ mm, $F_G = 1$ mm, $H_1 = 1.6$ mm, $H_2 = 3.2$ mm. Shaded grey areas represent metallization layers and dotted lines represent embroidered conducting walls. From left to right: (a) 2D layered view, (b) 3D exploded view, (c) cross sectional view of seam compression at the cavity walls.

The next phase is to design a standard cavity-backed slot antenna following the procedure in [123]. The design of the standard cavity-backed slot antenna begins by determining the planar dimensions of the cavity which should be $0.5\lambda_G \times 0.5\lambda_G$ where λ_G is the guide wavelength as can be determined from [123]. The thickness of the cavity is set based on the minimum thickness of materials that are used to fabricate the antenna. As the antenna is desired to be flexible this design uses Cumming Microwave PF-4 as the substrate. The reason why the minimum thickness is used is that later operations will result in an increase in the thickness. At this stage the metalized areas of the cavity can be modeled as perfect electric conductors.

Having designed the cavity the next step is to cut out a slot on one of the ground planes. Henceforth the ground plane which contains the slot is known as the top ground plane and the other ground plane is known as the bottom ground plane. The length of this slot should be mildly smaller than the cavity dimensions. As an empirical guideline

based on numerical studies suggested that the length of the slot be 10% smaller than the the cavity dimensions. The width of the slot is set at 1 mm which represents the minimum dimension that can be fabricated using textile materials.

At this stage a resonating element is generated and needs to be excited. The initial excitation mechanism is through an SMA connector. To accommodate the SMA connector a small circular cut which has a radius of the same dimension of the teflon of the SMA connector is made on the bottom ground plane. The body of the SMA connector is then placed flush against the bottom ground plane and the inner pin of the SMA connector is protruded through the cavity and makes electrical contact with the top ground plane. Initially the SMA connector is centered with respect to the cavity width and displaced from the slot width by a few millimeters. The exact position of the SMA connector will later be optimized. With the introduction of the SMA the antenna should look as shown in Fig. 6.5(a)

At this stage the resonance frequency is observed and if necessary slight modifications of the cavity or slot dimensions are performed to adjust the resonance frequency. For impedance matching the position of the SMA connector is varied across the length of the cavity. Having obtained the desired resonance frequency the next phase of the design is to miniaturize the antenna.

Initial miniaturization is achieved by folding the cavity resulting in a multi-layer cavity structure as described in [122, 124–128]. The folding operations naturally double the antenna thickness whilst providing in the middle of the antenna a metallic layer which is separated from the cavity walls by an in-plane gap G as shown in the middle Fig. 6.5(b). If this gap G is properly chosen then the resonance frequency of the folded and unfolded structure can be made the same [125, 129]. The gap can be seen as providing capacitive loading in the cavity due to the confinement of the electric field inside the gap. The concept of capacitive loading forms the core underlying design methodology of this antenna. That is to alter the resonance frequency by changing the amount of capacitance within the antenna. Whilst the folding operations result in a large reduction in the dimensions of the cavity along one direction the remainder of the cavity remains physically and electrically large. To obtain even greater miniaturization the middle metallic layer can be completely disconnected from all the cavity walls as shown in Fig. 6.5(c) which generates another capacitance between the middle plate and the cavity walls along the Y axis. Once this is performed the antenna can no

longer be seen as folded but has none the less been referred to as folded in the literature [23]. A more appropriate expression would be multi-layer and henceforth this expression will be used.

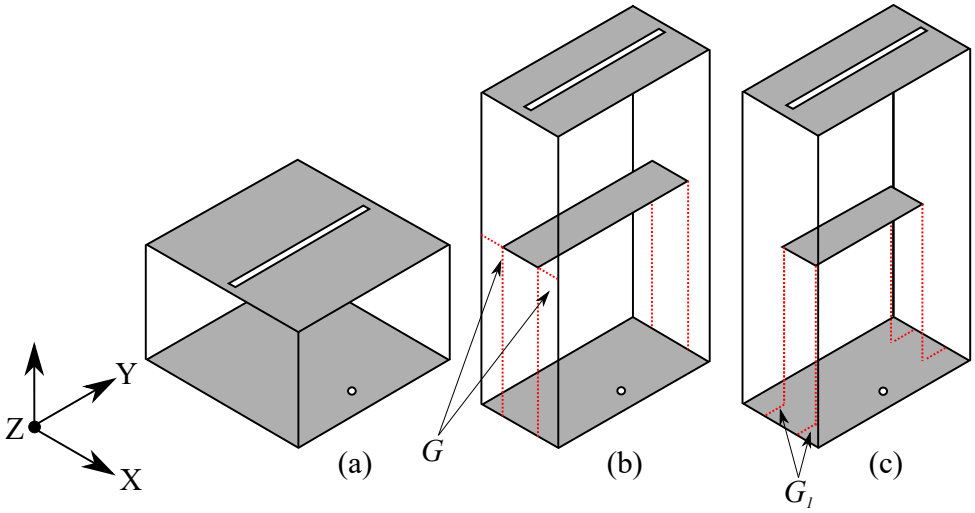

Figure 6.5. Evolution of the proposed geometry from: (a) Standard cavity backed slot antenna, (b) Folded cavity backed slot antenna, (c) Multi-layer cavity backed slot antenna.

Observing the antenna structure it can be seen that there are three metal layers - top, middle and bottom. As there is an electric field inside the substrate there is naturally a capacitance between the ground planes and the middle layer. As is well known the capacitance between two metal layers is highly dependent on the spacing between them. Therefore by raising the middle layer closer to the radiating slot the capacitive loading on the slot is increased leading to a lower resonance frequency. Considering the available thickness of the material the separation between the top layer and the middle layer, H_1 as shown in Fig. 6.4, is set to be 1.6 mm and the separation between the middle layer and bottom layer, H_2 as shown in Fig. 6.4, is set to be 3.2 mm leading to an overall thickness of 4.8 mm or 0.0149 of the target free-space wavelength. By applying the aforementioned techniques the resonance frequency of the antenna is reduced by 16%.

Up until now miniaturization techniques have been applied to the cavity structure whilst the slot element itself remained unchanged. By altering the shape of the slot an even larger reduction in resonance frequency can be achieved. To understand how modifying the slot shape helps miniaturization consider an analogous monopole antenna. It is well known that by adding a top plate to a monopole antenna the resonance frequency can be significantly reduced due to the capacitive loading provided by the

top plate [130]. From duality this principle can also be applied to a slot antenna which amounts to having another slot perpendicular to the main slot which results in the H-slot structure. If the top hat provides capacitive loading for a monopole antenna then the H-arms provide inductive loading for a slot antenna. Alternatively it can be seen that the introduction of the H-arms increase the current path length on the top ground plane which leads to a further reduction in the resonance frequency by 30%. The introduction of the perpendicular slot raises two new parameters for further optimization - the length and width of the H-arm which should be tuned to obtain the lowest possible resonance frequency.

Observing now that a slot antenna operated in the fundamental resonant mode has a magnetic wall boundary condition in its center a further substantial size reduction is achieved by simply cutting the antenna in half [131] across the ZX plane (which corresponds to the cavity length) resulting in a semi-closed cavity. At this stage the antenna is now asymmetric and the position of the SMA connector needs to be re-optimized. This re-optimization is performed over the length and width of the interior plate till an impedance match below -10 dB at the desired resonance frequency is obtained. It should be noted that despite cutting the antenna in half there is no radiation through the newly created aperture along the cavity length due to the opposing phase of the electric fields in the top and bottom substrates, as shown Fig. 6.6 in blue and red respectively, resulting in negligible radiation in the far field.

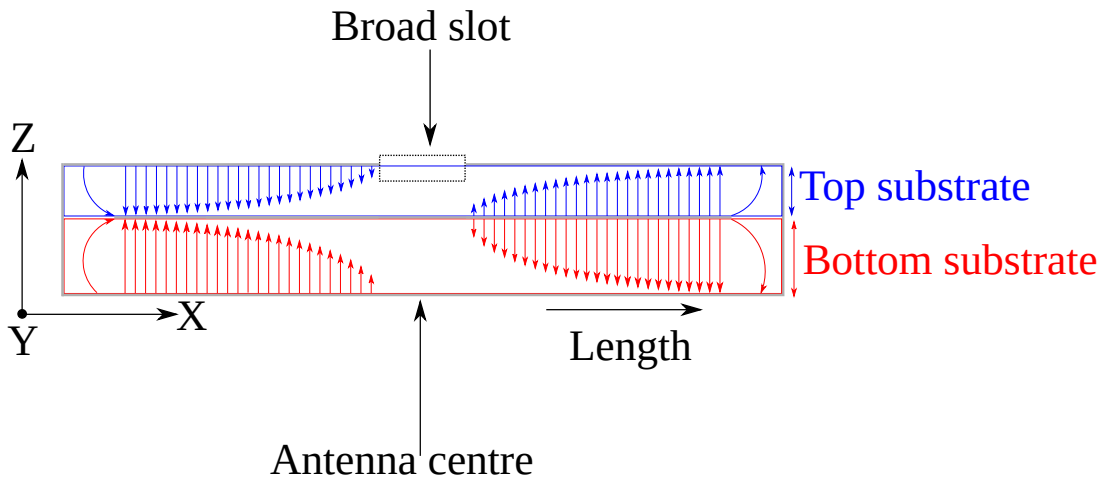

Figure 6.6. Electric field across the length of the antenna after cutting the antenna in half.

After having obtained the maximum downshift in resonance frequency through the aforementioned miniaturization techniques the next step is to scale the frequency back to the target of 923 MHz. The upshifting of the resonance frequency is achieved through

a combination of four techniques - 1) reducing the overall cavity dimensions, 2) enlarging the slot width as this reduces the current path length on the top ground plane [132], 3) relaxing the miniaturization by increasing the gap size G and 4) making the slot length shorter. In addition to increasing the operating frequency, the above options two and three also enhance the bandwidth. Option two increases the bandwidth by increasing the radiating aperture whereas option three increases the bandwidth by reducing the field confinement within the antenna. Utilizing a combination of these techniques the final antenna size comes to $0.31\lambda_0 \times 0.19\lambda_0$ with 3.8% bandwidth. At this stage the nominal free-space design using a SMA connector is finished and the integration of a textile feeding mechanism is the next focus.

As the antenna has three metal layers, two of which are connected ground planes and the fields in the upper and lower half cavity are in opposite directions, a shielded stripline feeding mechanism [86] is a natural choice. To accommodate the feeding mechanism the cavity needs to be modified following the procedure shown in Fig. 6.7 and herein described.

1. The first step is to extend the length of the top and bottom substrates by the dimension L_E as shown in Fig. 6.7(a).

2. After extending the substrates by the aforementioned dimension a cut into one of the back walls of the cavity is made as shown in Fig. 6.7(b). The dimension of this cut, W_F, is chosen in accordance with the procedure described in [86]. In the initial stage the cut can be centered with respect to the width of the cavity. That is W_{CO} and W_{CC} should be made equal. Later these parameters will be optimized.

3. From the position of the aforementioned cut two lengthwise walls are created with the dimension L_E as shown in Fig. 6.7(c). Then these two lengthwise walls are connected through a wall of dimension W_F at the very edge of the substrates as shown in Fig. 6.7(c). Finally a circular cut is made on the top and bottom ground planes. This circular cut should be centered in between the two lengthwise walls of dimension L_E. As the purpose of this cut is to accommodate the SMA connector the radius of this cut should have the same radius as the teflon of the SMA connector. The SMA conenctor is only for measurement purposes and in practical the antenna will be fed by the stripline.

4. Now the stripline is added in between the top and bottom substrate and is connected to the middle layer as shown in Fig. 6.7(d). The back of the stripline

should be separated from the back cavity wall by the dimension F_X whilst the inner pin of the SMA connector should contact the stripline at a distance of F_Y from the back cavity wall. These dimensions are chosen in accordance with the procedure detailed in chapter 3 section 3.2.

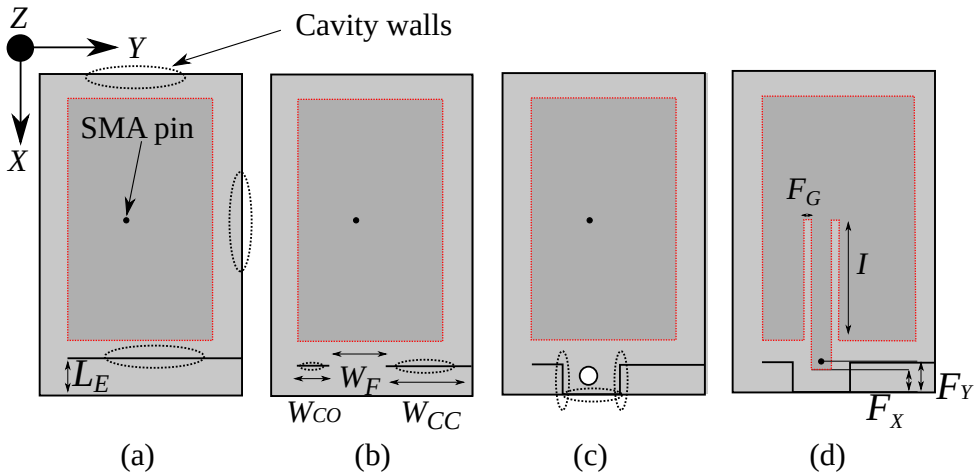

Figure 6.7. The modifications to the cavity structure to accommodate the shielded stripline feeding mechanism. For the sake of clarity only the bottom ground plane is shown. The dotted red lines depict the middle layer.

Impedance matching is facilitated by adjusting the termination point of the stripline, i.e the dimension I, into the middle layer and the position of the stripline along the width of the cavity, i.e the dimension W_{CO}. Both of these parameters need to be jointly optimized as the antenna is asymmetric. Finally the feedgaps F_G are set at 1 mm for fabrication simplicity.

6.4 Design Adaptation for Wearable Implementation

Wearable antennas require special design considerations some of which are dependent on the utilized materials [86] and method of fabrication. Generally the metalized materials for wearable antennas have conductivity that is significantly lower than copper which must be accounted for. One method of accounting for the non-ideal nature of the materials is to model them as a lossy metallic sheet with a certain sheet resistance [86]. As was mentioned in chapter 2 section 2.2 the antennas made in this thesis utilize a combination of conductive yarns and conductive fabrics. For this specific design the conductive threads that are utilized are Elitex Skin Contact 235 threads and the conductive fabric is MarkTeX silver fabric and therefore the non-ideal conductivity of the

textile materials must be accounted for. Thus the next step in the design process is to extract an *effective* sheet resistance for these materials over the desired frequency range. The sheet resistance is an *effective* parameter as it abstracts away from the complex microscopic structure of the materials [133].

The *effective* sheet resistance can be calculated according to equation $R_S = 1/\sigma\delta$ [86] where σ represents the DC conductivity and δ is the skin depth of the material. The skin depth δ can itself be expressed as $\delta = \sqrt{\rho/f\pi u_r u_0}$ where ρ is the DC resistivity which is the inverse of the DC conductivity σ.

To extract the DC resistivity the resistance must first be measured. Then according to $R = \rho L/Wt$ the conductivity σ can be taken as the inverse of the resistivity ρ. In the last expression R is the resistance, L is the length, W is the width and t is the thickness of the material under test.

To extract the sheet resistance for the silver fabric three samples of 100 mm $\times$ 100 mm were created and the DC resistance was measured. Then the DC conductivity was extracted and the RF sheet resistance was calculated. Over the frequency of interest the silver fabric has a sheet resistance of 0.04 $\Omega/\square$. To measure the resistance of the embroidered walls three samples of length 100 mm were made as shown in Fig. 6.8. The embroidered walls were made on a piece of 4.8 mm foam with conductive fabric on either side. The 4.8 mm thick foam was achieved by adhering 1.6 mm and 3.2 mm foam pieces together using fabric glue. By using the same procedure as for the silver fabric a RF sheet resistance of 3.0 $\Omega/\square$ was extracted for the embroidered walls over the frequency of interest.

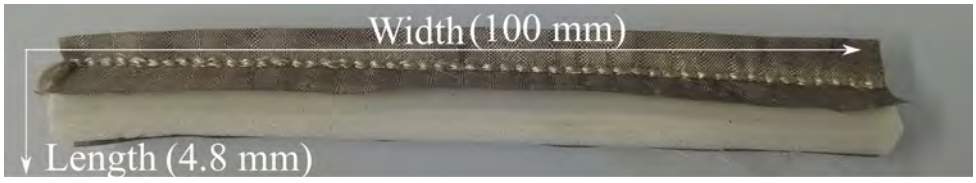

Figure 6.8. A section of an embroidered wall used to obtain a effective frequency dependent sheet resistance.

Another consideration stems from the method of fabrication. Previous studies have demonstrated that antennas which exploit computerized embroidery to realize cavity walls exhibit seam compression where the embroidery is performed [24]. This effect is shown in Fig. 6.9 where it is seen that the antenna becomes tapered at the location of the embroidery. This seam compression is due to the mechanical force of the needle

going through the substrate and the malleable nature of the foam [24, 134, 135]. This alteration in the geometry naturally alters the resonance frequency. Consequently it is necessary to re-optimize the antenna for the desired resonance frequency taking into account the effects of seam compression. This can be accounted for by progressively reducing the thickness of the cavity walls from h_s to d_h and tapering the ground planes as shown in the inset of Fig. 6.9.

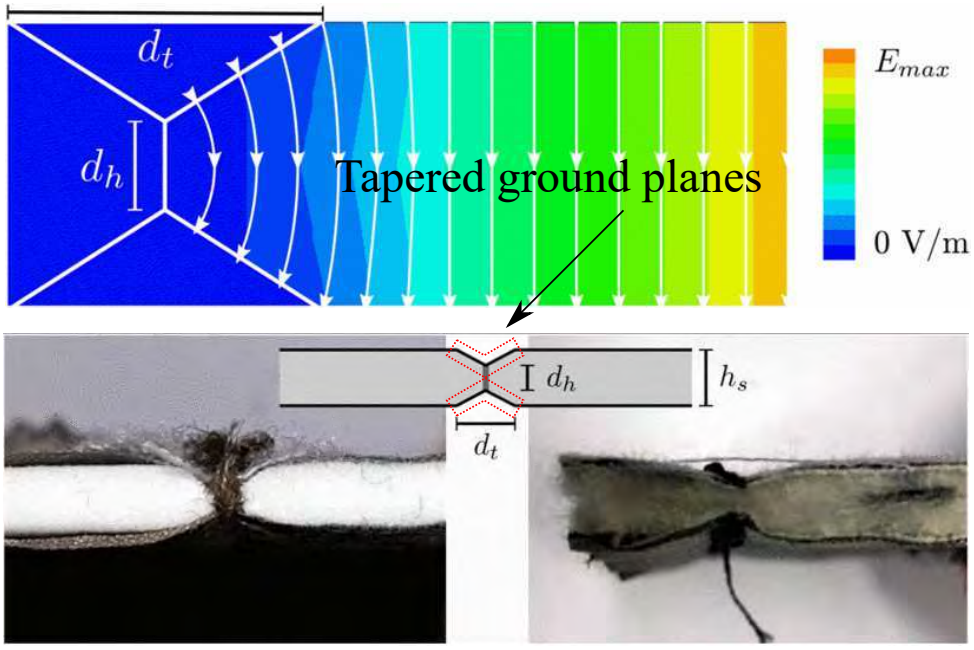

Figure 6.9. Depiction of seam compression as adapted from [24].

The last consideration for wearable structures pertains to the operating environment. Wearable antennas are naturally going to be placed in close proximity to human body tissue which will alter the radiation characteristics. Thus to evaluate the effect of the human body, simulations were performed where the antenna was placed 1 mm above the body tissue as this is expected to be a typical case. To approximate the human body an arrangement of three homogeneous layers is used. The three layers are skin, fat and muscle with thickness of 2 mm, 2 mm and 10 mm respectively. Simulation results shown in Fig. 6.10 reveal that both the resonance frequency and bandwidth are altered. The resonance frequency exhibits a drift *upwards* of 1.6% whilst the bandwidth is *reduced* from 3.8% to 3.0% .

Both of these results are rather counter-intuitive as the presence of a lossy dielectric load with a large relative permittivity is expected to lower the resonance frequency and increase the bandwidth [136]. To understand both of these effects it must first be noted that due to the H-arms there are significant currents across the length of the antenna

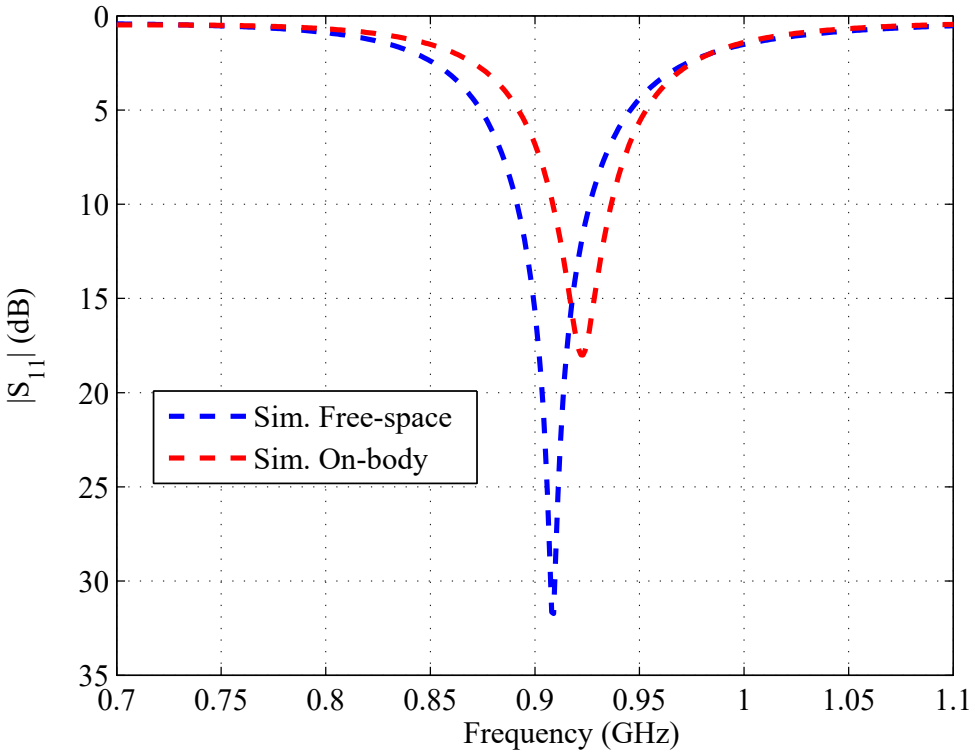

Figure 6.10. Simulated reflection coefficient in free-space and on-body.

on the top ground plane. These currents then spread out from the top ground plane and appear as along the lengthwise cavity wall. This is shown in Fig. 6.11(a) which shows the current distribution along the lengthwise, ZX, cavity wall at the free-space operating frequency. In the free-space case these currents on the cavity wall radiate impinged. However when the antenna is placed above the three layer body model these currents are naturally altered [73] as shown in Fig. 6.11(b). This variation in the current distribution accounts for the observed variations in resonance frequency and bandwidth. For clarity in Fig. 6.11(b) the body is shown as a three layer model comprising of skin (pink), fat (yellow) and muscle (brown).

Continuing with the effects of the body in practical situations the spacing between the antenna and body tissue is highly variable due to the wide range of movements made by the wearer and the intrinsic separation offered by various forms of clothing attire [137]. Therefore simulations were performed where the spacing between the antenna and body tissue was varied between 1 and 10 mm. The simulation results shown in Fig. 6.12 reveal that at 10 mm the operating bandwidth is mildly shifted.

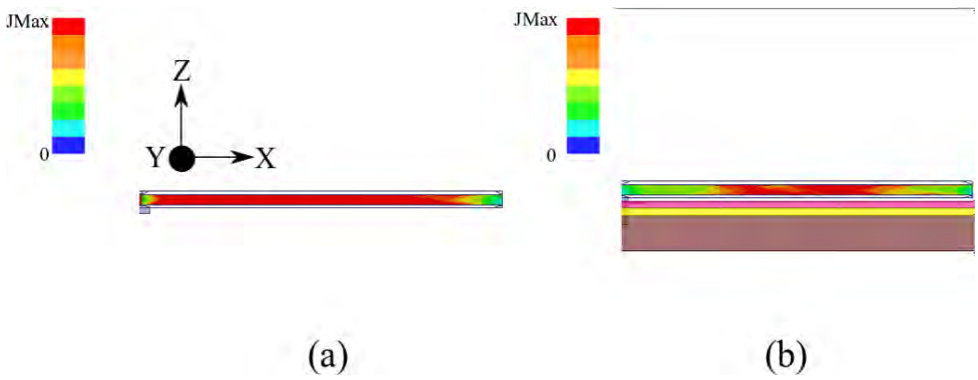

Figure 6.11. Magnitude of the currents along the cavity length in (a) free-space and (b) on-body.

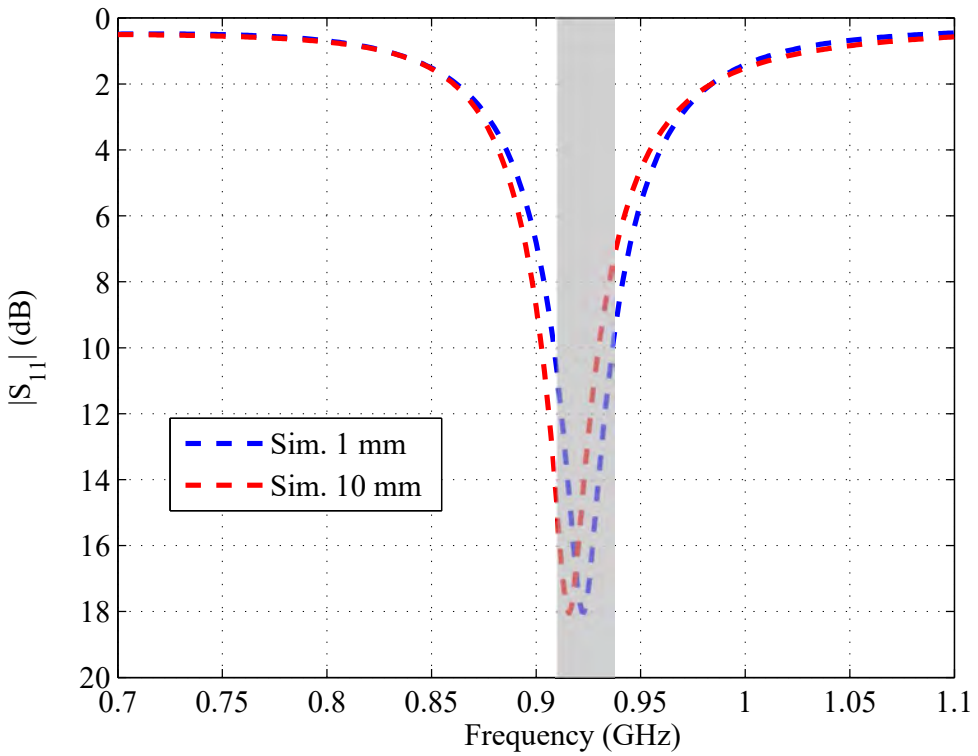

Figure 6.12. Simulated reflection coefficient when in proximity to human body tissue.

Till now the focus of the effects of the body on the antenna have been constrained to the near-field characteristics such as the operating frequency and bandwidth. The effects of the human body can also affect the far-field characteristics such as the gain [53]. Specifically the body can absorb some of the energy radiated from the antenna which results in a reduced gain. This is shown in the first and third row of Tab. 6.1 which shows the variation in the broadside gain when the antenna is in free-space and when separated from the body tissue by 1 mm. Clearly it is observed that when the antenna is placed above the human body the peak gain reduces by 0.5 dB. This effect can be

G_{EXT} (mm)	Peak realized gain (dBi)	Operation condition
0	2.5	Free-space
10	3.0	Free-space
0	2.0	On-body
10	2.5	On-body
20	2.4	On-body
30	2.3	On-body

Table 6.1. Simulated peak realized gain variations as a function of ground plane extension G_{EXT} under various conditions.

mitigated by extending the ground plane by a certain distance along the open aperture [138]. This ground plane extension is denoted as G_{EXT} in Fig. 6.4. To determine the optimum dimension for this extension a numerical investigation into the variation of the broadside realized gain as function of G_{EXT} was undertaken and the results are shown in Tab. 6.1. The results demonstrate that with a mild increase in the ground plane dimensions of 10 mm the peak realized gain can be substantially enhanced by 0.5 dB. Beyond this the peak gain starts to slightly *decrease* which is attributed to increased ohmic losses of the ground plane. Additionally it is noted that with the ground plane extension the free-space gain increases by 0.5 dB.

6.5 Manufacture

The multi-step fabrication procedure is as detailed below:

1. Cut out 1.6 mm and 3.2 mm thick foam pieces to total antenna dimensions.

2. Cut out three pieces of silver fabric to total antenna dimensions.

3. Iron two pieces of fabric onto either side of the thinner piece of foam and the remaining fabric piece onto one side of the thicker piece of foam. By ironing the fabric onto the foam a small recess is made into the foam into which the fabric settles into. This approach helps to raise the radiation efficiency which is presumed to happen through three mechanisms: 1) by melting of a thin layer of plastic off the fabric, 2) by making the structure more homogeneous at the microscopic level and 3) by removing the need for glue between the fabric and

foam. The combination of these effects leads to improvements in the conductivity of the silver fabric across the frequencies of interest.

4. Laser etch out radiating slot and middle layer on opposite sides of the thinner piece of foam as shown in Fig. 6.13(a) and Fig. 6.13(b).

5. Laser etch out ground plane on one side of 3.2 mm thick foam piece.

6. Adhere both pieces of foam using fabric glue.

7. Prepare embroidery frame with embroidery fabric.

8. Adhere complete antenna structure to embroidery fabric using fabric glue.

9. Perform computerized embroidery to realize cavity walls *without conductive threads*. This was done to remove any solidified glue along the cavity dimensions to prevent the conductive threads from being coated in glue which improves the radiation efficiency.

10. Perform computerized embroidery to realize cavity walls using Elitex Skin Contact 235 threads. Repeat the embroidery four times over to realize a dense cavity wall.

11. Adhere the body of the SMA connector to the bottom ground plane through conductive epoxy and push the inner pin of SMA through the substrates such that it passes through the hole made in the stripline and reaches the top layer as shown by the dotted red circle in Fig. 6.13(a). By accessing the interface between the inner pin and the stripline through the circular cut made in the top ground plane as shown in the inset of Fig. 6.13(a) apply conductive epoxy between the inner pin of the SMA and the stripline.

12. Add non-conductive epoxy between the SMA connector and ground plane for extra mechanical strength.

6.6 Experimental validation

The simulated and measured free-space reflection coefficient is shown in Fig. 6.14 where two measurement cases are shown. Test one shows a single band response whilst test

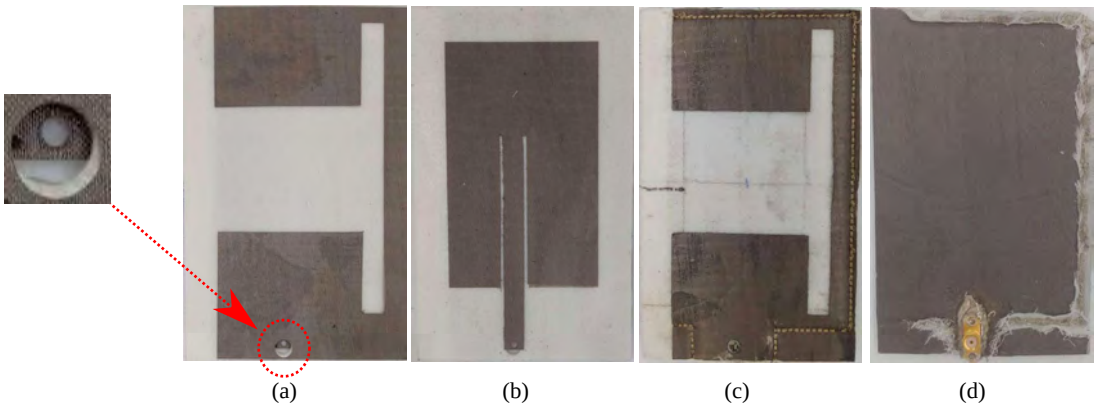

Figure 6.13. From left to right: (a) Top ground plane with radiating slot on 1.6 mm thick foam, (b) Middle layer on opposite side of 1.6 mm foam, (c) Front view of final antenna, (d) Bottom view of final antenna.

two shows a mild notch. As these results are for the same antenna it is determined that this difference is not a feature of the antenna but rather arise from difficulties in obtaining repeatable measurement conditions such as antenna flatness due to the flexible nature of the antenna. The simulated and measured on-body reflection coefficient is shown in Fig. 6.15 where there is good agreement. Additionally it is noted that there is only a small frequency variation between the free-space and on-body case. This might seem surprising as firstly there is a discrepancy in the free-space case which is not translating to the on-body case and secondly the measured drift between free-space and on-body case is much smaller than simulated. This could be due to a combination of factors ranging from uncertainties in the properties of the body tissue [139,140] to difficulties in getting the antenna flat on the human body tissue. In regards to the latter point the presence of the SMA connector causes the antenna to significantly lift upwards when placed on the body and as previously shown in Fig. 6.12 the performance of antenna is dependent on the separation between the antenna and the body. In that regard the main conclusion from the measured results is that when the antenna is in proximity to human body tissue the effects of the body can be largely mitigated through a suitable thin spacer.

Given the curvature of the human body wearable antennas are expected to be bent [72]. Therefore the effects of bending were also investigated. The measured results for bending across the width are shown in Fig. 6.16 for two bending radii of 40 mm and 60 mm respectively. It is observed that bending across the width has minimal variation which is to be expected as neglecting the currents along the H-arm the currents in the upper and lower half of the top ground plane are in opposing phase as depicted in

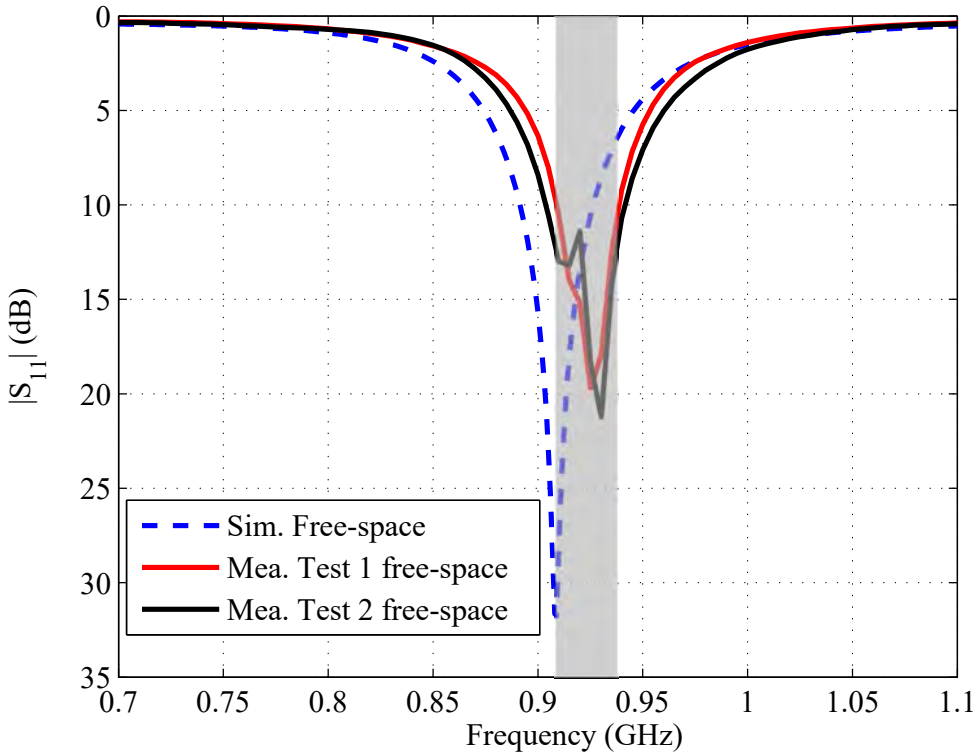

Figure 6.14. Simulated and measured reflection coefficient in free-space.

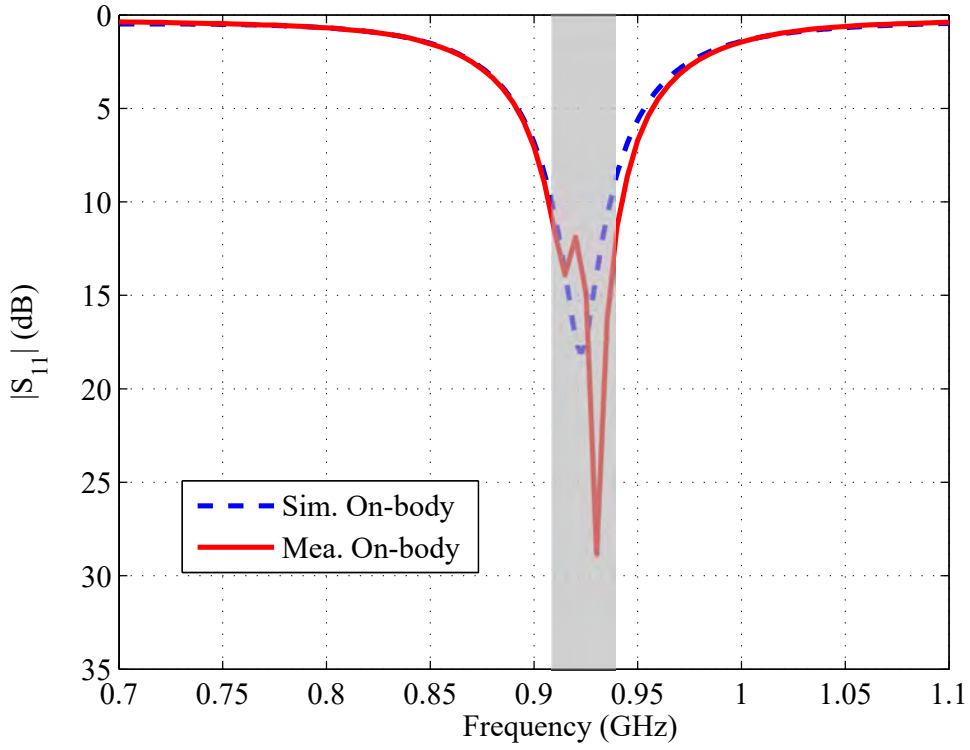

Figure 6.15. Simulated and measured reflection coefficient on-body.

the inset of Fig. 6.16. The measured results for bending across the length are shown in Fig. 6.17 for the same bending radii of 40 mm and 60 mm. From Fig. 6.17 it can be concluded that bending across the length does cause more variation which is to be expected given the significant currents along the H-shaped arms. With the most severe bending across the length corresponding to a radii of 40 mm the reflection coefficient rises to a worst case of -6.0 dB within the band which is still acceptable for wearable applications.

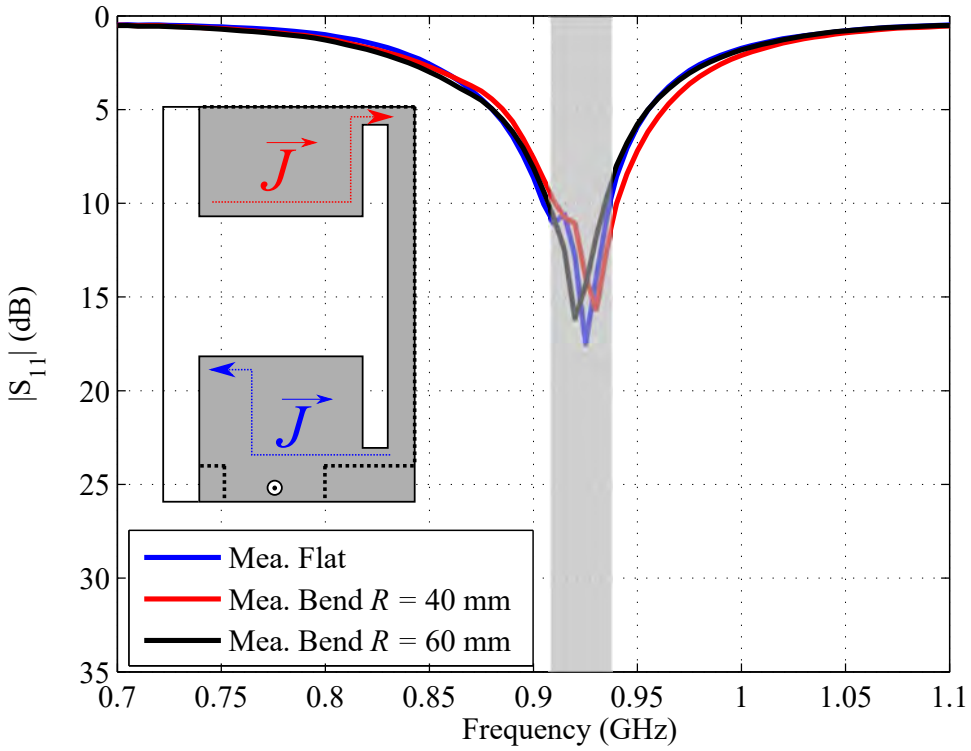

Figure 6.16. Measured reflection coefficient of the antenna when bent along the width. The inset shows the opposing phase of the currents on the top ground plane.

The measured radiation patterns in free-space are shown in Fig. 6.18(a) and Fig. 6.18(b) where there is generally good agreement between the simulated and measured results. Whilst there are some discrepancies in the radiation patterns these are very mild and occur off broadside implying that the discrepancies comes from limitations of the measurement setup such as scattering from the cables. It is also noted that there is increased cross-polarization in both planes which is most likely due to low-frequency limitations of our anechoic chamber as noted in previous studies [45]. Noteworthy is the lack of a null in the ZY plane or equivalently across the width of the antenna. This is a consequence of cutting the cavity in half and therefore reducing the slot length to a half of its original value. It has been observed in previous studies that these operations result

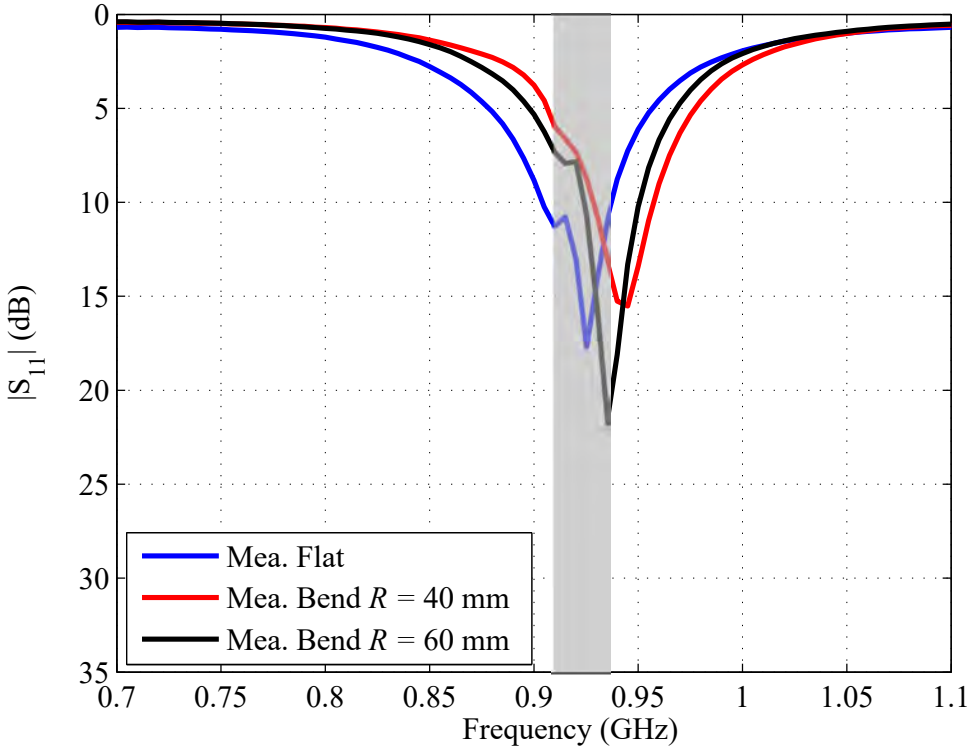

Figure 6.17. Measured reflection coefficient of the antenna when bent along the length.

in a smaller directivity in the plane corresponding to the slot length which leads to the observed patterns [131].

Simulations reveal a peak realized gain occurring at broadside of 2.4 dB whilst measurements display a peak realized gain of 2.6 dB. The simulated radiation efficiency is 78% and the good agreement between simulated and measured gain patterns suggest that the experimental efficiency attained with the manufactured device should be similar.

The radiation patterns were also measured when the antenna was mounted on a human body phantom as shown in Fig. 6.19 where once again there is generally good agreement as shown in Fig. 6.19(c) and Fig. 6.19(d). The observed discrepancies in the shape of the pattern between the simulated and measured radiation patterns on the phantom could be caused by the different phantom shapes and lifting of the antenna above the phantom due to the presence of the coaxial connector as shown in Fig. 6.19.

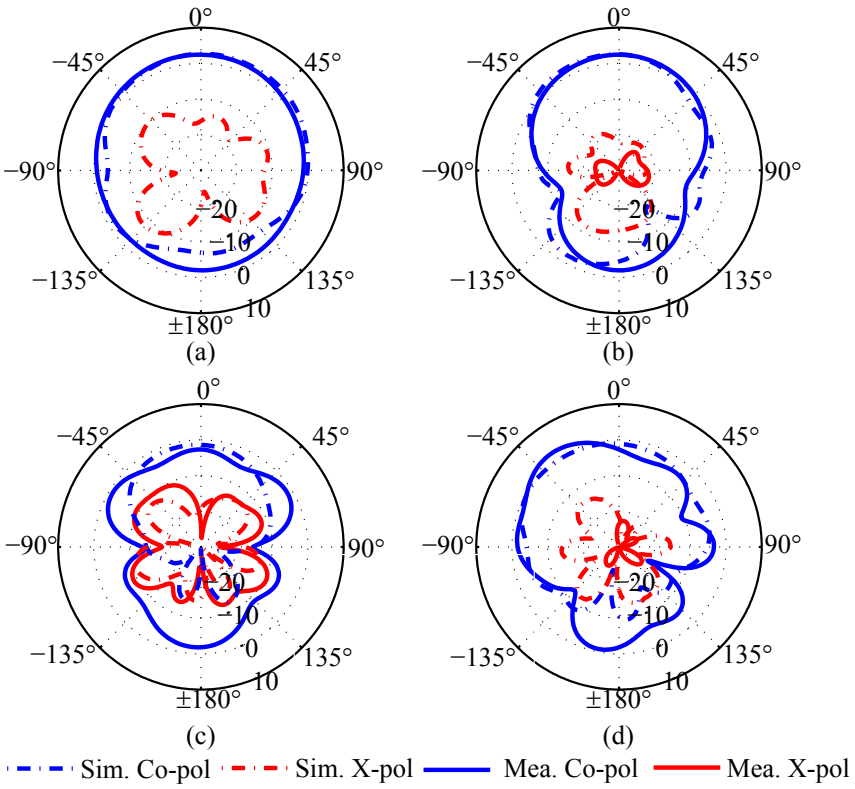

Figure 6.18. Simulated and measured radiation patterns: (a) Free-space patterns in ZY plane at 0.93 GHz, (b) Free-space patterns in ZX plane at 0.93 GHz, (c) On-body patterns in ZY plane at 0.93 GHz, (d) On-body in ZX plane at 0.93 GHz.

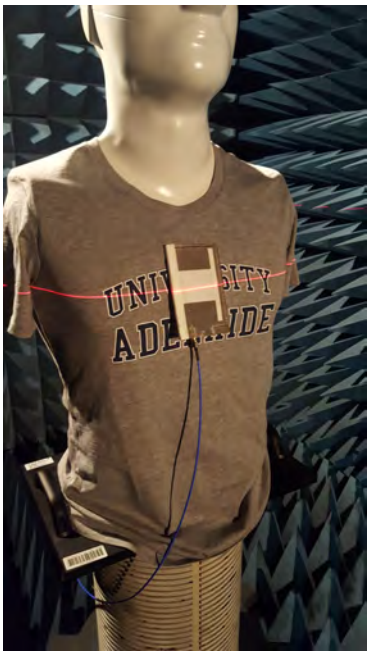

Figure 6.19. Measurement setup for the radiation patterns of the antenna when in close proximity to body tissue which is approximated here by a human body phantom.

6.7 Design variation

In this section a design variation is presented wherein through the introduction of a slot in the middle layer of the cavity the antenna can be miniaturized whilst retaining a similar bandwidth to the previously presented antenna in free-space. Additionally this design variation allows for a fully closed cavity. To appreciate why a slot can be introduced in the middle layer consider Fig. 6.20(a) which shows the magnitude of the Z component of the electric field on the top surface of the middle layer of the antenna after having increased the slot width whilst excluding the step of cutting the cavity in half. It can clearly be seen that there is a null field in the center of the antenna. The current distribution on the middle layer is shown in Fig. 6.20(b) where it can be seen that there is a sizable current distribution in the center of the middle plate.

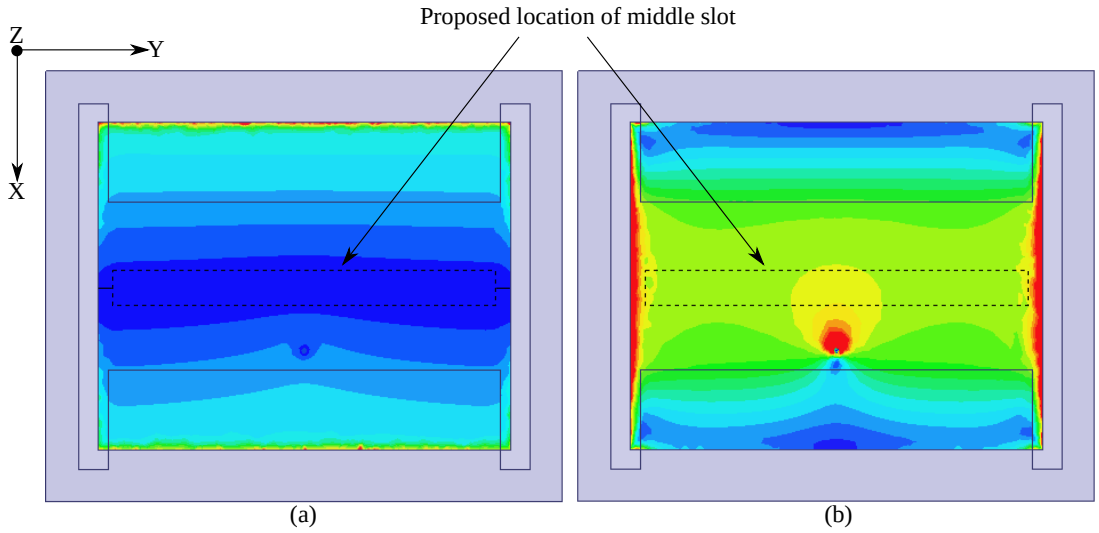

Figure 6.20. (a) A top view of the magnitude of the Z component of the instantaneous electric field on the top surface of the middle plate for the multi-layer cavity-backed slot antenna using a SMA connector as the feeding mechanism and (b) A top view of the current distribution on the middle plate. The black dashed lines denote the position where a slot will be cut onto in the middle layer.

Because of this null field there is no capacitance generated between the center of the middle layer and the top ground plane nor the center of the middle layer and the bottom ground plane. Therefore a slot can be cut in the center of the middle plate without altering the capacitance generated between the middle plate and either ground plane. However the introduction of the slot forces the currents on the middle layer to meander around the slot which increases the current path length within the antenna leading to a reduction in the resonance frequency.

As an empirical guideline as determined from numerical studies it is suggested that the length of the interior slot be 10 - 15 % of the cavity width. The width of the interior slot be 1 mm for fabrication simplicity. From here the length of the interior slot is increased whilst re-optimizing the SMA connector position to retain impedance matching below -10 dB. Once it is not possible to increase the length of the interior slot without degrading the impedance matching above -10 dB the width of the interior slot is increased and once again the SMA connector position is re-optimized until the slot width can no longer be increased without degrading the impedance matching. At the end of this procedure the dimensions of the interior slot should be as large as possible leading to the largest possible reduction in the resonance frequency. Then to scale the frequency backup to the desired frequency the cavity is miniaturized which is achieved by simultaneously reducing the cavity length and width. After having obtained the desired resonance frequency the bandwidth is observed. If the bandwidth is not large enough then the aforementioned procedure of enlarging the interior slot dimensions is performed till the dimensions of the interior slot reach their maximum value whilst retaining impedance matching below -10 dB. Now the width of the slot on the top layer is increased till the desired resonance frequency and bandwidth is obtained. This concludes the design using a coaxial feeding mechanism and the integration of a planar feeding mechanism is the next focus.

In the semi-open cavity of the previous section, the feeding mechanism was an inset fed shielded stripline that was directly connected to the middle layer. In contrast, the present antenna design variation with the middle slot utilizes a coplanar waveguide feeding mechanism which does not directly connect to the middle layer. To illustrate the difference, the middle layers of both the semi-open and fully closed cavity are shown in Fig. 6.21(a) and Fig. 6.21(b) respectively. To facilitate impedance matching of the current antenna the gap between the feedline and the middle layer is tuned. At this stage mild re-optimization of the length and width of the top slot is performed to obtain the desired resonance frequency and bandwidth. This concludes the design incorporating the middle slot.

Based on the above principles the fully-closed cavity antenna can be miniaturized to a cavity size of 70 mm $\times$ 110 mm. The simulated reflection coefficient for the antenna in free-space and on-body are shown in Fig. 6.22. For the free-space case the antenna displays a bandwidth of 3.2%. When the antenna is placed above the body tissue a

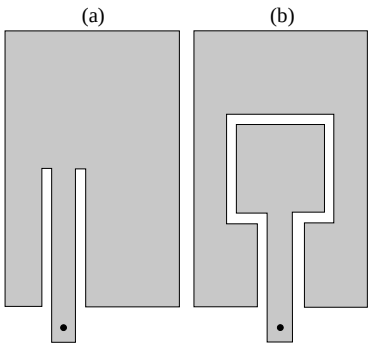

Figure 6.21. The middle layers of both the semi-open (a) and fully closed cavities (b).

slight performance degradation is observed. As before this degradation is attributed to the variation in currents on the side walls of the cavity.

6.8 Conclusion

In this chapter a new antenna geometry based on a combination of design techniques has been presented. This allows the antenna to be miniaturized whilst retaining a sufficient bandwidth and high radiation efficiency. Additionally the antenna was integrated with a textile feeding mechanism making it suitable for integration into wearable systems. A streamlined design process in conjunction with a simple fabrication procedure exploiting the use of a computerized embroidery machine is a salient feature of the proposed geometry. The antenna was evaluated in two main environmental conditions: in free-space and when in close proximity to human body tissue where in both cases the antenna performance was demonstrated to remain robust. Additionally the antenna was shown to be tolerant to typical bending scenarios making it a strong candidate for future on-body communication applications. Good agreement between simulation and measurement results validates the proposed structure. A design variation has also been proposed where the antenna geometry is changed from a semi-open structure to a fully closed structure whilst retaining the same size and comparable bandwidth in free-space.

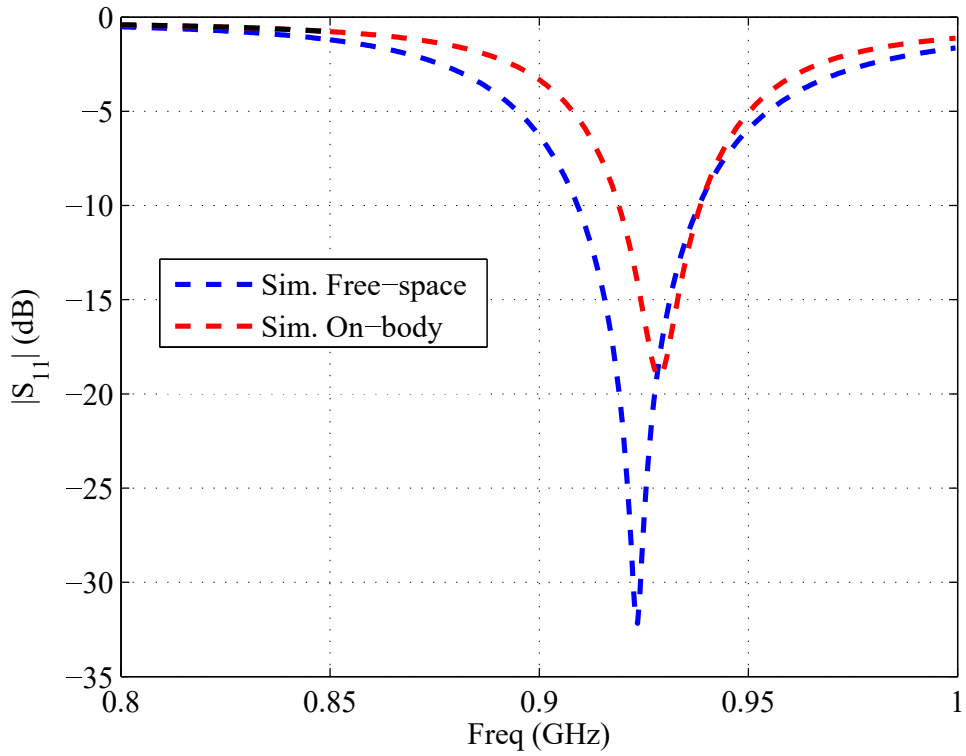

Figure 6.22. Simulated reflection coefficient for the fully-closed cavity antenna with slot in its middle layer under free-space and on-body.

Chapter 7

Dual-band half-mode substrate-integrated cavity

THIS chapter presents a new dual-band cavity-backed slot antenna based on the concept of a half-mode substrate-integrated cavity. The antenna resonates at 2.45 GHz and 5.8 GHz which correspond to the center frequencies of the lower and upper microwave ISM bands. Additionally broadside radiation patterns are obtained at both bands. To enhance wearability the antenna is fully integrated with a textile feeding mechanism making it a strong candidate for future body-worn communications.

7.1 Introduction

There exist an appreciable amount of antenna types suitable for wearable applications such as metamaterial inspired antennas [57, 141, 142], complementary antennas and cavity resonators [21, 143, 144] as will be reviewed in detail later in this section. Therefore the judicious selection of the antenna topology required for a particular wearable application has to be balanced with other requirements such as operation frequency and radiation patterns. For wearable applications it might be desired to have dual-band performance for transmission and reception at the different frequencies from off-body node to an on-body node as shown in Fig.7.1 [54]. Therefore a dual-band antenna with broadside radiation patterns is of interest. To address this requirement several dual-band wearable designs have been presented in the literature.

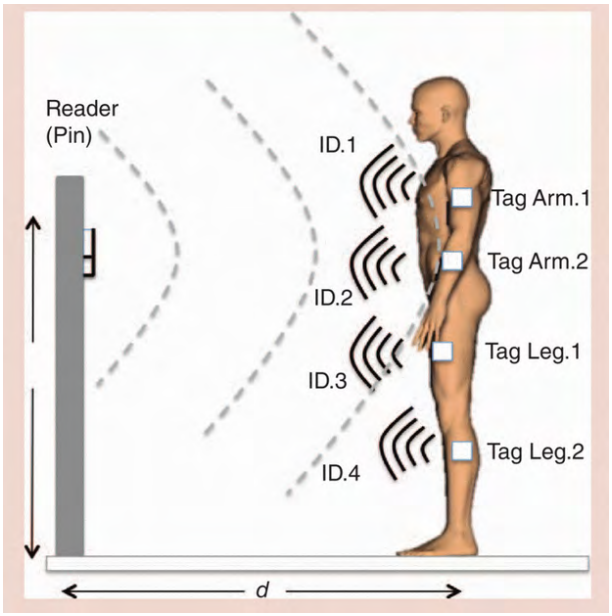

Figure 7.1. A typical wearable antenna application scenario where a number of antennas on-body communicate with an off-body node as reproduced from [54].

A metamaterial-inspired dual-band antenna was proposed in [55] and is shown in Fig. 7.2. The antenna was based on a composite right/left-hand transmission line (CRLH-TL) structure. The CRLH-TL topology was chosen as it can support negative and positive order modes with identical field distributions allowing for identical radiation patterns at two distinct frequencies. This design exploited this unique property to realize a heavily miniaturized dual-band antenna operating at 2.4 GHz and 5.4 GHz

corresponding to the n = -1 and n = +1 modes respectively. Whilst the antenna has certain advantages such as a simple fabrication and design procedure the heavily miniaturized nature of the antenna resulted in a structure which displayed a low radiation efficiency at the lower frequency band. Additionally the obtained bandwidth at the lower operating range was inadequate to fully cover the lower microwave ISM band (2.4 - 2.5 GHz).

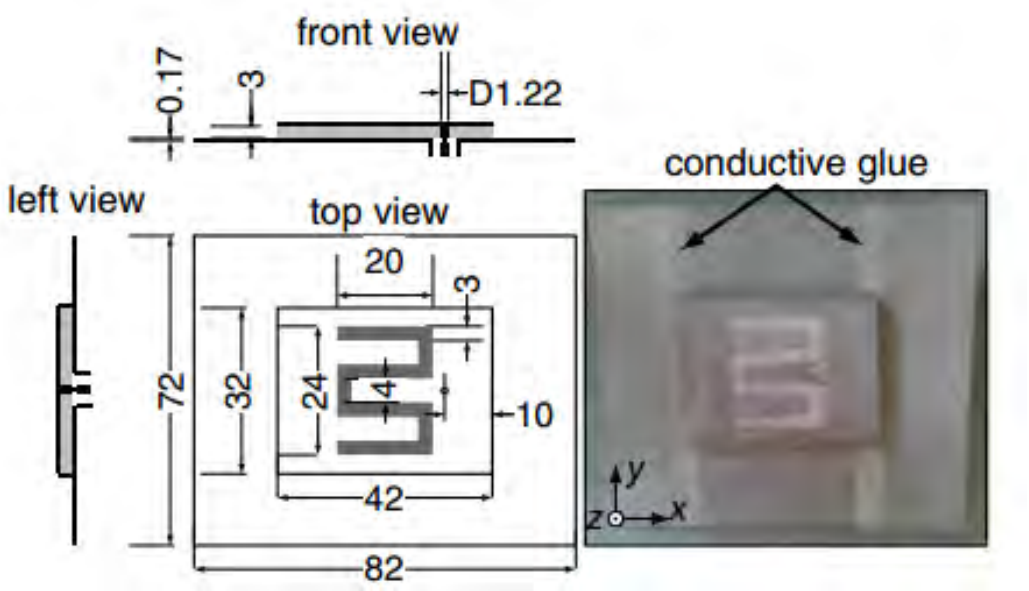

Figure 7.2. A heavily miniaturized dual-band antenna based on the composite right-hand/left-hand transmission line (CRLH-TL) as reproduced from [55].

A specific periodic structure known as a high impedance surface (HIS) was utilized as a ground plane for a dual-band coplanar patch antenna operating at 2.45 GHz and 5.8 GHz as shown in Fig. 7.3. As a coplanar patch antenna lacks a ground plane the HIS was used to isolate the antenna from the body. Whilst the introduction of the HIS made the antenna very insensitive to the effects of the human body this came at the cost of large planar dimensions which were nearly a full wavelength at the lower frequency of operation. Additionally the presence of the HIS raised further design challenges. Designing a dual-band HIS with a sufficiently large bandwidth to fully cover the lower and upper bands was claimed as a difficult task by the authors [56].

Recently complementary antennas which consist of crossed electric and magnetic dipoles, have attracted increasing attention as they can be made wideband with stable radiation patterns [145–148]. A wearable realization of a dual-band complimentary antenna was presented in [57] and is shown in Fig. 7.4. Whilst the antenna displayed dual-band

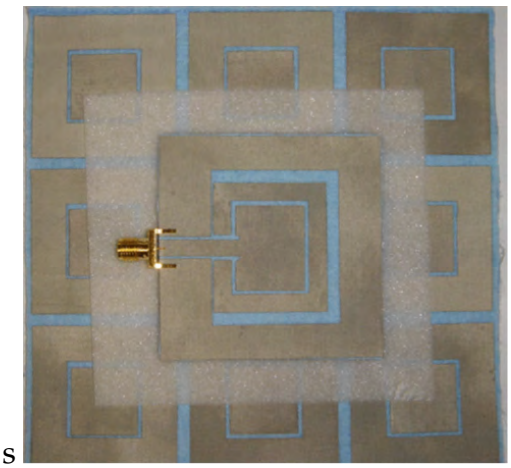

Figure 7.3. A dual-band coplanar patch antenna with a high impedance surface ground plane for isolation from the body as reproduced from [56].

performance with stable radiation patterns the fabrication was delicate and more involved than would be desirable for wearable antennas. Furthermore it was found that due to limitations of the fabrication procedure the measured reflection coefficient reached -7.5 dB at the lower frequency band. This implies that small non-idealities in the fabrication had a significant influence on the performance of the antenna.

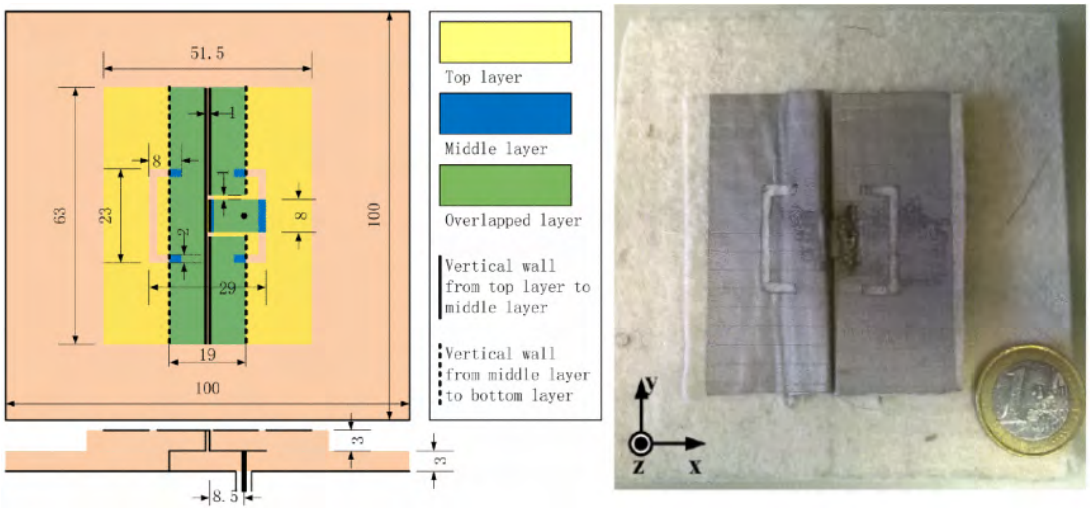

Figure 7.4. A dual-band textile complementary antenna as reproduced from [57].

A notable dual-band antenna inspired by the half-mode substrate-integrated cavity (HMSIC) was presented in [58] and is shown in Fig. 7.5. Half-mode substrate-integrated structures have attracted increasing attention in both PCB and wearable technology due to a simple fabrication performance, low loss, high radiation performance and

compact size [24, 149, 150]. Whilst the antenna presented in [58] certainly had attractive properties such as high radiation efficiency, simple fabrication procedure, good immunity to dielectric loading by the body and robust performance under bending there were certain limitations. To obtain two radiation bands the fundamental and higher order mode of the cavity were used. This naturally makes the independent control of both frequency bands cumbersome. Additionally the antenna was fed using a SMA connector which whilst elegant for testing purposes is not practically suitable for interfacing with electronic circuits [24].

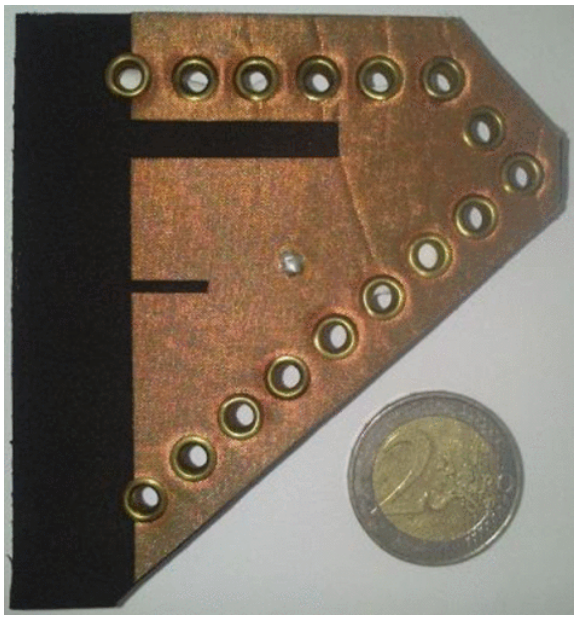

Figure 7.5. A dual-band textile antenna based on half-mode substrate-integrated cavity (HMSIC) as reproduced from [58].

From the preceding discussion it can be concluded that whilst there have been a variety of wearable dual-band antennas presented in the literature these have all displayed limitations either in terms of performance, large physical area as in the case of the HIS ground plane, difficult fabrication procedure or have used feeding mechanisms not amenable for wearable applications. Therefore this chapter presents a new dual-band antenna based on the concept of a half-mode substrate-integrated cavity (HMSIC). The antenna is fully integrated with a textile feeding mechanism and the utilization of a computerized embroidery machine to realize the cavity walls is a salient feature of the antenna. Performance-wise the antenna displays good immunity to the effects of the human body and is robust to bending. Additionally the antenna features a high radiation efficiency with broadside radiation patterns at both bands.

7.2 Geometry Overview

As the proposed antenna is based on a half-mode substrate-integrated cavity, an understanding of the HMSIC is required and herein presented. A substrate-integrated cavity (SIC) which is operated in the fundamental TE_{10} mode has a magnetic wall boundary condition in the center as shown in Fig. 7.6. The magnetic wall boundary condition allows the SIC to be cut in half whilst retaining the performance characteristics of the SIC [24]. As the cut structure is half the size of the uncut structure it earns the name half-mode substrate-integrated cavity. An example of a textile half-mode substrate-integrated cavity is shown in Fig. 7.7.

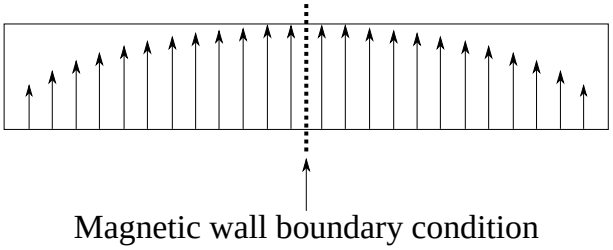

Figure 7.6. Electric field distribution of a substrate-integrated cavity when operated in the fundamental TE_{10} mode.

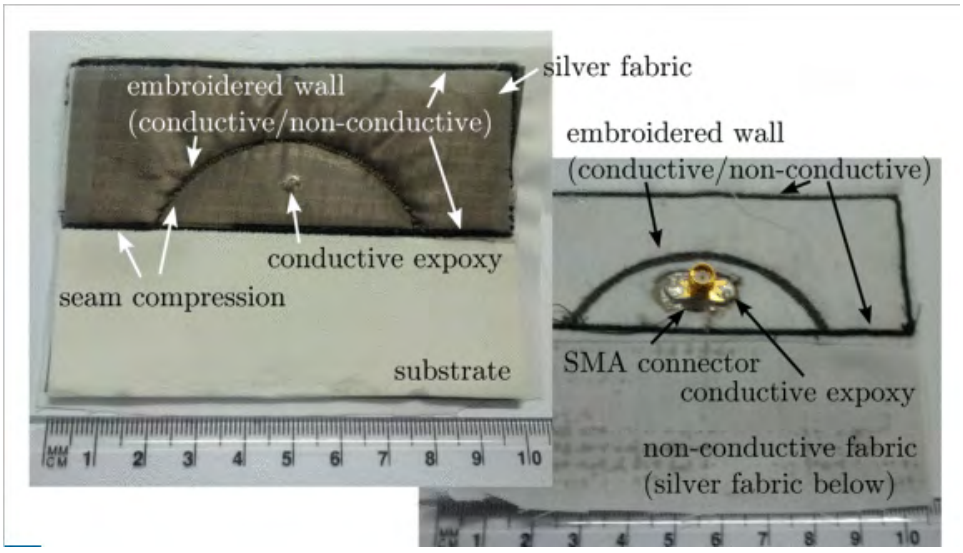

Figure 7.7. A textile HMSIC antenna as reproduced from [24]

A schematic of the proposed antenna is shown in Fig. 7.8 where it is seen that the antenna is a multi-layer structure where the top layer is a ground plane with a slot, the middle layer contains the feeding element and the bottom layer is an additional ground plane which is short circuited to the top ground plane. The cavity walls are

realized through computerized embroidery. A major contribution of this work is that the shielded stripline is able to simultaneously excite the cavity and slot modes which have different field distributions and correspond to two different frequencies. These frequencies are 2.45 GHz and 5.8 GHz which correspond to the center frequencies of the lower and upper microwave ISM bands [84].

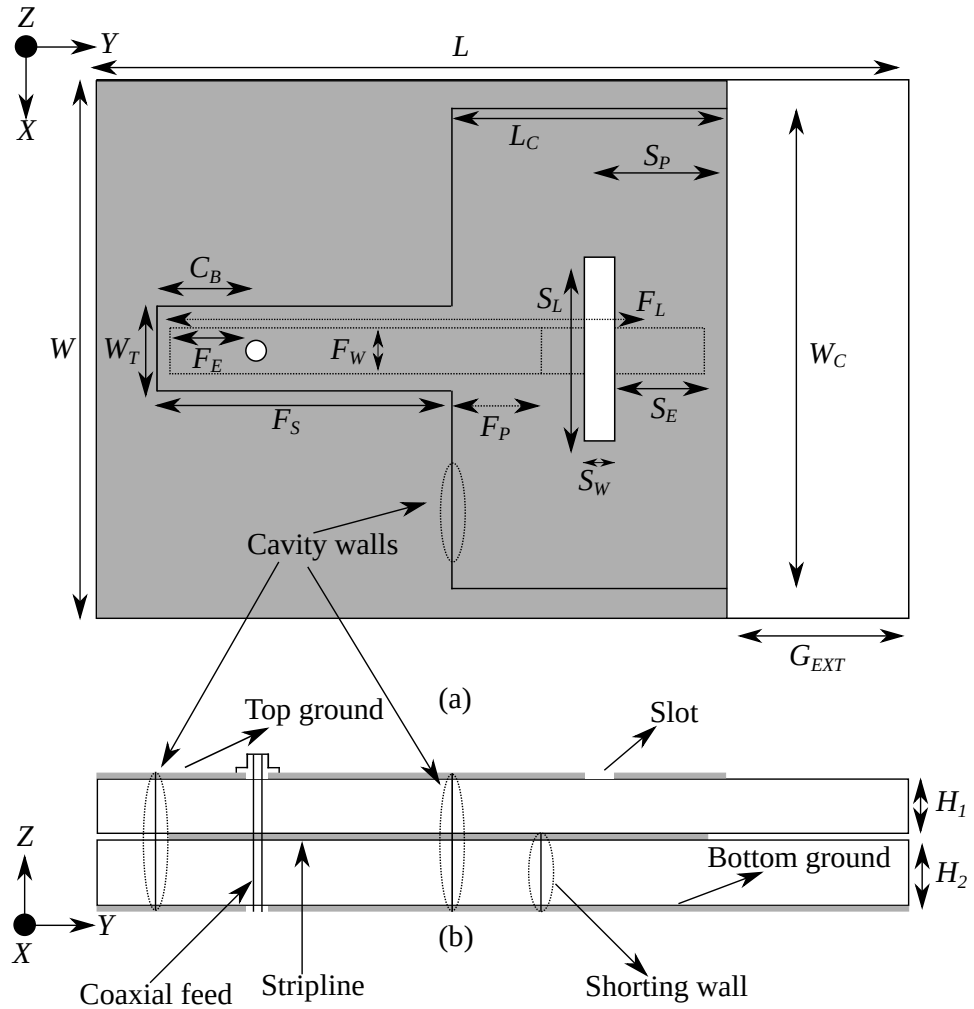

Figure 7.8. Schematic of the proposed geometry: (a) Top view, (b) Side view. The optimized parameters are $G_{EXT} = 30.5$ mm, $C_B = 4$ mm, $F_E = 2$ mm, $W_T = 12$ mm, $F_S = 20$ mm, $W_C = 81.5$ mm, $L_C = 35.5$ mm, $F_P = 9$ mm, $F_L = 40$ mm, $F_W = 6$ mm, $S_W = 1$ mm, $S_E = 5.2$ mm, $S_P = 18$ mm, $H_1 = 1.6$ mm, $H_2 = 3.2$ mm, $W = 100$ mm, $L = 95$ mm, $S_L = 18$ mm.

At both bands the radiation occurs through an effective magnetic dipole. At the lower frequency band the half-mode cavity is excited which results in an electric field along the open aperture of the HMSIC as shown by the dashed red lines in Fig. 7.9. From the field equivalence principle it can be shown that the aperture field produces an effective radiating magnetic dipole. The same field equivalence principle also applies

to understand the radiation mechanism at the higher frequency. By cutting a suitably dimensioned slot into the top metalization layer the ground currents are altered. This alteration creates an electric field across the slot which is equivalent to a radiating magnetic dipole.

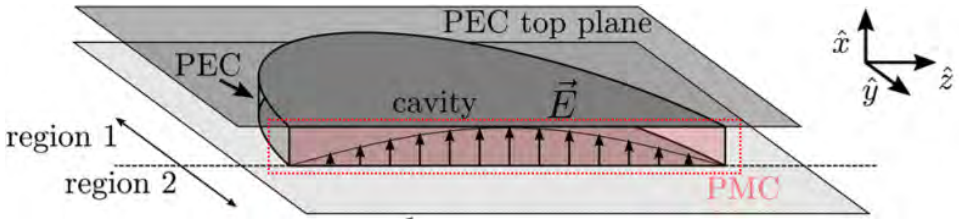

Figure 7.9. A depiction of the electric field developed along the HMSIC aperture. This image is adapted from [24]

7.3 Design

The design starts by dimensioning the cavity to resonate at the lower operating frequency. The planar dimensions of the cavity should be approximately $0.5\lambda_G \times 0.25\lambda_G$ where λ_G is the guide wavelength which can be calculated per the procedure in [123]. After determining the planar dimensions of the cavity the next step is to determine the total ground plane dimensions to suitably isolate the antenna from the human body. As per the suggestion in [134] the total planar ground plane dimensions are set at 100 mm $\times$ 100 mm. Half of the total ground plane is used to accommodate the cavity structure and from here the dimension of the ground plane extension G_{EXT} as shown in Fig. 7.8 can be analytically determined.

After having determined the planar dimensions of the cavity the next step is to decide on the materials used for the antenna. To realize a flexible antenna the utilized substrate is Cumming Microwave PF-4 foam. The foam has a relative permittivity of 1.06 and a loss tangent of 0.0001. In the initial stages the thickness of the cavity is set at 1.6 mm which is the minimum thickness of the foam material. Later the thickness will be altered to meet the desired bandwidth. The planar metalization layers are made from MarkTeX silver fabric and the embroidered cavity walls are made from Statex Shieldex 117/12 2PLY. For now all the metalized materials can be modeled as perfect electric conductors. As in the previous chapter when adapting the design for wearable considerations the metalized layers will be modeled as lossy metallic sheets.

At this stage the cavity can be excited through an SMA connector which is centered with respect to the width of the cavity as shown in Fig. 7.10. The inner pin of the SMA connector is protruded through the cavity and is short circuited to the top ground plane. To obtain impedance matching the position of the SMA connector is varied across the length of the cavity. Once the antenna is adequately excited the resonance frequency is observed. If the resonance frequency is not as desired then the dimensions of the cavity are mildly re-optimized. After having obtained the desired frequency the focus is shifted to the bandwidth.

It is well known that the bandwidth of cavity structures is highly dependent on the cavity thickness where a thicker cavity leads to a larger bandwidth [73]. Thus to cover the lower ISM band (100 MHz bandwidth) the thickness of the HMSIC is gradually increased whilst re-optimizing the SMA connector position till the desired bandwidth was obtained. Numerically it was determined that a thickness of 4.8 mm is needed to cover the lower ISM band. Practically this thickness can be achieved by combining a 1.6 and 3.2 mm thick foam pieces. The simulated reflection coefficient for the antenna at this stage is shown in Fig. 7.11 where the inset shows the fundamental half TE_{10} mode of the cavity.

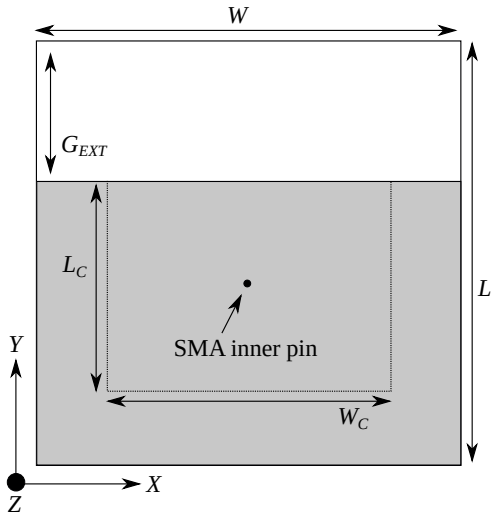

Figure 7.10. A depiction of how the half-mode cavity can be excited through an SMA connector. The black dot represents the position where the inner pin of SMA connector making electrical contact with the top ground plane.

After impedance matching is obtained for the cavity mode at the lower frequency with the desired bandwidth the focus shifts to the generation of the higher frequency. In that regard a slot is added on the top metal ground layer of the cavity to create the higher-frequency band resonant radiating mode. At this stage the antenna should like

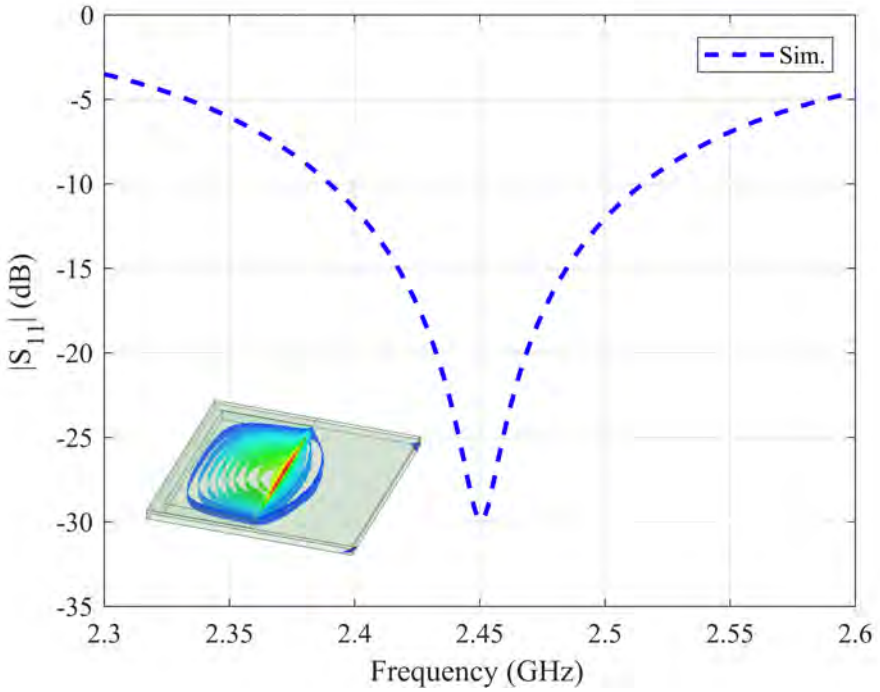

Figure 7.11. Simulated reflection coefficient of the HMSIC structure operating at the fundamental TE_{10} mode as shown in the inset.

Fig. 7.12. To begin with this slot can be centered with respect to the cavity length. Later the position of the slot can be optimized. The length of the slot has initial dimensions of $0.5\lambda_G$ where λ_G is the guide wavelength at 5.8 GHz which comes to approximately 35 mm. The width is kept at 1 mm which represents the minimum dimension that can be precisely cut out from metalized textile material. It is noted that even if the length of the slot is $0.5\lambda_G$ the generated higher frequency will be less than 5.8 GHz. The reason for this lower than desired frequency is due to the planar dimensions of the cavity.

Whilst the half-mode cavity is designed to operate at the lower resonance frequency it does also have electromagnetic importance at the higher frequency. This can be appreciated by considering the hypothetical scenario of a slot on an infinite ground plane. A slot on an infinite ground plane displays bi-directional radiation which is undesired for wearable applications as this case represents power radiated into the body [151]. A well-known solution to this issue is to add a cavity behind the slot to make the radiation uni-directional resulting in what is known as a cavity-backed slot [21]. In this sense the half-mode substrate-integrated cavity serves two purposes: to resonate at the lower frequency and to act as a backing cavity for the slot at the higher frequency. Usually for cavity-backed slots the resonance frequency is jointly determined by the cavity

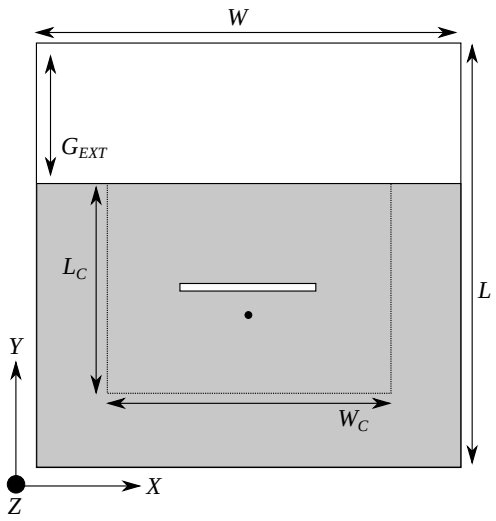

Figure 7.12. A depiction of how the half-mode cavity is modified by incorporating a slot on the top layer to generate another resonance at 5.8 GHz.

and slot dimensions where the cavity dimensions are approximately $0.5\lambda_G \times 0.5\lambda_G$ where λ_G is the guide wavelength at the desired operation frequency. For the current antenna the cavity is designed to operate at 2.45 GHz. This means at the higher frequency the cavity is much larger than needed resulting in a resonance frequency of the combined cavity-backed slot structure lower than 5.8 GHz as shown in Fig. 7.13. The inset labeled (1) in Fig. 7.13 shows the electric field distribution within the cavity at the slot frequency. From the inset it can be seen that there also appears to be some excitation of the HMSIC aperture suggesting that the higher-order mode of the cavity is also being excited. The excitation of the higher-order mode of the cavity is more pronounced in the inset labeled (2). To obtain the desired higher frequency the length of the slot should be parametrically optimized.

As previously mentioned the position of the slot on the top ground plane can also be optimized. The parameter of interest in this case is S_P as shown in Fig. 7.8 which represents the position of the slot as measured from the HMSIC aperture. This parameter controls the amount of mutual coupling between the magnetic dipole at the cavity aperture and the magnetic dipole from the slot. As S_P gets smaller there is more interaction between the two magnetic dipoles resulting in a larger bandwidth and as S_P gets larger there is less interaction between the magnetic dipole from the slot and the HMSIC aperture.

With the nominal design using a SMA connector completed the next focus is on the integration of a planar feeding structure. Whilst there are numerous planar feeding

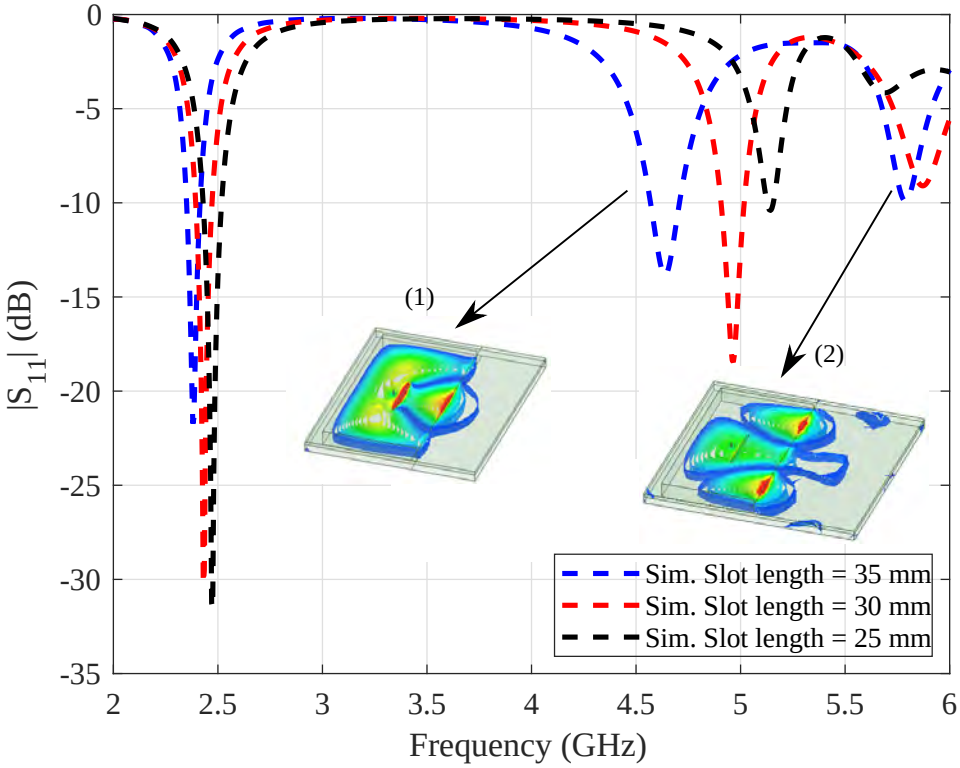

Figure 7.13. Simulated reflection coefficient of the HMSIC structure with a slot incorporated on the top ground plane. The inset shows the slot mode and the higher order mode of the cavity.

transmission lines available such as microstripline, stripline and grounded coplanar waveguide, it is desirable to have a feeding mechanism that has minimal interaction with the radiating elements and adequately utilizes the layered topology.

Given that the half-mode cavity antenna design possess two short circuited ground planes a perpendicularly fed textile shielded stripline [86] is a natural choice. As the stripline is a closed structure and since it can be removed from the radiating apertures, it is expected that it will have minimal impact on the radiation performance [55]. Additionally the shielded stripline does not result in an increase in the antenna thickness and can easily be designed to have excellent transmission characteristics over a wide bandwidth. For example Fig. 7.14 and Fig. 7.15 shows the reflection and transmission coefficient of a back-to-back shielded stripline with a length of 100 mm. This length was chosen as it represents the overall size of the antenna. It can be seen that there is excellent wideband impedance matching below -15dB from 2 to 6 GHz and a transmission coefficient below -0.5 dB from 2 - 6 GHz. The geometry of the shielded stripline is shown as an inset in Fig. 7.14. For the sake of clarity only two shielding walls are shown but as previously mentioned the whole structure is fully closed.

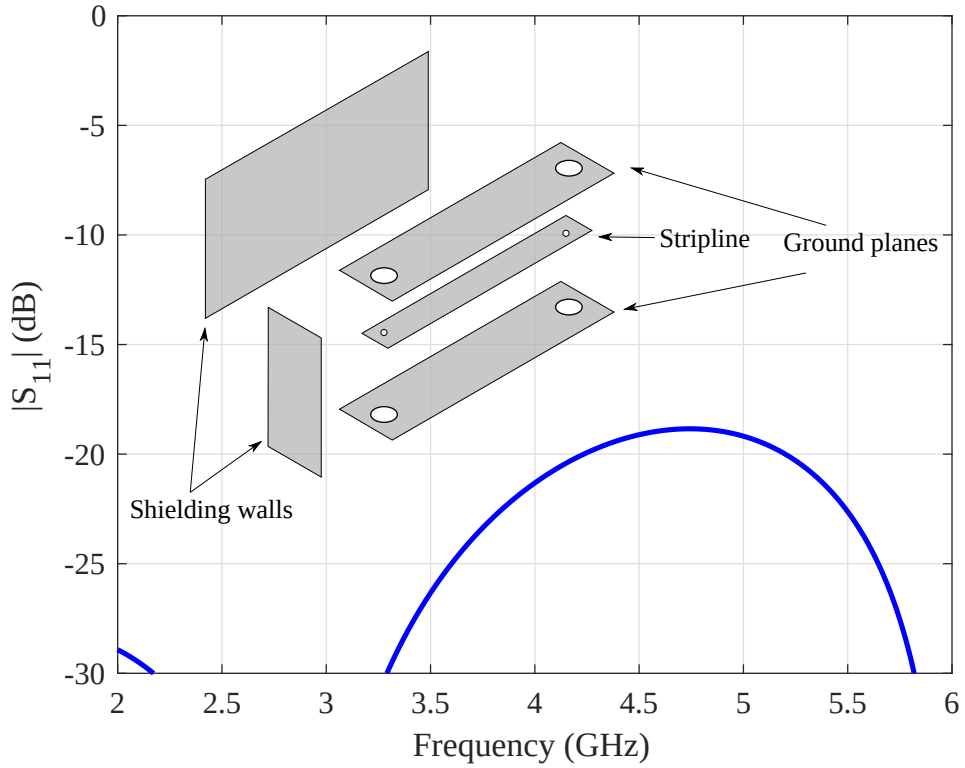

Figure 7.14. Simulated reflection coefficient of the shielded stripline for a length of 100 mm.

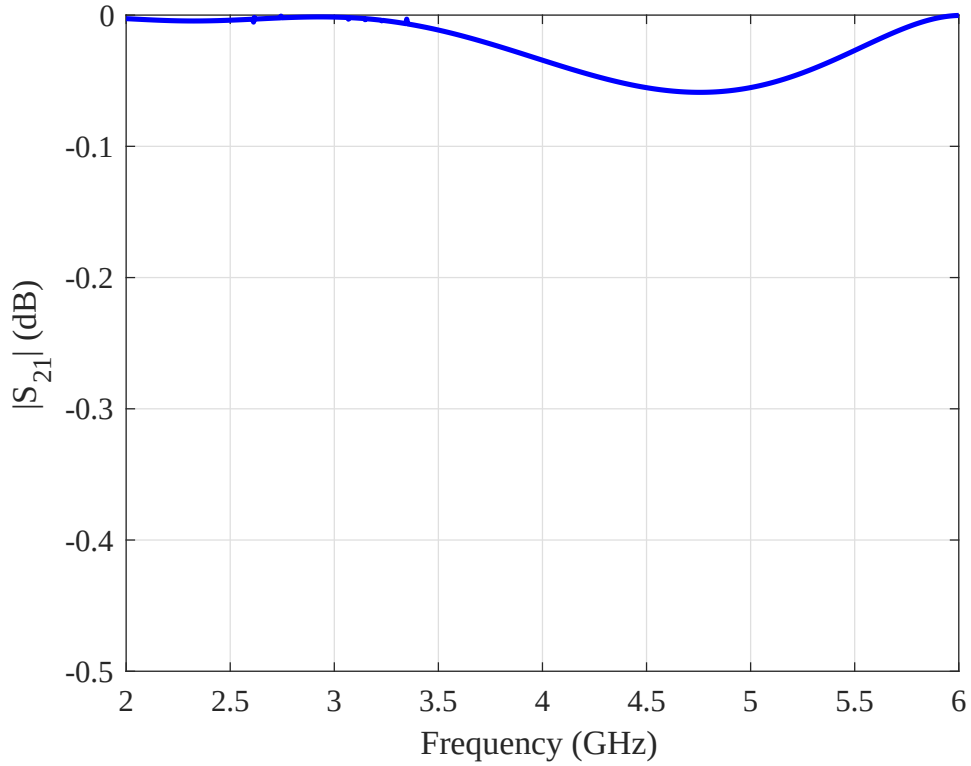

Figure 7.15. Simulated transmission coefficient of the shielded stripline for a length of 100 mm.

To accommodate the stripline the cavity structure is modified according to the procedure described in chapter 6 section 6.3. The stripline is itself modeled as a metallic strip of a certain width that is in between the 1.6 and 3.2 mm thick foam. The width of the stripline is numerically determined for a 50 Ω characteristic impedance.

Whilst the impedance matching of the antenna with a SMA connector is straight forward the integration of a planar feeding mechanism raises a challenge. As the cavity operates in the fundamental TE_{10} mode the stripline needs to excite this mode. However the stripline nominally operates in a transverse electromagnetic (TEM) mode. Therefore a suitable transition from a TEM mode to TE_{10} mode is required. As a shielded stripline can be thought of as a flat coaxial line the techniques available for excitation of cavity resonators through coaxial lines can provide inspiration. One well known method of exciting a cavity from a coaxial line is by short circuiting the inner pin of the coax to the interior walls of the cavity. The currents which are short circuited establish a magnetic field which in turn generates the fundamental TE_{10} mode [152, 153]. In the present realization this is achieved by short circuiting the stripline to the bottom ground plane as shown in Fig. 7.16

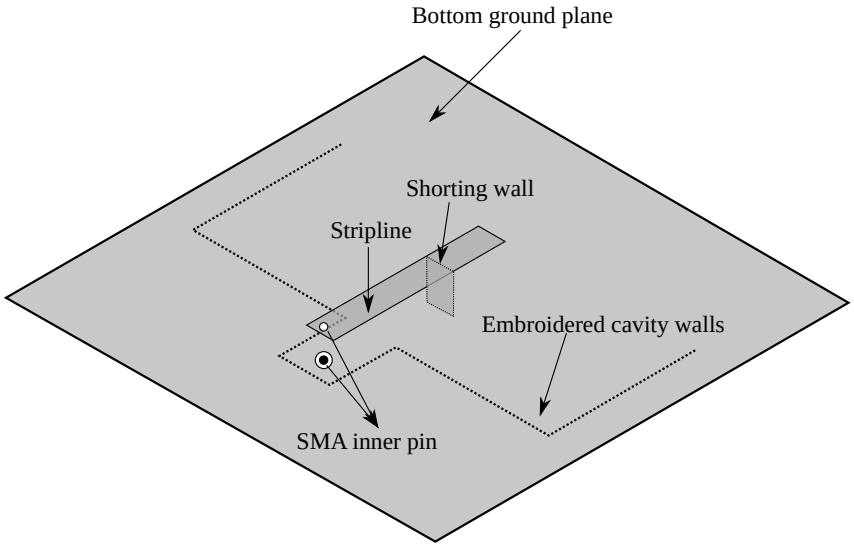

Figure 7.16. A depiction of how the stripline is short circuited to the bottom ground plane to excite the fundamental TE_{10} mode.

The position of the shorting wall within the cavity denoted as F_P in Fig. 7.8(a) is the parameter which determines the impedance matching at the lower band. The electric field distribution in the cavity with the shorted stripline is shown in Fig. 7.17(a) where it is clearly seen that half of the fundamental TE_{10} mode is excited. The next stage in impedance matching using a planar feed is the excitation of the slot. The slot excitation

is achieved by varying the termination of the feedline with a stub extending beyond the slot till a 50 Ω impedance match is obtained. The length of the stub beyond the slot is denoted as S_E in Fig. 7.8(a). When the slot is properly excited an electric field distribution similar to Fig. 7.17(b) is observed. In this figure it can be seen that in addition to the slot there is also additional radiation from the HMSIC aperture. This additional radiation from the HMSIC aperture may be due to the simultaneous excitation of the higher order mode of the cavity. This brings to a conclusion the second phase of the design which has focused on the generation of a dual-band antenna integrated with a planar feeding mechanism. The next phase of the design process considers the effects of textile materials, fabrication processes and the intended application: body-worn communications.

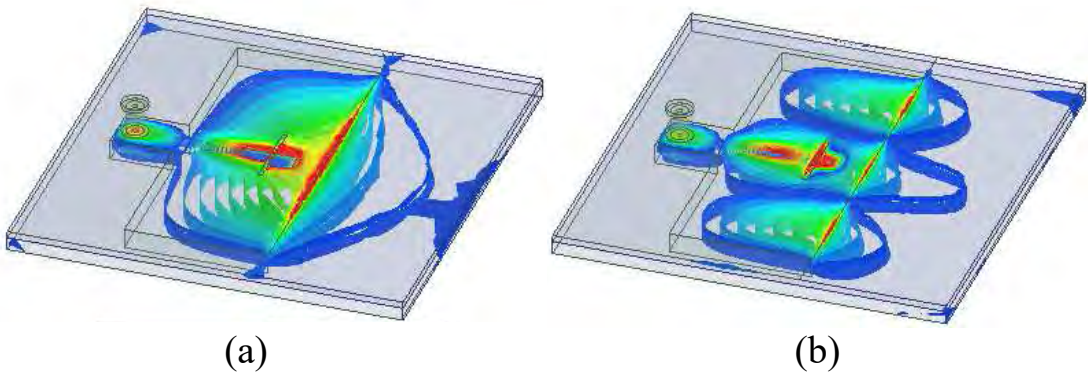

Figure 7.17. Simulated electric field distribution from left to right: (a) 2.45 GHz, (b) 5.8 GHz.

7.4 Design Adaptation for Wearable Considerations

In the previous Chapter it has been shown that wearable antennas which exploit computerized embroidery are subject to seam compression effects which must be accounted for in the design phase. This is done by modeling the approximate geometry of the seam compression and re-optimizing the dimensions of the antenna to obtain the right resonance frequencies. The next consideration in adapting the design for wearable applications pertains to the non-ideal conductivity of the materials used to realize the metal layers. In accordance with the procedure described in chapter 6 section 6.4 a frequency dependent sheet resistance for the silver fabric and embroidered walls is determined. The variation of the sheet resistance for the silver fabric and embroidered walls as a function of frequency is shown in Fig. 7.18.

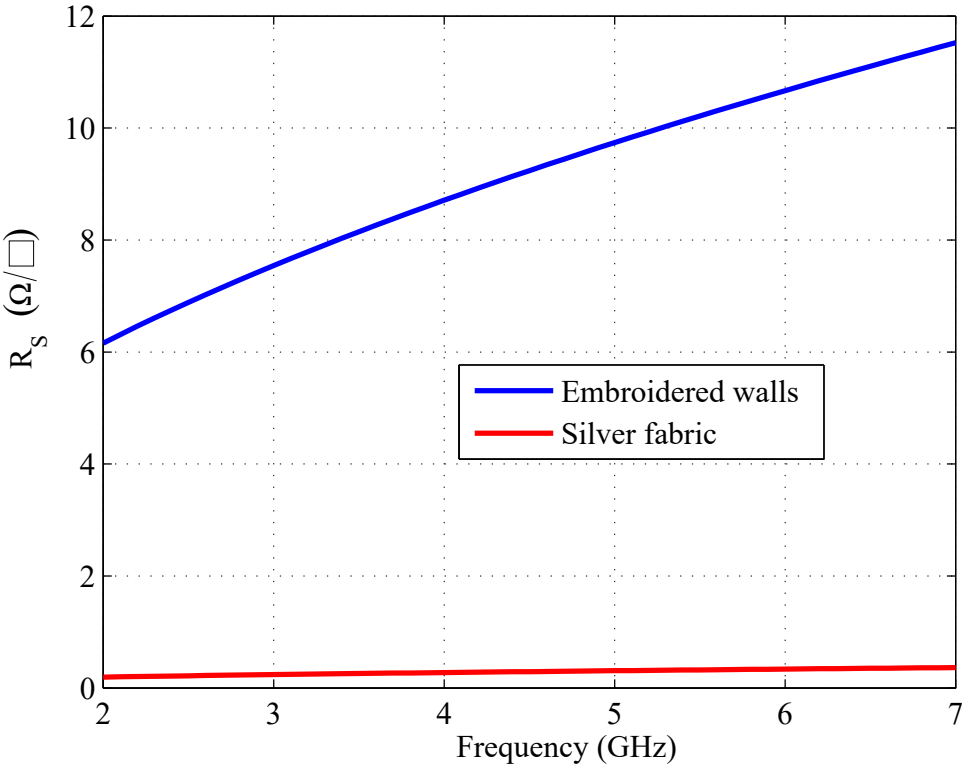

Figure 7.18. Extracted effective RF sheet resistance for the embroidered walls and silver fabric.

After having obtained the frequency-dependent sheet resistance for the conductive textiles the antenna is simulated using the obtained values. The simulated reflection coefficient after taking into account the non-ideal conductivity and seam compression is shown in Fig. 7.19. where the shaded regions represent the bandwidth to be covered. It is observed that in addition to the desired bands of operation at 2.45 and 5.8 GHz there is another band at approx 3.7 GHz. This band is due to the establishment of a quarter-wavelength mode on the transmission line. For the optimized dimensions the length of feedline within the cavity comes to 20 mm which is approximatively a quarter-wavelength at 3.7 GHz. Additionally it was found that this band becomes more pronounced when incorporating the losses of the silver fabric. This band is not claimed as part of the design as it is very lossy.

The last consideration for wearable applications is the effect of the human body. To evaluate the effect of the human body, simulations were performed where the antenna was 1 mm above the body tissue as this is likely to be a typical case given the thickness of clothing. According to standard practice [82], the body tissue was modeled as an arrangement of three homogeneous layers comprising of skin, fat and muscle with thicknesses of 2 mm, 2 mm and 10 mm respectively. At this stage the on-body

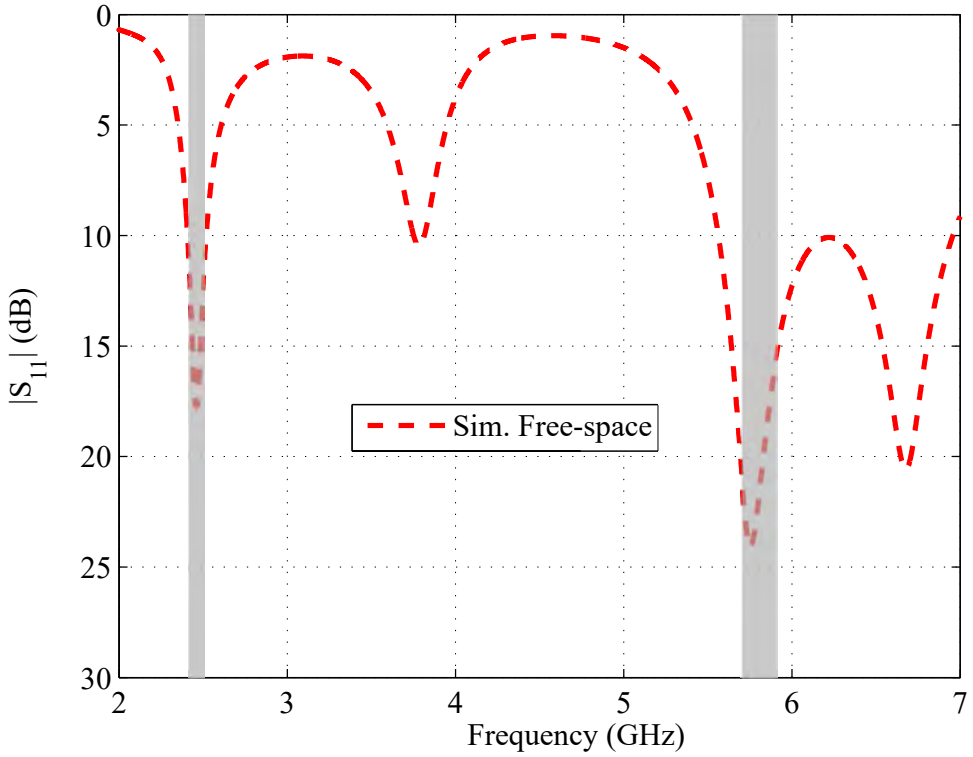

Figure 7.19. Simulated reflection coefficient of the seam compressed antenna with material losses. Dashed lines denote the bands to be covered.

performance of the antenna is compared to the free-space performance. If there is a significant undesired variation in the characteristics such as in the reflection coefficient of realized gain then the ground plane extension G_{EXT} needs to be parametrically optimized. The optimization of the ground plane extension G_{EXT} is done in such a way that the performance of the antenna is largely invariant whether in free-space or when placed in close proximity to human body tissue. After optimizing the ground plane extension G_{EXT} the antenna design is finished and the final antenna size comes to $0.28\lambda_0 \times 0.71\lambda_0 \times 0.04\lambda_0$ at the lowest operating frequency of 2.45 GHz. The optimized values of all the parameters are shown in the caption of Fig. 7.8.

7.5 Manufacture

The multi-stage fabrication procedure is as follows:

1. Cut out 1.6 and 3.2 mm thick foam pieces to total antenna dimensions (L and W) as shown in Fig. 7.8.

2. Cut out silver fabric for top ground plane, feedline and bottom ground plane. In cutting out the silver fabric for the feedline an additional small section of transmission line is cut out to a width of 1 mm to incorporate the wing connection strategy as described in chapter 1 section 1.4.
3. Bond top ground plane to one side of the 1.6 mm foam piece using fabric glue.
4. Bond feedline and bottom ground plane to opposite sides of 3.2 mm foam piece using fabric glue.
5. Prepare embroidery frame with embroidery fabric.
6. Adhere 3.2 mm foam piece to embroidery fabric using fabric glue.
7. Allow 24 hours for glue to dry.
8. Realize shorting wall between feedline and bottom ground plane as shown in Fig. 7.20(a).
9. Bond 1.6 mm thick foam piece to 3.2 mm thick foam piece using glue.
10. Allow 24 hours for glue to dry.
11. Pull the additional section of transmission line through the cut made in the top ground plane to accommodate the SMA connector.
12. Realize cavity walls using ShieldEx 117/17 2PLY conductive yarns. Repeat the embroidery an additional four times to realize a dense cavity wall to reduce ohmic losses.
13. Modify the SMA connector to accommodate the additional section of transmission line as described in chapter 1 section 1.4.
14. Whilst pressing the SMA connector firmly against the top ground plane add conductive epoxy between the SMA connector base and the top ground plane. At this stage the inner pin of the SMA should be protruded through the substrates and visible from the back side of the antenna.
15. Add non-conductive epoxy between SMA connector and the top ground plane for extra mechanical strength.
16. Allow 24 hours for the conductive and non-conductive epoxy to dry.

The antenna at fabrication steps 10 and 15 are shown in Fig. 7.20(a) and Fig. 7.20(b).

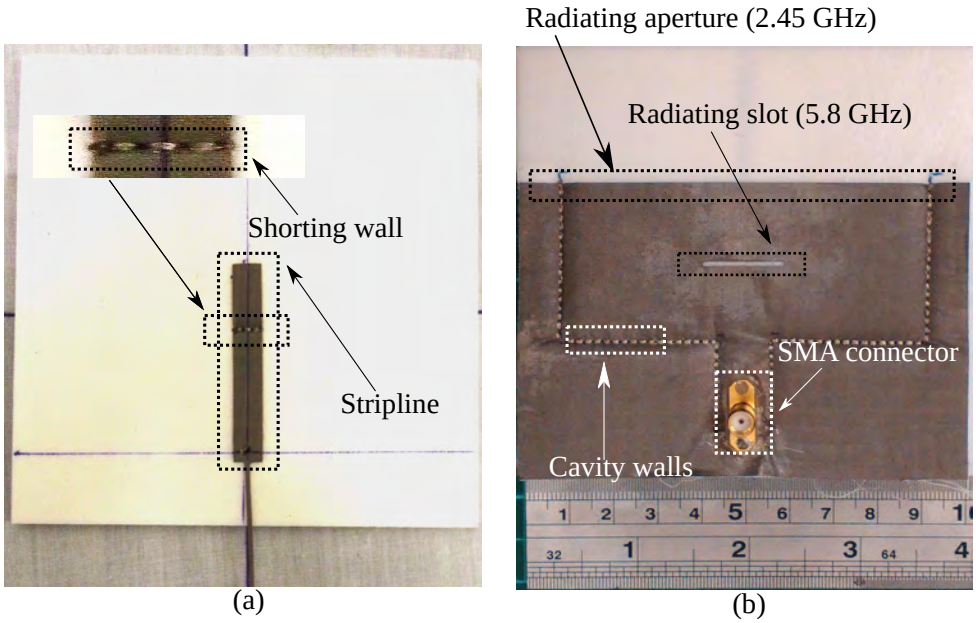

Figure 7.20. Selected steps of the fabrication process: (a) Computerized embroidery of the feedline, (b) Final structure after bonding both substrates and performing computerized embroidery to realize cavity walls.

7.6 Experimental validation

The near-field performance of the antenna was validated by testing the reflection coefficient in free-space and when in close proximity to a lossy dielectric load mimicking the properties of the body tissue. The later case was achieved by mounting the antenna on a human body phantom (TORSO-OTA-V5.1). The human body phantom consists of a homogeneous gel encapsulated in a plastic coating which mimics the electromagnetic properties of the human body over the desired frequency range. The simulated and measured results are shown in Fig. 7.21. where generally good agreement is observed. The insensitivity to loading by the body phantom is attributed to the ground plane which immunizes the antenna from the deleterious effects of the human body. The simulated bandwidths are 4.5% and 22.4% whilst the measured bandwidths are 4.2% and 22.6% at the low and high band respectively. The large bandwidth at the higher frequency comes from a combination of an electrically large substrate thickness and the excitation of the higher order mode of the cavity.

As wearable antennas are expected to be bent considering their desired applications the effects of bending were investigated by curving the antenna around foam cylinders of 40 and 60 mm. These results are shown in Fig. 7.22 and Fig. 7.23 which correspond to bending along the width (ZX plane) and the length (ZY plane). In the case of bending

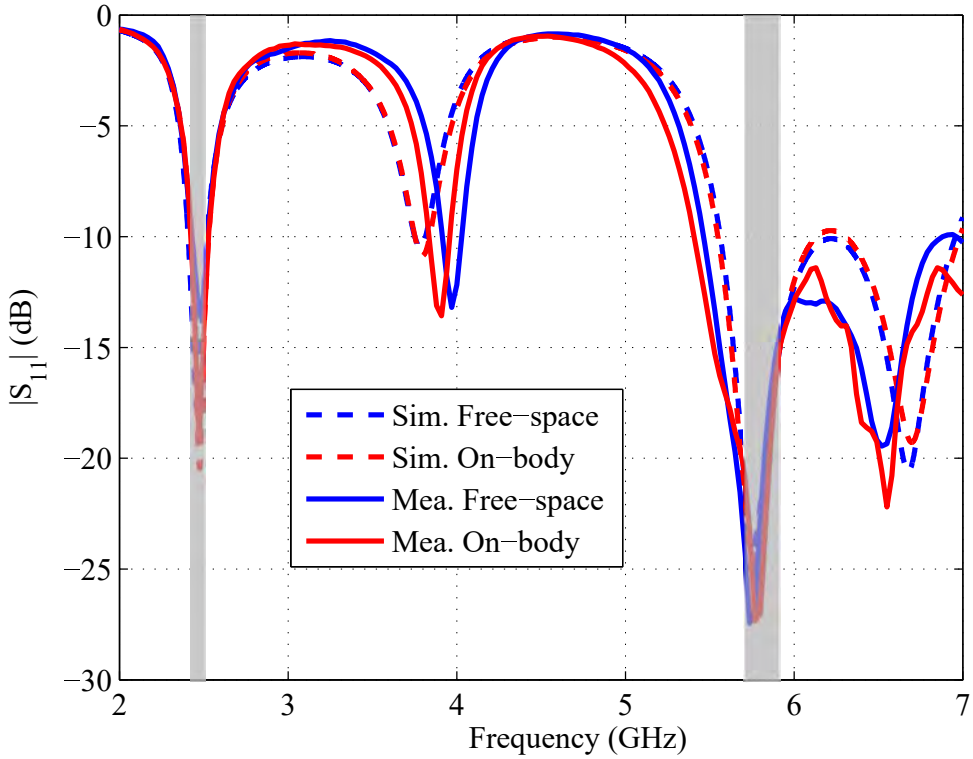

Figure 7.21. Simulated and measured reflection coefficient in free-space and on-body. Dashed lines are simulations and solid lines are measurements.

along the width there is minimal variation at the lower band whilst there appears to be more variation at the higher band. This is attributed to the differing interaction between the magnetic current at the HMSIC aperture and the magnetic current from the slot on the top ground plane. Despite the variation at the higher band it is observed that the antenna still largely covers the desired bandwidth. When the antenna is bent along the length the lower band remains quite stable but the higher band shows more variation. This is attributed to the variation in the electric field along the width of the slot. Despite the observed variation at the higher band it can be seen that the antenna still satisfies the desired bandwidth.

Having examined the near-field performance of the antenna through measurements of the reflection coefficient under various conditions the far-field performance is investigated next through the radiation patterns. The simulated and measured radiation patterns are shown in Fig. 7.24. As the antenna operates as an equivalent magnetic dipole at both frequency bands standard magnetic-dipole-like radiation patterns are expected and observed. However at the higher frequency band the patterns become more distorted which is attributed to the higher-order mode of the cavity interacting with the slot as shown in Fig. 7.17. These observed ripples at the higher band are not

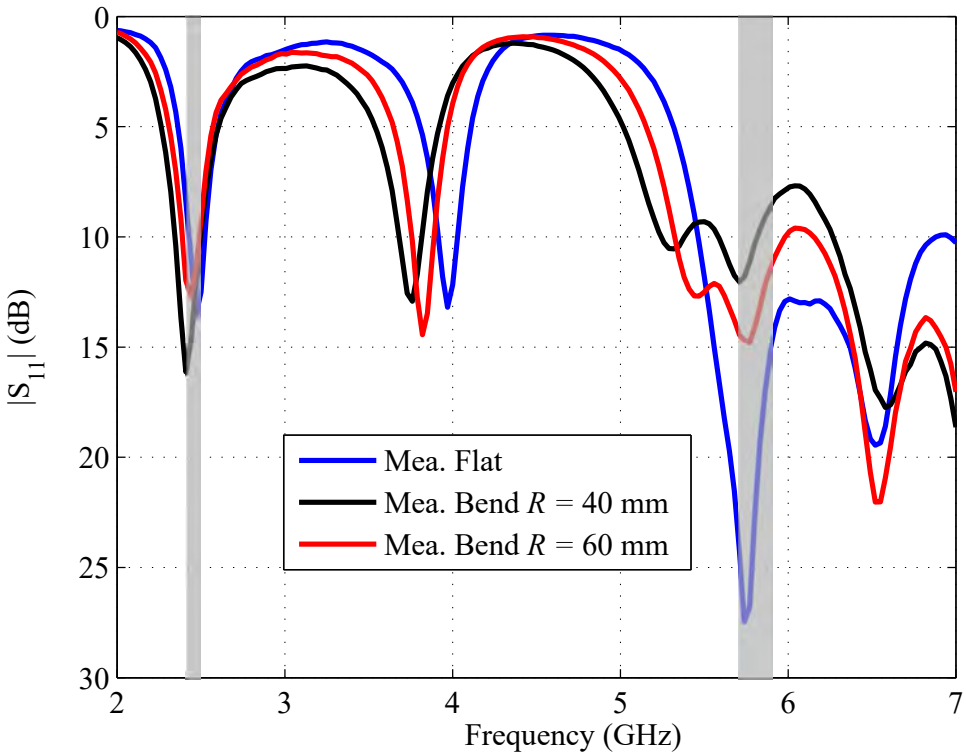

Figure 7.22. Measured reflection coefficient of the antenna when bent along the width (ZX plane).

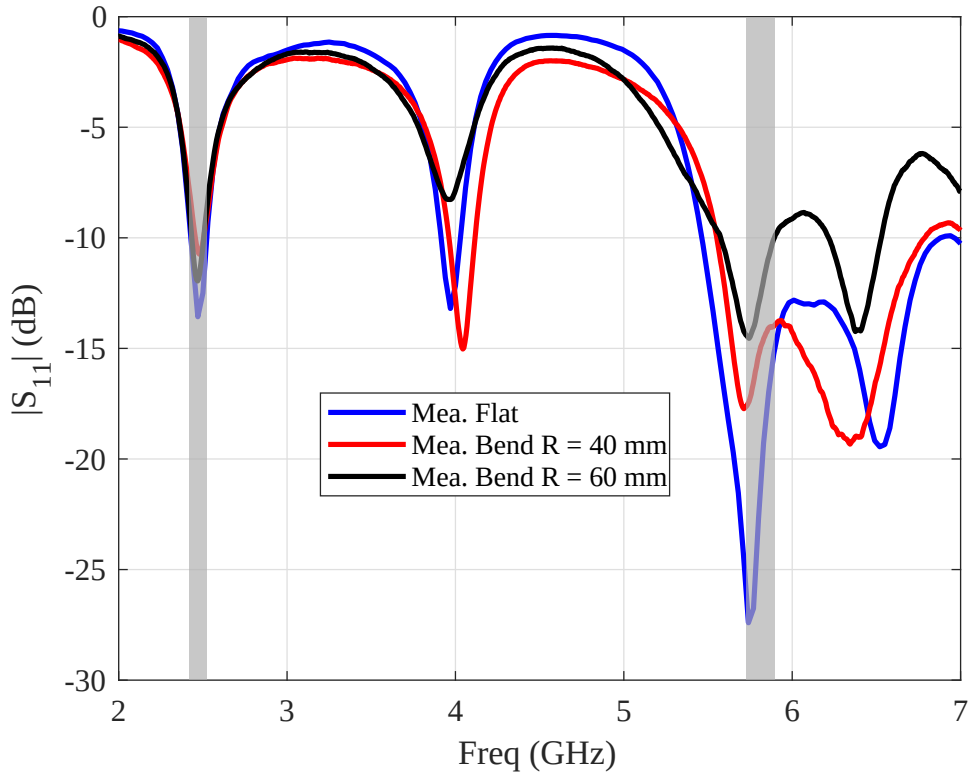

Figure 7.23. Measured reflection coefficient of the antenna when bent along the length (ZY plane).

necessarily of concern as any change in the wearer position will alter the patterns. Generally speaking there is reasonable agreement between simulations and measurements. Whilst there does appear to be more discrepancies at the higher frequency band this could be due to limitations of our anechoic chamber and the presence of the coaxial connector which acts as a scatterer at the high frequencies. The peak simulated realized gain is 6.6 dBi and 5.7 dBi at the lower and upper band respectively whilst the peak measured realized gain is 5.3 dBi and 4.1 dBi. In both cases the peak realized gain occurs off broadside.

The simulated efficiencies are 85% and 83% at the center of the lower and upper bands whilst the measured efficiencies are 77% and 63%. Whilst this amounts to a large difference at the upper frequency this does not imply that the antenna is inefficient. As previously mentioned due to limitations of the measurement setup the patterns at the higher frequency appear to show more discrepancies which manifests as a lower than expected radiation efficiency.

7.7 Design variation

As a design variation performed through numerical simulations, the bandwidth at the lower band is targeted for improvement. This is achieved by cutting out another slot near the HMSIC aperture henceforth denoted as the aperture slot. This modification is shown in Fig. 7.25 where the new slot is shown with a red outline. If the length of the aperture slot is made as large as possible (i.e the same width of the cavity) then the lower resonance frequency moves upwards as the cavity becomes effectively smaller. To compensate for this increase the width of the cavity is made mildly larger. With these modifications the cavity size comes to $0.28\lambda_0 \times 0.71\lambda_0 \times 0.04\lambda_0$ where λ_0 is the free-space wavelength at 2.45 GHz. This is in contrast to the cavity size without the aperture slot which is $0.28\lambda_0 \times 0.67\lambda_0 \times 0.04\lambda_0$. The simulated reflection coefficient of the antenna with and without the aperture slot is shown in Fig. 7.26 where it is that the a bandwidth enhancement occurs at the lower band.

It is presumed that this increase in bandwidth occurs through two means. Firstly the cavity is made slightly larger which increases the bandwidth and secondly the aperture slot makes the cavity appear more open which reduces the radiation Q-factor of resonant mode. This leads to a larger radiating aperture resulting in a larger bandwidth. The free-space radiation patterns for the antenna without the aperture slot are

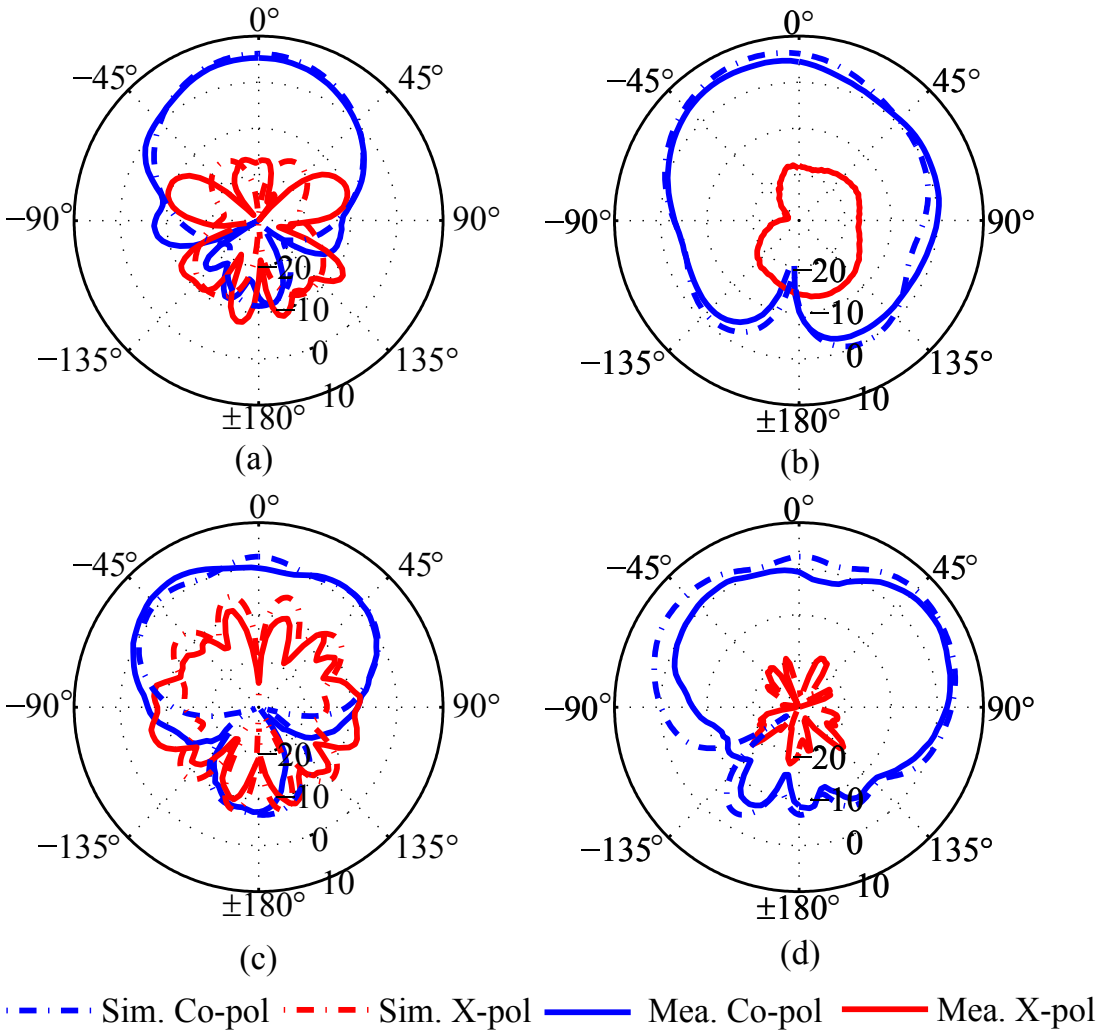

Figure 7.24. Simulated and measured radiation patterns: (a) ZY plane at 2.47 GHz, (b) ZX plane at 2.47 GHz, (c) ZY plane at 5.74 GHz, (d) ZX plane at 5.74 GHz.

compared to the free-space patterns with the aperture slot in Fig. 7.27 where for clarity the cross-polarization is depicted using thin lines. At the lower band the radiation patterns remain quite stable whilst the patterns at the higher band do show more variation which is attributed to the interaction of the radiated fields from the small slot and the aperture slot. As previously mentioned these variations are not of much consequence due to the range of movements made by the user.

7.8 Conclusions

In this chapter a new dual-band antenna based on a half-mode substrate-integrated cavity was proposed and experimentally validated. The main contributions of this

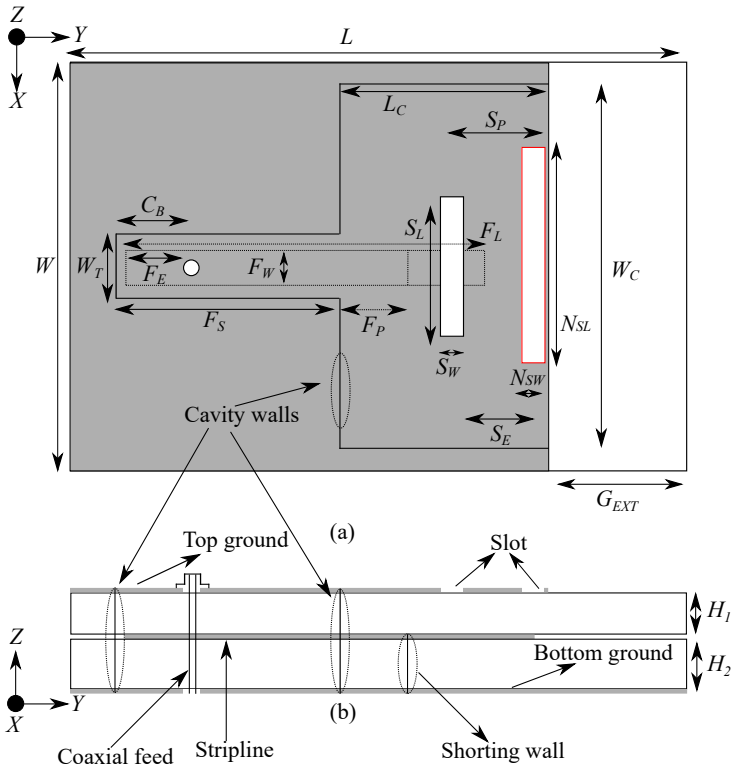

Figure 7.25. Schematic of the proposed design variation where the new aperture slot is shown in a red outline.

work are the addition of a second mode through an added slot and the the excitation of two different resonant modes within the same cavity through a textile feeding mechanism. A design framework was presented which allows a repeatable and scalable design. It was demonstrated the antenna could be bent whilst retaining adequate performance. Compared to other designs in the literature the proposed antenna features a high radiation efficiency and simple fabrication process. A design variation was provided whereby the introduction of an additional slot near the HMSIC aperture on the top ground plane the bandwidth at the lower band could be enhanced at the cost of a mild increase in the planar dimensions of the cavity. Noteworthy is that this bandwidth increase is obtained without increasing the cavity thickness.

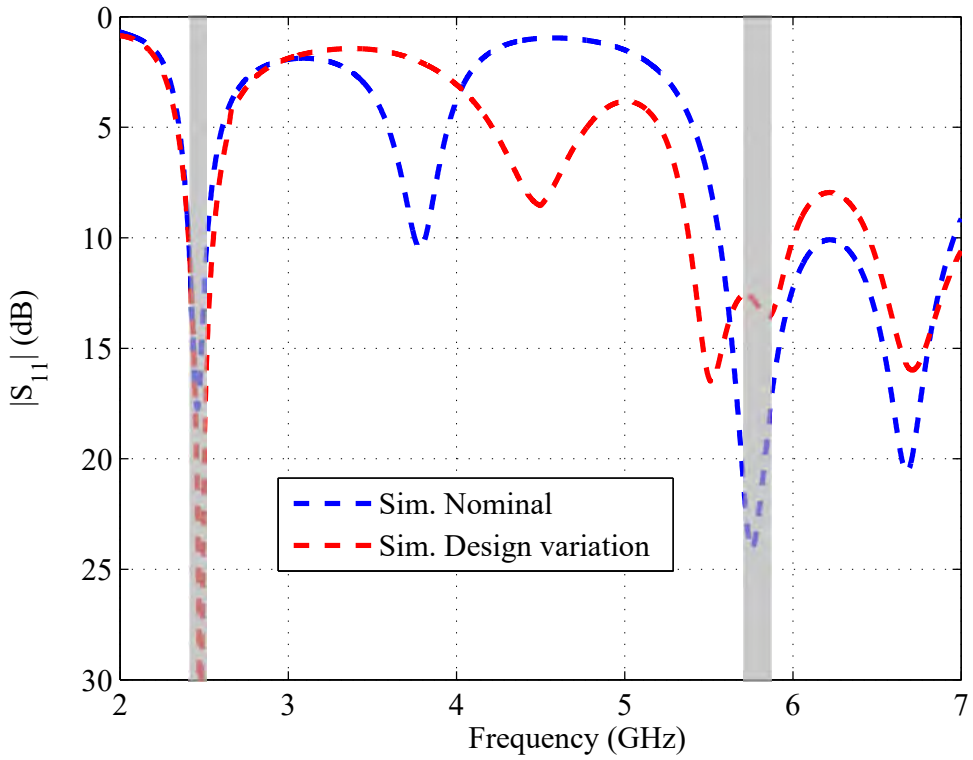

Figure 7.26. Simulated reflection coefficient of the nominal antenna and the antenna with a slot near the HMSIC aperture for bandwidth enhancement.

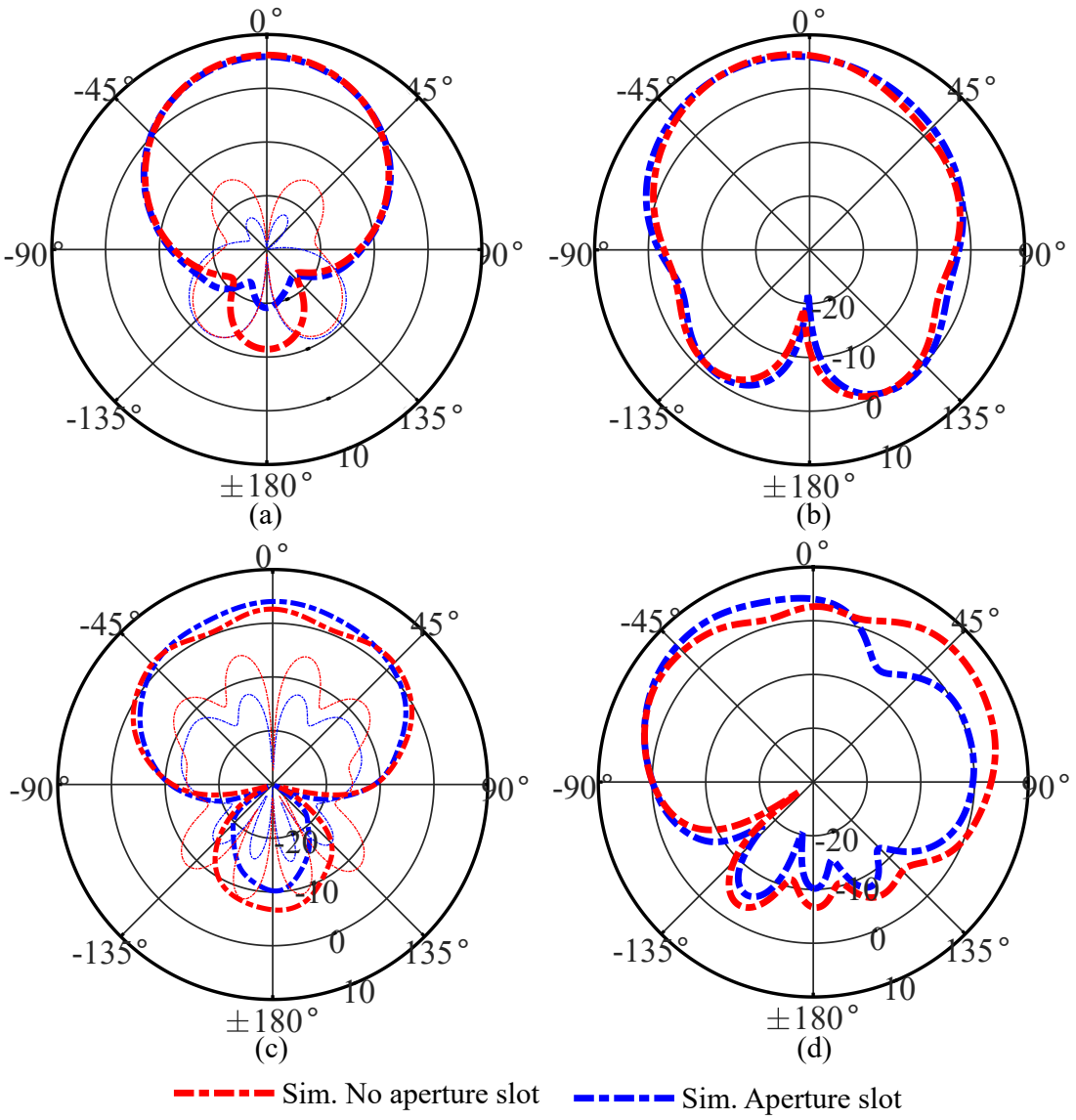

Figure 7.27. Simulated radiation patterns for two cases: The nominal design and the design variation incorporating the additional aperture slot. Dashed red lines correspond to the nominal design and dashed blue lines correspond to the design variation with the aperture slot. From top left to bottom right: (a) ZY plane at 2.45 GHz, (b) ZX plane at 2.45 GHz, (c) ZY plane at 5.8 GHz, (d) ZX Plane at 5.8 GHz.

Chapter 8

Detuning Quantification

IN recent years, reconfigurable antennas have attracted tremendous attention as a means to enhance antenna functionality. Within the domain of reconfigurable antennas there are four subcategories. Three of these categories are frequency, pattern, and polarization reconfigurable antennas. The last category, namely compound reconfigurable antennas, exploits combinations of any of the aforementioned forms of reconfigurability. Frequency reconfigurable antennas are advantageous for wearable applications as they can potentially compensate for detuning effects arising from hostile environmental conditions. A first step in realizing textile frequency reconfigurable antennas is determine the required tuning range which is the focus of this chapter.

8.1 Introduction

Traditionally, antennas have been designed for fixed performance where the antenna characteristics were unchangeable once designed and fabricated. Recently, the concept of reconfigurable antennas which can dynamically alter performance characteristics has gained traction [154]. The alterable performance characteristics can be: operating frequency or frequencies [60, 155–157], radiation patterns [158–160] or polarization [161–163]. The most advanced reconfigurable antennas can reconfigure multiple performance characteristics simultaneously [164–166]. Of all the types of reconfigurability, frequency reconfigurable antennas are particularly attractive for wearable applications. An example of a flexible frequency reconfigurable antenna is shown in Fig. 8.1. The advantages of frequency reconfigurable antennas are numerous, but one of the main advantages that pertains to body-worn communications is the ability to dynamically alter the operating frequency to compensate for detuning that may occur. For example, the bending that flexible antennas can be subjected to (as shown in Fig. 8.1(d)) may alter the operation frequency in undesired ways. If properly designed, a textile frequency reconfigurable antenna should be able to compensate for any undesired variations in the operating frequency. In this context, it is important to know how much detuning may need to be compensated for which is one of the focus areas of this chapter.

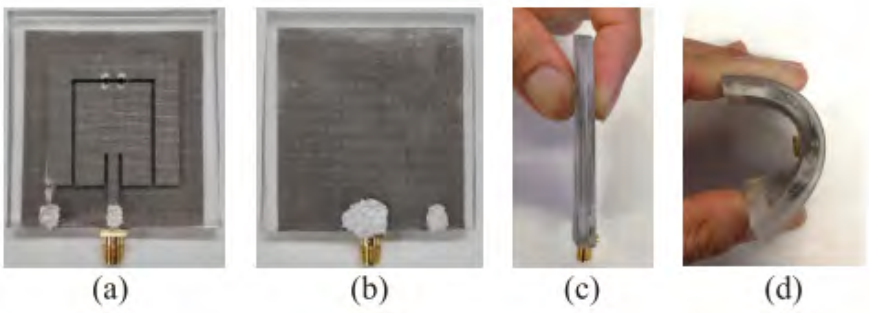

Figure 8.1. A fully flexible wearable frequency reconfigurable antenna as reproduced from [59]

8.2 Frequency detuning quantification

Prior to commencing the design of any textile frequency reconfigurable antenna, an important question needs to be addressed. Specifically, *what is the maximum required tuning range?* The maximum tuning range for wearable frequency reconfigurable antennas is determined by two factors. The first factor is what range of frequencies need

to be covered which can be determined based on design specifications. The second factor is how much *additional* tuning range needs to be incorporated to compensate for undesired variations in operating frequency due to adverse environmental conditions such as bending and proximity to human body tissue. A generic illustration of the second factor is provided in Fig. 8.2 where the solid blue line represents a wearable antenna operating at a desired frequency. The dashed red lines represent the undesired variations in operation frequency when the antenna is subjected to the environmental conditions in the corresponding insets. One of the focus areas of this chapter is on quantifying the maximum variations in the operating frequency which need to be compensated for. The details of an investigation quantifying the maximum variations in operating frequency of a typical wearable antenna are herein described.

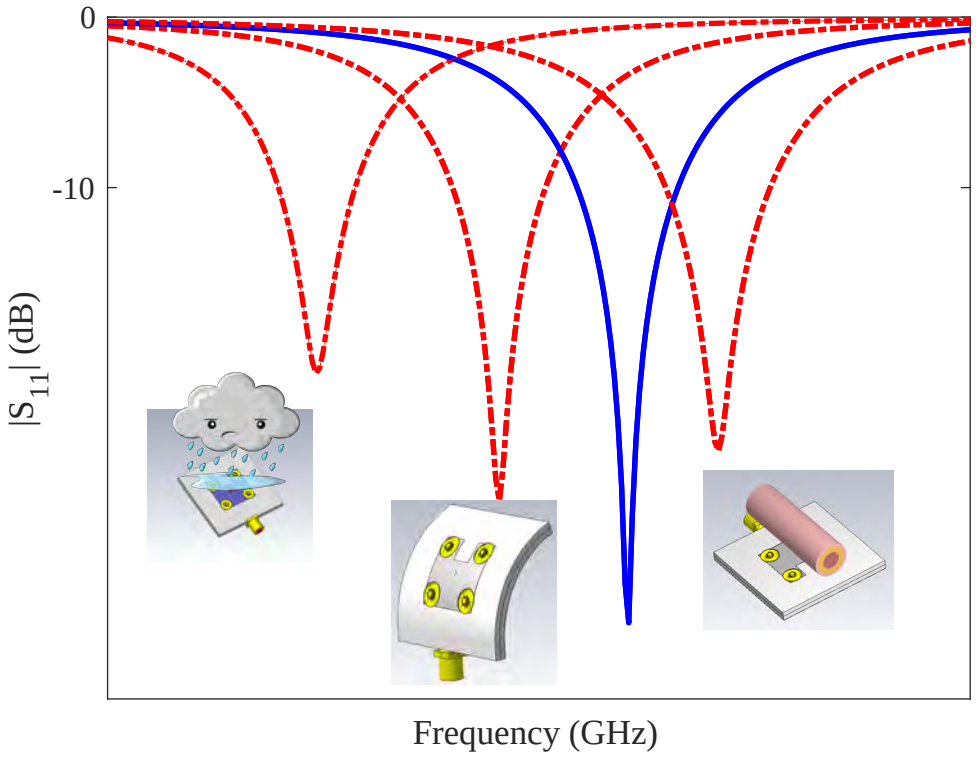

Figure 8.2. A general depiction of the effects of detuning on the operation frequency of a wearable antenna. The solid blue line represents the operation frequency that an antenna can be designed for. The dashed red lines with the corresponding insets demonstrate the potential undesired variations in operating frequency due to water absorption, bending and dielectric loading by human body tissue.

The investigation begins by choosing an appropriate antenna topology, which in this case is a modular patch antenna with a resonance frequency of 5.3 GHz. This geometry is chosen for two reasons. Firstly, the top layer of the patch is detachable by removing the snap-on buttons which allows for convenient testing. Specifically, by

changing the top patch module, different measurements can be easily facilitated [70]. Secondly, patch antennas are a common choice for wearable applications as they have a ground plane which helps in isolating them from human body effects. A schematic of the antenna and a prototype device is shown in Fig. 8.3(a) and Fig. 8.3(b) respectively. The antenna is a multi-layer structure which is made from two pieces of 1.6 mm thick Cumming Microwave PF-4 Foam which has a relative permittivity (ϵ_r) of 1.06 and a dielectric loss tangent (δ) of 0.0001 at the desired frequency of interest. The top layer of the structure consists of a rectangular patch which has a notch cut out for impedance matching purposes. The patch is fixed to the substrate through four snap-on buttons which are located at the periphery of the patch as shown in Fig. 8.3(a). The middle layer contains a microstrip line which excites the top layer through proximity coupling [73]. Finally, the bottom layer contains a full ground plane to isolate the antenna from the body. The overall dimensions of the antenna are 40 mm $\times$ 40 mm. The detailed design procedure for this antenna can be found in [70].

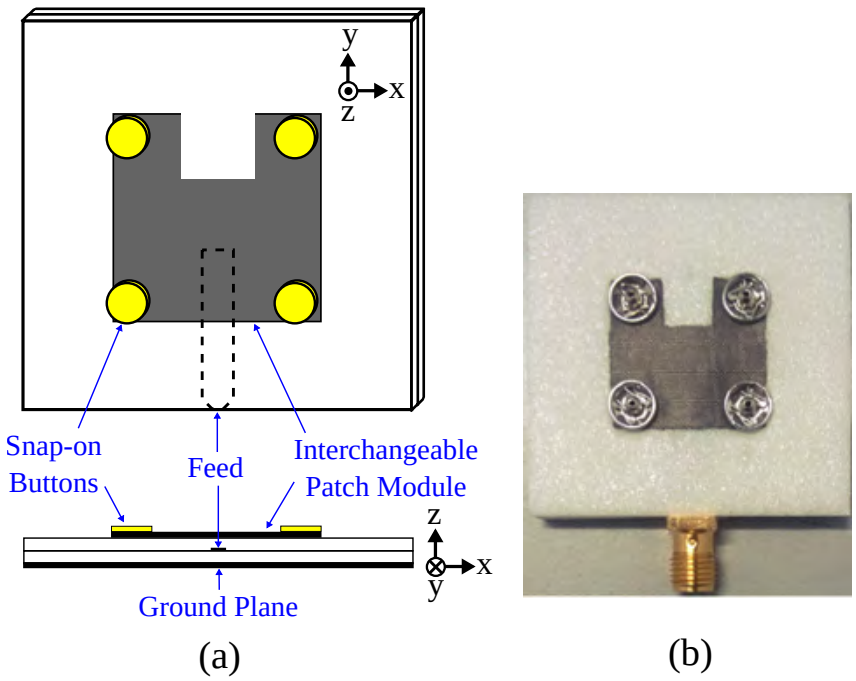

Figure 8.3. A schematic of the modular patch antenna that is used to quantify the variations in operation frequency (a) and a prototype of the antenna which is used in this investigation (b).

Having decided the antenna, the next step is to determine which adverse environmental conditions should be investigated. For the purposes of this study the following conditions are examined:

1. Moisture absorption, either due to sweating or rain.

2. Antenna curvature due to location on the human body.

3. Proximity to human body tissue.

These conditions are investigated as they represent the three main adverse environmental conditions that wearable antennas can be subjected to.

8.2.1 Simulations

The next step of the investigation is to simulate the effect of the various adverse environmental conditions. This is to get an appreciation of which of the aforementioned environmental conditions is most deleterious to the desired operation frequency of the antenna.

To model the effects of moisture absorption, the top layer of the patch is immersed in a layer of water, as shown in the inset of Fig. 8.4, with varying thickness. The water is modeled as a dielectric object with a relative permittivity (ϵ_r) of 78 and a conductivity (σ) of 1.59 S/m at the frequency of interest. It should be noted that the simulations for moisture absorption are intended to give a general qualitative appreciation of what can be expected when the antenna is subjected to water. Realistically, it is extremely difficult to model the physical distribution of water on the antenna, due to the inhomogeneity of the water distribution in practical scenarios. The simulated reflection coefficient for moisture absorption is shown in Fig. 8.4. It is observed that immersing the top layer of the patch in water causes a downshift in the resonance frequency. Additionally, the downshift is directly proportional to the thickness of the water layer. *From the simulated results, the maximum downshift in operating frequency is 2.6% which occurs for a water layer thickness of 0.5 mm*.

The next adverse condition which is investigated is antenna curvature. Flexible antennas which are integrated into clothing can be subject to severe variations in their geometry [72]. Therefore it is of importance to characterize the variations in operating frequency due to changes in geometry relative to the planar case. For the present study bending radii, denoted as R in the inset of Fig. 8.5(a) and Fig. 8.5(b) respectively, of 30 and 40 mm (approximately a forearm and upper arm radius) are chosen. The variation in the reflection coefficient for bending along the width (ZX) and along the length (ZY) are shown in Fig. 8.5(a) and Fig. 8.5(b) respectively. As is consistent with other studies in the literature [72], bending the antenna along the width has minimal impact.

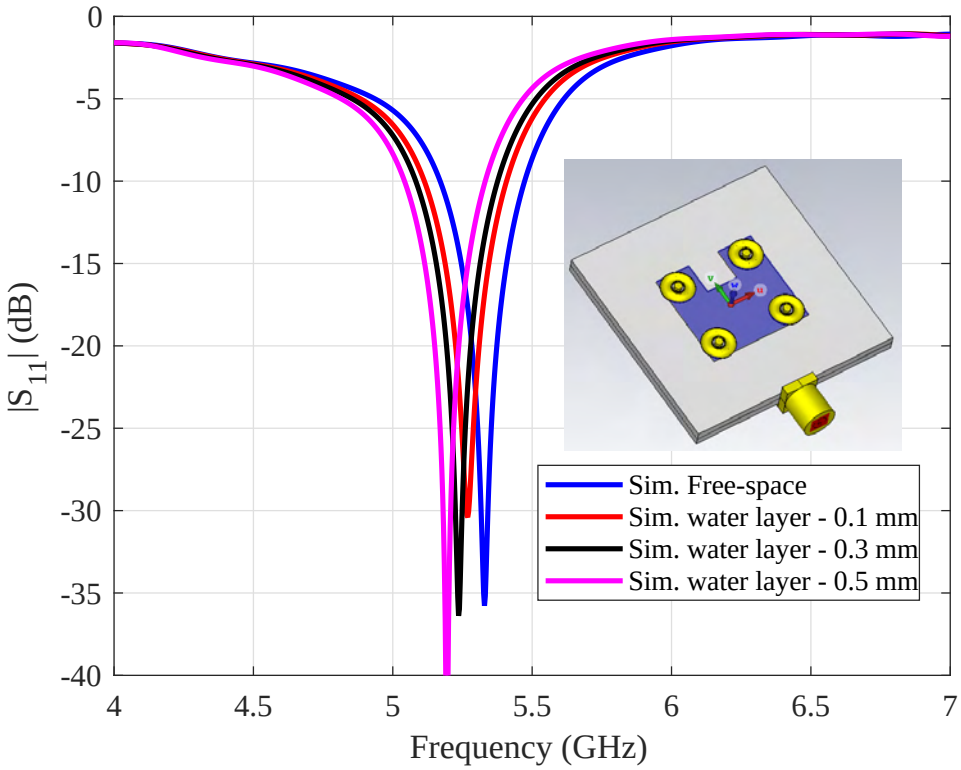

Figure 8.4. Simulation results for the top metalized layer of the modular patch antenna embedded in a homogeneous layer of water with varying thickness.

Surprisingly bending along the length also has minimal impact. The invariance under both bending scenarios is most likely because the antenna is physically compact and therefore needs a very small bending radii to cause a noticeable variation in the operating frequency [3]. *From the simulated results, the maximum upshift of 1.5% occurs when the antenna is bent along the length with a bending radii of 30 mm.*

The last adverse condition which is herein investigated is proximity to human body tissue. The human body having a large permittivity naturally presents a substantial loading effect for wearable antennas. Therefore it is of importance to appreciate what effect the human body may have on the operating frequency of the antenna. To this end, simulations are performed where the antenna is placed above a three layer body model consisting of skin, fat and muscle with thicknesses of 1, 3 and 18 mm respectively. The planar dimensions of the body tissue are 160 mm $\times$ 160 mm. In simulations, the antenna is separated from the human body tissue by 1 mm as this is likely to be a typical case when the antenna is embedded into clothing. The simulation results along with the simulation setup are shown in Fig. 8.6(a), where it is observed that there is minimal variation in the operation frequency of the antenna. This is expected as the

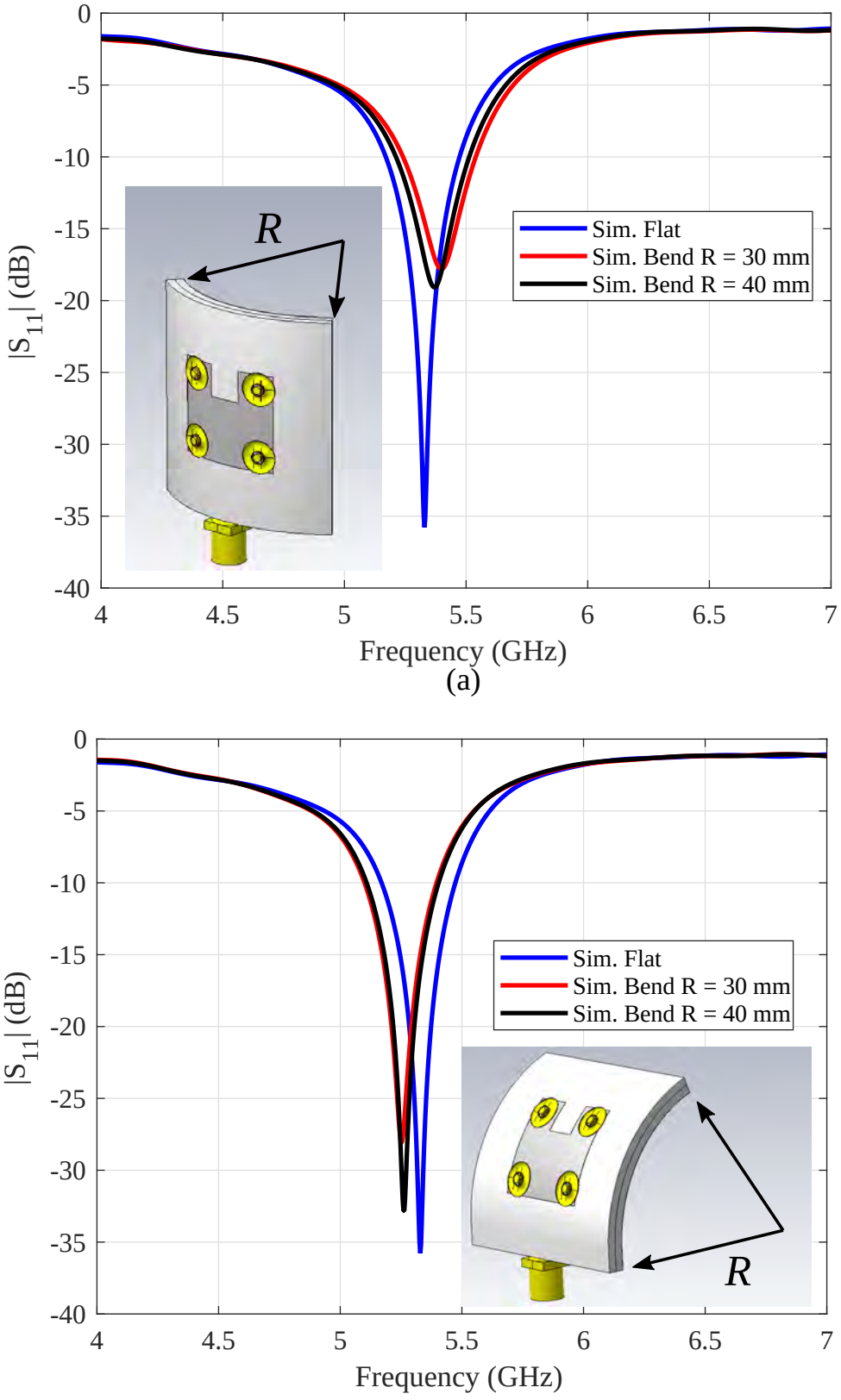

Figure 8.5. Simulation results for (a) the antenna bent along the width and (b) the antenna bent along the length. In both cases the antenna is cylindrically bent around a bending radius of R

ground plane acts as an isolating element which immunizes the antenna from human body effects as discussed in chapter 2.

Another form of human body loading is having the antenna *below* the human body. This scenario can occur when the antenna is shadowed either due to movements of the wearer or from other people. To approximate this situation, simulations are performed where the antenna is placed *below* a cylindrical three layer body model comprising of skin, fat and muscle by 3 and 5 mm. These spacings are chosen to get a general appreciation on the effects of having the antenna *below* the body. The cylindrical approximation of the human body can represent a human finger which could be shadowing the antenna. The simulation results for this case are shown in Fig. 8.6(b) where the inset shows the simulation setup. The simulation results reveal a resonance frequency *upshift*. This is very interesting as it is expected that the human body with a large permittivity would introduce dielectric loading and cause a downshift in the resonance frequency. The computed upshift however could be due to the field confinement caused by the presence of the human body tissue. Consider Fig. 8.7 which shows the radiated electric field when the antenna is below the cylindrical body model. It can be observed in the field plots of Fig. 8.7 that the fields that are radiated from the patch are partially confined in the region between the antenna and the body. When the body is in close proximity to the antenna, the field confinement occurs in the near-field. The field confinement results in electrically smaller geometry, translating into a higher operation frequency. *From the simulated results, the maximum upshift of 3.3% occurs when the antenna is 3 mm below the body*.

From these simulations, it is found that the adverse environmental conditions which cause the maximum variation in the operating frequency are moisture absorption and having a body part in the vicinity of the antenna. These conditions result in a variation in the operation frequency by 2.6% downwards and 3.3% upwards respectively. As these two conditions represent the most severe predicted detuning, it is only natural that these two conditions be experimentally investigated.

8.2.2 Experimental Validation

To investigate the effect of moisture absorption, the top layer of the antenna is sprayed with water 1, 3 and 5 times which will henceforth be known as 1, 3 and 5 spray cycles. The different spray cycles are investigated to get a qualitative appreciation of the

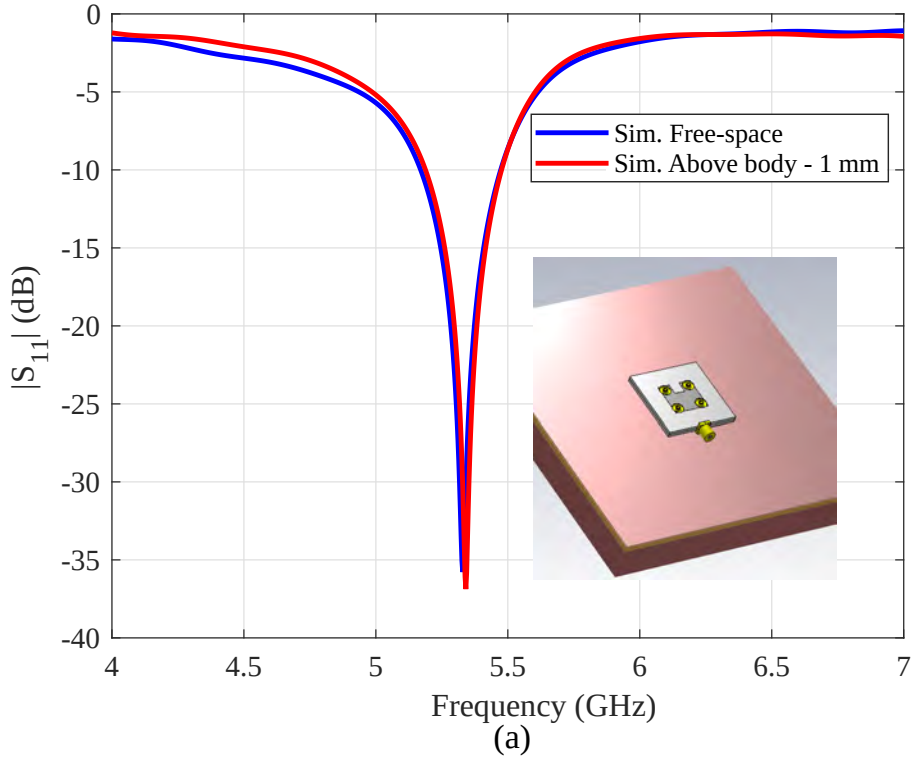

(a)

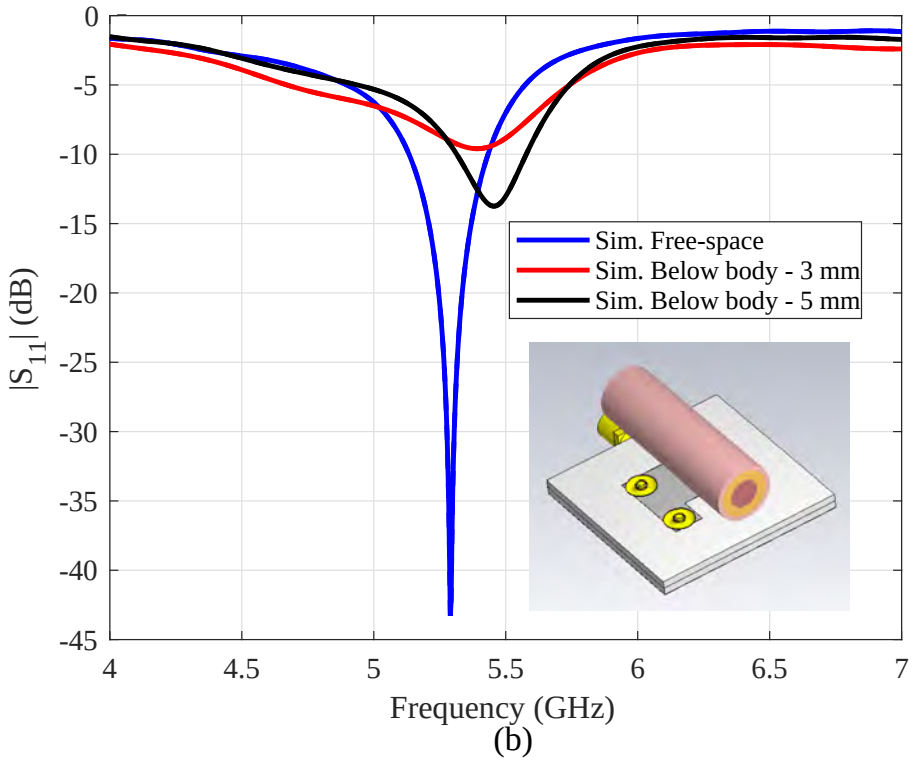

(b)

Figure 8.6. (a) Simulation results for the antenna in free-space and when placed above a human body tissue model by 1 mm and (b) Simulation results for the antenna in free-space and when a human finger is placed above the antenna at two different separations, namely 3 and 5 mm.

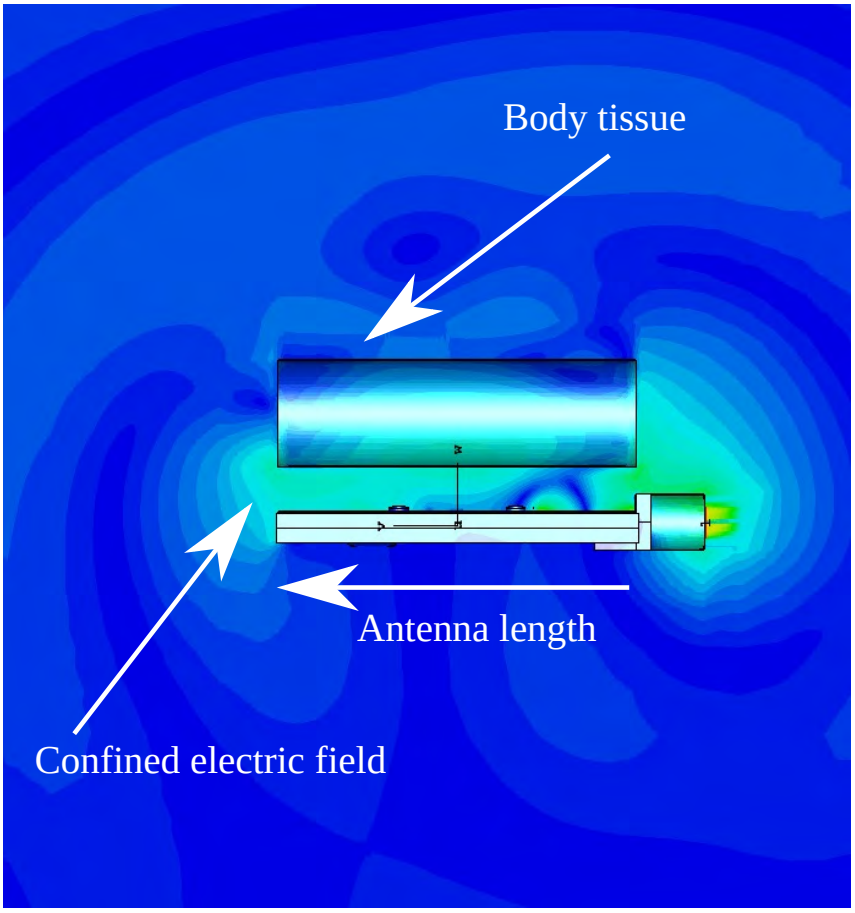

Figure 8.7. Simulated electric field distribution of the patch antenna when placed below a cylindrical three layer human body model.

variation in operation frequency as a function of moisture absorption. A spray cycle beyond 5 is not investigated as previous studies have shown that most of the performance degradation occurs in the initial stages [100]. The exact procedure to moisturize the antenna is as follows:

1. Use a water spritzer bottle to spray the top layer of the antenna with tap water at a close distance.
2. Measure the reflection coefficient.
3. Wait 5 minutes and re-measure the reflection coefficient. This step is to evaluate whether the effects of moisture absorption are temporary or permanent.
4. Lightly clean the surface of the antenna. This is the end of spray cycle 1.
5. Spray the top layer of the antenna twice to reach a spray cycle of 3.

6. Repeat steps 2 - 5 to reach a spray cycle of 5.

The measured near instantaneous and delayed results are provided in Fig. 8.8(a) and Fig. 8.8(b) respectively. Considering Fig. 8.8(a) it can clearly be seen that with an increasing number of spray cycles (or equivalently more moisture), there is a larger downshift in the resonance frequency. This clearly corroborates the simulation results. The frequency ratio between the dry case and the spray cycles of 1, 3 and 5 are 0.5%, 3% and 5% respectively. Additionally, from Fig. 8.8(b) it can be seen after a delay of 5 minutes the measured reflection coefficient across all spraying cycles reverts to the pre-sprayed case. The latter results indicate that the effects of moisture absorption are not permanent. This is due to the materials that are used: the Cumming Microwave PF-4 foam is a hydrophobic material and the conductive fabric has a water repellant protective plastic coating. It is postulated that the variations in resonance frequency arise from the water being trapped between the top layer of the conductive fabric and the substrate. Therefore, to desensitize the antenna from the effects of moisture it is imperative that the substrate and conductive textile materials exhibit some degree of hydrophobic behaviour. *From the measurements, the maximum observed downshift in resonance frequency which occurs at 5 spraying cycles is 5%.*

The final form of loading that is experimentally investigated is having the antenna *below* the human body tissue. This situation is experimentally realized by placing a human finger 3 and 5 mm above the top layer of the antenna. The rationale for having the finger above the antenna is that it is more practical and reproducible to have a finger flat than a human hand due to the inherent curvature of the hand. The measurement setup explains why the simulations for this case modeled the body tissue in a cylindrical form.

The measured results are shown in Fig. 8.9 where it can clearly be seen that there is a frequency upshift which corroborates the observations from simulations. The frequency ratio between the antenna without any loading and with a human finger is approximately 6.3% which is reasonably close with the simulated upshift of 3.3%. The difference of 3.0% could be due to ambiguity in knowing the exact properties of the human body [139, 140].

From the above measurements, it is concluded that wearable frequency reconfigurable antennas may need to have approximately $\pm$ 6% compensation factor in their tuning range to compensate for potential upshifts and downshifts in operating frequency.

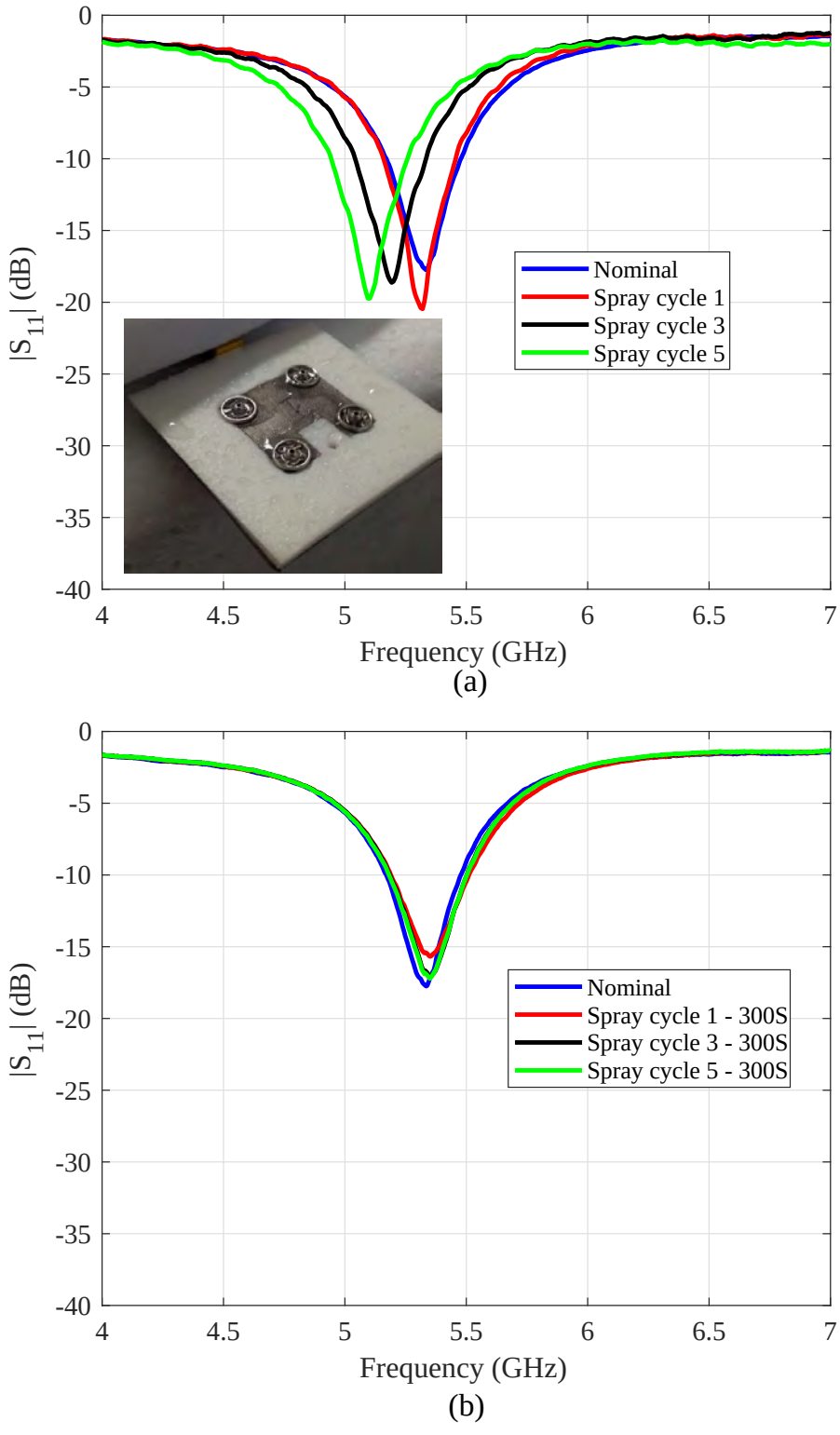

Figure 8.8. (a) Measured results for the top layer of the patch sprayed with water at a close distance where the inset shows the moisture on the top layer of the antenna and (b) Measured results after allowing the top layer of the patch to dry for 300 seconds.

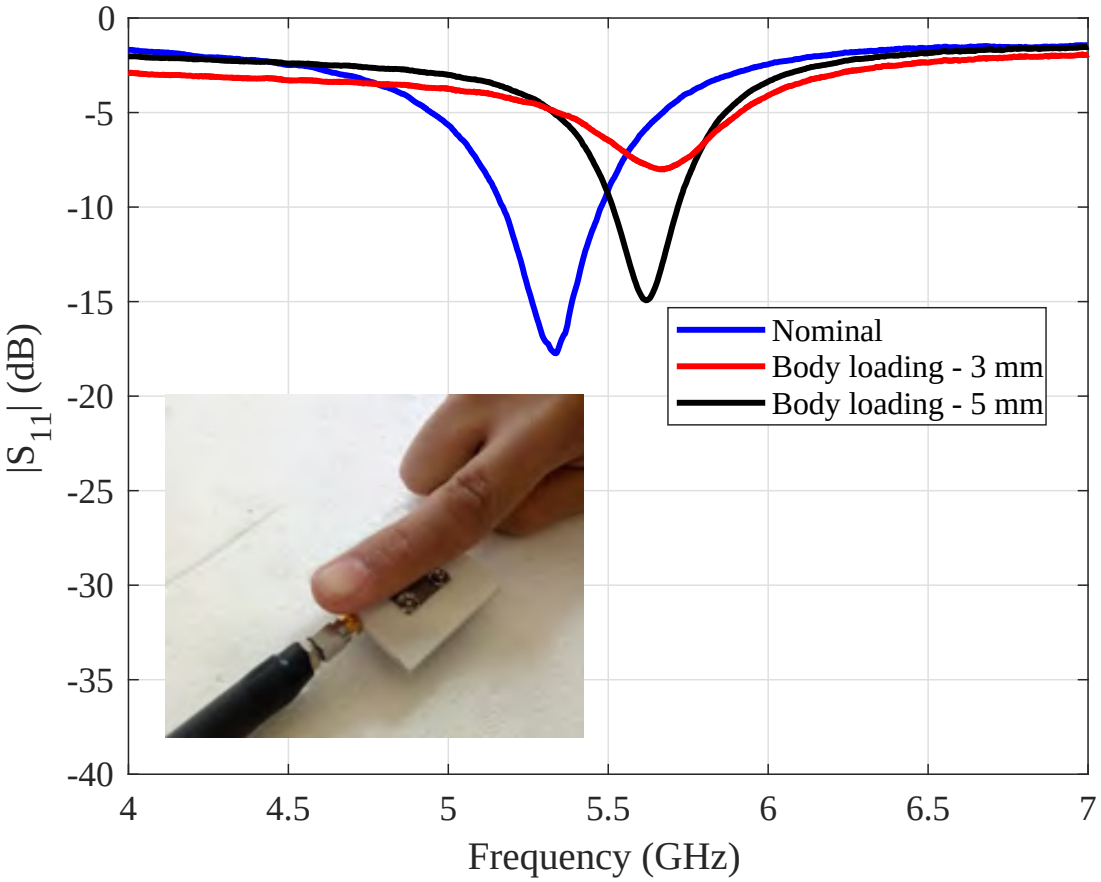

Figure 8.9. The measured results when the antenna is *placed below* a human finger for two spacings: 3 and 5 mm. The inset shows the measurement setup.

8.3 Conclusions

This chapter has laid the foundations for the realization of textile frequency reconfigurable antennas. Specifically, this was achieved by numerically and experimentally investigating the maximum variations in the operating frequency of a textile modular patch antenna when subjected to three adverse environmental conditions. These conditions were: moisture absorption, antenna curvature and proximity to human body tissue. A salient observation is that when the antenna is *placed below human body tissue* the resonance frequency can shift upwards by approximately 6%. This rather interesting observation was attributed to the field confinement between the antenna and the human body tissue above the antenna. On the contrary, when the antenna is exposed to moisture, the resonance frequency could shift downwards by 5%. Overall based on these factors it is suggested that textile frequency reconfigurable antennas have an approximate $\pm$ 6% compensation factor in the tuning range to compensate for detuning of the operating frequency due to adverse environmental conditions.

Chapter 9

Multi-Layer Cavity-Backed Broad-Slot Reconfigurable Antenna

IN this chapter the design of a new compact multi-layer cavity-backed broad slot antenna is presented. Initial measurement results are presented. For the purposes of validation the antenna is implemented in inflexible PCB technology but the geometry is amenable for implementation in wearable technologies. The reasonable agreement between simulations and measurements indicate that the antenna operates as expected.

9.1 Introduction

Following on from the previous chapter, this chapter presents a new type of frequency reconfigurable antenna that is suitable for wearable applications. The proposed antenna is similar to the wearable cavity antennas presented in chapter 6 and 7 in the sense that the radiation mechanism is through a cavity backed magnetic dipole. To get an appreciation of what challenges must be surmounted to realize textile frequency reconfigurable antennas a brief summary of some notable frequency reconfigurable antennas is herein presented. To appreciate the performance of frequency reconfigurable antennas, a suitable performance metric needs to be defined. Most often for frequency reconfigurable antennas the performance metric is the fractional tuning range for which the definition is herein provided. The fractional tuning range can be calculated according to:

$$TR = \frac{F_H - F_L}{F_C} \times 100. \tag{9.1}$$

In equation 9.1 F_H, F_L and F_C represent the highest, lowest and middle frequency respectively over some tunable frequency range. A larger tuning range implies an antenna that can cover a larger frequency range.

In recent years (specifically from 2015) there have been a range of frequency reconfigurable antennas implemented in rigid technology based on the concept of stub loading. For example consider Fig. 9.1 [60] which shows a frequency reconfigurable antenna whose geometry and operation principle is herein described. The antenna consisted of a half-mode substrate-integrated cavity that was periodically loaded with three stubs. At one end of the stubs a varactor was used to make a connection between the half-mode substrate-integrated cavity aperture and the stub. At the other end, each of the stubs were connected to a DC bias circuit which was itself interfaced with a DC connector. It was analytically shown that altering the varactor capacitance changed the propagation constant along the x-direction which lead to a tunable operating frequency. The antenna presented in [60] exhibited a fractional tuning range of 41% which was heavily dependent on the length of the stubs where it was shown that to an optimum limit a larger stub length led to a larger tuning range. The length of the stubs contributed to one of the main limitations of this antenna: the large planar dimensions. The antennas which have been designed based on the concept of stub loading are usually

quite large. For example the antenna presented in [60] exhibited planar dimensions of $0.63\lambda_0 \times 0.64\lambda_0$ at the lowest operation frequency of 2.60 GHz.

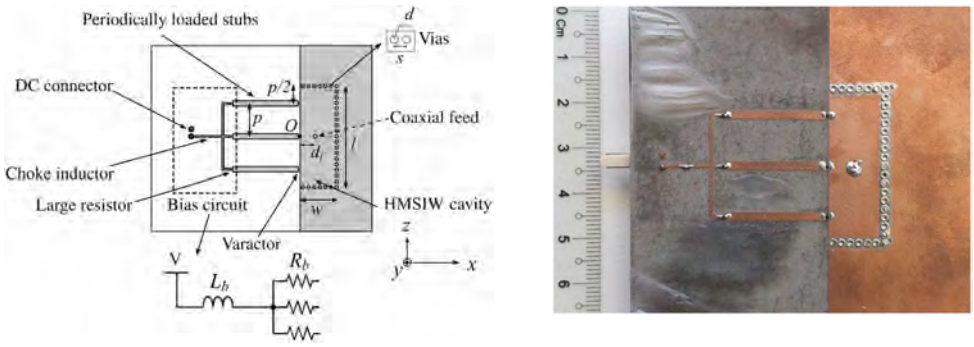

Figure 9.1. A rigid frequency reconfigurable half-mode substrate-integrated cavity antenna based on the concept of stub loading. This image is adapted from [60].

In contrast to the antenna presented in [60] that was excited by an SMA, connector a rigid frequency reconfigurable antenna that was excited by a microstrip line as shown in Fig. 9.2 was presented in [61]. The antenna was a cavity-backed slot antenna where the slot was offset from the centre of the cavity. By using PIN diodes to create short circuits at selective points within the cavity, the electric field within the antenna was altered which resulted in an adjustable operation frequency. Performance-wise the antenna featured a fractional tuning range of 67%. The two main limitations of the antenna were as follows: firstly the operating frequency could only be tuned in discrete steps and secondly the antenna was rather large with planar dimensions of $0.41\lambda_0 \times 0.41\lambda_0$ at the lowest operating frequency of 1.1 GHz. Additionally the antenna used a lumped inductor near the SMA connector to obtain impedance matching over the entire tunable range which increased system complexity.

A rigid cavity-backed slot antenna that had a continuously adjustable operation frequency as shown in Fig. 9.3 was presented in [62]. To tune the operating frequency a varactor was placed across the slot which was excited by a microstripline. For impedance matching purposes the microstripline incorporated a lumped inductive matching element. In terms of frequency reconfigurability the antenna exhibited a fractional tuning range of 62%. Unfortunately due to the location of the varactor a non-trivial biasing network was needed which included two DC blocking capacitors which is a limitation of this particular design.

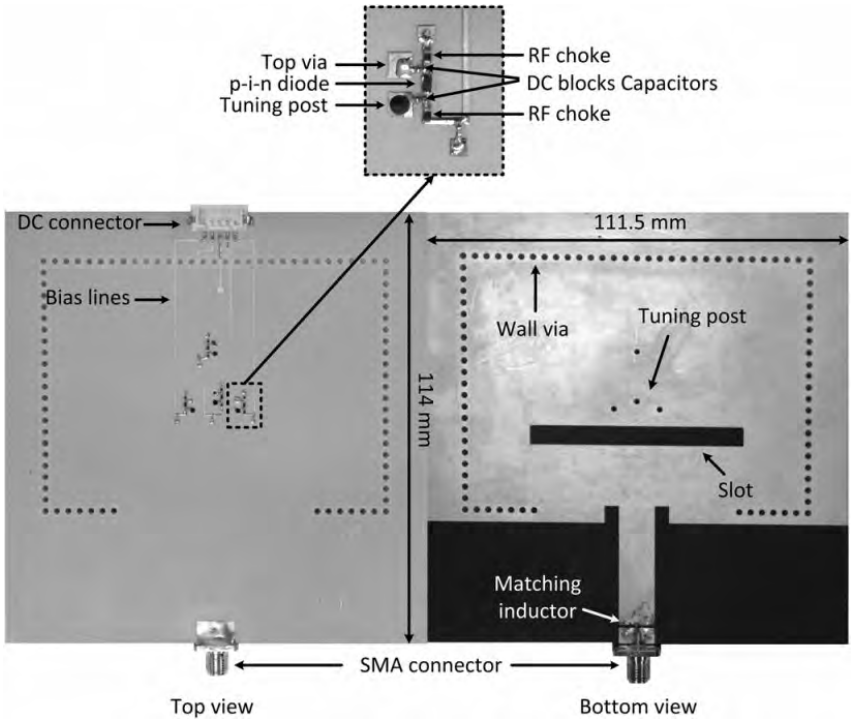

Figure 9.2. A frequency reconfigurable cavity-backed slot antenna with a fractional tuning range of 67% implemented in rigid substrate-integrated waveguide technology. This image is reproduced from [61].

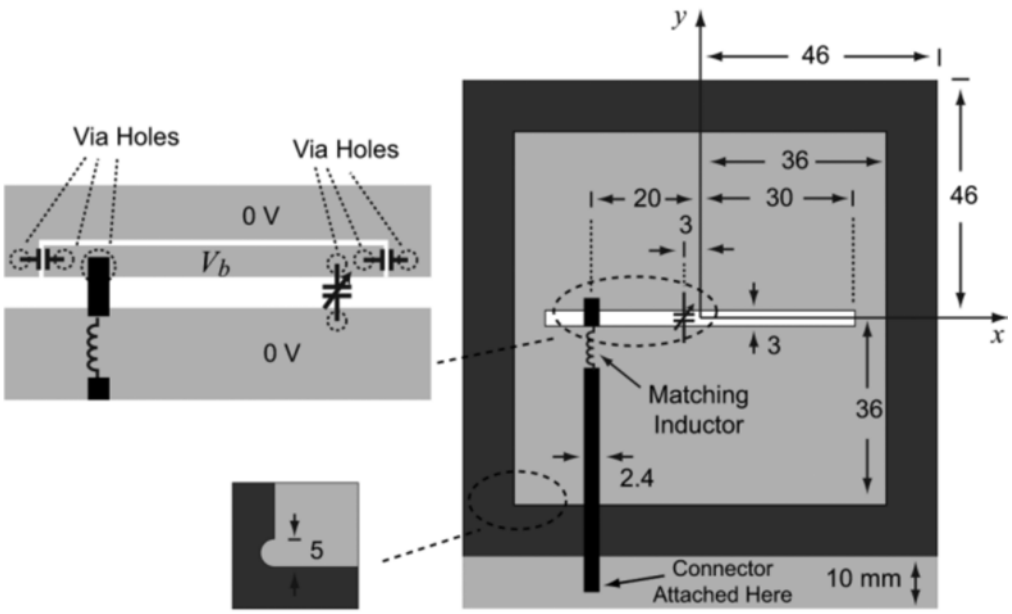

Figure 9.3. A frequency reconfigurable inflexible cavity-backed slot antenna obtained by loading the radiating slot with a varactor. This image is reproduced from [62].

A continuously tunable rigid frequency reconfigurable antenna, as shown in Fig. 9.4, was presented in [63] with a wide fractional tuning range of 67%. The antenna was essentially made from two microstrip patch antennas that were in close proximity to each other where each patch was individually excited by a corresponding microstripline. The large fractional tuning range of the antenna was achieved by using 6 varactors with an associated 9 biasing components. Unfortunately the antenna was rather large with maximum square planar dimensions of $0.67\lambda_0$ at the highest operation frequency of approximately 3.2 GHz and $0.44\lambda_0$ at the lowest operation frequency of 2.1 GHz. It should be noted that the antenna was realized using a substrate with a relative permittivity of 3.02 which would have assisted in miniaturization.

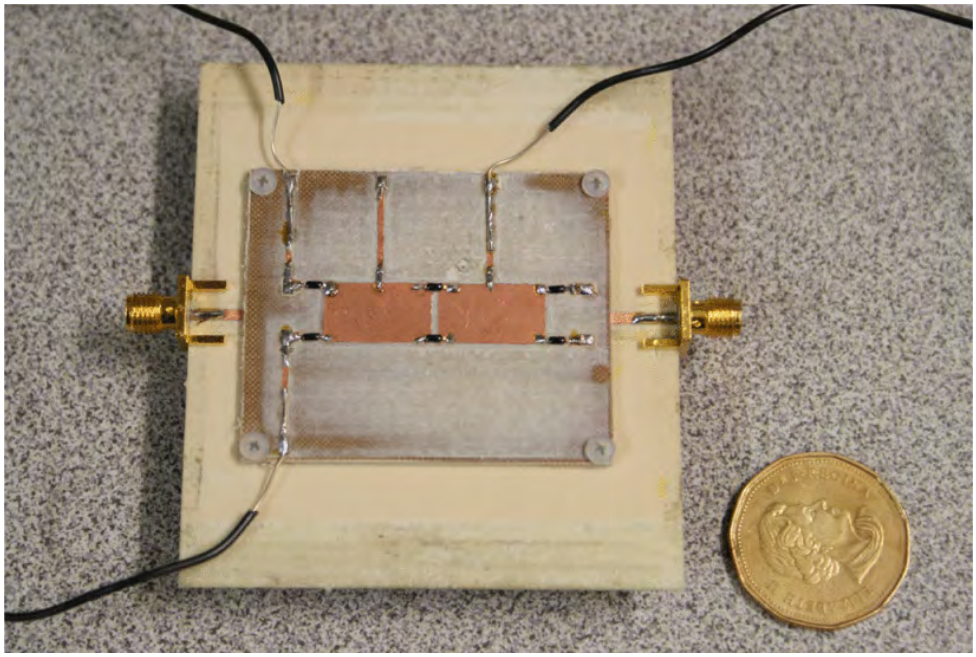

Figure 9.4. An inflexible frequency reconfigurable antenna with a very wide tuning range of 67% using two disconnected patches that are individually fed with microstrip lines. This image is reproduced from [63].

From the aforementioned discussions there are two key aspects that can be extracted. Firstly, frequency reconfigurable antennas which have an appreciable fractional tuning range tend to be physically large. Secondly, frequency reconfigurable antennas that are excited through a planar feeding mechanism usually require a lumped element for impedance matching purposes which is undesirable as it increases system complexity. In this context it is desirable to have a compact low-profile frequency reconfigurable antenna that can be excited through a planar feeding mechanism without the need for lumped matching elements. Motivated by these desires this chapter

presents a new frequency reconfigurable broad-slot multi-layer cavity antenna with a fractional tuning range of 20%. A salient feature of the current antenna is that it can be impedance matched without lumped matching elements. The lack of lumped elements for impedance matching purposes distinguishes the current design from a majority of other planar fed frequency reconfigurable antennas. Additionally in this design the reconfiguration elements (varactors) are embedded within the cavity structure which helps isolate the varactors from adverse mechanical forces.

9.2 Reconfigurable Cavity Antenna - Geometry Overview

The remainder of the current chapter deals with the design, realization and experimental validation of a new type of frequency reconfigurable cavity antenna. The geometry which is schematically depicted in Fig. 9.5 is similar to the multi-layer broad-slot cavity-backed antenna introduced in chapter 6. There are however two major differences: firstly, the current antenna has a slot in the middle layer and secondly the cavity has not been cut in half. The proposed antenna is excited by a coplanar waveguide (CPW) which is in the middle layer of the antenna as shown in Fig. 9.5(b). The operating frequency is adjustable by changing the capacitance between the middle layer and the cavity walls as will be described in detail in the following discussions. The bottom layer is a ground plane which has a small rectangular hole cut out for biasing purposes as will also be expanded upon in the following discussions. The antenna is designed to operate from approximately 2.0 to 2.45 GHz for the purposes of illustration. A salient feature of the antenna is the excellent impedance matching over a 20% tuning range through a planar feeding mechanism which does not require lumped matching elements. For the sake of validation, the antenna is implemented in PCB technology, but the geometry has been developed keeping in mind the feasibility of future implementation as flexible wearable cavity antenna.

9.3 Design Methodology

9.3.1 Cavity Design

Based on the desired tuning range, which in this case is 2.0 - 2.45 GHz for the purpose of demonstration, the first step of the design procedure is to realize a standard cavity-backed slot antenna resonating at the desired highest frequency, i.e 2.45 GHz. The

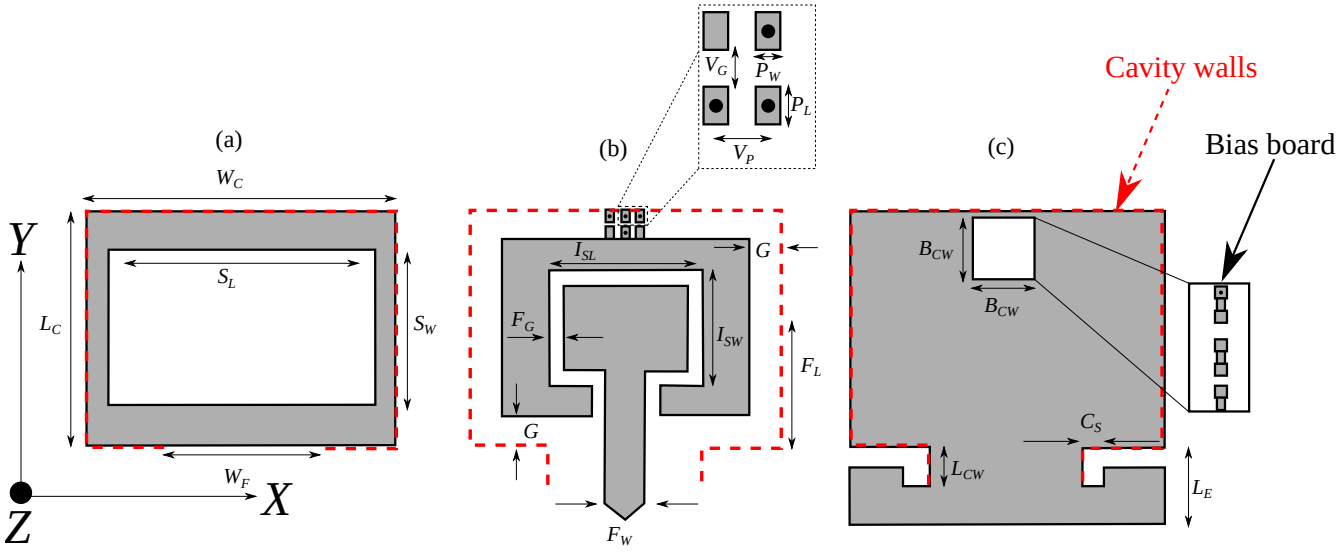

Figure 9.5. Layered view of the proposed antenna. From left to right: (a) Top layer which contains a broad radiating slot, (b) Middle layer which contains the feeding elements and varactors, (c) Bottom layer which contains the ground plane. Behind the ground plane is a small substrate which contains the bias network. The optimized parameters are: $W_C = 40$ mm, $L_C = 30.5$ mm, $S_W = 20$ mm, $S_L = 34$ mm, $W_F = 20$ mm, $P_W = 1.0$ mm, $P_L = 1.5$ mm, $V_P = 2$ mm, $V_G = 1$ mm, $I_{SW} = 5$ mm, $I_{SL} = 8$ mm, $F_G = 0.5$ mm, $F_{LW} = 5.0$ mm, $F_L = 11.25$ mm, $G = 4$ mm, $L_{CW} = 5$ mm, $C_S = 3$ mm, $L_E = 10$ mm, $B_{CW} = 1.5$ mm.

design of the standard cavity-backed slot antenna begins by determining the planar dimensions of the cavity which should be approximately $0.5\lambda_G \times 0.5\lambda_G$ where λ_G is the guide-wavelength that can be determined in accordance to the procedure in [123]. For this design the cavity substrate is realized from Rogers Duroid 5880 which has a relative permittivity ($\epsilon_r = 2.2$) and a loss tangent (tanδ = of 0.0009) over the desired frequency range. In the initial stages the cavity thickness is set at 1.6 mm.

The next step of the design is to cut out a slot on one of the metal layers of the cavity to create a cavity-backed slot antenna. The length of the slot should be mildly smaller than the planar dimensions of the cavity. As an empirical guideline determined from simulations it is suggested that the length of the slot should be approximately 20% shorter than the planar dimensions of the cavity. In the initial stages, the width of the slot can be set at 2% of the planar dimensions of the cavity. Later these parameters will be optimized in view of the tuning range. Henceforth the metal layer with the slot will be known as the top ground plane while the opposite metal layer will be known as the bottom ground plane. For now, the antenna can be excited through an SMA connector

where the body of the SMA connector is flush against the bottom ground plane. The inner pin of the SMA should protrude through the cavity substrate and short circuit the top ground plane at a location denoted as F_S in Fig. 9.6(a). A section of the cavity walls, which are fully across the length and width of the cavity, are encapsulated by the dashed red lines in Fig. 9.6.

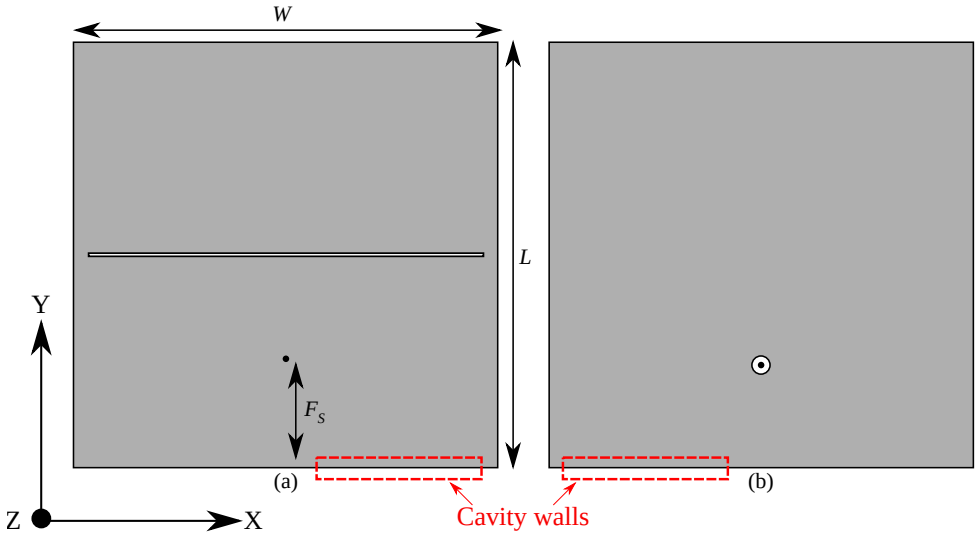

Figure 9.6. Top ground plane of the standard cavity-backed slot antenna (a) and bottom ground plane of the standard cavity-backed slot antenna (b).

The next phase of the design is to make the antenna multi-layer as described in chapter 6 section 6.3 resulting in the geometry depicted in Fig. 9.7(c). At this stage the length and width of the multi-layer cavity, denoted as W' and L' in Fig. 9.7(c), should be unequal. However, for the sake of analytical simplicity, after making the antenna multi-layer the length is set to be the same value as the width of the cavity resulting in a square cavity. Additionally, the gap between the middle plate and the cavity walls should be *at least* 3 mm. The reason for this absolute value is to incorporate the reconfiguration elements as will become clear in the following discussions.

At this stage the cavity thickness should be 3.2 mm, as obtained in the "folding" process from two substrates with equal thicknesses of 1.6 mm. As discussed in chapter 6 due to the presence of a disconnected middle metallic layer, there exists a capacitance between the middle layer and the cavity walls which influences the operation frequency of the antenna. Specifically, by reducing the dimensions of the gap, a downshift in the resonance frequency can be obtained due to the increased capacitance between the middle layer and the cavity walls. In this regard, Fig. 9.8 shows how the resonance frequency is altered by reducing the gap dimensions from 3 mm to 1 mm

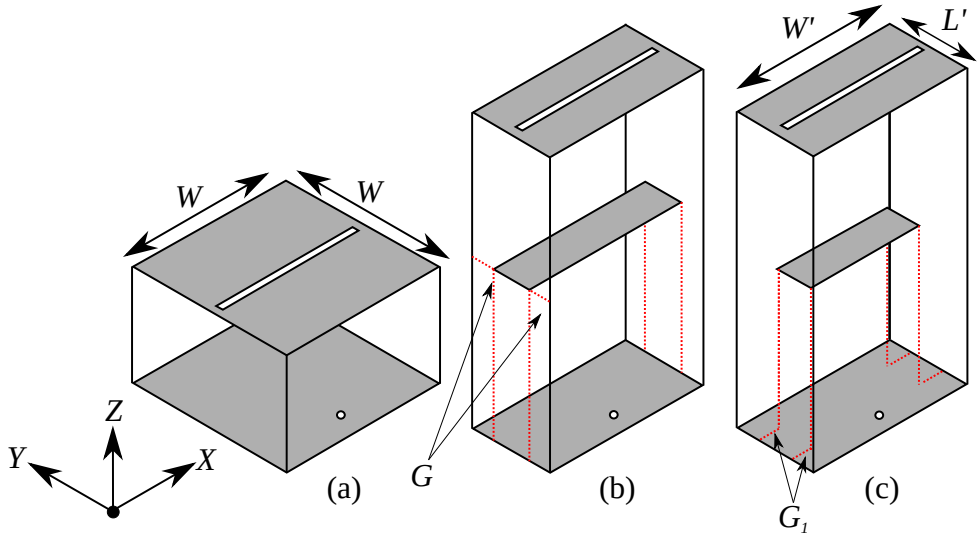

Figure 9.7. A depiction of how the cavity topology is modified as a consequence of the "folding" operations. From left to right: (a) Standard cavity, (b) Folded cavity and (c) Multi-layer cavity.

for the *square multi-layer cavity. As expected, the "folding" operations significantly reduce the operation frequency of the cavity. The cavity topology is shown in the inset of Fig. 9.8.* As the operation frequency of the antenna is well below 2.45 GHz, the next phase of the design is to scale back the antenna to operate at the desired resonance frequency of 2.45 GHz. There exist three means to scale up the resonance frequency as listed below and represented in Fig. 1.14:

1. Miniaturize the dimensions of the cavity till the antenna resonates at the desired highest frequency of operation. In this case the length and width of the cavity become $W_1 = L_1 = 38.2$ mm whilst the length and width of the slot are $SL_1 = 28.2$ mm and SW_1 1 mm respectively. *Henceforth this is known as Solution one.*

2. Miniaturize the dimensions of the cavity till the antenna resonates at approximately 10% (chosen for the purposes of illustration) below the desired highest frequency and then reduce the length of slot till the antenna resonates at 2.45 GHz. In this case the length and width of the cavity are $W_2 = L_2 = 41.5$ mm whilst the length and width of the top slot are $SL_2 = 23.5$ mm and $SW_2 = 1$ mm respectively. *Henceforth this is known as Solution two.*

3. Miniaturize the dimensions of the cavity till the antenna resonates at approximately 10% (once again chosen for the purposes of illustration) below the desired highest frequency and increase the width of top slot till the antenna resonates at 2.45 GHz. In this case the length and width of the cavity are $W_3 = L_3$ 41.5 mm

whilst the length and width of the top slot are $SL_3 = 31.5$ mm and $SW_3 = 32.7$ mm respectively. *Henceforth this is known as Solution three.*

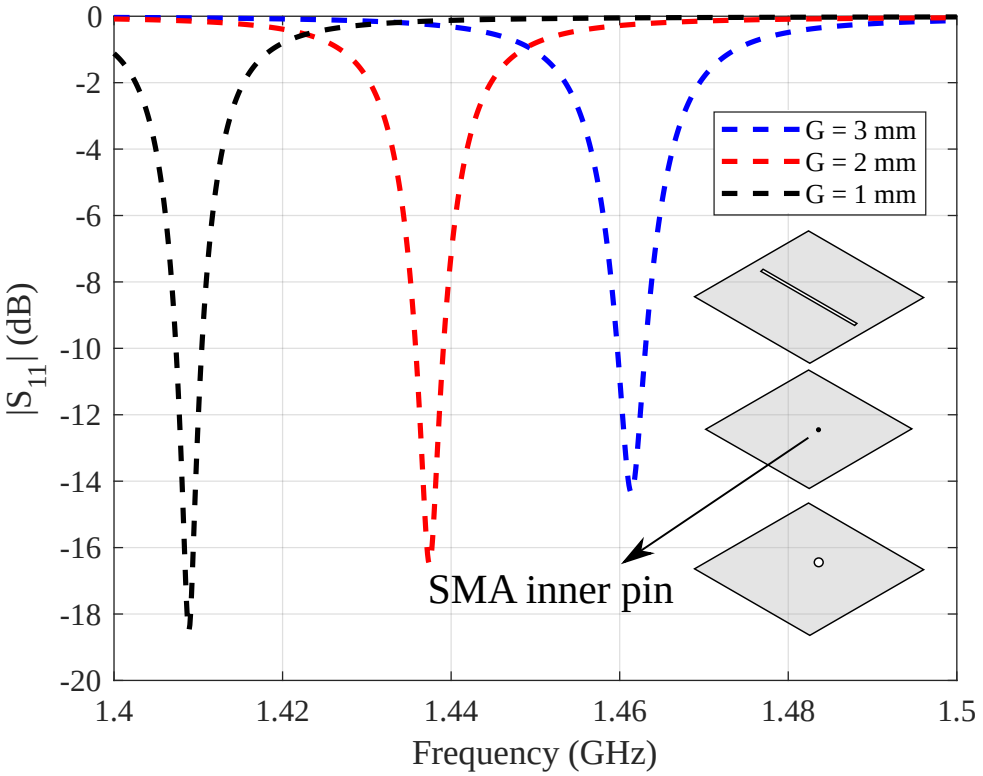

Figure 9.8. Variation in the resonance frequency as a function of the capacitive gap between the middle layer and the cavity walls when the standard cavity-backed slot antenna is transformed into a square multi-layer cavity. The inset shows the topology of the antenna.

The top layer of the cavity for each of the aforementioned solutions is shown in Fig. 9.9. At this stage the design of the cavity without any reconfiguration is completed and the focus is shifted to the incorporation on reconfigurability.

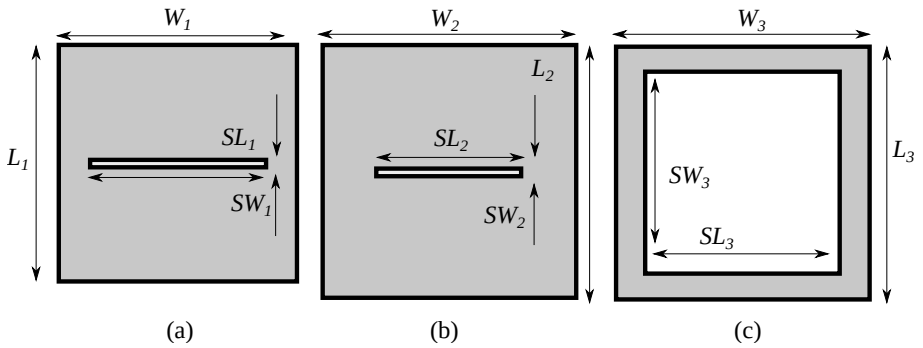

Figure 9.9. A schematic view of how the top layer of the cavity for each of the aforementioned solutions. From left to right: (a) Solution One, (b) Solution Two and (c) Solution Three.

9.3.2 Incorporation of the Reconfigurability

From the previous discussions, and more specifically from Fig. 9.8, it is evident that altering the gap between the middle metallic layer and the cavity walls can adjust the operation frequency. In particular, if the gap was to be made narrower, then the resonance frequency will shift downwards. The downshift in resonance frequency for a smaller gap dimension is attributed to the increased capacitance between the middle layer and the cavity walls. Now, if the capacitance across the gap can *electronically* be made larger, then the resonance frequency should shift downwards in a similar manner as when reducing the gap size. This can be achieved by utilizing a lumped element known as a varactor (variable capacitor) between the middle layer and the cavity walls. The reconfiguration mechanism can then be understood as follows: *adjusting the varactor capacitance in a capacitively sensitive region of the antenna alters the overall antenna capacitance, allowing the operation frequency to be tuned*. In the initial design stages, a single varactor can be used but later, the number of varactors will be increased in view of improving the radiation efficiency. To include the varactor in simulations two small pads (henceforth known as the varactor pads) are incorporated into the middle layer of the antenna as shown by the inset of Fig. 9.10.

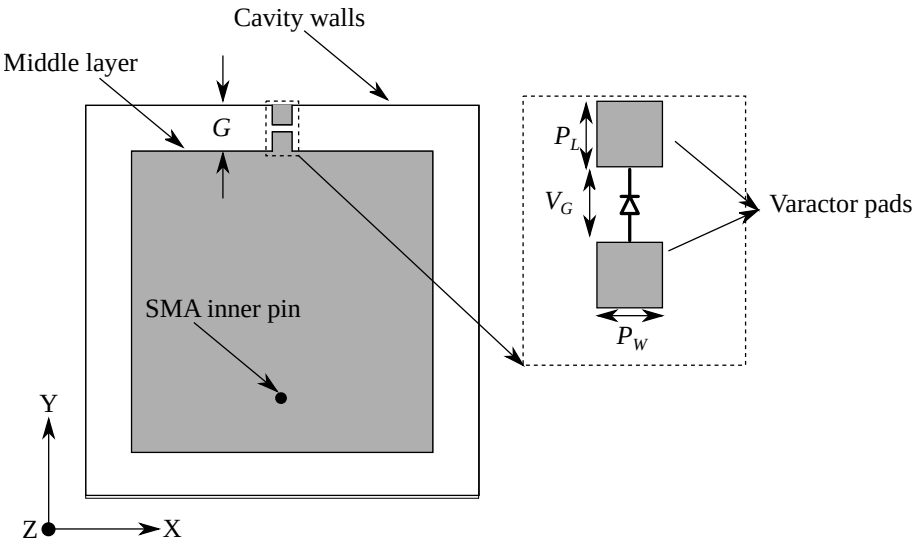

Figure 9.10. The topology of the middle layer after the inclusion of the varactor pads.

The length of these pads, which is denoted as P_L in Fig. 9.10, is calculated as: $P_L = 0.5 \times (G - V_G)$, where G is the gap between the middle layer and the cavity walls whilst V_G is the length of the varactor which is 1.5 mm. The varactors selected for this design have the SC-79 footprint for which the nominal length (including the component leads) is

1.5 mm. This leads to a value of P_L = 0.75 mm. Now the rationale for selecting the minimum gap size to be 3 mm can be understood, since this gap must accommodate the physical dimensions of the varactor and the corresponding varactor pads. The width of the varactor pads which is denoted as P_W in Fig. 9.10 is set to be 1 mm to account the typical widthwise footprint of SC-79 components. Finally, to provide space for the physical thickness of the varactors, a small trench is cut out of the underside of the top substrate. The depth of this trench is set at 1 mm which is deeper than the typical height of SC-79 components. The lateral dimensions of the trench should be large enough to encapsulate the varactor pads.

The varactor is then modeled as a lumped series RLC element between the varactor pads. In the initial design stages, the parasitic inductance and resistance can be set to zero while the capacitance is parameterized to identify the most appropriate range for selection of practical devices. The parasitic parameters will be determined from datasheets after selection of appropriate varactors with a capacitance tuning range as required by the design. At this stage, the middle layer of the antenna should resemble Fig. 9.10. The next phase of the design is to observe which parameters, i.e the cavity size or the slot dimensions, are most critical in altering the operating frequency of the antenna. This can be achieved by observing the variation in the operating frequency for the three solutions, shown in Fig. 9.10, that were introduced in the last section. As the three solutions were largely obtained by optimizing different parameters, the variation in the resonance frequency as a function of the varactor capacitance gives an indication of which parameters have the greatest effect on the tuning range. Consequently, for each of the three solutions shown in Fig. 9.10 a parameter sweep over a large capacitance range is performed.

The variation in resonance frequency as a function of varactor capacitance for the three aforementioned solutions is shown in Fig. 9.11. A zoomed in version of the same graph over the capacitance range of 0.9 pF - 11 pF is provided in Fig. 9.12. This selected capacitance range is chosen as it represents the region where the largest variation in the resonance frequency is observed. For the purposes of illustration, and following the design framework presented in [167], a typical maximum to minimum capacitance ratio of 10:1, is considered for evaluation of each of the solutions. An appropriate capacitance range of 1.0 pF - 10.0 pF is represented by the shaded grey region of Fig. 9.12. The fractional tuning range is defined as $TR = (F_{\text{Max}} - F_{\text{Min}}/F_{\text{Max}} + F_{\text{Min}}) \times 100$.

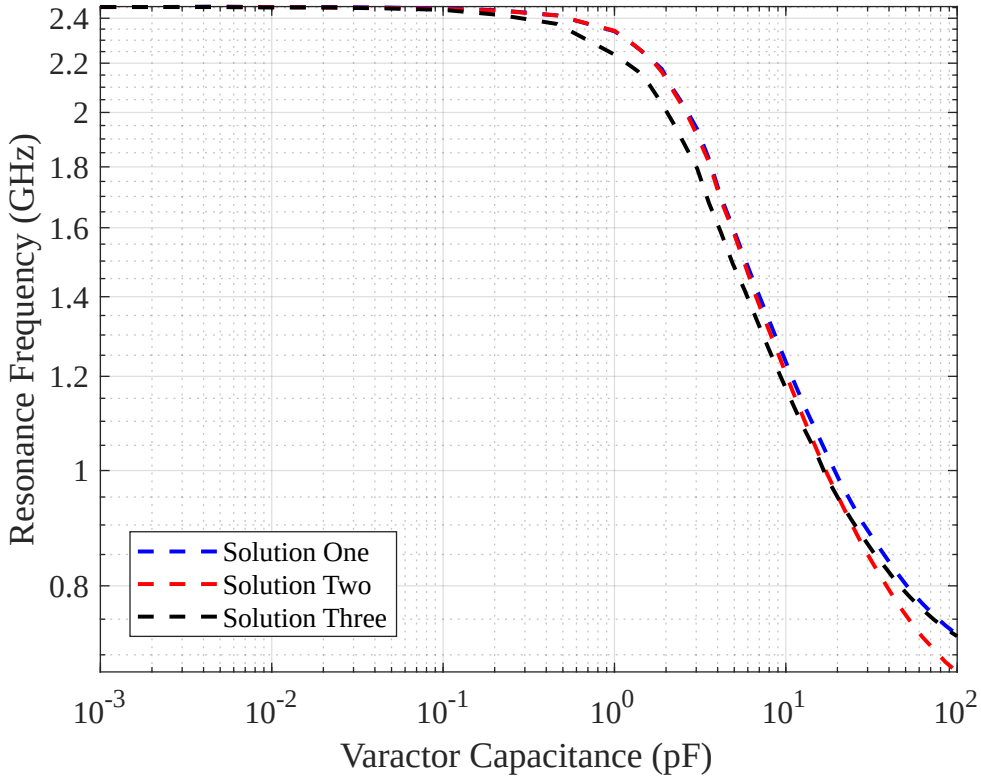

Figure 9.11. Variation in the resonance frequency as a function of varactor capacitance for three different values of cavity and slot dimensions described previously as: Solution one, Solution two and Solution Three.

Numerically, the fractional tuning range amounts to 62%, 64% and 63% for solution one, two and three respectively. The fact that these values are rather similar suggest that either the cavity size, slot length or slot width could be used to optimize the tuning range. Therefore, to make a holistic judgment on which parameter is the most critical, another performance metric must be considered. For reconfigurable antennas the other performance metric tends to be the radiation efficiency. Consequently, the variation in the radiation efficiency as a function of varactor capacitance for all three solutions is provided from Fig. 9.13 to Fig. 9.15. For the purposes of illustration, a varactor internal resistance of 1.0 Ω is considered.

Persisting with the capacitance range from 1.0 - 10.0 pF, it can clearly be seen that solution three, i.e the solution obtained by increasing slot width, results in the largest radiation efficiency at 1.0 pF. Additionally, for all the solutions at a capacitance of 10.0 pF the radiation efficiency drops to almost 0%. Consequently, in view of balancing the tuning range and radiation efficiency it is suggested that the main parameter to be optimized is the slot width. Additionally across all solutions, it is observed that the capacitance range which corresponds to the largest reduction in the resonance frequency

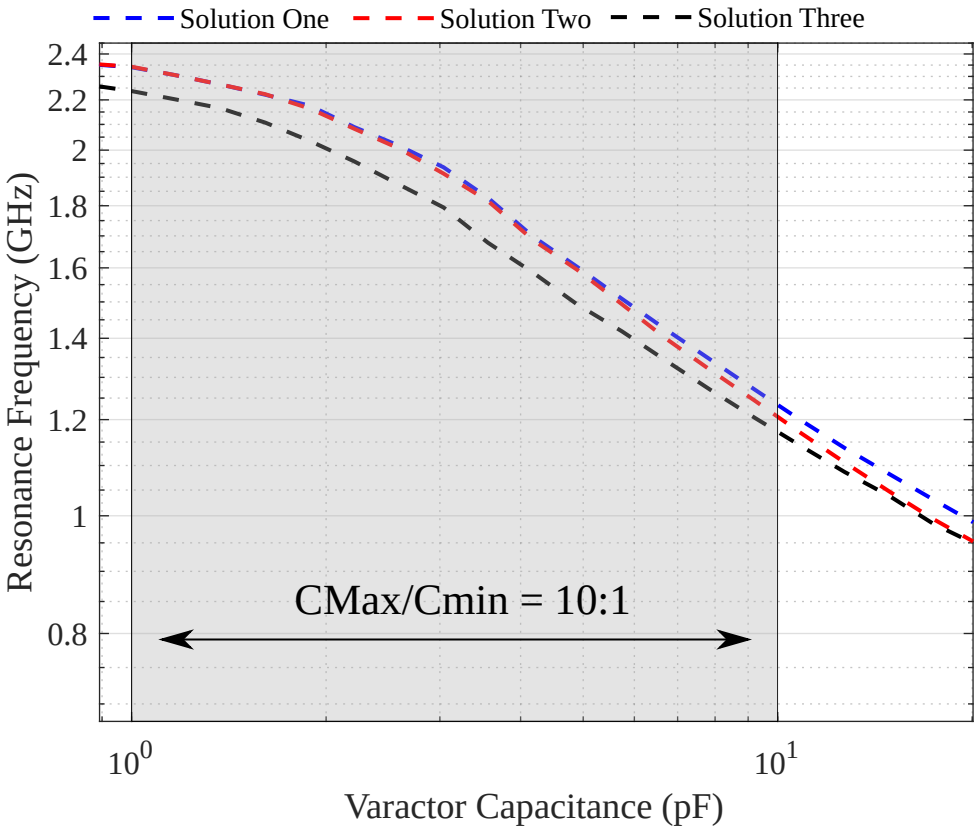

Figure 9.12. A zoomed in version of Fig. 9.11 over the capacitance range of approximately 1.0 - 10 pF. This range has been chosen as it represents a region where there is a large variation in the operating frequency.

also corresponds to the region with the largest reduction in the radiation efficiency. Therefore, at this stage it is important decide upon the minimum desired radiation efficiency. For this design the minimum target radiation efficiency is set at 40% which is generally deemed acceptable for reconfigurable applications [60]. Based on Fig. 9.15 to obtain a minimum radiation efficiency of 40% a maximum capacitance value of 1.6 pF is needed. Additionally, from Fig. 9.15 the minimum capacitance value can be taken as 0.1 pF as there is a minimal variation in the operating frequency below this value. Therefore, for these particular dimensions a varactor with a capacitance range of 16:1 is required. Generally, it is not always possible to find a single varactor with the desired capacitance range. The common approach to circumvent this limitation is to combine multiple varactors in parallel to provide the requisite capacitance whilst also improving the radiation efficiency [167]. In this design for reasons of system complexity, the maximum number of varactors is set at 3. Now, consider Fig. 9.16 which shows the

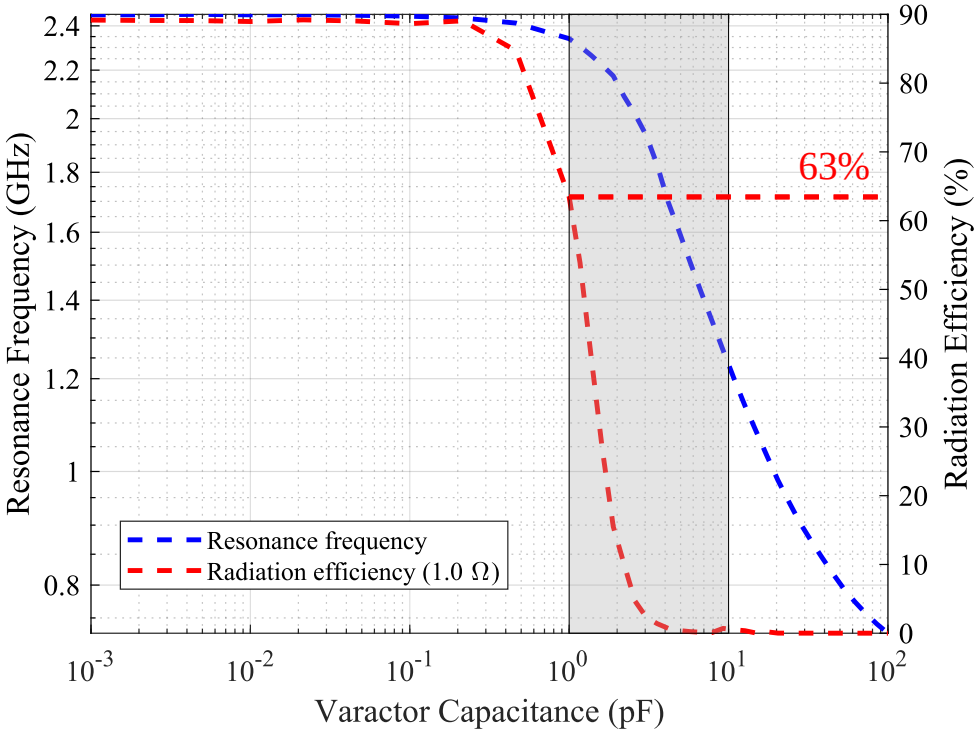

Figure 9.13. Variation in the resonance frequency and radiation efficiency as a function of varactor capacitance for solution one.

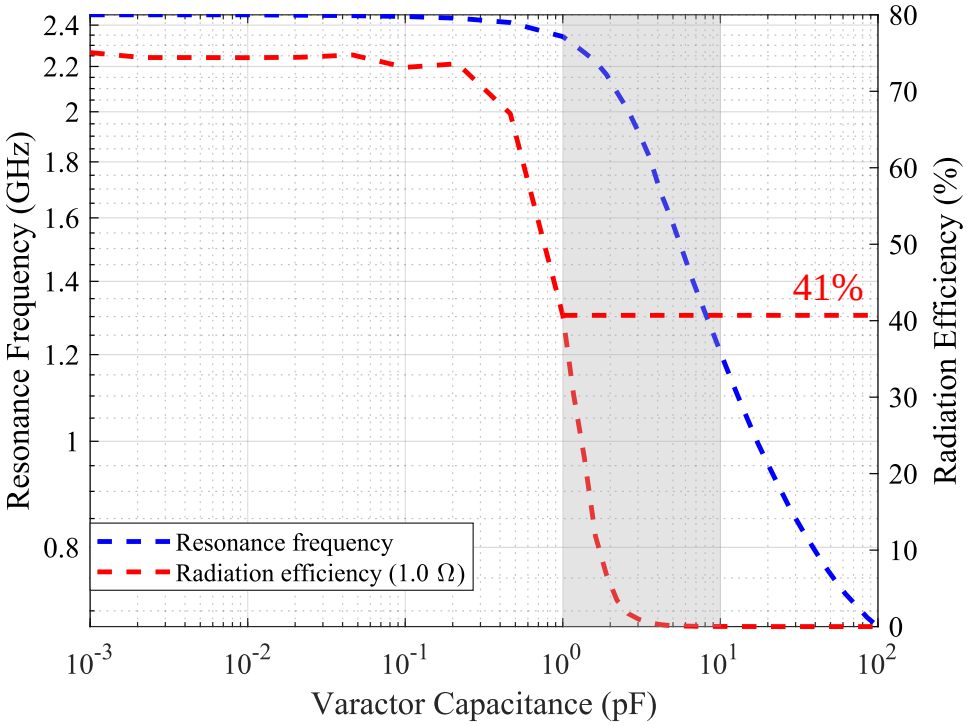

Figure 9.14. Variation in the resonance frequency and radiation efficiency as a function of varactor capacitance for solution two.

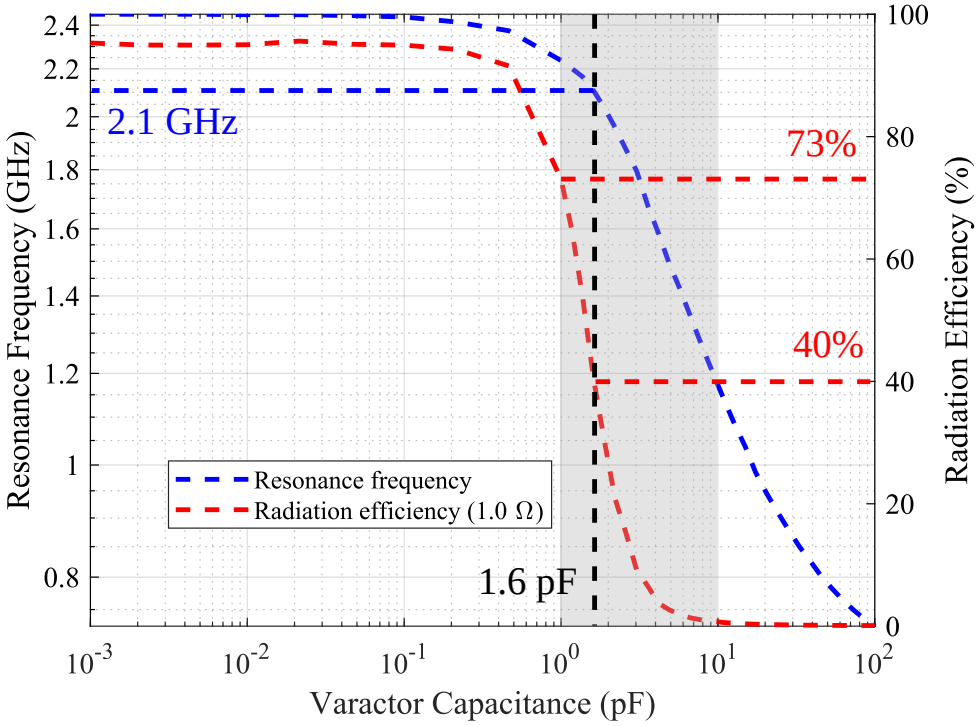

Figure 9.15. Variation in the resonance frequency and radiation efficiency as a function of varactor capacitance for solution three.

variation in the resonance frequency and radiation efficiency for solution three assuming three varactors. Clearly, it is observed that the capacitance which results in a minimum radiation efficiency of 40% amounts to 1.1 pF. Therefore, assuming that the minimum capacitance value is 0.1 pF these results suggest that a capacitance ratio of 11:1 is required. One option is to use Skyworks SMV2202 varactors which have a capacitance range from 0.31 pF - 3.14 pF which amounts to a capacitance ratio of approximately 10:1. Unfortunately, these varactors have a rather large internal resistance of 3.0 Ω which would result in a substantial reduction in the radiation efficiency. Generally, it is challenging to find varactors which simultaneously have a large capacitance ratio and small internal resistance. On the contrary, varactors which have a smaller capacitance range tend to have a smaller internal resistance. Consider now Fig. 9.17 which shows a zoomed in version of Fig. 9.16 segmented into three distinct regions. For the sake of clarity the radiation efficiency has been removed. The first, second and third regions corresponds to a capacitance from 0.1 - 0.4 pF, 0.4 - 1.6 and 1.6 - 6.4 pF. In all three regions of Fig. 9.17 the ratio of the maximum to minimum capacitance is 4:1 which is chosen for the purposes of illustration. The fractional tuning range for these three regions are: 8%, 22% and 45% respectively. Whilst region three has the largest tuning range it also corresponds to region of lowest radiation efficiency. Therefore, for

this design, varactors which have the intermediate capacitance range from approximately 0.4 - 1.6 pF, or equivalently a maximum to minimum capacitance of 4:1 should be selected. A close match can be found in the Skyworks SMV1405 varactors which have a capacitance range from 0.63 - 2.67 pF, or equivalently a maximum to minimum capacitance of 4:1. Henceforth, these varactors will be used. At this stage the internal inductance and resistance of the varactor are set at 0.7 nH and 0.8 Ω as determined from the datasheet for this varactor. Additionally, for this design using the Skyworks SMV1405 varactors the antenna is scaled to operate at 2.45 GHz. This last step is utilized to reduce the planar dimensions of the antenna. The upscaling of the resonance frequency is achieved through a combination of changing the gap dimension and the dimensions of the cavity. If need be, the dimensions of the slot can also be fine-tuned.

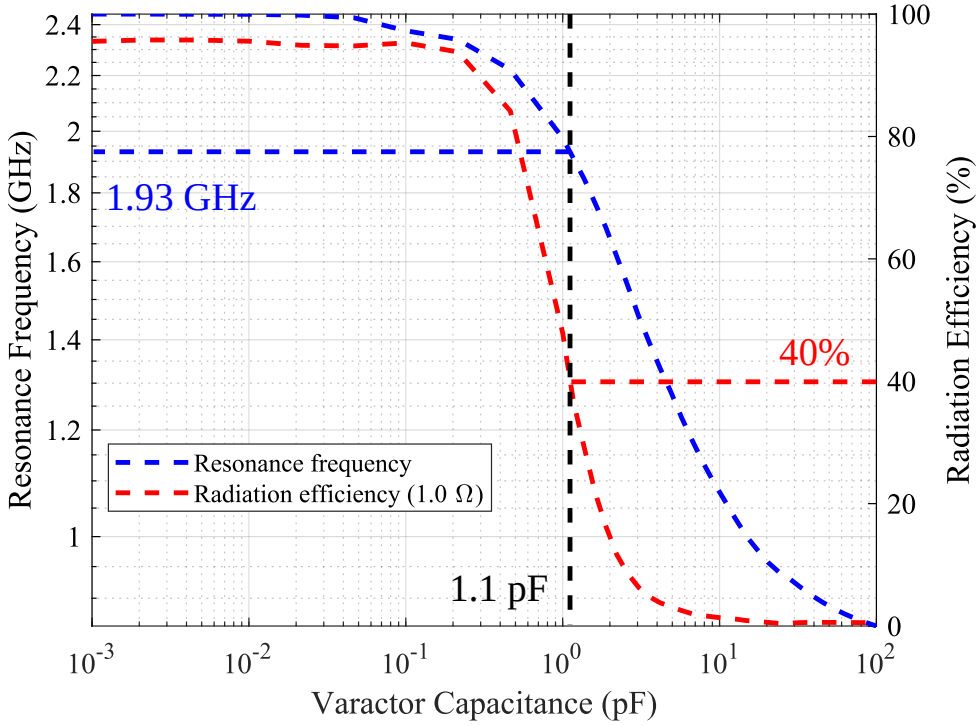

Figure 9.16. Variation in the resonance frequency and radiation efficiency for solution three using three varactors.

9.3.3 Feeding and Biasing

The next phase of the design is the incorporation of a planar feeding mechanism. Prior to introducing the planar feeding mechanism it is helpful to consider what is known as a DC bias network. A DC bias network which is an essential component of any reconfigurable antenna has two main functions as listed below:

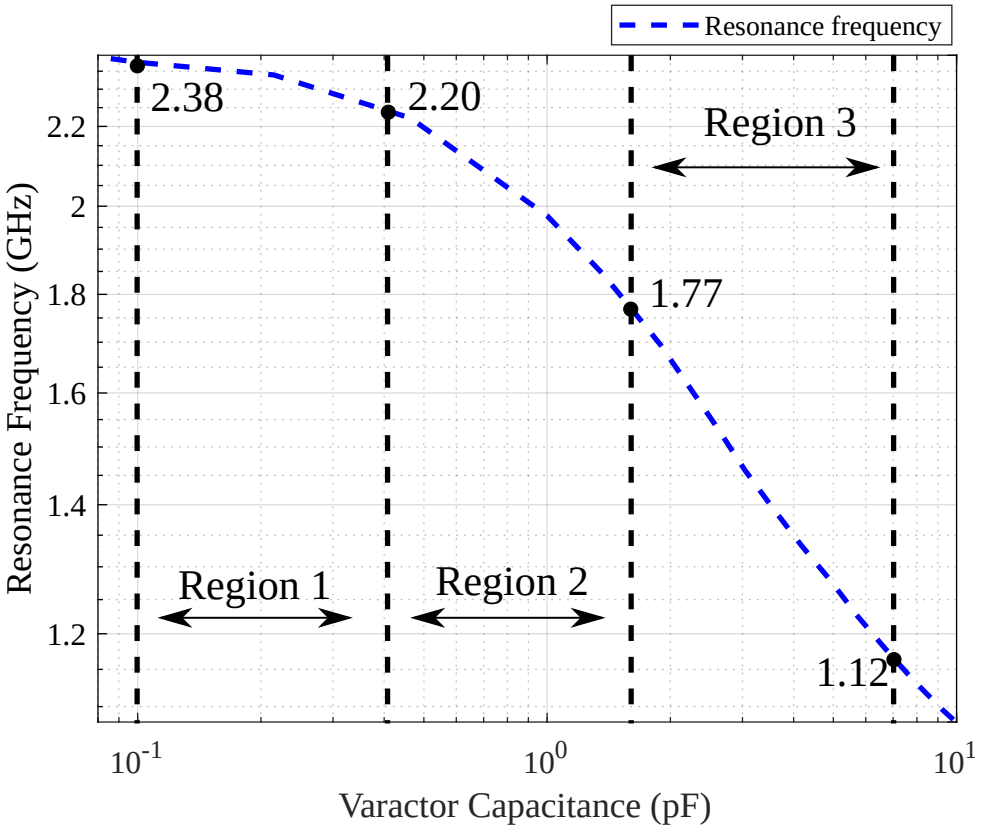

Figure 9.17. A zoomed in version of the variation in the resonance frequency as a function of varactor capacitance for solution three using three varactors. Three regions known as Region 1, Region 2 and Region 3 corresponding to a capacitance range from 0.1 - 0.4 pF, 0.4 - 1.6 pF and 1.6 - 6.4 pF are shown. In all three regions the ratio of maximum to minimum capacitance is 4:1.

1. Prevent DC voltages which are required for operating the varactors from interfering with the RF source.

2. Isolate the RF components from the DC sources.

The choice of the feeding mechanism can either facilitate or impede the first requirement (i.e. isolation of the DC voltages from the RF source). As a first considered option, Fig. 9.18(a) shows the topology of the middle layer assuming that a shielded stripline which is itself excited by a coaxial line would be used as the feeding mechanism. In this case, one of the varactor pads is directly DC-connected to the inner pin of the exciting coaxial element. Thus this feeding mechanism *does not isolate the DC signal from the exciting RF source*. The nominal topology can be amended to include a DC blocking capacitor between one of the varactor pads and the middle layer for isolation purposes as in [155]. However, the introduction of a DC blocking capacitor would increase system complexity which is undesirable. For the aforementioned reasons an alternative

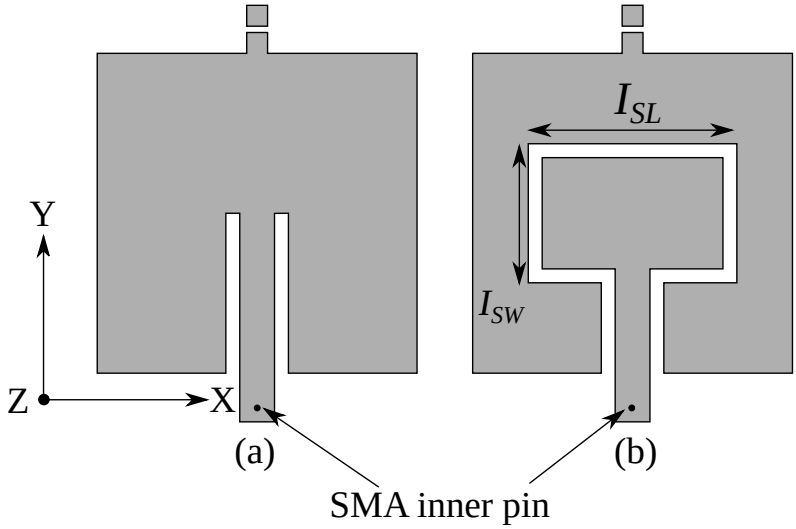

Figure 9.18. Two potential planar feeding mechanisms: (a) Shielded stripline and (b) Capacitively excited CPW.

feeding mechanism which inherently isolates the varactor pad that is connected to the middle layer from the inner pin of the coaxial line is desirable. One option would be to use a capacitively coupled CPW feeding mechanism, which was briefly introduced in chapter 6 section 6.7, as shown in Fig. 9.18(b). The first step in realizing the CPW feeding mechanism is to cut a slot in the middle plate. For simplicity, this slot is centered on middle plate. The length and width of this slot which is henceforth known as the interior slot is denoted as I_{SL} and I_{SW} in Fig. 9.18(b). Initially, I_{SL} and I_{SW} can be made equal with a numerical value of 7 mm. The rationale for selecting this value will be expanded upon in the following discussions. To incorporate the CPW feeding mechanism the nominal topology must be amended in accordance with the following procedure:

1. The first step is to extend the bottom substrate by the dimension L_E as shown in Fig. 9.19(a).

2. After extending the bottom substrate by L_E, the next step is to make a cut in one of the back cavity walls as shown in Fig. 9.19(b). The width of the cut, which is denoted as W_F in Fig. 9.19(b), is chosen such that the fringing fields of the feeding line are not affected by the proximity of the cavity walls which will be introduced in the last step. For now, the width of the cut can be set at 20 mm which is an empirical guideline determined from numerical simulations.

3. From the position of the aforementioned widthwise cut two lengthwise cavity walls with a length of L_{CW} are introduced as shown in Fig. 9.19(c). The length of this extension can be set at 5 mm. These additional cavity walls allow for more mechanical stability as will be expanded upon in section 9.3.4.

4. Now, the middle layer is modified to include the CPW feeding mechanism which is excited by an edge-fed SMA connector as shown in Fig. 9.19(d). It is emphasized that the region of the feedline outside the dashed black lines in Fig. 9.19(d) is a *microstripline* as there is no metallization on top. The width of the microstripline which is denoted as F_W in Fig. 9.19(d) should be calculated for a 50 Ω characteristic impedance. In this design F_W comes to 5 mm. Now the rationale for making the length and width of the interior slot 7 mm can be appreciated: firstly, the interior slot must be larger than 5 mm to accommodate the feedline. Secondly, the extra 2 mm which is an empirical guideline determined from extensive numerical studies provides an initial range of values over which the capacitive matching gap F_G can be optimized. It is emphasized the capacitive matching gap is the separation between the CPW line and the remainder of the middle layer.

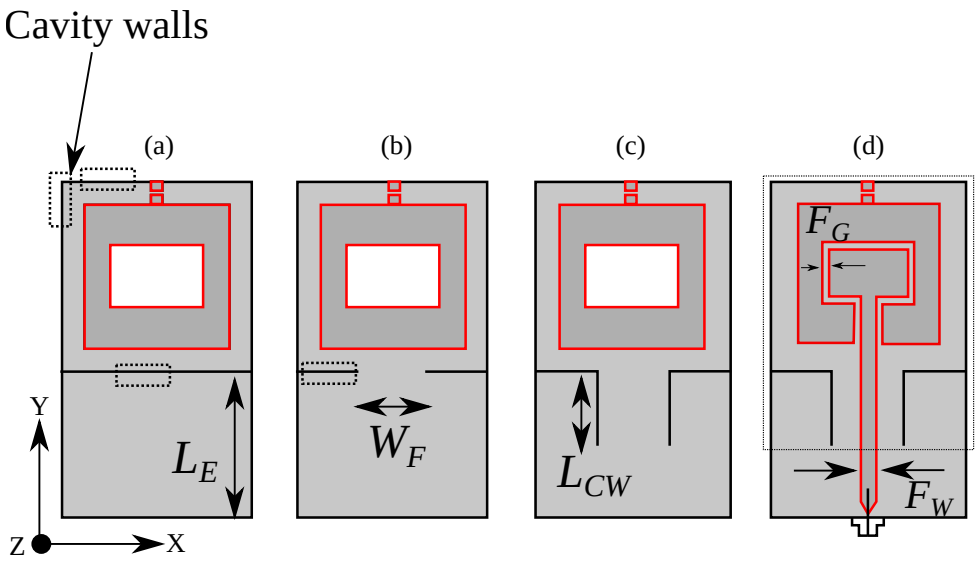

Figure 9.19. Modifications to the cavity structure to accommodate the planar CPW feeding mechanism. The top substrate has been omitted as there is no variation in the topology. The solid red lines depict the middle layer. From left to right (a) Extending the bottom substrate, (b) introducing a width-wise cut in one of th cavity walls, (c) Introducing two length-wise cavity walls from the position of the aforementioned width-wise cut and (d) Introducing the microstripline - CPW feedig mechanism.

The next focus is to deliver the required reverse biased DC voltages across the varactors. In this context consider Fig. 9.20 which depicts the middle layer of the antenna where the varactor pads have been divided into two sets. These two sets are pad set one and pad set two where all of the pads in pad set one and two are held at DC values of V_{DC1} and V_{DC2} respectively. At this point it must be decided whether pad set one or two should act as the ground pads for the varactors. As the varactor pads in pad set one are connected to the cavity walls which themselves are connected to the antenna ground planes, it is only natural to hold the varactor pads within pad set one at 0V DC. In this manner the antenna ground planes act as both an RF and DC ground. To ensure a robust ground connection, each of the varactor pads within pad set one are short circuited to the ground plane through copper vias. As a consequence of making the varactor pads in pad set one ground pads, the varactor pads in pad set two must be held at some non-zero DC voltage. To deliver the DC voltage to the middle metallic layer, a copper via is introduced which on one side is connected to the middle varactor pad in pad set two and on the other side is connected to a bias board whose topology is shown in Fig. 9.21.

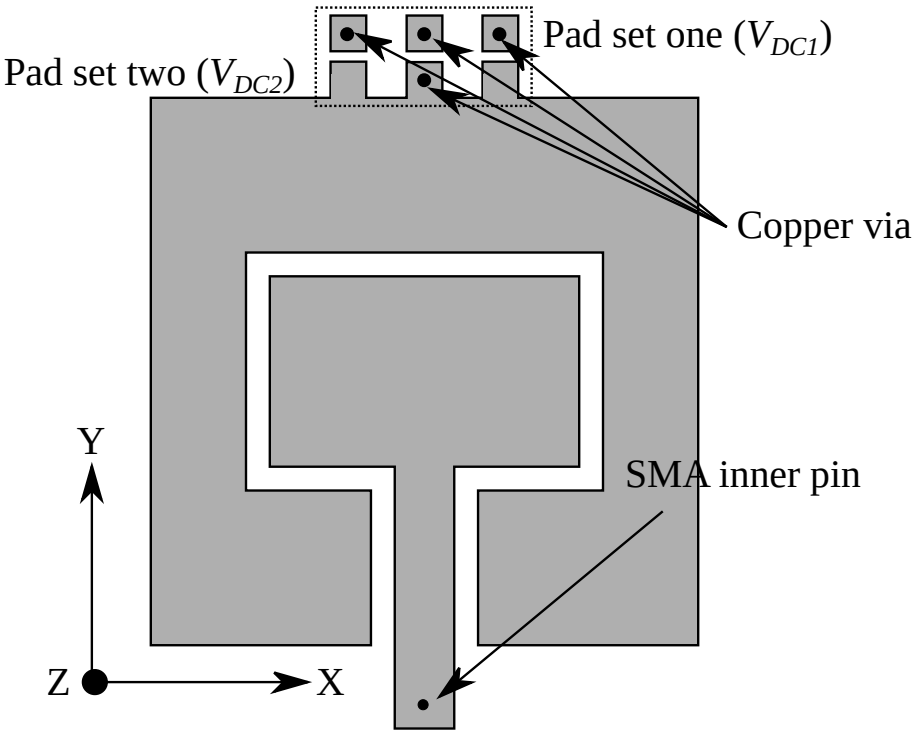

Figure 9.20. A depiction of the middle layer which shows the introduction of shorting rods on the varactor pads for the purposes of biasing.

In addition to delivering the required reverse biased voltage across the varactors this board also serves to isolate the RF component from the DC sources which is applied

at the pad denoted as IC3 in Fig. 9.21. To prevent the RF component at BP1 from interfering with the DC source at IC3 an RF choke is needed. A simple option is to use a sufficiently high inductor. Therefore, a 100 nH inductor is placed between BP5 and BP4. Additionally, to limit the RF current flowing into the varactor a 1 MΩ resistor is placed between BP3 and BP2. These values have been chosen based on prior experience [60]. The remaining sections of copper (i.e IC1 and IC2) are simply to provide physical clearance between the resistor and inductor.

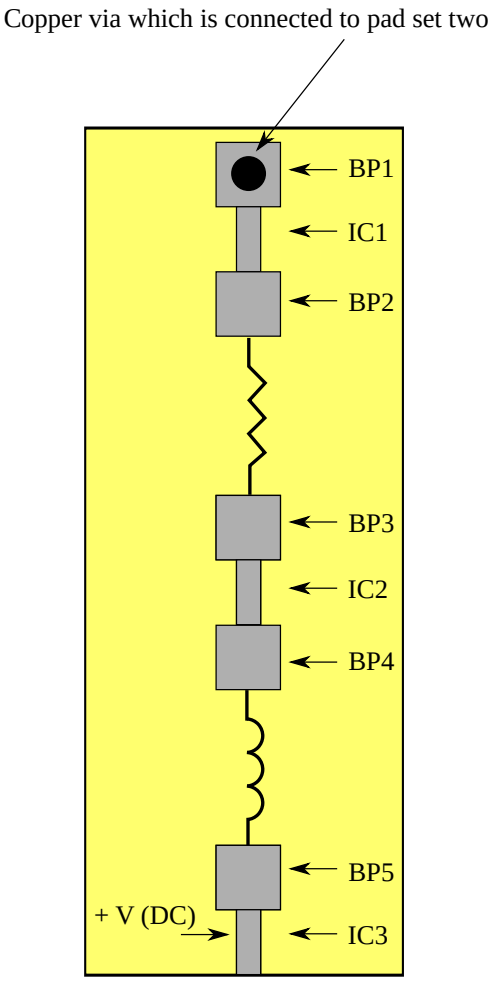

Figure 9.21. The topology of the biasing board which is realized from Rogers Duroid 5880.

9.3.4 Practical Realization

The last step of the design procedure relates to the cavity walls. Till now the simulations have been performed assuming infinitely thin cavity walls which is valid as an initial approximation of the cavity geometry. Realistically cavity walls are usually realized by a number of closely spaced vias [60] which results in a finite sized cavity

walls. Realizing the cavity walls from a number of closely spaced vias can be a time consuming and difficult process especially for a manual fabrication in university settings. Consequently, an alternative method to realize the cavity walls is desirable for manual fabrication. The method which is used in this design is to realize the cavity walls from a single continuous piece of metal. Realizing the cavity walls from a finite thickness material is straight forward for the top substrate as the cavity walls occur at the perimeter. However, for the bottom substrate a section of the cavity walls occur within the substrate. Therefore to access the interior of the bottom substrate a L-shaped cut is made as shown in Fig. 9.5(c). A L-shaped cut is chosen over a simple rectangular cut for reasons of mechanical stability. The width of the L-shaped cut, denoted by C_S in Fig. 9.5(c), is set at 3 mm for fabrication simplicity.

9.3.5 Design Summary

The variation in resonance frequency and radiation efficiency as a function of available varactor capacitance for the final optimized design is shown in Fig. 9.22. From Fig. 9.22 it can be seen that whilst a tuning range from approximately 2.5 GHz - 1.7 GHz is available, which corresponds to a fractional tuning range of 38%, the radiation efficiency at the lowest frequency drops to approximately 15%. Therefore for this design the lowest frequency is capped at approximately 2.0 GHz which corresponds to a fractional tuning range of 20% with a radiation efficiency of 40%.

9.4 Manufacture

The specific multi-step fabrication procedure used to realize the antenna is as follows:

1. Utilize a laser milling machine to realize the top ground plane pattern on one side of a 1.6 mm thick Rogers Duroid 5880 substrate as shown in Fig. 9.23(a). On the other side of the substrate realize a trench with lateral dimensions of 4 mm $\times$ 6 mm and a depth of 1 mm to accommodate the varactors as shown in the inset of Fig. 9.23(b)

2. On another Rogers Duroid 5880 substrate utilize a laser milling machine to realize the middle metallic layer on one side and the bottom ground plane on the other side as shown in Fig. 9.23(c) and Fig. 9.23(d) respectively.

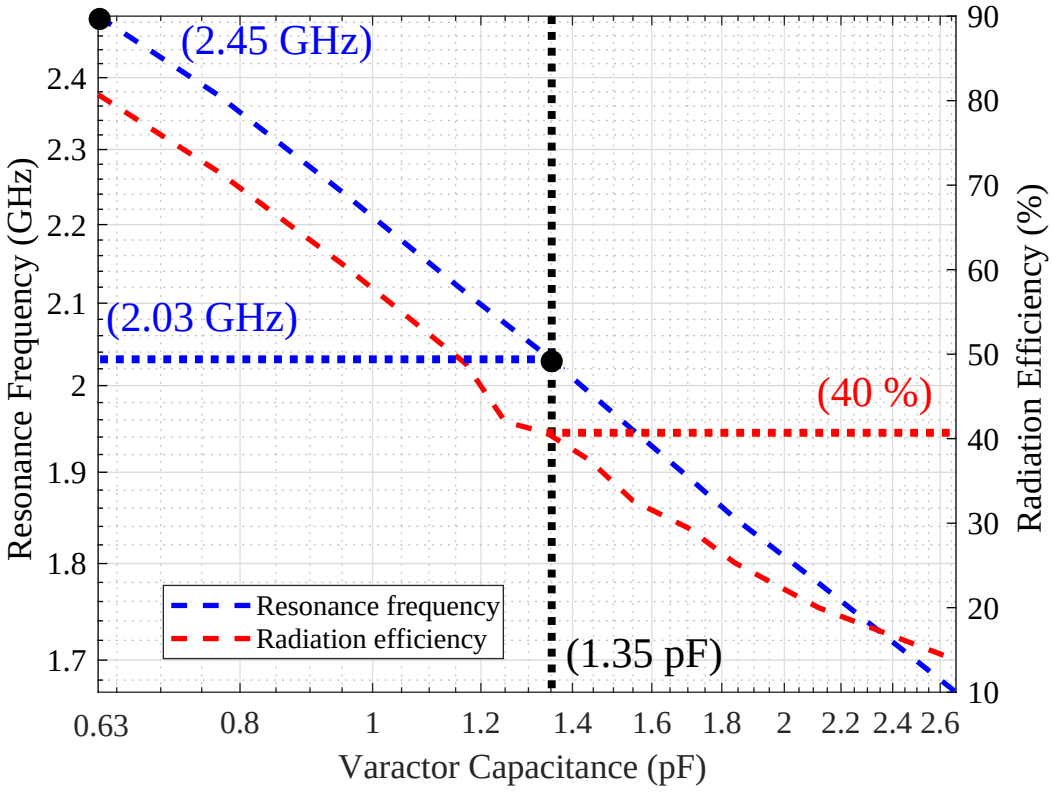

Figure 9.22. Variation in the resonance frequency and radiation efficiency for the antenna.

3. Utilize a laser milling machine to realize the topology of the bias board on a 1.6 mm thick Rogers Duroid 5880 as shown in the inset of Fig. 9.23(d).

4. Solder varactors between the varactor pads on the middle layer.

5. Utilize three copper vias to short circuit each of the varactor pads in pad set one as designated in Fig. 9.20 to the bottom ground plane.

6. Utilize a via to connect the varactor pad on the middle layer with the corresponding pad on the bias substrate.

7. Place the top substrate on top of the bottom substrate.

8. Realize the cavity walls from a single piece of brass through an industrial process known as water jetting. The topology of the cavity walls is shown in Fig. 9.24.

9. Adhere the cavity walls to the substrate through solder.

10. Incorporate an edge-fed SMA connector where the inner pin is in electrical contact with the center conductor of the microstripline which transitions into the

CPW feeding mechanism. The body of the SMA connector should be in electrical contact with the bottom ground plane.

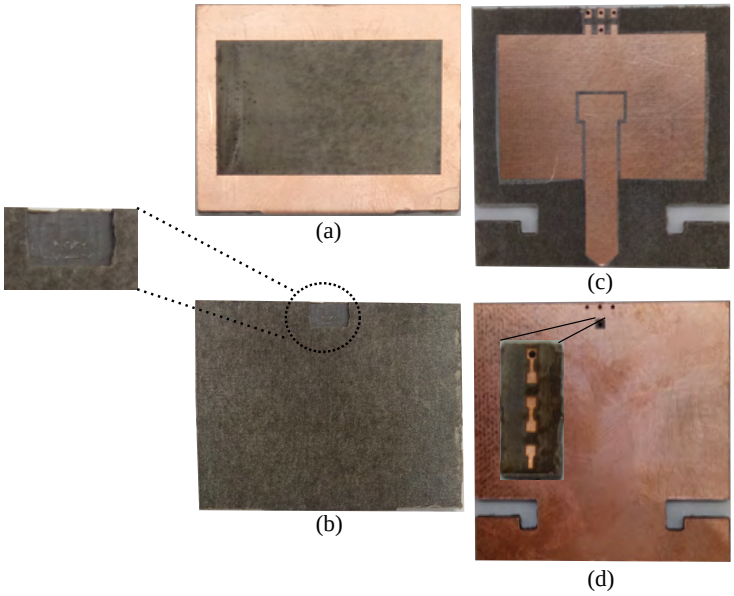

Figure 9.23. Top view of the top and bottom substrates.

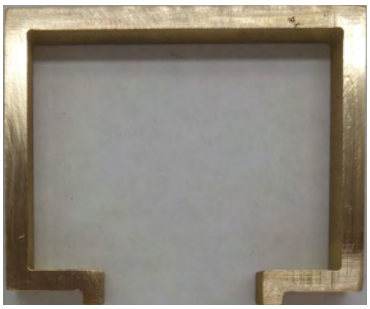

Figure 9.24. Topology of the cavity walls which are realized from a 3.2 mm thick section of brass.

The top and bottom layer of the fabricated antenna are shown in Fig. 9.25(a) and Fig. 9.25(b) respectively.

9.5 Experimental Validation

The near-field performance of the antenna is investigated by considering how the operating frequency of the antenna is altered as a function of the reverse biased DC voltage, or equivalently the varactor capacitance. Figure. 9.26 compares the simulated and measured operating frequency as a function of varactor capacitance. Two sets of simulation results are provided: Set 1 represents the simulation results of the nominal

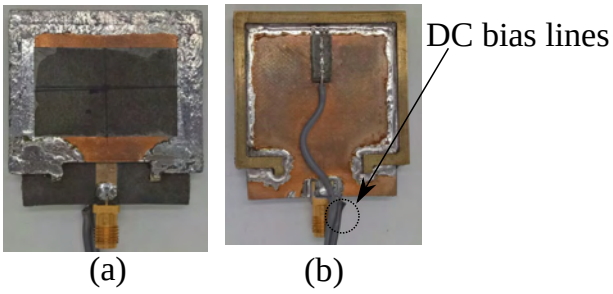

Figure 9.25. The top layer (a) and bottom layer (b) of the fabricated antenna.

design. Set 2 is obtained using a spacer of 1 mm between the top and bottom substrate, which corresponds to a fabrication error that was discovered after the antenna was manufactured. Overall the measured results show that the antenna operating frequency can be adjusted as expected from simulations in either case. The mild discrepancies between the simulated results for Set 2 and the measured frequencies could be due to uncertainties in knowing the varactor properties. Unless otherwise stated, for the remainder of this chapter the simulation results will be based on Set 2.

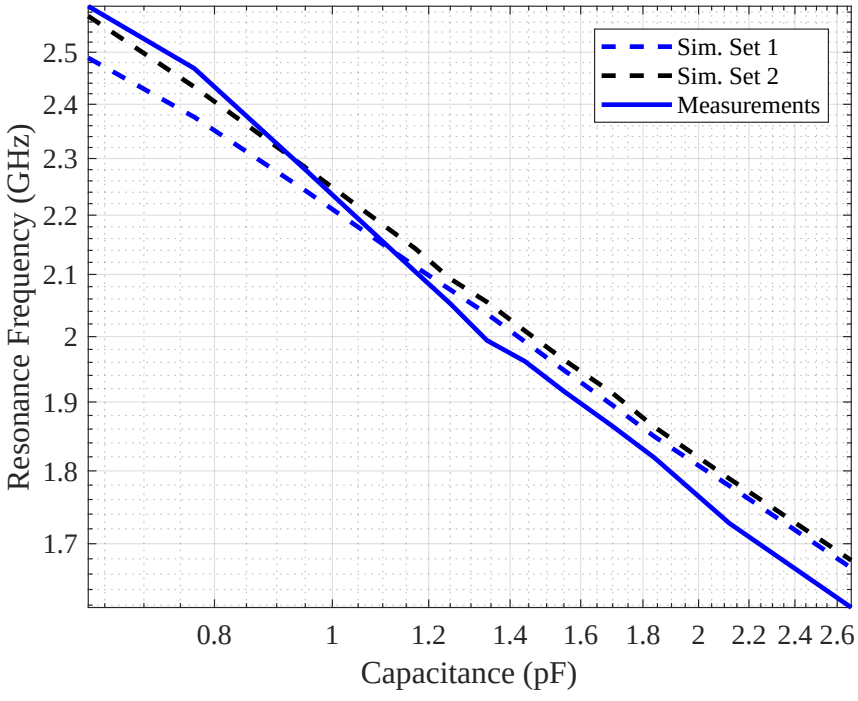

Figure 9.26. Simulated and measured variation in the resonance frequency of the antenna as a function of varactor capacitance.

For the purposes of illustration the simulated and measured reflection coefficient at a varactor capacitance of 0.63 pF and 0.95 pF are shown in Fig. 9.27(a) and Fig. 9.27(b)

respectively. For both cases the simulation results are presented for two values of varactor internal resistance: 0.8 Ω and 1.5 Ω. It appears that the measured results are in closer agreement with the simulations using an internal resistance of 1.5 Ω. It must be emphasized that the varactor internal resistance is specified at 500 MHz. As the varactor is being operated at a significantly larger frequency it is not unreasonable to expect that the varactor resistance will be higher than quoted at 500 MHz.

The measured radiation patterns at 0.63 pF and 0.95 pF using an internal resistance of 1.5 Ω are presented in Fig. 9.28 and Fig. 9.29 respectively. Generally, there is a reasonable agreement between simulations and measurements. The discrepancies off broadside could be due to measurement non-idealities. Specifically, to support the antenna a 3D printed stand is utilized which may have some effect on the patterns.

9.6 Conclusions

In this chapter the design framework of a new compact frequency-reconfigurable multi-layer cavity-backed broad-slot antenna was presented. The antenna which is excited through a planar feeding mechanism can be impedance matched over a large fractional tuning range of 20% without requiring lumped elements for impedance matching purposes. Additionally, due to the choice of the feeding mechanism the design of the DC bias network was highly simplified. Initial results for the reflection coefficient and radiation patterns were presented which suggests that the antenna behaves as expected. These results suggest that the proposed antenna could be adapted for body-worn applications, following fabrication methods similar as used for flexible cavity antennas presented in Chapter 6 and 7. Wearable reconfigurable antennas will allow to dynamically compensate for adverse environmental conditions such as bending, humidity and proximity to human body tissue.

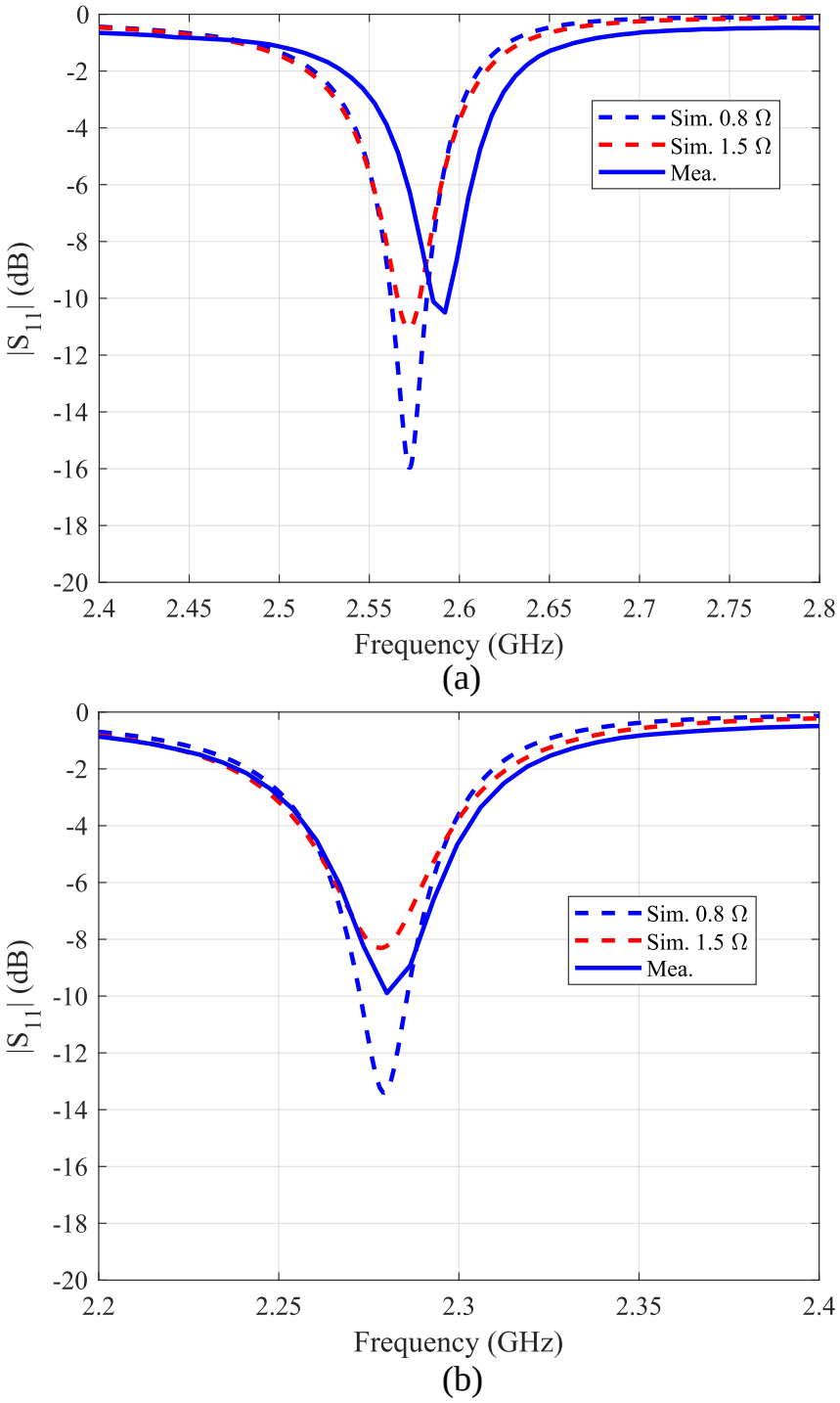

Figure 9.27. (a) Simulated and measured results for a varactor capacitance of 0.63 pF and (b) simulated and measured results for a varactor capacitance of 0.95 pF. In both cases the simulation results are presented for an varactor resistance of 0.8 Ω and 1.5 Ω.

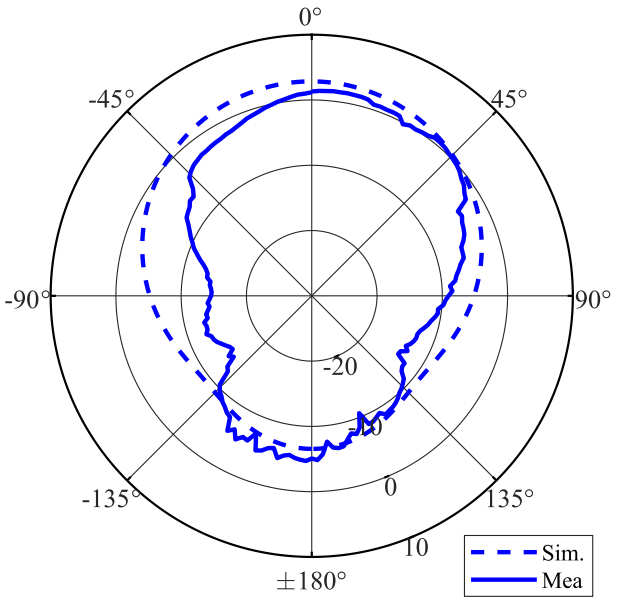

Figure 9.28. Simulated and measured radiation patterns for 0.63 pF.

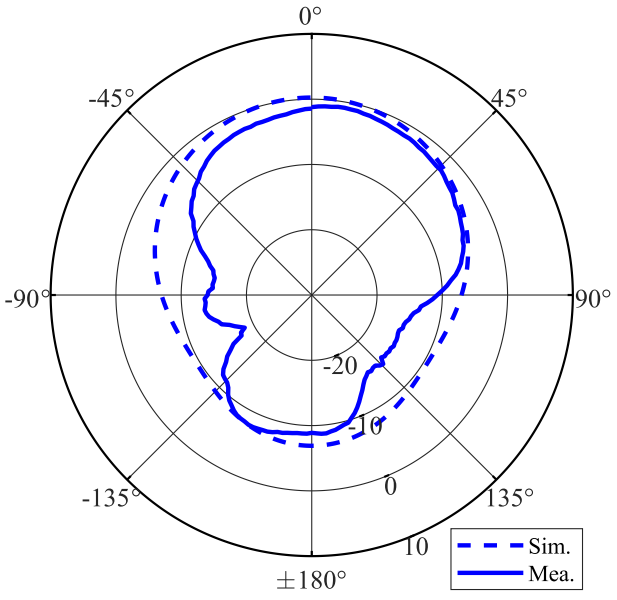

Figure 9.29. Simulated and measured radiation patterns for 0.95 pF.

Chapter 10

Summary and Outlook

THIS chapter concludes the thesis by summarizing the main outcomes of each chapter. Thereafter potential avenues for further research are explored. Lastly, a concluding statement is provided and the thesis is ended.

10.1 Summary

This thesis has been segmented into three main parts. The first part focused on practical issues related to the design and utilization of wearable antennas. The second part focused on the design, implementation and validation of new wearable cavity antennas. The final part laid the ground work for the realization of textile frequency reconfigurable antennas. A summary of each chapter is provided below.

10.1.1 Part One - Practical Issues: Summary

The first chapter of this thesis focused on the necessity of obtaining a reliable and robust connection between flexible and rigid devices. Three new connection strategies for interfacing flexible and rigid devices which could be realized solely through textile technology were proposed, implemented and examined on the merits of electrical and mechanical suitability. The major outcome of this chapter was the development of a new economical connection strategy known as the "wing solution" that can be useful in interfacing flexible and rigid devices.

The second chapter of this part focused on the effects of conformal ground planes on the far-field radiation characteristics of a low-profile monopolar antenna for two cases: off-body to on-body and on-body to on-body. Regarding the off-body to on-body case, the first step of the investigation was to determine a suitable ground plane dimension in a vehicular application. Thereafter the ground plane was curved around cylinders and spheres of different radii to obtain different degrees of curvature. To quantify the variation in the far-field radiation characteristics for the off-body to the on-body case, the ratio of radiated power in the upper to lower half-space was evaluated at 0.9 GHz and 2.45 GHz. Through numerical means it was shown that even mildly curving the ground plane could significantly alter the far-field radiation characteristics at 0.9 GHz and 2.45 GHz. More specifically, the end-fire gain was shown to be highly dependent on the degree of ground plane curvature. For the on-body to on-body case a similar trend was observed. Overall, it was shown that the effects of ground plane curvature can significantly affect the far-field radiation characteristics and hence must be accounted for in the design phase.

The last chapter within this part focused on realizing high performance wearable antenna ground planes through computerized embroidery. The motivation for exploring the utilization of computerized embroidery to realize robust ground planes was

framed from the perspective of user comfort and efficient material utilization. Scattering experiments were then employed to systematically investigate how the performance of embroidered structures varies as a function of three fabrication parameters. The three fabrication parameters for investigation were: stitch/grid spacing, embroidery density and embroidery layout. It was found that increasing the stitch and grid spacing resulted in structures with degraded performance. The degradation in performance for a particular stitch spacing could be mitigated by increasing the embroidery density. However, excessively increasing the embroidery density may actually degrade the performance due to surface roughness effects. Finally, it was shown that by laying the conductive threads perpendicular to each other, largely isotropic performance could be achieved. To characterize the embroidered structures an effective sheet resistance was numerically determined by two means: approximating the embroidered structures as homogeneous surfaces and approximating the physical layout of the threads. The validity of both methods was examined by designing the ground plane for a textile patch antenna using one of the embroidered structures. An excellent agreement between simulations and measurements for the textile patch antenna with a partially embroidered ground plane was observed in free-space and when in close proximity to human body tissue. Based on the obtained results for the textile patch antenna with an embroidered ground plane, it was concluded that scattering experiments are a viable method of characterizing the performance of embroidered structures. Additionally, it was concluded that approximating the physical distribution of the threads is the preferred approach in characterizing and modeling embroidered structures.

10.1.2 Part Two - Wearable Cavity Antennas: Summary

The second part of this thesis presented two new wearable cavity antennas. The first chapter in this part presented a new miniaturized UHF cavity-backed slot antenna which had a relatively large bandwidth for a compact size. Starting from a standard cavity-backed slot antenna, extensive miniaturization was achieved by combining folding techniques, inductive loading of the radiating slot and then finally removing half of the antenna by exploiting a magnetic wall symmetry condition in the center of the antenna. After having miniaturized the antenna the focus shifted onto the bandwidth, which was enhanced by increasing the width of the radiating slot. Through the aforementioned steps a miniaturized multi-layer cavity-backed slot-monopole antenna was realized which exhibited a free-space bandwidth of 3.8% for a cavity thickness of

$0.0149\lambda_0$. To enhance the wearability, a shielded-stripline was used to excite the cavity. Based on numerical methods it was shown that the antenna could be made relatively robust to the effects of the human body through a small extension of the ground plane. By experimental means, the antenna was shown to be robust to the effects of the human body and mechanical deformations. An excellent agreement between simulations and measurements validated the geometry. Lastly a design variation was presented whereby through the introduction of a slot which was centered in the middle metallic layer, the antenna could be further miniaturized whilst retaining a substantial free-space bandwidth.

The second chapter in this part presented a new dual-band slot loaded half-mode substrate-integrated cavity-antenna operating at 2.45 GHz and 5.8 GHz. Dual-band operation was achieved by integrating two radiating elements into the single geometry. Specifically, a single radiation band was achieved by designing the half-mode substrate-integrated cavity to operate at 2.45 GHz. Then, to generate another radiation band at 5.8 GHz a suitably dimensioned slot was added on the top ground plane. An attractive feature of this antenna was the largely independent control of the lower and higher frequencies. To enhance wearability a shielded-stripline was utilized as the excitation element for the antenna. To excite the fundamental cavity mode (TE_{10}) through the shielded-stripline which nominally operates in the quasi-TEM mode, a stripline to waveguide transition was required. The transition was achieved by short-circuiting the stripline to the bottom ground plane. A salient feature of the antenna was the excitation of two different modes at two widely separated frequencies through the shielded-stripline. Through experimental means the antenna was shown to be robust to the effects of the human body and mechanical deformations. Finally, a design variation was presented wherein the bandwidth at the lower band could be significantly enhanced through the introduction of an aperture slot. Importantly, the introduction of the aperture slot did not significantly affect the higher operation band.

10.1.3 Part Three - Adaptive Antennas: Summary

The first chapter of the last part of this thesis focused on an important first step in realizing textile frequency reconfigurable antennas. Specifically, how much tuning range should textile frequency reconfigurable antennas have, to compensate for variations in the operating frequency due to adverse environmental conditions? To address this

pertinent question a numerical and experimental study was performed which quantified the variations in operating frequency of a modular textile patch when subjected three adverse environmental conditions. These conditions were: moisture absorption, antenna curvature and proximity to human body tissue. An interesting outcome of this study, based on simulations, was that when the antenna was subjected to loading by the human body above it the resonance frequency of the antenna *shifts upwards* by approximately 3.0%. Experimentally it was even shown that when the antenna was below a loading body part the frequency could shift upwards by 6.0%. In contrast, through numerical and experimental methods it was determined that if the top metalized layer of the antenna was exposed to moisture the resonance frequency could shift downwards by 5.0%. Overall these results suggest that textile frequency reconfigurable antennas may need to have approximately $\pm$ 6.0% compensation factor in the tuning range to mitigate the effect of the aforementioned adverse environmental conditions.

The final technical chapter of this thesis presented the design methodology for a new type of frequency reconfigurable cavity-backed slot antenna. The main mechanism of reconfiguration was to adjust the capacitance of the antenna by strategically placing varactors inside the cavity. As the varactors are inside the cavity they are mechanically insulated from adverse external forces. Due to the choice of the feeding element, the design of the DC bias network is highly simplified. Additionally, as the DC bias network is behind the antenna ground plane there is minimal interaction between the radiating element and the DC bias network. It was shown that the antenna can be impedance matched over a relatively large fractional tuning range of 20% without needing lumped impedance matching elements such as inductors or capacitors. The detailed fabrication procedure to realize the antenna was also presented. Finally, initial measurement results were presented, showing a reasonable agreement between simulations and measurements. These initial results suggest that the antenna behaves as expected.

10.2 Outlook

In this section future research directions are presented. The first area relates to artificially synthesized ground planes such as artificial magnetic conductors. One major challenge in using artificial magnetic conductors for body-worn applications relates

to the planar size. Most of the textile artificial magnetic conductors that have been presented are usually rather large, since they are composed of extended periodic structures. The overall dimensions of the artificial magnetic conductors is highly dependent on the unit cell topology. A majority of the wearable artificial magnetic conductors use simple rectangular shapes as the unit cells. An alternative option could be to explore semi-circular unit-cells which can potentially be more compact than rectangular unit-cells. The current proposition is inspired by a recent contribution in the terahertz region which exploited coaxial type unit-cells [168]. Due to the symmetry of the unit-cell it may be possible to cut the unit-cell in half whilst still retaining the attractive features such as zero-reflection phase.

Another challenge that pertains to artificial magnetic conductors is the bandwidth over which a zero reflection phase property can be obtained. Generally speaking it is challenging to realize artificial magnetic conductors that have a large operational bandwidth. It may be worth investigating if artificial magnetic conductors can be realized from self-complementary unit-cells. Artificially synthesized structures based on self-complementary unit-cells has recently started gaining attention courtesy of the work presented in [169]. In this contribution a theoretical study was performed which showed that when properly designed, self-complementary unit-cells could be used to design a very wideband (theoretical limit of 70%) linear to circular polarization converter. It was also implied that non-resonant self-complementary unit-cells could be used to design wideband artificial magnetic conductors with robust performance under a range of polarizations and incidence angles. However, no experimental results for a wideband artificial magnetic conductor were presented, which may suggest there could be some difficulties that may need to be addressed. As a first step towards a textile realization, a thorough study of various self-complementary unit-cells needs to be performed.

The next potential area of future research pertains to reconfigurable metasurfaces to facilitate beam steering, beamwidth and polarization reconfigurability. Reconfigurable metasurfaces can be particularly attractive in cases where it is difficult to directly alter the far-field radiation characteristics of an antenna. For example, to alter the far-field radiation properties of the miniaturized UHF multi-layer cavity-backed slot-monopole, a modification of the slot topology is necessary. However, dynamically altering the slot topology can be quite challenging. On the contrary, reconfigurable metasurfaces

can be designed independently from the antenna. A challenge in using reconfigurable metasurfaces is to minimize the losses in the structure.

10.3 Concluding statement

Overall this thesis has holistically investigated and advanced the concept of body-worn antennas. Initially, subsidiary issues related to the utilization of wearable antennas were been studied with several new contributions presented and validated. Additionally, two new wearable cavity antennas have been presented which are excellent candidates for body-worn communications. Finally, initial ground work was laid for the realization of textile frequency reconfigurable antennas. Then the design of a new type compact low-profile frequency reconfigurable antenna was presented. The proposed frequency reconfigurable antenna features many attractive features making it a strong candidate for adaptive body-worn antennas. Further research into wearable antennas will accelerate the development of body-worn communications which will revolutionize fields such as healthcare and security.

Bibliography

[1] P. Nepa and H. Rogier, "Wearable Antennas for Off-Body Radio Links at VHF and UHF Bands: Challenges, the state of the art, and future trends below 1 GHz." *IEEE Antennas and Propagation Magazine*, vol. 57, no. 5, pp. 30–52, October 2015.

[2] N. J. Kirsch, N. A. Vacirca, E. E. Plowman, T. P. Kurzweg, A. K. Fontecchio, and K. R. Dandekar, "Optically transparent conductive polymer RFID meandering dipole antenna," in *IEEE International Conference on RFID*, April 2009, pp. 278–282.

[3] S. J. Chen, C. Fumeaux, P. Talemi, B. Chivers, and R. Shepherd, "Progress in conductive polymer antennas based on free-standing polypyrrole and PEDOT: PSS," in *17th International Symposium on Antenna Technology and Applied Electromagnetics (ANTEM)*, July 2016, pp. 1–4.

[4] G. Shaker, S. Safavi-Naeini, N. Sangary, and M. M. Tentzeris, "Inkjet Printing of Ultrawideband (UWB) Antennas on Paper-Based Substrates," *IEEE Antennas and Wireless Propagation Letters*, vol. 10, pp. 111–114, January 2011.

[5] S. Kim, Y. J. Ren, H. Lee, A. Rida, S. Nikolaou, and M. M. Tentzeris, "Monopole Antenna With Inkjet-Printed EBG Array on Paper Substrate for Wearable Applications," *IEEE Antennas and Wireless Propagation Letters*, vol. 11, pp. 663–666, June 2012.

[6] E. K. Kaivanto, M. Berg, E. Salonen, and P. de Maagt, "Wearable Circularly Polarized Antenna for Personal Satellite Communication and Navigation," *IEEE Transactions on Antennas and Propagation*, vol. 59, pp. 4490–4496, December 2011.

[7] A. Kiourti and J. L. Volakis, "High-Geometrical-Accuracy Embroidery Process for Textile Antennas with Fine Details," *IEEE Antennas and Wireless Propagation Letters*, vol. 14, pp. 1474–1477, October 2015.

[8] T. Acti, A. Chauraya, S. Zhang, W. G. Whittow, R. Seager, J. C. Vardaxoglou, and T. Dias, "Embroidered Wire Dipole Antennas Using Novel Copper Yarns," *IEEE Antennas and Wireless Propagation Letters*, vol. 14, pp. 638–641, November 2015.

[9] C.-Y.-D. Sim, C.-W. Tseng, and H.-J. Leu, "Embroidered wearable antenna for ultrawideband applications," *Microwave and Optical Technology Letters*, vol. 54, no. 11, 2012.

[10] Y. Ouyang and W. J. Chappell, "High Frequency Properties of Electro-Textiles for Wearable Antenna Applications," *IEEE Transactions on Antennas and Propagation*, vol. 56, pp. 381–389, February 2008.

[11] T. Kaufmann, Z. Xu, and C. Fumeaux, "Wearable substrate-integrated waveguide with embroidered vias," in *The 8th European Conference on Antennas and Propagation (EuCAP 2014)*, April 2014, pp. 1746–1750.

[12] B. Sanz-Izquierdo, F. Huang, and J. C. Batchelor, "Covert dual-band wearable button antenna," *Electronics Letters*, vol. 42, pp. 668–670, June 2006.

[13] M. Mantash, A. C. Tarot, S. Collardey, and K. Mahdjoubi, "Wearable monopole zip antenna," *Electronics Letters*, vol. 47, pp. 1266–1267, November 2011.

[14] M. Klemm and G. Troester, "Textile UWB Antennas for Wireless Body Area Networks," *IEEE Transactions on Antennas and Propagation*, vol. 54, pp. 3192–3197, November 2006.

[15] S. Zhang, A. Paraskevopoulos, C. Luxey, J. Pinto, and W. Whittow, "Broad-band embroidered spiral antenna for off-body communications," *IET Microwaves, Antennas Propagation*, no. 13, pp. 1395–1401, October 2016.

[16] P. B. Samal, P. J. Soh, and G. A. E. Vandenbosch, "UWB All-Textile Antenna With Full Ground Plane for Off-Body WBAN Communications," *IEEE Transactions on Antennas and Propagation*, vol. 62, pp. 102–108, October 2014.

[17] L. A. Y. Poffelie, P. J. Soh, S. Yan, and G. A. E. Vandenbosch, "A High-Fidelity All-Textile UWB Antenna With Low Back Radiation for Off-Body WBNA Applications," *IEEE Transactions on Antennas and Propagation*, vol. 64, no. 2, pp. 757–760, February 2016.

[18] A. A. Serra, P. Nepa, and G. Manara, "A Wearable Two-Antenna System on a Life Jacket for Cospas-Sarsat Personal Locator Beacons," *IEEE Transactions on Antennas and Propagation*, vol. 60, pp. 1035–1042, February 2012.

[19] L. Y. Ji, Y. J. Guo, P. Y. Qin, S. X. Gong, and R. Mittra, "A Reconfigurable Partially Reflective Surface (PRS) Antenna for Beam Steering," *IEEE Transactions on Antennas and Propagation*, vol. 63, pp. 2387–2395, June 2015.

[20] D. Blanco and E. Rajo-Iglesias, "Textile Fabry-Pèrot Antenna," *IEEE Antennas and Wireless Propagation Letters*.

[21] R. Moro, S. Agneessens, H. Rogier, and M. Bozzi, "Wearable textile antenna in substrate integrated waveguide technology," *Electronics letters*, vol. 48, no. 16, pp. 985–987, August 2012.

[22] Y. Hong, J. Tak, and J. Choi, "An All-Textile SIW Cavity-Backed Circular Ring-Slot Antenna for WBAN Applications," *IEEE Antennas and Wireless Propagation Letters*, vol. 15, pp. 1995–1999, April 2016.

[23] R. Moro, S. Agneessens, H. Rogier, A. Dierck, and M. Bozzi, "Textile Microwave Components in Substrate Integrated Waveguide Technology," *IEEE Transactions on Microwave Theory and Techniques*, vol. 63, no. 2, pp. 422–432, Feburary 2015.

[24] T. Kaufmann and C. Fumeaux, "Wearable Textile Half-Mode Substrate-Integrated Cavity Antenna Using Embroidered Vias," *IEEE Antennas and Wireless Propagation Letters*, vol. 12, June 2013.

[25] S. Agneessens, S. Lemey, T. Vervust, and H. Rogier, "Wearable, Small, and Robust: The Circular Quarter-Mode Textile Antenna," *IEEE Antennas and Wireless Propagation Letters*, vol. 14, pp. 1482–1485, January 2015.

[26] H. Lee, J. Tak, and J. Choi, "Wearable Antenna Integrated into Military Berets for Indoor/Outdoor Positioning System," *IEEE Antennas and Wireless Propagation Letters*, vol. 16, pp. 1919–1922, March 2017.

[27] S. Yan, V. Volskiy, and G. A. E. Vandenbosch, "Compact Dual-Band Textile PIFA for 433-MH/2.4-GHz ISM Bands," *IEEE Antennas and Wireless Propagation Letters*, vol. 16, pp. 2436–2439, July 2017.

[28] R. B. V. B. Simorangkir, Y. Yang, L. Matekovits, and K. P. Esselle, "Dual-Band Dual-Mode Textile Antenna on PDMS Substrate for Body-Centric Communications," *IEEE Antennas and Wireless Propagation Letters*, vol. 16, pp. 677–680, August 2017.

[29] S. Yan, P. J. Soh, and G. A. E. Vandenbosch, "Dual-Band Textile MIMO Antenna Based on Substrate-Integrated Waveguide (SIW) Technology," *IEEE Transactions on Antennas and Propagation*, vol. 63, pp. 4640–4647, November 2015.

[30] Z. Wang, L. Z. Lee, D. Psychoudakis, and J. L. Volakis, "Embroidered Multiband Body-Worn Antenna for GSM/PCS/WLAN Communications," *IEEE Transactions on Antennas and Propagation*, vol. 62, pp. 3321–3329, June 2014.

[31] C. L. Holloway, E. F. Kuester, J. A. Gordon, J. O'Hara, J. Booth, and D. R. Smith, "An Overview of the Theory and Applications of Metasurfaces: The Two-Dimensional Equivalents of Metamaterials," *IEEE Antennas and Propagation Magazine*, vol. 54, pp. 10–35, April 2012.

[32] E. Rajo-Iglesias, I. Gallego-Gallego, L. Inclan-Sanchez, and O. Quevedo-Teruel, "Textile Soft Surface for Back Radiation Reduction in Bent Wearable Antennas," *IEEE Transactions on Antennas and Propagation*, vol. 62, pp. 3873–3878, July 2014.

[33] J. Tak, Y. Hong, and J. Choi, "Textile antenna with EBG structure for body surface wave enhancement," *Electronics Letters*, vol. 51, pp. 1131–1132, July 2015.

[34] C.-J. Lee, K. M. K. H. Leong, and T. Itoh, "Composite right/left-handed transmission line based compact resonant antennas for rf module integration," *IEEE Transactions on Antennas and Propagation*, vol. 54, pp. 2283–2291, August 2006.

[35] S. Yan, P. J. Soh, and G. A. E. Vandenbosch, "Compact all-textile dual-band antenna loaded with metamaterial-inspired structure," *IEEE Antennas and Wireless Propagation Letters*, vol. 14, pp. 1486–1489, November 2015.

[36] T. F. Kennedy, P. W. Fink, A. W. Chu, N. J. Champagne, G. Y. Lin, and M. A. Khayat, "Body-Worn E-Textile Antennas: The Good, the Low-Mass, and the Conformal," *IEEE Transactions on Antennas and Propagation*, vol. 57, pp. 910–918, April 2009.

[37] N. Chahat, M. Zhadobov, S. A. Muhammad, L. L. Coq, and R. Sauleau, "60-GHz Textile Antenna Array for Body-Centric Communications," *IEEE Transactions on Antennas and Propagation*, vol. 61, no. 4, pp. 1816–1824, April 2013.

[38] C. Hertleer, A. Tronquo, H. Rogier, L. Vallozzi, and L. V. Langenhove, "Aperture-Coupled Patch Antenna for Integration Into Wearable Textile Systems," *IEEE Antennas and Wireless Propagation Letters*, vol. 6, pp. 392–395, August 2007.

[39] A. Kiourti and J. L. Volakis, "Stretchable and Flexible E-Fiber Wire Antennas Embedded in Polymer," *IEEE Antennas and Wireless Propagation Letters*, vol. 13, pp. 1381–1384, July 2014.

[40] D. Govender, J. Arnold, and W. Martinsen, "Radio frequency performance and strain testing of an iron-on fabric shielded stripline," in *2015 International Symposium on Antennas and Propagation (ISAP)*, November 2015, pp. 1–4.

[41] A. A. Kostrzewski, K. S. Leea, E. Gansa, C. A. Winterhalter, and T. P. Jannsona, *Proc. SPIE 6538, Sensors, and Command, Control, Communications, and Intelligence (C31) Technologies for Homeland Security and Homeland Defense VI, 653804*.

[42] T. Kellomäki, "Snap-on buttons in a coaxial-to-microstrip transition," in *Loughborough Antennas Propagation Conference (LAPC)*, November 2009, pp. 437–440.

[43] D. S. Fonseca, R. D. Seager, and J. A. Flint, "Textile-to-rigid microstrip transition using permanent magnets," *Electronics Letters*, vol. 51, no. 9, pp. 709–710, April 2015.

[44] R. D. Seager, A. Chauraya, S. Zhang, W. Whittow, and Y. Vardaxoglou, "Flexible radio frequency connectors for textile electronics," *Electronics Letters*, vol. 49, no. 22, pp. 1371–1373, October 2013.

[45] N. Nguyen-Trong, A. Piotrowski, T. Kaufmann, and C. Fumeaux, "Low-Profile Wideband Monopolar UHF Antennas for Integration Onto Vehicles and Helmets," *IEEE Transactions on Antennas and Propagation*, vol. 64, no. 6, pp. 2562–2568, June 2016.

[46] Z. Wang, L. Zhang, Y. Bayram, and J. L. Volakis, "Embroidered Conductive Fibers on Polymer Composite for Conformal Antennas," *IEEE Transactions on Antennas and Propagation*, vol. 60, pp. 4141–4147, September 2012.

[47] Z. Wang, L. Z. Lee, D. Psychoudakis, and J. L. Volakis, "Embroidered Multiband Body-Worn Antenna for GSM/PCS/WLAN Communications," *IEEE Transactions on Antennas and Propagation*, vol. 62, pp. 3321–3329, June 2014.

[48] K. Koski, A. Vena, L. Sydänheimo, L. Ukkonen, and Y. Rahmat-Samii, "Design and Implementation of Electro-Textile Ground Planes for Wearable UHF RFID Patch Tag Antennas," *IEEE Antennas and Wireless Propagation Letters*, vol. 12, pp. 964–967, August 2013.

[49] E. Moradi, T. Bjorninen, L. Ukkonen, and Y. Rahmat-Samii, "Effects of Sewing Pattern on the Performance of Embroidered Dipole-Type RFID Tag Antennas," *IEEE Antennas and Wireless Propagation Letters*, vol. 11, pp. 1482–1485, December 2012.

[50] C. Wolff. Rayleigh- versus Mie- scattering. [Online]. Available: http://www.radartutorial.eu/01.basics/Rayleigh-%20versus%20Mie-Scattering.en.html

[51] A. G. Santiago, J. R. Costa, and C. A. Fernandes, "Broadband UHF RFID Passive Tag Antenna for Near-Body Applications," *IEEE Antennas and Wireless Propagation Letters*, vol. 12, pp. 136–139, January 2013.

[52] M. Svanda and M. Polivka, "Small-Size Wearable High-Efficiency TAG Antenna for UHF RFID of People," *International Journal of Antennas and Propagation*, vol. 2014, Article ID 509768 5 pages.

[53] T. Kaufmann, D. C. Ranasinghe, M. Zhou, and C. Fumeaux, "Wearable Quarter-Wave Folded Microstrip Antenna for Passive UHF RFID Applications," *International Journal of Antennas and Propagation*, vol. 2013, Article ID 129839, 11 pages.

[54] S. Amendola, L. Bianchi, and G. Marrocco, "Movement Detection of Human Body Segments: Passive radio-frequency identification and machine-learning technologies." *IEEE Antennas and Propagation Magazine*, vol. 57, pp. 23–37, June 2015.

[55] S. Yan, P. J. Soh, and G. A. E. Vandenbosch, "Wearable dual-band composite right/left-handed waveguide textile antenna for WLAN applications," *Electronics Letters*, vol. 50, no. 6, pp. 424–426, 2014.

[56] S. Zhu and R. Langley, "Dual-Band Wearable Textile Antenna on an EBG Substrate," *IEEE Transactions on Antennas and Propagation*, vol. 57, no. 4, pp. 926–935, 2009.

[57] S. Yan, P. J. Soh, and G. A. E. Vandenbosch, "Wearable Dual-Band Magneto-Electric Dipole Antenna for WBAN/WLAN Applications," *IEEE Transactions on Antennas and Propagation*, vol. 63, no. 9, pp. 4165–4169, September 2015.

[58] S. Agneessens and H. Rogier, "Compact Half Diamond Dual-Band Textile HMSIW On-Body Antenna," *IEEE Transactions on Antennas and Propagation*, vol. 62, no. 5, pp. 2374–2381, Feburary 2014.

[59] R. B. V. B. Simorangkir, Y. Yang, K. P. Esselle, and B. A. Zeb, "A Method to Realize Robust Flexible Electronically Tunable Antennas Using Polymer-Embedded Conductive Fabric," *IEEE Transactions on Antennas and Propagation*, vol. 66, pp. 50–58, January 2018.

[60] N. Nguyen-Trong, T. Kaufmann, L. Hall, and C. Fumeaux, "Analysis and Design of a Reconfigurable Antenna Based on Half-Mode Substrate-Integrated Cavity," *IEEE Transactions on Antennas and Propagation*, vol. 63, no. 8, pp. 3345–3353, August 2015.

[61] A. P. Saghati and K. Entesari, "A Reconfigurable SIW Cavity-Backed Slot Antenna With One Octave Tuning Range," *IEEE Transactions on Antennas and Propagation*, vol. 61, no. 8, pp. 3937–3945, August 2013.

[62] C. R. White and G. M. Rebeiz, "A Shallow Varactor-Tuned Cavity-Backed Slot Antenna With a 1.9:1 Tuning Range," *IEEE Transactions on Antennas and Propagation*, vol. 58, no. 3, pp. 633–639, March 2010.

[63] S. V. Hum and H. Y. Xiong, "Analysis and Design of a Differentially-Fed Frequency Agile Microstrip Patch Antenna," *IEEE Transactions on Antennas and Propagation*, vol. 58, no. 10, pp. 3122–3130, October 2010.

[64] P. Hall, , and Y. Hao, *Antennas and Propagation For Body-Centric Wireless Communications*. 2nd Edition Artech House, 2012.

[65] D. Psychoudakis and J. L. Volakis, "Conformal Asymmetric Meandered Flare (AMF) Antenna for Body-Worn Applications," *IEEE Antennas and Wireless Propagation Letters*, vol. 8, pp. 931–934, July 2009.

[66] T. Kaufmann, A. Verma, V. T. Truong, B. Weng, R. Shepard, and C. Fumeaux, "Efficiency of a Compact Elliptical Planar Ultra-Wideband Aantenna Based on Conductive Polymers," *International Journal of Antennas and Propagation*, vol. 2012, Article ID 972696, 11 pages.

[67] W. G. Whittow, A. Chauraya, J. C. Vardaxoglou, Y. Li, R. Torah, K. Yang, S. Beeby, and J. Tudor, "Inkjet-Printed Microstrip Patch Antennas Realized on Textile for Wearable Applications," *IEEE Antennas and Wireless Propagation Letters*, vol. 13, pp. 71–74, January 2014.

[68] A. Tsolis, W. G. Whittow, A. A. Alexandridis, and J. C. Vardaxoglou, "Embroidery and Related Manufacturing Techniques for Wearable Antennas: Challenges and Opportunities," *Electronics*, vol. 3, no. 2, pp. 314–338, 2014.

[69] A. Kiourti, C. Lee, and J. L. Volakis, "Fabrication of Textile Antennas and Circuits with 0.1 mm Precision," *IEEE Antennas and Wireless Propagation Letters*, vol. 15, pp. 151–153, May 2016.

[70] S. J. Chen, T. Kaufmann, D. C. Ranasinghe, and C. Fumeaux, "A Modular Textile Antenna Design Using Snap-on Buttons for Wearable Applications," *IEEE Transactions on Antennas and Propagation*, vol. 64, pp. 894–903, March 2016.

[71] A. P. Feresidis and J. C. Vardaxoglou, "High gain planar antenna using optimised partially reflective surfaces," *IEE Proceedings - Microwaves, Antennas and Propagation*, vol. 148, pp. 345–350, December 2001.

[72] D. Ferreira, P. Pires, R. Rodrigues, and R. F. S. Caldeirinha, "Wearable Textile Antennas: Examining the effect of bending on their performance." *IEEE Antennas and Propagation Magazine*, vol. 59, pp. 54–59, June 2017.

[73] C. A. Balanis, *Antenna Theory Analysis And Design*. 3rd Edition John Wiley & Sons Inc., New York, 2005.

[74] P. S. Kildal, "Definition of artificially soft and hard surfaces for electromagnetic waves," *Electronics Letters*, vol. 24, pp. 168–170, Feburary 1988.

[75] A. Lai, T. Itoh, and C. Caloz, "Composite right/left-handed transmission line metamaterials," *IEEE Microwave Magazine*, vol. 5, pp. 34–50, September 2004.

[76] S. R. Best, "The Significance of Composite Right/Left-handed (CRLH) Transmission-Line Theory and Reactive Loading in the Design of Small Antennas," *IEEE Antennas and Propagation Magazine*, vol. 56, pp. 15–33, August 2014.

[77] Y. Dong and T. Itoh, "Promising Future of Metamaterials," *IEEE Microwave Magazine*, vol. 13, pp. 39–56, March 2012.

[78] C. Caloz, T. Itoh, and A. Rennings, "Crlh metamaterial leaky-wave and resonant antennas," *IEEE Antennas and Propagation Magazine*, vol. 50, pp. 25–39, October 2008.

[79] N. F. M. Aun, P. J. Soh, A. A. Al-Hadi, M. F. Jamlos, G. A. E. Vandenbosch, and D. Schreurs, "Revolutionizing Wearables for 5G: 5G Technologies: Recent Developments and Future Perspectives for Wearable Devices and Antennas," *IEEE Microwave Magazine*, vol. 18, pp. 108–124, May 2017.

[80] C. Hertleer, A. V. Laere, H. Rogier, and L. V. Langenhove, "Influence of Relative Humidity on Textile Antenna Performance," *Textile Research Journal*, vol. 80, no. 2, pp. 177–183, 2010.

[81] M. L. Scarpello, I. Kazani, C. Hertleer, H. Rogier, and D. V. Ginste, "Stability and Efficiency of Screen-Printed Wearable and Washable antennas," *IEEE Antennas and Wireless Propagation Letters*, vol. 11, pp. 838–841, July 2012.

[82] S. Yan and G. A. E. Vandenbosch, "Radiation Pattern-Reconfigurable Wearable Antenna Based on Metamaterial Structure," *IEEE Antennas and Wireless Propagation Letters*, vol. 15, pp. 1715–1718, February 2016.

[83] S. J. Chen, C. Fumeaux, D. C. Ranasinghe, and T. Kaufmann, "Paired Snap-On Buttons Connections for Balanced Antennas in Wearable Systems," *IEEE Antennas and Wireless Propagation Letters*, vol. 14, pp. 1498–1501, October 2014.

[84] P. S. Hall and Y. Hao, "Characterization of wireless channels on the human body," *URSI Radio Science Bulletin*, vol. 83, no. 4, pp. 12–25, December 2010.

[85] K. C. Gupta, R. Garg, I. Bahl, and P. Bhartia, *Microstrip Lines and Slotlines*. 2nd Edition Artech House, 1979.

[86] Z. Zu, T. Kaufmann, and C. Fumeaux, "Wearable Textile Shielded Stripline for Broadband Operation," *IEEE Microwave and Wireless Components Letters*, vol. 24, no. 8, pp. 566–568, June 2014.

[87] D. Bolle and M. Morganstern, "Monopole and conic antennas on spherical vehicles," *IEEE Transactions on Antennas and Propagation*, vol. 17, no. 4, pp. 477–484, July 1969.

[88] F. M. Tesche, A. R. Neureuther, and R. E. Stovall, "The Analysis of Monopole Antennas Located on a Spherical Vehicle: Part 2, Numerical and Experimental Results," *IEEE Transactions on Electromagnetic Compatibility*, vol. EMC-18, no. 1, pp. 8–15, Feburary 1976.

[89] S. P. Pinapati, N. Nguyen-Trong, A. Piotrowski, and C. Fumeaux, "Integration of a Wideband Low-Profile Monopolar Antenna onto Curved Metallic Surfaces," in *2017 IEEE-APS Topical Conference on Antennas and Propagation in Wireless Communications (APWC)*, September 2017, pp. 203–206.

[90] E. W. Seeley, "An experimental study of the disk-loaded folded monopole," *IRE Transactions on Antennas and Propagation*, vol. 4, no. 1, pp. 27–28, January 1956.

[91] C. Delaveaud, P. Leveque, and B. Jecko, "New kind of microstrip antenna: The monopolar wire-patch antenna," *Electronics letters*, vol. 30, no. 1, pp. 1–2, January 1994.

[92] J. S. Row, S. H. Yeh, and K. L. Wong, "A wide-band monopolar plate-patch antenna," *IEEE Transactions on Antennas and Propagation*, vol. 50, no. 9, pp. 1328–1330, December 2002.

[93] K. L. Lau, P. Li, and K. M. Luk, "A monopolar patch antenna with very wide impedance bandwidth," *IEEE Transactions on Antennas and Propagation*, vol. 53, no. 3, pp. 1004–1010, March 2005.

[94] K. L. Lau, K. C. Kong, and K. M. Luk, "Super-wideband monopolar patch antenna," *Electronics Letters*, vol. 44, no. 12, pp. 716–718, June 2008.

[95] T. Kaufmann and C. Fumeaux, "Low-Profile Magnetic Loop Monopole Antenna Based on a Square Substrate-Integrated Cavity," *International Journal of Antennas and Propagation*, vol. 2015, Article ID 694385, 6 pages.

[96] N. Nguyen-Trong, L. Hall, and C. Fumeaux, "A Frequency-and Pattern-Reconfigurable Center-Shorted Microstrip Antenna," *IEEE Antennas and Wireless Propagation Letters*, vol. 15, pp. 1955–1958, March 2016.

[97] A. Tsolis, W. G. Whittow, A. A. Alexandridis, and J. Vardaxoglou, "Embroidery and Related Manufacturing Techniques for Wearable Antennas: Challenges and Opportunities," *Electronics*, vol. 3, no. 2, pp. 314–338, 2014.

[98] T. Acti, A. Chauraya, S. Zhang, W. G. Whittow, R. Seager, J. C. Vardaxoglou, and T. Dias, "Embroidered Wire Dipole Antennas Using Novel Copper Yarns," *IEEE Antennas and Wireless Propagation Letters*, vol. 14, pp. 638–641, November 2015.

[99] B. Ivsic, D. Bonefacic, and J. Bartolic, "Considerations on Embroidered Textile Antennas for Wearable Applications," *IEEE Antennas and Wireless Propagation Letters*, vol. 12, pp. 1708–1711, March 2013.

[100] M. Toivonen, T. Bjrninen, L. Sydnheimo, L. Ukkonen, and Y. Rahmat-Samii, "Impact of Moisture and Washing on the Performance of Embroidered UHF RFID Tags," *IEEE Antennas and Wireless Propagation Letters*, vol. 12, pp. 1590–1593, November 2013.

[101] K. Koski, L. Sydnheimo, Y. Rahmat-Samii, and L. Ukkonen, "Fundamental Characteristics of Electro-Textiles in Wearable UHF RFID Patch Antennas for Body-Centric Sensing Systems," *IEEE Transactions on Antennas and Propagation*, vol. 62, pp. 6454–6462, December 2014.

[102] R. Seager, S. Zhang, A. Chauraya, W. Whittow, Y. Vardaxoglou, T. Acti, and T. Dias, "Effect of the fabrication parameters on the performance of embroidered antennas," *IET Microwaves, Antennas Propagation*, vol. 7, pp. 1174–1181, November 2013.

[103] T. C. Baum, R. W. Ziolkowski, K. Ghorbani, and K. J. Nicholson, "Embroidered Active Microwave Composite Preimpregnated Electronics - Pregtronics," *IEEE Transactions on Microwave Theory and Techniques*, vol. 64, pp. 3175–3186, October 2016.

[104] S. Zhang, W. Whittow, R. Seager, A. Chauraya, and J. C. Vardaxoglou, "Non-uniform mesh for embroidered microstrip antennas," *IET Microwaves, Antennas Propagation*, vol. 11, pp. 1086–1091, July 2017.

[105] I. J. Bahl, M. Bozzi, and R. Garg, *Microstrip Lines and Slotlines*. Third Edition Artech House, 2013.

[106] R. K. Shawl, B. R. Longj, D. H. Werner, and A. Gavrin, "The Characterization of Conductive Textile Materials Intended for Radio Frequency Applications," *IEEE Antennas and Propagation Magazine*, vol. 49, pp. 28–40, June 2007.

[107] D. Cottet, J. Grzyb, T. Kirstein, and G. Tröster, "Electrical Characterization of Textile Transmission Lines," *IEEE Transactions on Advanced Packaging*, vol. 26, no. 2, pp. 182–190, May 2003.

[108] Y. Ouyang and W. J. Chappell, "High Frequency Properties of Electro-Textiles for Wearable Antenna Applications," *IEEE Transactions on Antennas and Propagation*, vol. 56, pp. 381–389, February 2008.

[109] K. Koski, E. Moradi, A. Vena, T. Björnien, L. Sydänheimo, L. Ukkoken, and Y. Rahmat-Samii, "Ccharacterization of Electro-textiles Using Wireless Reflectometry for Optimization of Wearable UHF RFID Tags," *Progress in Electromagnetics Research*, pp. 1188 – 1192, August 2013.

[110] S. P. Pinapati, D. C. Ranasinghe, and C. Fumeaux, "Characterization of Conductive Textiles for Wearable RFID Applications," in *2016 International Conference on Electromagnetics in Advanced Applications (ICEAA)*, September 2016, pp. 341–344.

[111] T. Tantisopharak, H. Moon, P. Youryon, K. Bunya-athichart, M. Krairiksh, and T. K. Sarkar, "Non-destructive Determination of the Maturity of the Durian Fruit in the Frequency Domain Using the Change in the Natural Frequency," *IEEE Transactions on Antennas and Propagation*, vol. 64, pp. 1779–1787, May 2016.

[112] E. F. Knott, J. F. Shaeffer, and M. T. Tuley, *Radar Cross Section*. Second Edition Scitech Publishing, 2004.

[113] E. Hecht, *Optics*. 2nd Edition Addison-Wesley, 1987.

[114] SPEAG. Phantoms. [Online]. Available: https://www.speag.com/products/em-phantom/phantoms/

[115] S. Manzari, C. Occhiuzzi, and G. Marrocco, "Feasibility of Body-Centric Systems Using Passive Textile RFID Tags," *IEEE Antennas and Propagation Magazine*, vol. 54, no. 4, pp. 49–62, August 2012.

[116] C. Occhiuzzi, S. Cippitelli, and G. Marrocco, "Modeling, Design and Experimentation of Wearable RFID Sensor Tag," *IEEE Transactions on Antennas and Propagation*, vol. 58, no. 8, pp. 2490–2498, August 2010.

[117] G. Marrocco, "The art of UHF RFID antenna design: impedance-matching and size-reduction techniques," *IEEE Antennas and Propagation Magazine*, vol. 50, no. 1, pp. 66–79, Feb 2008.

[118] G. A. Casula, A. Michel, P. Nepa, G. Montisci, and G. Mazzarella, "Robustness of Wearable UHF-Band PIFAs to Human-Body Proximity," *IEEE Transactions on Antennas and Propagation*, vol. 64, no. 5, pp. 2050–2055, May 2016.

[119] E. A. Soliman, M. O. Sallam, W. D. Raedt, and G. A. E. Vandenbosch, "Miniaturized RFID Tag Antenna Operating at 915 MHz," *IEEE Antennas and Wireless Propagation Letters*, vol. 11, pp. 1068–1071, August 2012.

[120] Z. L. Ma, L. J. Jiang, J. Xi, and T. T. Ye, "A Single-Layer Compact HF-UHF Dual-Band RFID Tag Antenna," *IEEE Antennas and Wireless Propagation Letters*, vol. 11, pp. 1257–1260, October 2012.

[121] M. Rossi, S. Agneessens, H. Rogier, and D. V. Ginste, "Assembly-Line-Compatible Electromagnetic Characterization of Wearable Antenna Substrates," *IEEE Antennas and Wireless Propagation Letters*, vol. 16, pp. 1365–1368, December 2017.

[122] N. Nguyen-Trong, T. Kaufmann, L. Hall, and C. Fumeaux, "Variational Analysis of Folded Substrate-Integrated Waveguides," *IEEE Microwave and Wireless Components Letters*, vol. 25, no. 6, pp. 352–354, June 2015.

[123] D. M. Pozar, *Microwave Engineering*. 4th Edition Wiley, 2012.

[124] J. S. Hong, "Compact folded-waveguide resonators and filters," *IEE Proceedings - Microwaves, Antennas and Propagation*, vol. 153, no. 4, pp. 325–329, August 2006.

[125] N. Grigoropoulos, B. Sanz-Izquierdo, and P. R. Young, "Substrate integrated folded waveguides (SIFW) and filters," *IEEE Microwave and Wireless Components Letters*, vol. 15, no. 12, pp. 829–831, December 2005.

[126] G. L. Chen, T. L. Owens, and J. H. Whealton, "Theoretical study of the folded waveguide," *IEEE Transactions on Plasma Science*, vol. 16, no. 2, pp. 305–311, April 1988.

[127] C. Zhao, C. Fumeaux, and C. C. Lim, "Folded Substrate-Integrated Waveguide Band-Pass Post Filter," *IEEE Microwave and Wireless Components Letters*, vol. 27, no. 1, pp. 22–24, January 2017.

[128] W. Che, L. Geng, K. Deng, and Y. L. Chow, "Analysis and Experiments of Compact Folded Substrate-Integrated Waveguide," *IEEE Transactions on Microwave Theory and Techniques*, vol. 56, no. 1, pp. 88–93, January 2008.

[129] C. Zhao, C. Fumeaux, and C. C. Lim, "Folded Substrate-Integrated Waveguide Band-Pass Post Filter," *IEEE Microwave and Wireless Components Letters*, vol. 27, no. 1, pp. 22–24, January 2017.

[130] M. A. Morgan and F. K. Schwering, "Eigenmode analysis of dielectric loaded top-hat monopole antennas," *IEEE Transactions on Antennas and Propagation*, vol. 42, no. 1, pp. 54–61, January 1994.

[131] H. Li, J. Xiong, Y. Yu, and S. He, "A Simple Compact Reconfigurable Slot Antenna With a Very Wide Tuning Range," *IEEE Trans. Antennas Propag.*, vol. 58, no. 11, pp. 3725–3728, November 2010.

[132] M. V. Varnoosfaderani, D. V. Thiel, and J. W. Lu, "A Wideband Slot Antenna in a Box for Wearable Sensor Nodes," *IEEE Antennas and Wireless Propagation Letters*, vol. 14, pp. 1494–1497, January 2015.

[133] K. Koski, A. Vena, L. Sydänheimo, L. Ukkonen, and Y. Rahmat-Samii, "Design and Implementation of Electro-Textile Ground Planes for Wearable UHF RFID Patch Tag Antennas," *IEEE Antennas and Wireless Propagation Letters*, vol. 12, pp. 964–967, August 2013.

[134] F. X. Liu, T. Kaufmann, Z. Xu, and C. Fumeaux, "Wearable Applications of Quarter-Wave Patch and Half-Mode Cavity Antennas," *IEEE Antennas and Wireless Propagation Letters*, vol. 14, pp. 1478–1481, December 2015.

[135] T. Kaufmann and C. Fumeaux, "Quantifying the impact of seam compression on embroidered textile substrate-integrated structures," in *9th European Conference on Antennas and Propagation (EuCAP)*, May 2015, pp. 1–4.

[136] D. Psychoudakis and J. L. Volakis, "Conformal Asymmetric Meandered Flare (AMF) Antenna for Body-Worn Applications," *IEEE Antennas and Wireless Propagation Letters*, vol. 8, pp. 931–934, July 2009.

[137] G. A. Conway, S. L. Cotton, and W. G. Scanlon, "An Antennas and Propagation Approach to Improving Physical Layer Performance in Wireless Body Area networks," *IEEE Journal on Selected Areas in Communications*, vol. 27, no. 1, pp. 27–36, January 2009.

[138] G. A. Casula, A. Michel, G. Montisci, P. Nepa, and G. Valente, "Energy-Based Considerations for Ungrounded Wearable UHF Antenna Design," *IEEE Sensors Journal*, vol. 17, no. 3, pp. 687–694, Feburary 2017.

[139] S. Gabriel, R. W. Lau, and C. Gabriel, "The dielectric properties of biological tissues: II measurements in the frequency range 10 Hz to 20 20 GHz," *Physics in medicine and biology*, vol. 41, no. 11, pp. 2251–2269, April 1996.

[140] ——, "The dielectric properties of biological tissues: III parametric models for the dielectric spectrum of tissues," *Physics in medicine and biology*, vol. 41, no. 11, pp. 2271–2293, April 1996.

[141] A. Y. I. Ashyap, Z. Z. Abidin, S. H. Dahlan, H. A. Majid, S. M. Shah, M. R. Kamarudin, and A. Alomainy, "Compact and Low-Profile Textile EBG-Based Antenna for Wearable Medical Applications," *IEEE Antennas and Wireless Propagation Letters*, vol. 16, pp. 2550–2553, July 2017.

[142] Z. H. Jiang, D. E. Brocker, P. E. Sieber, and D. H. Werner, "A Compact, Low-Profile Metasurface-Enabled Antenna for Wearable Medical Body-Area Network Devices," *IEEE Transactions on Antennas and Propagation*, vol. 62, no. 8, pp. 4021–4030, August 2014.

[143] Y. Hong, J. Tak, and J. Choi, "An All-Textile SIW Cavity-Backed Circular Ring-Slot Antenna for WBAN Applications," *IEEE Antennas and Wireless Propagation Letters*, vol. 15, pp. 1995–1999, April 2016.

[144] N. F. M. Aun, P. J. Soh, A. A. Al-Hadi, M. F. Jamlos, G. A. E. Vandenbosch, and D. Schreurs, "Revolutionizing Wearables for 5G: 5G Technologies: Recent Developments and Future Perspectives for Wearable Devices and Antennas," *IEEE Microwave Magazine*, vol. 18, no. 3, pp. 108–124, May 2017.

[145] T. Niemi, P. Alitalo, A. O. Karilainen, and S. A. Tretyakov, "Electrically small Huygens source antenna for linear polarisation," *IET Microwaves, Antennas Propagation*, vol. 6, no. 7, pp. 735–739, May 2012.

[146] D.-H. Kwon, "On the radiation Q and the gain of crossed electric and magnetic dipole moments," *IEEE Transactions on Antennas and Propagation*, vol. 53, no. 5, pp. 1681–1687, May 2005.

[147] R. W. Ziolkowski, "Low Profile, Broadside Radiating, Electrically Small Huygens Source Antennas," *IEEE Access*, vol. 3, pp. 2644–2651, December 2015.

[148] K. M. Luk and B. Wu, "The Magnetoelectric Dipole–A Wideband Antenna for Base Stations in Mobile Communications," *Proceedings of the IEEE*, vol. 100, no. 7, pp. 2297–2307, July 2012.

[149] W. Hong, B. Liu, Y. Wang, Q. Lai, H. Tang, X. X. Yin, Y. D. Dong, Y. Zhang, and K. Wu, "Half Mode Substrate Integrated Waveguide: A New Guided Wave Structure for Microwave and Millimeter Wave Application," in *Joint 31st International Conference on Infrared Millimeter Waves and 14th International Conference on Teraherz Electronics (IRMMW-THz)*, September 2006, pp. 219–219.

[150] N. Nguyen-Trong, T. Kaufmann, and C. Fumeaux, "A Wideband Omnidirectional Horizontally Polarized Traveling-Wave Antenna Based on Half-Mode Substrate Integrated Waveguide," *IEEE Antennas and Wireless Propagation Letters*, vol. 12, pp. 682–685, May 2013.

[151] H. G. Booker, "Slot aerials and their relation to complementary wire aerials (Babinet's principle)," *Journal of the Institution of Electrical Engineers - Part IIIA: Radiolocation*, vol. 93, no. 4, pp. 620–626, 1946.

[152] R. E. Collin, *Foundations for Microwave Engineering*. 2nd Edition Wiley-IEEE Press, 2000.

[153] A. Ivanivsky, "Stripline-to-waveguide transition," September 1996, US Patent 5,559,480.

[154] R. L. Haupt and M. Lanagan, "Reconfigurable Antennas," *IEEE Antennas and Propagation Magazine*, vol. 55, no. 1, pp. 49–61, February 2013.

[155] N. Nguyen-Trong, A. Piotrowski, and C. Fumeaux, "A Frequency-Reconfigurable Dual-Band Low-Profile Monopolar Antenna," *IEEE Transactions on Antennas and Propagation*, vol. 65, no. 7, pp. 3336–3343, July 2017.

[156] L. Ge, M. Li, J. Wang, and H. Gu, "Unidirectional Dual-Band Stacked Patch Antenna With Independent Frequency Reconfiguration," *IEEE Antennas and Wireless Propagation Letters*, vol. 16, pp. 113–116, April 2017.

[157] L. Ge and K. M. Luk, "Frequency-Reconfigurable Low-Profile Circular Monopolar Patch Antenna," *IEEE Transactions on Antennas and Propagation*, vol. 62, no. 7, pp. 3443–3449, July 2014.

[158] L. Ge, K. M. Luk, and S. Chen, "360° Beam-Steering Reconfigurable Wideband Substrate-Integrated Waveguide Horn Antenna," *IEEE Transactions on Antennas and Propagation*, vol. 64, no. 12, pp. 5005–5011, December 2016.

[159] S. H. Chen, J. S. Row, and K. L. Wong, "Reconfigurable Square-Ring Patch Antenna With Pattern Diversity," *IEEE Transactions on Antennas and Propagation*, vol. 55, no. 2, pp. 472–475, February 2007.

[160] W. Lin, H. Wong, and R. W. Ziolkowski, "Wideband Pattern-Reconfigurable Antenna With Switchable Broadside and Conical Beams," *IEEE Antennas and Wireless Propagation Letters*, vol. 16, pp. 2638–2641, August 2017.

[161] H. H. Tran, N. Nguyen-Trong, T. T. Le, and H. C. Park, "Wideband and Multipolarization Reconfigurable Crossed Bowtie Dipole Antenna," *IEEE Transactions on Antennas and Propagation*, vol. 65, no. 12, pp. 6968–6975, December 2017.

[162] X. X. Yang, B. C. Shao, F. Yang, A. Z. Elsherbeni, and B. Gong, "A Polarization Reconfigurable Patch Antenna With Loop Slots on the Ground Plane," *IEEE Antennas and Wireless Propagation Letters*, vol. 11, pp. 69–72, January 2012.

[163] Y. J. Sung, T. U. Jang, and Y. S. Kim, "A reconfigurable microstrip antenna for switchable polarization," *IEEE Microwave and Wireless Components Letters*, vol. 14, no. 11, pp. 534–536, November 2004.

[164] L. Ge, Y. Li, J. Wang, and C. Y. D. Sim, "A Low-Profile Reconfigurable Cavity-Backed Slot Antenna With Frequency, Polarization, and Radiation Pattern Agility," *IEEE Transactions on Antennas and Propagation*, vol. 65, no. 5, pp. 2182–2189, May 2017.

[165] P. Y. Qin, Y. J. Guo, Y. Cai, E. Dutkiewicz, and C. H. Liang, "A Reconfigurable Antenna With Frequency and Polarization Agility," *IEEE Antennas and Wireless Propagation Letters*, vol. 10, pp. 1373–1376, December 2011.

[166] N. Nguyen-Trong, L. Hall, and C. Fumeaux, "A Frequency- and Pattern-Reconfigurable Center-Shorted Microstrip antenna," *IEEE Antennas and Wireless Propagation Letters*, vol. 15, March 2016.

[167] N. Nguyen-Trong and C. Fumeaux, "Tuning Range and Efficiency Optimization of a Frequency-Reconfigurable Patch Antenna," *IEEE Antennas and Wireless Propagation Letters*, vol. 17, no. 1, pp. 150–154, January 2018.

[168] W. S. L. Lee, S. Nirantar, D. Headland, M. Bhaskaran, S. Sriram, C. Fumeaux, and W. Withayachumnankul, "Broadband Terahertz Circular Polarization Beam Splitter," *Advanced Optical Materials*, vol. 6, no. 3, p. 1700852.

[169] J. D. Baena, S. B. Glybovski, J. P. del Risco, A. P. Slobozhanyuk, and P. A. Belov, "Broadband and Thin Linear-to-Circular Polarizers Based on Self-Complementary Zigzag Metasurfaces," *IEEE Transactions on Antennas and Propagation*, vol. 65, no. 8, pp. 4124–4133, August 2017.